



A University of Sussex PhD thesis

Available online via Sussex Research Online:

<http://sro.sussex.ac.uk/>

This thesis is protected by copyright which belongs to the author.

This thesis cannot be reproduced or quoted extensively from without first obtaining permission in writing from the Author

The content must not be changed in any way or sold commercially in any format or medium without the formal permission of the Author

When referring to this work, full bibliographic details including the author, title, awarding institution and date of the thesis must be given

Please visit Sussex Research Online for more information and further details



From Flavour and Higgs Precision Physics to LHC Discoveries

Sandra Kvedaraitė

Submitted for the degree of Doctor of Philosophy

University of Sussex

September 2020

Declaration

I hereby declare that this thesis has not been and will not be submitted in whole or in part to another University for the award of any other degree. The work presented in this thesis has been done in collaboration with Sebastian Jaeger, Martin Gorbahn, Gilad Perez, Inbar Savoray, Seung J. Lee, Gabriel Lee, Andrea Banfi, Barry M. Dillon and Wissarut Ketaiam and includes one published paper verbatim:

- S. Jäger, S. Kvedaraitė, G. Perez and I. Savoray, “Bounds and prospects for stable multiply charged particles at the LHC”, published in JHEP **04** (2019) 041, [1]. The calculations and plots have been done jointly by myself and Inbar, with suggestions and supervision from Sebastian and Gilad.

Parts of the following publication are included in Chapter 5:

- A. Banfi, B. M. Dillon, W. Ketaiam and S. Kvedaraitė, “Composite Higgs at high transverse momentum”, published in JHEP **01** (2020) 089, [2]. I have contributed to the calculation of CP-odd contribution to Higgs+jet in relevant QCD limits.

The rest of the thesis comprises of the following unpublished work:

- Chapter 2 and Chapter 3. The work has been done in collaboration with Sebastian and Martin. I have derived and calculated everything presented in these chapters. The method has been cross-checked with Sebastian and the diagrams with Martin.
- Chapter 5 and Chapter 6. The calculations presented in this chapter have been done by myself. The precise model details and cross-checks have been performed by Sebastian, Seung and Gabriel.

Parts of the work in Chapter 2 and 3 have also been presented in conference proceedings:

- S. Jäger, S. Kvedaraitė, “SMOM- $\overline{\text{MS}}$ Matching for B_K at Two-loop Order”, published in PoS LATTICE2018 (2018) 214, [3].

Signature:

Sandra Kvedaraitė

UNIVERSITY OF SUSSEX

SANDRA KVEDARAITĖ, DOCTOR OF PHILOSOPHY

FROM FLAVOUR AND HIGGS PRECISION PHYSICS TO LHC DISCOVERIESSUMMARY

While the Standard Model is a great experimental success, it is unsatisfactory as a theory. For instance, it does not explain the origin of the hierarchies between quark masses, nor resolve the hierarchy problem or unify couplings in the UV. In this thesis, we address these shortcomings by performing precision calculations, building BSM models and studying their collider phenomenology.

We improve the precision for the QCD prediction of the kaon bag parameter, which enters a dominant short-distance contribution to indirect CP violation. This is achieved by performing the first conversion between the SMOM and the $\overline{\text{MS}}$ scheme at two-loop order.

Furthermore, we consider scalar and fermionic top partners that carry exotic charges and can propagate through the detector independently as well as form a charmonium-like bound state. The first bounds on the masses of coloured particles up to charge $|Q| = 8$ are presented and the prospects of exclusion and discovery at higher luminosities are discussed.

We also consider composite Higgs models as they promise a natural solution to the hierarchy problem and fermion masses. In particular, we investigate the p_T spectra of the top partners for the Higgs+Jet process and obtain QCD limits for CP-odd contributions.

Moreover, we discuss a specific CH realisation with partial compositeness and pNGB Higgs in an $SO(11)/SO(10)$ GUT model. We identify many promising parameter points that are consistent with most of the EW and collider constraints.

Acknowledgements

First and foremost I would like to thank my parents and grandparents who have always supported me. I also owe gratitude to my collaborators Gabe, Seung, Charanjit, Wissarut, Andrea, Barry, Brad and Eric. I am especially grateful to Inbar, Gilad and Shikma for hosting me at Weizmann and Martin for the invitation to visit Liverpool. I would also like to thank Sebastian for the supervision and support throughout this PhD. Many thanks for food, company and tech advice to Tom, Gustavo, Basem, Sonali, Luke and Jack. Last but not least I acknowledge my excellent office mates and dear colleagues Kirsty, Tugba, Boris, Alba, Charlie, Yannick, Ibere, Djuna, Folkert, Dan, John, Luiz, Andy, Alex and Ryan.

Contents

List of Tables	xi
List of Figures	xvii
1 Introduction	1
1.1 Indirect CP Violation in Kaon Physics	3
1.2 Heavy Stable Multiply Charged Particles	5
1.2.1 Open Particle Production	5
1.2.2 Bound States and Resonances	7
1.3 Hierarchy Problem in the Electro-weak Sector	9
1.4 Thesis Outline	10
2 Renormalisation and NNLO Techniques	11
2.1 Renormalisation of QCD	12
2.1.1 The QCD Lagrangian	13
2.1.2 Perturbation Theory	13
2.1.3 Dimensional Regularisation	15
2.1.4 Renormalisation	16
2.2 Operator Renormalisation and Matching	20
2.2.1 $\overline{\text{MS}}$ NDR Scheme and Evanescent Operators	21
2.2.2 Four-quark Operators in MOM Schemes	22
2.2.3 Matching between $\overline{\text{MS}}$ and RI-(S)MOM schemes	24
2.2.4 Operator Anomalous Dimensions	25
2.3 Technical Aspects of Loop Integrals	26
2.4 Summary	30
3 NNLO Matching of RI/(S)MOM Schemes to $\overline{\text{MS}}$ for B_K	31
3.1 Four-quark Amplitude in Perturbation Theory	32

3.1.1	Amplitude at Leading Order	32
3.1.2	Amplitude at Next-to-Leading Order	33
3.1.3	Amplitude at NNLO	34
3.2	Full Amplitude from Direct Diagrams	37
3.2.1	Bilinears and Invariants	38
3.2.2	Matrix Elements Entering the Total Amplitude	39
3.2.3	Projectors and Evanescent Structures	39
3.2.4	Obtaining Coefficients A_i and \tilde{A}_i	41
3.2.5	Obtaining the (S)MOM Projections	42
3.2.6	Fierz-evanescent Operators	42
3.3	One-loop Amplitude and Counterterms	43
3.3.1	Projected Diagrams	44
3.3.2	Counterterms	44
3.3.3	Renormalised Amplitude	44
3.4	Validation against C_{B_K} at Next-to-Leading Order	45
3.5	Two-loop Amplitude and Counterterms	46
3.5.1	Projected Diagrams	47
3.5.2	Defining Topologies	47
3.5.3	Master Integrals	51
3.5.4	One-loop Counterterms	54
3.5.5	Two-loop Counterterms	55
3.5.6	Renormalised Amplitude	56
3.6	C_{B_K} at NNLO	56
3.7	Conversion factors to Brod–Gorbahn Basis	58
3.8	B_K in $\overline{\text{MS}}$ Scheme	60
3.9	Summary	61
	Preface to Chapter 4	62
4	Bounds and Prospects for Stable Multiply Charged Particles at the LHC	63
4.1	Introduction	64
4.2	Stable Multiply-Charged Particles at the LHC	66
4.2.1	Recalculating Production Cross Sections	68
4.2.2	Efficiency Calculation	69
4.3	Bound State Signal at the LHC	74

4.4	Current Status – Recast Bounds	77
4.4.1	Bounds from Open Signatures of MCHSPs	78
4.4.2	Bounds from Closed Signatures of Multiply-Charged Heavy Stable Particles (MCHSPs)	81
4.4.3	Combined Bounds	81
4.4.4	The Leptonic Case – Comparison to the Literature	81
4.5	Future Scenarios – Discovery and Exclusion	83
4.6	Conclusions and Outlook	86
5	Composite Higgs Models	89
5.1	The PNGB Higgs	89
5.1.1	Salient Features	90
5.1.2	CCWZ Formalism	91
5.1.3	Minimal Composite Higgs Models	92
5.1.4	Mass spectrum	100
5.2	PNGB Higgs at Colliders	103
5.2.1	Brief Summary of Experimental Bounds	103
5.2.2	Higgs plus One Jet	105
5.3	Electro-weak Observables	111
5.3.1	Higgs Potential	112
5.3.2	Oblique Corrections	112
5.4	Summary	116
6	Gauge and Matter Unification in Composite Higgs Models	117
6.1	The Model Setup	117
6.1.1	Embedding of the Hypercharge	119
6.1.2	Baryon and Lepton Number	120
6.2	CCWZ for SO(11)/SO(10)	120
6.3	Lagrangian and Mass Matrices	121
6.3.1	Embedding into Anti-symmetric Tensors	122
6.3.2	Mass Terms	122
6.3.3	Mixing Terms	124
6.3.4	The Two Models: 2-3-4-5 and 3-3-5-5	130
6.3.5	Mass Matrices: 2-3-4-5 Model	132
6.3.6	Mass Matrices: 3-3-5-5 Model	133

6.3.7	Simplified Mass Matrices	134
6.3.8	Mass Matrix Diagonalization	135
6.4	Higgs Potential	136
6.4.1	Gauge Contribution	136
6.4.2	Fermion Contribution	137
6.5	T Parameter	140
6.6	Results	141
6.6.1	Gauge versus Fermion Contribution	141
6.6.2	Higgs and Top Mass Constraints	143
6.6.3	Higgs Mass versus Composite Masses and Mixings	145
6.6.4	T Parameter versus Composite Masses and Mixings	147
6.6.5	Collider, S and T Parameter Constraints	149
6.6.6	Coloured NGB Mass	151
6.7	Summary	151
7	Conclusion	153
	Bibliography	155
A	Appendix for Chapter 4	169
A.1	Open-Production Signatures	169
A.1.1	Cross Sections	169
A.1.2	Simplified Efficiency Calculation	169
A.1.3	Effective Cross Sections	178
A.2	Closed-Production Signatures – Diphoton Cross Sections	181
B	Appendix for Chapter 5	182
B.1	CP-odd Contribution to Higgs plus One Jet in Relevant Limits	182
B.1.1	Higgs+Jet Production Amplitudes	182
B.1.2	Decoupling limit	184
B.1.3	Soft limit	185
B.1.4	Collinear limits	186

List of Tables

3.1	$B_{ij} = \Pi_i Q_j^s$ for projectors, defined in Eqs.(2.41-2.42), and the structures, given in Sec.(3.2.1).	42
3.2	Conversion factors $C_{B_K}^{(X,Y)}$ in Landau ($\xi = 0$) and Feynman ($\xi = 1$) gauges from four RI-SMOM schemes, where $X = \gamma_\mu, \not{q}$ and $Y = \gamma_\mu, \not{q}$, to $\overline{\text{MS}}$. The factors are in agreement with [4].	46
3.3	Momentum configurations, denoted as ‘c. number’, of the diagrams in Figure 3.5 for SMOM scheme. The ‘index’ corresponds to external leg labels in aforementioned figure. For the box diagrams tilde indicates one of p^2 that is linearly independent from the other two.	52
3.4	Required order of ϵ for each of the diagrams in Figure 3.5. Diagrams are indicated by their first index.	53
3.5	NNLO coefficient of conversion factors $C_{B_K}^{(X,Y)}$ in Landau and Feynman gauges with $\nu = \mu$ for four RI-SMOM schemes, where $X = \gamma_\mu, \not{q}$ and $Y = \gamma_\mu, \not{q}$, to $\overline{\text{MS}}$. The prefactor $\frac{\alpha_s^2}{16\pi^2}$ is omitted.	57
3.6	Conversion factors $C_{B_K}^{(X,Y)}$ evaluated with $\alpha_s(\mu)$ including NLO (i.e. 1+NLO) and NNLO (i.e. 1+NLO+NNLO) corrections, as well as the difference [diff.] between the two (i.e. NNLO) in Landau and Feynman gauges from four RI-SMOM schemes, where $X = \gamma_\mu, \not{q}$ and $Y = \gamma_\mu, \not{q}$, to $\overline{\text{MS}}$. The results are computed at three different scales $\nu = \mu$	58
3.7	$C_2^{MS \rightarrow MS, BG}$ for the two projectors $P_{(\gamma_\mu)}$ and $P_{(\not{q})}$, evaluated at $\alpha_s(\mu)$	60
3.8	Bag parameter B_K from the (\not{q}, \not{q}) and (γ_μ, γ_μ) schemes for $\mu = 3 \text{ GeV}$ and $\xi = 0$. Lattice results are taken from [70]. The remaining columns correspond to the SMOM to $\overline{\text{MS}}$ one-loop, two-loop and two-loop Brod–Gorbahn (BG) matching respectively.	60

4.1	Fractions of produced R-hadrons with specific charges, obtained using MadGraph and Pythia simulation of partner pair-production and hadronization.	69
4.2	Simplified efficiency calculation steps and criteria used in this analysis. Each step is applied only to candidates passing the selections in the steps above it. The online timing requirement is 50 ns for $ \eta \leq 1.6$ and 25 ns for $ \eta > 1.6$. The multiplicative factor accounts for the offline selection criteria, which are not explicitly simulated, and instead the efficiencies associated with them are taken from [5]. More details in text.	73
4.3	Current lower bounds on the masses of MCHSPs. The bounds were obtained from the diphoton resonance signatures at $\sqrt{s} = 13$ TeV, $\mathcal{L} = 35.9$ fb $^{-1}$ (closed-production channel) and from the MCHSPs signatures at $\sqrt{s} = 8$ TeV, $\mathcal{L} = 18.8$ fb $^{-1}$ (open-production channel). The colored cells are the corresponding combined bounds, given by naively taking the stricter bound of the two searches. <i>Blue</i> – scalar Colorful Twisted Top Partners (CTTPs), <i>red</i> – fermion CTTPs and <i>black</i> – lepton-like particles. Mass bounds are given in GeV. *Fermion CTTPs with $Q = 23/3, -22/3$, are excluded below 2250 GeV, however the exact bound could not be inferred from the search. More details in text.	80
6.1	Embeddings of $\{d, s, b\}_L$, $\{e, \mu, \tau\}_L$, $\nu_R^{e, \mu, \tau}$, $\{u, c, t\}_R$ and the Higgs \mathcal{H} for our partially composite Higgs model with custodial symmetry, which result in full unification with $Y = T_{3R} + X$. The subscripts denote the $U(1)_X$ charge. The branching rule for $SU(4) \supset SU(3) \times U(1)$ relevant here is: $(101) = \mathbf{15} = \mathbf{1}_0 \oplus \mathbf{3}_{2/3} \oplus \bar{\mathbf{3}}_{-2/3} \oplus \mathbf{8}_0$	119
6.2	Elementary and composite fermion embeddings into $SO(11)$ and $SO(10)$ anti-symmetric tensors (AS) respectively. $[n]$ denotes the n -index AS tensor. $A, B..$ and $a, b..$ correspond to indices in range 1..6 and $K, L..$ with $k, l..$ - 7..10 of $SO(11)$ and $SO(10)$ respectively.	123
6.3	Embedding options for elementary and composite quarks and leptons in $SO(11)$. Composites that are the same can be used to get contributions to the top or bottom mass. H1 and H2 stand for Higgs coupling at the elementary-composite vertex corresponding to composite 1 or 2. Even and odd indicate powers of the Higgs. More details are given in the main text. .	129

A.1	Efficiencies for color-triplet scalars at $\sqrt{s} = 8$ TeV.	175
A.2	Efficiencies for color-triplet fermions at $\sqrt{s} = 8$ TeV.	175
A.3	Efficiencies for color-singlet fermions at $\sqrt{s} = 8$ TeV.	175
A.4	Efficiencies for color-triplet scalars at $\sqrt{s} = 13$ TeV.	176
A.5	Efficiencies for color-triplet fermions at $\sqrt{s} = 13$ TeV.	177
A.6	Efficiencies for color-singlet fermions at $\sqrt{s} = 13$ TeV.	177

List of Figures

1.1	$K^0 - \bar{K}^0$ mixing diagrams.	5
1.2	Scalar partner χ_s pair-production processes at the Large Hadron Collider (LHC).	6
1.3	Fermion partner χ_f pair-production processes at the LHC.	6
1.4	Fermion, gauge bosons and Higgs self-energy diagrams contributing to the Higgs mass.	9
2.1	Momentum subtraction point, where $q = p_1 - p_2$ and the square corresponds to insertion of an operator. Solid lines denote fermions and dashed line momentum transfer.	19
2.2	Momentum subtraction point for a four-quark operator: $p_1^2 = p_2^2 = (p_1 - p_2)^2$ and $q = p_1 - p_2$. The solid black lines with arrows indicate fermion and momentum flow, the dashed line with arrow indicates momentum flow into the vertex.	23
2.3	The massless two-loop bubble with a vertical line, $I(\vartheta_1, \vartheta_2, \vartheta_3, \vartheta_4, \vartheta_5)$, with p external momentum and the ϑ 's corresponding to the powers of the propagators.	27
2.4	Two diagrams corresponding to $I(2, 1, 1, 1, 0)$ and $I(2, 1, 0, 1, 1)$. Dot represents propagator squared.	29
2.5	Obtaining an auxiliary topology based on one of the diagrams.	30
3.1	The four configurations of the external indices, corresponding to the following structures described in the text: $(\Gamma \otimes \Gamma 1 \otimes 1)$, $(\Gamma \tilde{\otimes} \Gamma 1 \tilde{\otimes} 1)$, $(\Gamma \otimes \Gamma 1 \tilde{\otimes} 1)$, $(\Gamma \tilde{\otimes} \Gamma 1 \otimes 1)$ (left to right, top to bottom). Each dot corresponds to an insertion of a current Γ and arrows indicate fermion and momentum flow.	32

3.2	28 classes of diagrams corresponding to the two-loop radiative corrections to the $\Lambda_{\alpha\beta,\gamma\delta}^{ij,kl}$. The hatched blobs correspond to the sum of one-loop insertions into the propagators. Kinematics are defined in Figure 2.2.	35
3.3	Topologies A, B, C and D. “Top” indicates that the diagram has linearly dependent propagators. All external momenta are defined as incoming. Numbers correspond to propagator labels, as defined in Section 3.5.2. . . .	48
3.4	Two additional topologies. All external momenta are defined as incoming. Numbers correspond to propagator labels, as defined in Section 3.5.2. . . .	49
3.5	Two-loop master integrals. Black dots represent squared propagators. All of the momentum configurations of these diagrams can be found in Table 3.3. Dashed lines indicate external legs that do not appear in all momentum configurations of a particular diagram and are chosen such that momentum conservation holds.	51
4.1	(a) Divergent top loop correction to the Higgs mass. (b) Loop contribution of a scalar top-partner. (c) Loop contribution of a fermion top-partner. The diagrams are taken from [6].	64
4.2	Different subprocesses for pair-production of a scalar CTPP with charges of $Q = 1, 4, 8$	69
4.3	Energy loss per distance traveled in iron as a function of γ . <i>Solid</i> - ionization energy loss for $Q = 1, 2, 3$ [7]. <i>Dashed</i> - average nuclear energy loss for a hadronized stable stop [8].	71
4.4	Simplified efficiency calculation validation. (a) The ratio between our resulting efficiencies and the respective CMS efficiencies for $\sqrt{s} = 8$ TeV [9], [5]. Indicated as well are the efficiency deviation bands corresponding to less than 5% (<i>red</i>), 10% (<i>light blue</i>) and 15% (<i>light green</i>) deviation in the mass bound. (b) Reproduced mass bounds for lepton-like particles, following the production mechanism used by CMS. <i>Dashed</i> – the bounds published by CMS [9], using a full detector simulation. <i>Solid</i> – our results using the simplified efficiency calculation. Indicated as well are the 5% (<i>red</i>) and 10% (<i>light blue</i>) mass deviation bands, around the our final mass bounds plot. . .	73

- 4.5 Lower mass bounds, as given by the most recent searches. *Solid* – a diphoton resonance search at $\sqrt{s} = 13$ TeV, $\mathcal{L} = 35.9 \text{ fb}^{-1}$ [10] (closed-production channel). *Round markers* – a search for MCHSP tracks at $\sqrt{s} = 8$ TeV, $\mathcal{L} = 18.8 \text{ fb}^{-1}$ [9] (open-production channel). *Shaded* – regions excluded by each channel. More details in text. 79
- 4.6 Detection efficiency, production cross section and the resulting effective cross section $\sigma \cdot \epsilon$ for a color-triplet scalar of $m = 1000$ GeV, at $\sqrt{s} = 8$ TeV. All are presented relative to their value for a color-triplet scalar of $Q = 14/3$. 80
- 4.7 Comparing the lower mass bounds on multiply-charged lepton-like particles, coming from the different analyses of the open-production signature. *Dashed* – results published by CMS [9]. *Dash-dotted red* – bounds for $Q = 2, 3$ given in [11]. *Solid blue* – mass bounds calculated in this study with 5% (*Red*) and 10% (*Light blue*) deviation bands. 82
- 4.8 Expected lower mass bounds at $\sqrt{s} = 13$ TeV, $\mathcal{L} = 35.9 \text{ fb}^{-1}$ (*magenta*), 100 fb^{-1} (*blue*), and 300 fb^{-1} (*green*). *Solid* – diphoton resonance searches (closed-production channel). *Round markers* – searches for MCHSP tracks with luminosity-scaling (open-production channel). *Dashed* – searches for MCHSP tracks with luminosity and pileup scaling (open-production channel). 84
- 4.9 The combined signatures of a hypothetical MCHSP with $m = 1500$ GeV, for different choices of its quantum numbers. In case of a discovery in both channels, combining the observables measured in the two searches could be used to determine the quantum numbers of the newly discovered particle. The lines correspond to different spin-color combinations studied in this work. *Black* – color-singlet fermions. *Blue* – color-triplet scalars with positive charges. *Cyan* – color-triplet scalars with negative charges. *Red* – color-triplet spin-1/2 fermions with positive charges. *Magenta* – color-triplet spin-1/2 fermions with negative charges. *Round markers* indicate charges spaced by one unit, colored labels indicate the charges. The two subplots on the top-left are magnified views. *Top box* – negatively-charged and positively-charged color-triplet fermions. *Bottom box* – negatively-charged and positively-charged color-triplet scalars. 86
- 5.1 The masses of the two light top-partners T^1 or T^2 as functions of the heavier vector-like mass, for $m_{\psi_1} = 1200$ GeV, $y = 1$, and $f = 600/1000$ GeV. The figure is taken from [2]. 103

5.2	The contour plots of $\delta(p_T^{\text{cut}})$ with $\sin^2 \theta_L = 0.1$ and $p_T^{\text{cut}} = 200$ GeV for each of the singlet models with one top partner multiplet. The solid lines correspond to constant values of the coupling y . The region marked by dashed white lines indicates when $\kappa_t \leq 0.8$. The figure is taken from [2].	107
5.3	The contour plots of $\delta(p_T^{\text{cut}})$ with $\sin^2 \theta_R = 0.1$ and $p_T^{\text{cut}} = 200$ GeV for each of the fourplet models with one top partner multiplet. The solid lines correspond to constant values of the coupling y . None of the parameter space on these plots result in $\kappa_t \leq 0.8$. The figure is taken from [2].	108
5.4	The contour plots of $\delta(p_T^{\text{cut}})$ with $\sin^2 \theta_L = 0.1$ and $p_T^{\text{cut}} = 600$ GeV for each of the singlet models with one top partner multiplet. The corresponding values of y are indicated by the solid lines. The region marked by dashed white lines indicates when $\kappa_t \leq 0.8$. The figure is taken from [2].	108
5.5	The contour plots of $\delta(p_T^{\text{cut}})$ with $\sin^2 \theta_R = 0.1$ and $p_T^{\text{cut}} = 600$ GeV for each of the fourplet models with one top partner multiplet. The corresponding values of y are indicated by the solid lines. None of the parameter space on these plots result in $\kappa_t \leq 0.8$. The figure is taken from [2].	109
5.6	The contour plots of $\delta(p_T^{\text{cut}})$ with $\sin^2 \theta_L = 0.025$ and $p_T^{\text{cut}} = 600$ GeV for the singlet models with one top partner multiplet. The corresponding values of y are indicated by the solid lines. The region marked by dashed white lines indicates when $\kappa_t \leq 0.8$. The figure is taken from [2].	110
5.7	The contour plots for δ with $\sin^2 \theta_R = 0.4$ and $p_T^{\text{cut}} = 600$ GeV for each of the fourplet models with one top partner multiplet. The corresponding values of y are indicated by the solid lines. As indicated by the dashed white lines, all points on these plots result in $\kappa_t \leq 0.8$. The figure is taken from [2].	110
5.8	The distribution $\delta(p_T^{\text{cut}})$ for benchmark scenario with $y = 1$, $M_{\Psi_1} = 1200$ GeV, $1300 \text{ GeV} < M_{\Psi_2} < 3000 \text{ GeV}$, $f = 800 \text{ GeV}$ (see Figs. 5.1) and the four models considered in Section 5.1.4. The figure is taken from [2].	111
5.9	Vacuum-polarization amplitude with two different fermions.	112
5.10	1, 2 and 3 σ $S - T$ ellipse comparison of PDG (black) and Gfitter (yellow).	113
6.1	Gauge vs. fermion contribution to $\alpha' = -\alpha/f^2$ (above) and $\beta' = -\beta/f^2$ (below) for the 3-3 model (blue and light blue) and the 2-3 model (yellow).	142
6.2	m_ψ vs. m_Ψ (above) and λ_R vs. λ_L (below) for the 3-3 model (blue and light blue) and the 2-3 model (yellow).	144

6.3	Higgs mass vs. m_Ψ , m_ψ (above and below respectively). Red dashed line marks the $m_h = 126$ GeV. The 3-3 model is blue and light blue and the 2-3 model is yellow.	145
6.4	Higgs mass vs. λ_L and λ_R (above and below respectively). Red dashed line marks the $m_h = 126$ GeV. The 3-3 model is blue and light blue and the 2-3 model is yellow.	146
6.5	Fermion contribution to $\hat{T} \times 10^3$ vs. m_Ψ , m_ψ (above and below respectively) for the 3-3 model (blue and light blue) and the 2-3 model (yellow).	147
6.6	Fermion contribution to $\hat{T} \times 10^3$ vs. λ_L and λ_R (above and below respectively) for the 3-3 model (blue and light blue) and the 2-3 model (yellow).	148
6.7	T vs. S for the 3-3 model (top left and right) and the 2-3 model (bottom). At each point, it is indicated if the lightest fermion mass is less than 1.3 TeV (grey), 1.5 TeV (pink), 2.0 TeV (dark pink) and less than 2.5 TeV (dark red). Black are the 1, 2 and 3σ S-T constraint from PDG.	150
6.8	$m_{\hat{T}}$ vs. m_Ψ for the 3-3 model (top left and right) and the 2-3 model (bottom). Points that fall within the 2σ S-T contour indicated by red, within 3σ - blue, outside 3σ - grey. Pink lines indicate collider mass constraint for our particles: 1.3 TeV.	150
6.9	Coloured NGB masses for our points. 3-3 model (blue and light blue) and 2-3 model (yellow).	151
A.1	Open-production cross sections at $\sqrt{s} = 8$ TeV.	170
A.2	Open-production cross sections at $\sqrt{s} = 13$ TeV.	171
A.3	(a) Minimal distance traveled within the muon trigger time window for high momentum tracks as a function of η . (b) Distance traveled in matter, relevant for ionization energy loss, within the muon trigger time window as a function of η . Both (a) and (b) are based on the layout given in [12].	172
A.4	$r = \alpha^{\text{sim}}(m, q)/\alpha^{\text{CMS}}(m, q)$, the ratio of multiplicative factors required to convert the muon trigger event efficiency into the global-muon offline particle efficiency for our procedure, and for CMS.	174
A.5	Open-production channel signatures. Effective cross sections $\sigma \cdot \epsilon$ for CMS search [9] at $\sqrt{s} = 8$ TeV, together with the observed upper bound. <i>Solid</i> – theoretical effective cross sections, <i>dashed</i> – observed limit.	179

- A.6 Open-production channel signatures. Effective cross sections $\sigma \cdot \epsilon$ for future CMS searches at $\sqrt{s} = 13$ TeV, together with expected upper bounds. *Solid* – theoretical effective cross sections. *Round markers* – luminosity scaling. *Dashed* – luminosity scaling and pileup scaling. *Magenta* – $\mathcal{L} = 35.9 \text{ fb}^{-1}$, *blue* – $\mathcal{L} = 100 \text{ fb}^{-1}$, *green* – $\mathcal{L} = 300 \text{ fb}^{-1}$ 180
- A.7 Diphoton resonant production cross sections, given by a bound state of mass $2m$ at $\sqrt{s} = 13$ TeV. *Magenta* – upper-limits observed at $\mathcal{L} = 35.9 \text{ fb}^{-1}$ [10], (*solid* – narrow, *dashed* – mid-width, *dash-dotted* – wide). *Dashed blue* – upper limits expected at $\mathcal{L} = 100 \text{ fb}^{-1}$ [13]. *Dashed green* – upper-limits expected at $\mathcal{L} = 300 \text{ fb}^{-1}$ [13]. 181

Chapter 1

Introduction

The observation of meson and baryon spectra in the 1960's led to the idea of quarks as a building block of hadronic matter [14, 15]. Indeed, it has been found that a meson is a bound state of a quark and an anti-quark and a baryon is a bound state of three quarks, held together by the strong force. Thus, the theory of Quantum Chromodynamics (QCD), characterised by an $SU(3)_c$ gauge symmetry, that describes the interactions of quarks via gluons, was born [16].

Around the same time the Glashow–Weinberg–Salam (GWS) model for the electroweak (EW) interactions was proposed [17–19]. GWS theory combines electromagnetic and weak interactions into a single gauge group $SU(2)_L \times U(1)_Y$ which is broken spontaneously by the Higgs mechanism to $U(1)_{\text{em}}$ [20–22]. This provides an explanation for how W and Z gauge bosons acquire masses. However, introduction of quark and lepton mass terms becomes non-trivial as the left- and right-handed fermions belong to different weak isospin multiplets. Instead, the SM introduced Yukawa terms coupling quarks and the Higgs, thus generating masses via the spontaneous symmetry breaking (SSB).

QCD, GWS and the Higgs sector together form the main pillars of the Standard Model of Particle Physics (SM). This theory has been very successful at describing many microscopic phenomena – it contains all elementary particles that have been observed as well as three fundamental forces of nature. In 2012 the SM has been completed as the Higgs was discovered [23–25]. However, even today some issues still remain unaddressed by the Standard Model.

While the SM contains all particle masses, their values are not predicted by it, instead they have to be fixed by measurement. Hence, the origin of the relative hierarchies between different quark and lepton masses is unclear. Similarly, there is no explanation for the particle mixing or Charge-conjugation and Parity (CP) violation in the SM. Instead

these effects are merely parametrised by the Cabibbo-Kobayashi-Maskawa (CKM) [26, 27] and the Pontecorvo-Maki-Nakagawa-Sakata (PMNS) [28, 29] matrices. In addition, the Higgs mass should be sensitive to the high-energy physics, yet it is relatively small, which is known as the hierarchy problem. On a different note, there is not much known about what happens in the high-energy limit. The SM indicates that all gauge interactions approximately unify, however there is no theoretical framework describing this phenomenon, often referred to as Grand Unified Theory (GUT). There are many more open issues, such as a dark matter (DM) candidate or explanations for various flavour anomalies. All of this suggests that the Standard Model is not the end of the story, but there is new physics to be discovered.

In this thesis, we address these problems using three complementary approaches. First, we conduct a precision calculation that can constrain the size of new physics effects. In particular, we improve the precision of the kaon bag parameter. It parameterises the dominant short distance contributions to the indirect CP violation, which is sensitive to new physics. To this end, Section 1.1 discusses the indirect CP violation in more detail. As the computation of the bag parameter is closely related to the renormalisation of QCD and its low-energy operators, we review this subject in Chapter 2, as we introduce our notations and collect necessary literature results. This sets up the two-loop calculation performed in Chapter 3, where we obtain the matching factors and perform the conversion for the bag parameter between minimal and momentum subtraction schemes as well as the translation to the Brod–Gorbahn operator basis. In particular, we find that the two-loop conversion factors lead to 0.5–4% corrections for the different momentum subtraction schemes and that the error on the Kaon bag parameter is reduced to around 1%.

Second, we look for specific signatures of physics beyond the Standard Model (BSM) at particle colliders. To be more precise, in Chapter 4, we recast searches for stable multiply charged particles and obtain the first bounds on coloured scalars and fermions. We find that the limits coming from the open searches are flat while the ones from the bound states increase with charge. This means that both approaches can be used in complimentary fashion to obtain the prospects of exclusion and discovery of multiply charged particles in future searches. These particles are predicted by various SM extensions. An introduction to this type of searches can be found in Section 1.2. Additionally, in Chapter 5, we investigate top partner signatures for various composite Higgs (CH) models via the p_T spectrum of the Higgs+Jet process and compute the decoupling, soft and collinear limits to the CP-odd contribution. This allows us to distinguish between the various choices of

CH models.

Finally, we directly propose SM extensions that address multiple shortcomings in Chapter 6. For this purpose we consider CH models which resolve the hierarchy problem and can also explain the heavy top mass. A short review of the hierarchy problem and its solutions is provided in Section 1.3. In particular, we construct partially composite theories with pseudo-Nambu-Goldstone (pNGB) Higgs. In addition to aforementioned features, they include gauge unification, could help resolve flavour anomalies and potentially provide dark matter candidates. We investigate whether such theories are viable given the current collider and EW constraints. In the end we find various promising parameter points, but the production of sufficiently heavy coloured pNGBs still remains a challenge. After having introduced all the basic concepts, we provide an outline of the thesis in Section 1.4.

1.1 Indirect CP Violation in Kaon Physics

As there is no manifest flavour symmetry in the SM, the Yukawa couplings may not be Hermitian and can be diagonalised by unitary transformations into mass eigenstates of the physical quarks [30]. This introduces the mixing and weak decays of quarks between different generations in the form of Cabibbo-Kobayashi-Maskawa (CKM) matrix [26, 27]. As not all phases entering CKM matrix are physical, this allows for up to five fields to be rephased. Due to its unitarity, one can represent the CKM matrix as a unitary triangle with equal sides, given by the modulus of elements $|V_{ud}V_{ub}^*|$, $|V_{cd}V_{cb}^*|$, $|V_{td}V_{tb}^*|$ and angles. The phase invariance simply translates to rotations of this triangle as all aforementioned quantities are physical observables. The area of this triangle is then proportional to the amount of CP (charge conjugation and parity) violation in SM, parametrised by the Jarlskog invariant J . Indirect CP violation is proportional to J , which makes it an extremely important observable in constraining the CKM matrix and the unitary triangle [30, 31]. Due to confinement of the strong interaction CP violation on parton level translates into effects on mesons and baryons.

For kaons indirect CP violation is parametrised by ϵ_K , defined as the ratio between decay amplitudes of a long-lived and a short-lived kaon, K_L and K_S , into an isospin zero state, given by

$$\epsilon_K \equiv \frac{\langle (\pi\pi)_{I=0} | T | K_L \rangle}{\langle (\pi\pi)_{I=0} | T | K_S \rangle}, \quad (1.1)$$

where T is the unitary transition matrix related to the S-matrix by $S = 1 + iT$ [30]. If we define the flavour eigenstates as $K^0 = (\bar{s}d)$ and $\bar{K}^0 = (s\bar{d})$, which mix via weak

interactions, as shown in Figure 1.1, we can relate the long-lived and the short-lived kaon states to flavour states as follows

$$|K_L\rangle = p_K|K^0\rangle + q_K|\bar{K}^0\rangle, \quad (1.2)$$

$$|K_S\rangle = p_K|K^0\rangle - q_K|\bar{K}^0\rangle, \quad (1.3)$$

where $p_K^2 + q_K^2 = 1$ and $p_K/q_K = (1 + \bar{\epsilon})/(1 - \bar{\epsilon})$ with $\bar{\epsilon}$ being a small complex parameter [4]. As both of the flavour eigenstates can be chosen to be CP odd, via the phase conventions, we can define CP eigenstates as

$$K_1 = \frac{1}{\sqrt{2}}(K^0 - \bar{K}^0), \quad \text{CP even}, \quad (1.4)$$

$$K_2 = \frac{1}{\sqrt{2}}(K^0 + \bar{K}^0), \quad \text{CP odd}. \quad (1.5)$$

Kaons follow the $|\Delta I| = 1/2$ rule, meaning that they predominantly decay into an isospin zero state, $|0\rangle$, rather than into isospin two state, $|2\rangle$. This results in $|K_S\rangle$ decaying mostly into the 2 pion state and $|K_L\rangle$ mostly into the 3 pion state, which also explains the difference in their lifetimes. As a result, the name indirect CP violation comes from the fact that the decay $|K_L\rangle \rightarrow 2\pi$ occurs indirectly, via the admixture of the CP even state in the $|K_L\rangle$ [31].

Generally, ϵ_K can be written as

$$\epsilon_K = \frac{e^{i\frac{\pi}{4}}}{\sqrt{2}\Delta M_K} \left(\text{Im}M_{12} + 2\text{Re}M_{12} \frac{\text{Im}A_0}{\text{Re}A_0} \right), \quad (1.6)$$

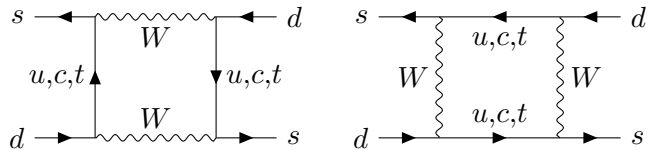
where the decay amplitude A_0 is defined as $\langle I_{out}|T|K^0\rangle = A_I e^{i\delta_I}$ with $I = 0$ [31]. ΔM_K is the mass difference between the mass eigenstates K_L and K_S . M_{12} is the off-diagonal element in the kaon mass matrix, which arises from the mixing box diagrams in Figure 1.1. These box diagrams can be translated into an effective $\Delta S = 2$ Hamiltonian and in 4 dimensions represented by an operator

$$Q = (\bar{s}\gamma_\mu(1 - \gamma_5)d)(\bar{s}\gamma_\mu(1 - \gamma_5)d), \quad (1.7)$$

giving a matrix element

$$M_{12} \propto \langle K^0|Q|\bar{K}^0\rangle. \quad (1.8)$$

Along with various other QCD corrections, it enters the dominant short-distance contri-

Figure 1.1: $K^0 - \bar{K}^0$ mixing diagrams.

bution to the ϵ_K , for which the expression is given by

$$\epsilon_K = \kappa_{\epsilon_K} \hat{B}_K \frac{G_F^2 f_K^2 M_K M_W^2}{6\sqrt{2}\pi^2 \Delta M_K} \text{Im}(\lambda_t) e^{i\frac{\pi}{4}} \times (\text{Re}(\lambda_c)(\eta_1 S_0(x_c) - \eta_3 S_0(x_c, x_t)) - \text{Re}(\lambda_t)\eta_2 S_0(x_t)), \quad (1.9)$$

where κ_t are subdominant corrections, \hat{B}_K is the kaon bag parameter parametrising the $\Delta S = 2$ operator, f_K is the leptonic decay constant, $\lambda_x = V_{xd}V_{xs}^*$ with CKM matrix elements V_{xy} , η_i are perturbative QCD corrections and S_0 are Inami-Lim functions of mass ratios $x_q = m_q^2/m_W^2$ [4].

1.2 Heavy Stable Multiply Charged Particles

While the usual new coloured particles have already been studied extensively and only constraints on their masses have been put so far at colliders. Hence there is increasing interest in more elusive signatures as well as more exotic scenarios. In particular in [6] scalar and fermionic top partners that carry such charges have been proposed. These particles would be stable on collider scales and can propagate through the detector independently as well as form a charmonium-like bound state. In this section we will introduce both of the production mechanisms for such particles.

1.2.1 Open Particle Production

To begin with, we consider pair produced particles, which can travel through the detector independently. This is also known as the open production. In the following, we are going to provide a brief introduction to the open production mechanism, including the relevant production processes, showering and hadronisation.

Pair Production

Coloured particles tend to be predominantly produced via gluon fusion. In addition, they can be produced via Drell-Yan (DY) process, i.e. the quark-anti-quark production mediated by a gluon. For colourless fermions and coloured particles with relatively large

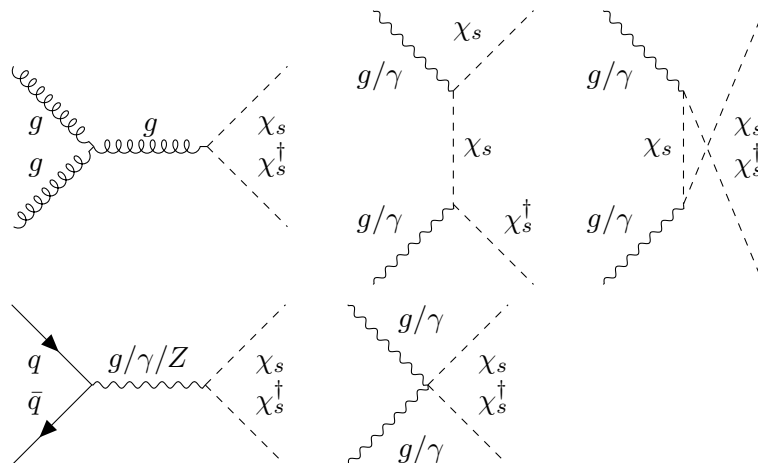


Figure 1.2: Scalar partner χ_s pair-production processes at the LHC.

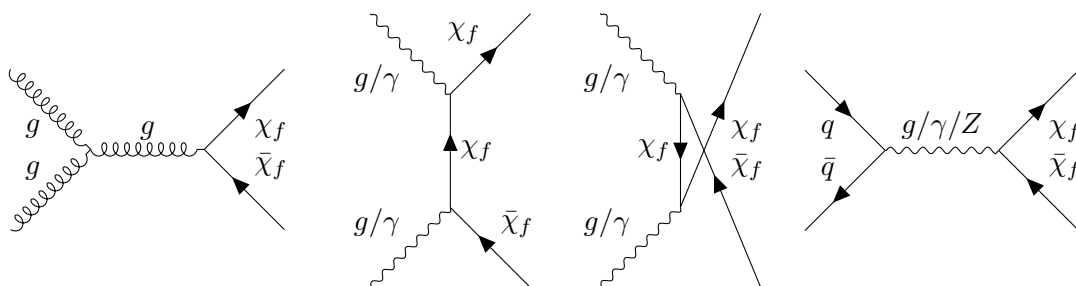


Figure 1.3: Fermion partner χ_f pair-production processes at the LHC.

charges photon-photon, photon-gluon fusion and DY processes, mediated by a photon and Z boson, are important. In Figures 1.2-1.3, the diagrams relevant for the production of scalar and fermionic top partners are presented.

Shower and Hadronisation

Coloured particles hadronise within a time scale of $t_{\text{had}} \approx 1/\Lambda_{\text{QCD}}$, where Λ_{QCD} is the energy scale at which QCD becomes strongly coupled. The stable fermion or scalar colour-triplet partners are expected to form ‘‘R-hadrons’’, similarly to quarks and squarks [32]. R-hadrons consisting of partners are mesons and baryons of the forms $\chi\bar{q}$ and χqq , where χ is the partner and q is a SM quark. The spin and the electric charge of the heavy partner are effectively irrelevant to the hadronisation process and can be disregarded.

Since hadronisation takes place almost independently for the rather heavy partner and the anti-partner, they may hadronise into two differently charged R-hadrons. This should be taken into account when considering the detection of a pair-production event.

1.2.2 Bound States and Resonances

In the previous Section we have considered particles that can transverse the detector independently from each other. However, heavy top partners could also be produced with the energy just above the threshold and form a bound state. Since the momentum of the bound state is close to zero, it can be modelled as a non-relativistic system, similar to hydrogen atom [33]. Here, we will cover all of the important features of the bound state formalism at the leading order, including potential, wave function, resonances and their decays.

Potential

Particles forming the bound state are held together by a Coulomb-like potential. For coloured particles the dominant LO contribution generally comes from the gluon potential defined as

$$V^{QCD}(r) = -C \frac{\bar{\alpha}_s}{r}, \quad (1.10)$$

where r is the distance between the two particles, C is the Casimir of $SU(3)_c$ and $\bar{\alpha}_s$ is the running strong coupling evaluated at the average distance between the two particles given by the inverse Bohr radius $a_0^{-1} = C\bar{\alpha}_s\mu$. Here $\mu = m_1m_2/(m_1 + m_2)$ is the reduced mass of the constituent particles [33, 34]. For colour-triplets $C_3 = 4/3$ and for colour-singlets $C_0 = 0$. Since we consider leptons and coloured particles with large charges, we also have a significant contribution to their binding potential coming from the EM force

$$V^{QED}(r) = -Q^2 \frac{\alpha}{r}, \quad (1.11)$$

where Q is the charge of the constituents and α is the electromagnetic coupling evaluated at m_Z [11]. For $m = 1$ TeV and $Q = 8$ top partners this contribution could be ~ 4 times larger than the one coming from the QCD.

Wave Function

The bound state is essentially a superposition of free particles with position or momentum weighted by the bound state wave function $\Psi(\mathbf{r})$. This wave function at the origin is only non-vanishing for S-waves. Thus, the matrix element for the bound state \mathcal{M}_B is given in terms of the matrix element for the free states \mathcal{M}_0 by

$$\mathcal{M}_B = \frac{\Psi(0)}{\sqrt{2\mu}} \mathcal{M}_0. \quad (1.12)$$

The bound state at the origin is given by

$$|\Psi(0)|^2 = \frac{(C\bar{\alpha}_s + Q^2\alpha)^3 M^3}{8\pi n}, \quad (1.13)$$

where n is the radial excitation level. Since the contributions from $n \geq 2$ states are negligible, we keep only the ground state contribution [33].

Resonances

Resonant cross-sections are generally given by Breit-Wigner formula

$$\sigma(E) = \frac{2J+1}{(2S_1+1)(2S_2+1)} \frac{4\pi}{k^2} \left[\frac{\Gamma^2/4}{(E-E_0)^2 + \Gamma^2/4} \right] B_{in} B_{out}, \quad (1.14)$$

where E is the centre-of-mass energy, J is the spin of the resonance, S is the number of polarization states for each constituent particle, k is the centre-of-mass momentum in the initial state, E_0 centre-of-mass energy at resonance and B is the branching ratio [35]. For narrow width approximation the expression in the square bracket in Eq.(1.14) becomes $\pi\Gamma\delta(E-E_0)/2$.

This ansatz allows for the cross section of the resonance and the branching ratio of the decay to factorise, for instance

$$\sigma(e^+e^- \rightarrow f\bar{f}) = \sigma(e^+e^- \rightarrow Z)\text{Br}(Z \rightarrow f\bar{f}), \quad (1.15)$$

for the Z resonance and corresponds to producing the particle on-shell.

Resonance Decays

The partnerium is unstable due to the annihilation of its constituents, and can be detected as a resonance, with invariant-mass peak at $M \approx 2m_{\text{partner}}$. The bound state decay rate to two mass m_0 particles is given by

$$\Gamma = \frac{|\Psi(0)|^2}{64\pi m_1 m_2} \sqrt{1 - \frac{m_0^2}{(M/2)^2}} \int_0^\pi d\theta \sin\theta \sum_{\epsilon_1, \epsilon_2} |\mathcal{M}_0(\theta)|^2, \left(\times \frac{1}{2} \text{ for identical particles} \right) \quad (1.16)$$

where m_1, m_2 are the masses of the constituent particles and the sum is over photon polarizations ϵ_1 and ϵ_2 [34].

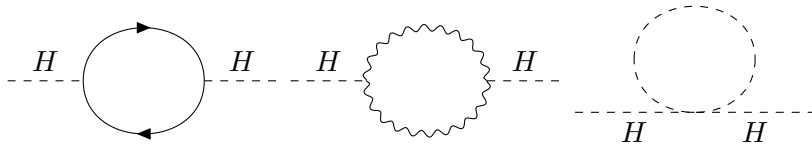


Figure 1.4: Fermion, gauge bosons and Higgs self-energy diagrams contributing to the Higgs mass.

1.3 Hierarchy Problem in the Electro-weak Sector

The hierarchy (or naturalness) problem in the SM arises as follows. We can view the SM as an effective field theory with some large energy cut-off Λ_{SM} , which could potentially be as large as the GUT scale $\Lambda_{\text{GUT}} \sim 10^{15}$ GeV, or even the Planckian energies, $\Lambda_{\text{Planck}} \sim 10^{19}$ GeV. The Lagrangian of such a theory contains terms of mass dimension four. Hence, if we have higher dimensional ($D > 4$) operators in such Lagrangian, we expect them to be suppressed by appropriate powers of the cut-off $1/\Lambda_{\text{SM}}^{D-4}$. The Higgs mass, on the other hand, results from a dimension two operator $H^\dagger H$, therefore we expect it to be enhanced by Λ_{SM}^2 . Since the Higgs mass has been measured to be $m_H = 126$ GeV [23], the coefficient in front of this term must be very small. Such coefficient could only be considered natural if setting it to zero would restore a symmetry of the Lagrangian [36]. However, there is no symmetry in the SM protecting the Higgs mass which results in large quantum corrections. Such corrections to the Higgs mass get contributions from fermions, gauge bosons and Higgs self interactions, given in Figure 1.4, which can be written as

$$m_H^2 = \frac{3y_t^2}{8\pi^2}\Lambda_{\text{SM}}^2 - \frac{2g_W^2}{8\pi^2}\left(\frac{1}{4} + \frac{1}{8\cos^2\theta_W}\right)\Lambda_{\text{SM}}^2 - \frac{3\lambda}{8\pi^2}\Lambda_{\text{SM}}^2, \quad (1.17)$$

where y_t is the top Yukawa coupling, g_W is the EW coupling, θ_W is the weak angle and λ is the Higgs quartic coupling [37].

There are two ways to remedy this problem. The first one involves introducing a new scale of order of a few TeV at which the Higgs mass is protected due to symmetries. Then the corrections to the Higgs mass depend on this new scale rather than the high UV scale. This is for instance implemented for composite Higgs models, see Chapter 5. The second way involves introducing new fields to the theory such that they give contributions that could cancel these divergent terms, as it is the case for e.g. supersymmetry, or the models in Chapter 4.

1.4 Thesis Outline

The thesis comprises of six chapters involving published and unpublished work conducted during my doctoral studies and is structured as follows:

- Chapter 2: **Renormalisation and NNLO Techniques.**

This serves a survey chapter for Chapter 3. We introduce basic notions of renormalisation and Greens functions in QCD. In addition, we review operator renormalisation in minimal subtraction and momentum subtraction schemes. We also cover integration by parts method, which will be used for the computation of two-loop diagrams.

- Chapter 3: **NNLO Matching of RI/(S)MOM Schemes to $\overline{\text{MS}}$ for B_K .**

In this chapter we perform the first two-loop conversion for the kaon bag parameter B_K from symmetric momentum subtraction schemes to the $\overline{\text{MS}}$ scheme.

- Chapter 4: **Bounds and Prospects for Stable Multiply Charged Particles at the LHC.**

Here we present our recast of collider searched for scalar and fermionic matter with exotic charges. This chapter has appeared as [1] in verbatim.

- Chapter 5: **Composite Higgs Models.**

This serves both as preparation for Chapter 6 and also includes results from our publication [2]. Here we provide a review of the salient features of composite Higgs with particular focus on pNGB Higgs. We also discuss the relevant collider and electro-weak constraints.

- Chapter 6: **Gauge and Matter Unification in Composite Higgs Models.**

This chapter contains our model building efforts of composite Higgs theories with gauge and matter unification. We investigate the viability of such models given the current EW and collider constraints. The work presented in this chapter is part of an ongoing project.

- Chapter 7 contains the conclusion of the thesis.

Chapter 2

Renormalisation and NNLO Techniques

In this thesis, we are going to compute a change of operator renormalisation scheme from SMOM to $\overline{\text{MS}}$. An introduction to these schemes will follow later in this chapter. Specifically, we focus on the $\Delta S = 2$ four-quark operator

$$Q = (\bar{s}\gamma^\mu P_L d)(\bar{s}\gamma_\mu P_L d), \quad (2.1)$$

as given in Eq.(1.7). The operators in the two schemes are related as

$$Q^{\text{SMOM}} = C^{\overline{\text{MS}} \rightarrow \text{SMOM}} Q^{\overline{\text{MS}}}. \quad (2.2)$$

This conversion is a key ingredient in for connecting the perturbative loop calculations in the high-energy regime to non-perturbative lattice results of the strong interaction at low energies. The one-loop conversion has already been determined in [4]. We will extend this to two-loop order.

Phenomenologically this allows to determine the CP-violating observables in kaon decays to high precision. They are defined in terms of $K \rightarrow \pi\pi$ decay amplitudes

$$\langle (\pi\pi)_I | T | K^0 \rangle = A_I e^{i\delta_I}, \quad (2.3)$$

where A_I are the isospin amplitudes. The indirect CP violation ϵ_K is then given by

$$\epsilon_K = \frac{e^{i\frac{\pi}{4}}}{\sqrt{2}\Delta M_K} \left(\text{Im}M_{12} + 2\text{Re}M_{12} \frac{\text{Im}A_0}{\text{Re}A_0} \right), \quad (2.4)$$

which we have already introduced in Eq.(1.6). In addition, we can define direct CP violation as

$$\epsilon' = \frac{ie^{i(\delta_2 - \delta_0)}}{\sqrt{2}} \frac{\text{Re}A_2}{\text{Re}A_0} \left(\frac{\text{Im}A_2}{\text{Re}A_2} - \frac{\text{Im}A_0}{\text{Re}A_0} \right), \quad (2.5)$$

taken from [38]. The short-distance contributions to ϵ_K involve the matrix element

$$\langle K^0 | Q | \bar{K}^0 \rangle = \frac{2}{3} f_K^2 M_K^2 B_K, \quad (2.6)$$

which is parametrised by the kaon bag parameter B_K . Hence, the conversion in Eq.(2.2) translates to

$$B_K^{\text{SMOM}} = C^{\overline{\text{MS}} \rightarrow \text{SMOM}} B_K^{\overline{\text{MS}}}. \quad (2.7)$$

Related conversion factors can also be used to convert the matrix element

$$\langle (\pi\pi)_{I=2} | Q_{\Delta S=1} | \bar{K}^0 \rangle, \quad (2.8)$$

contributing to the $\Delta I = 3/2$ amplitude A_I , an ingredient for ϵ' . Here $Q_{\Delta S=1}$ are the operators of the $N_f = 3$ and $\Delta S = 1$ Hamiltonian, build purely out of left-handed fields.

The main calculation of radiative corrections to the Green's function of Q in Eq.(2.1) up to two-loop order and the matching between perturbation theory and lattice QCD will be presented in Chapter 3. In this chapter we will review the prior work and technical ingredients needed to perform this calculation. Moreover, we will define our notation and conventions. In particular in Section 2.1 we will introduce the basic aspects of QCD, Green's functions and their renormalisation. In Section 2.2 we will discuss the operator renormalisation and their matching between different schemes. Finally, in Section 2.3 we will review the loop methods needed for the two-loop computation and summarise the chapter in Section 2.4.

2.1 Renormalisation of QCD

In this section we will cover the aspects of QCD and its renormalisation that are relevant for this thesis. A more detailed introduction to QCD and renormalisation can be found in [16, 39, 40].

2.1.1 The QCD Lagrangian

The QCD Lagrangian density [41] is given by

$$\begin{aligned}
\mathcal{L}_{QCD} = & \bar{q}_i^\alpha (i\not{\partial} - m_q) q_{i\alpha} + g_s \bar{q}_i T_{ij}^a \gamma^\mu q_j A_\mu^a \\
& - \frac{1}{4} (\partial_\mu A_\nu^a - \partial_\nu A_\mu^a) (\partial^\mu A^{a\nu} - \partial^\nu A^{a\mu}) - \frac{1}{2\xi} (\partial^\mu A_\mu^a)^2 \\
& - \frac{g_s}{2} f^{abc} (\partial_\mu A_\nu^a - \partial_\nu A_\mu^a) A^{b\mu} A^{c\nu} - \frac{g_s^2}{4} f^{abe} f^{cde} A_\mu^a A_\nu^b A^{c\mu} A^{d\nu} \\
& + \chi^{a*} \partial^\mu \partial_\mu \chi^a + g_s f^{abc} (\partial^\mu \chi^{a*}) \chi^b A_\mu^c,
\end{aligned} \tag{2.9}$$

where q are the quark fields, α count over the N_f flavours and indices i, j denote N_c colours. A_μ^a stands for the gluon field carrying colour in the $SU(N_c)$ adjoint representation $a = 1, \dots, N_c^2 - 1$. The strong coupling is denoted by g_s and ghost field by χ^a . The T^a are the generators of the fundamental representation, f^{abc} are the structure constants of $SU(N_c)$ and ξ is the gauge-fixing parameter.

All of the physical information from this Lagrangian density can be extracted via time-ordered Green's functions in either position or momentum space. The two are related via Fourier transformation. We can define the Green's functions in momentum space as

$$\begin{aligned}
G^{ijk}(g_s, m_q, p_i^q, p_j^{\bar{q}}, p_k^A, \xi) & \times (2\pi)^4 \delta^4 \left(\sum_{n=1}^i p_n^q + \sum_{m=1}^j p_m^{\bar{q}} + \sum_{l=1}^k p_l^A \right) \\
& = \langle 0 | T q_1(p_1^q) \dots q_i(p_i^q) \bar{q}_1(p_1^{\bar{q}}) \dots \bar{q}_j(p_j^{\bar{q}}) A_1^{\mu_1}(p_1^A) \dots A_k^{\mu_k}(p_k^A) | 0 \rangle,
\end{aligned} \tag{2.10}$$

where i, j, k are labels of the quark, anti-quark and gluon fields respectively, $p_i^q, p_j^{\bar{q}}, p_k^A$ are their momenta and T is the time-ordering operator. Ghost fields are not physical states, they only remove the unphysical degrees of freedom from the gauge fields. Hence, they only appear within quantum corrections.

In general, Green's functions can be computed using non-perturbative methods e.g. lattice QCD or by employing perturbation theory. This will be addressed in the next section.

2.1.2 Perturbation Theory

The Lagrangian in Eq.(2.9) can be split into a free action S_0 , containing kinetic terms of non-interacting fields, and interaction part S_{int} , via $\int d^4x \mathcal{L}_{QCD} = S_0 + S_{\text{int}}$. In perturbation theory the Green's functions in Eq.(2.10) are computed by expanding them in powers

of interactions S_{int} as

$$G^{ijk}(g_s, m_q, p_l, \xi) \propto \int \mathcal{D}q \mathcal{D}\bar{q} \mathcal{D}A \mathcal{D}\chi \mathcal{D}\chi^* T q_1 \dots q_i \bar{q}_1 \dots \bar{q}_j A_1^{\mu_1} \dots A_k^{\mu_k} e^{iS_{\text{int}}}, \quad (2.11)$$

where p_l is used to indicate momentum dependence. Diagrammatically, propagators from S_0 and interaction vertices from S_{int} can be expressed as Feynman rules. The quark, gluon and ghost propagators are given by

$$\begin{aligned} \begin{array}{c} i \quad \xrightarrow{p} \quad j \\ \hline a, \mu \quad \xrightarrow{k} \quad b, \nu \\ \hline a \quad \xrightarrow{p} \quad b \end{array} &= \frac{i(\not{p} + m)}{p^2 - m^2 + i0}, \\ &= -i\delta^{ab} \left(\frac{g_{\mu\nu}}{k^2 + i0} - (1 - \xi) \frac{k_\mu k_\nu}{(k^2 + i0)^2} \right), \\ &= \frac{i\delta^{ab}}{p^2 + i0}, \end{aligned}$$

respectively, where p and k are the momenta, $i0$ is the Feynman prescription. The quark-gluon, triple and quartic gluon and ghost-gluon vertices are

$$\begin{aligned} \begin{array}{c} a, \mu \\ \uparrow \\ i \quad \xrightarrow{\quad} \quad j \\ \downarrow \end{array} &= ig_s \gamma^\mu T^a, \\ \begin{array}{c} a, \mu \\ \uparrow p_1 \\ c, \rho \quad \swarrow p_3 \quad \searrow p_2 \quad b, \nu \end{array} &= -g_s f^{abc} (g^{\mu\nu} (p_1 - p_2)^\rho + g^{\nu\rho} (p_2 - p_3)^\mu + g^{\rho\mu} (p_3 - p_1)^\nu), \\ \begin{array}{c} a, \mu \quad \searrow \quad \swarrow b, \nu \\ \swarrow \quad \searrow \\ c, \rho \quad \swarrow \quad \searrow d, \sigma \end{array} &= -ig_s^2 (f^{abe} f^{cde} (g_{\mu\rho} g_{\nu\sigma} - g_{\mu\sigma} g_{\nu\rho}) \\ &\quad + f^{ace} f^{bde} (g_{\mu\nu} g_{\rho\sigma} - g_{\mu\sigma} g_{\nu\rho}) \\ &\quad + f^{ade} f^{bce} (g_{\mu\nu} g_{\rho\sigma} - g_{\mu\rho} g_{\nu\sigma})), \\ \begin{array}{c} b, \mu \\ \uparrow \\ c \quad \xrightarrow{p} \quad a \end{array} &= -g_s f^{abc} p^\mu. \end{aligned}$$

In practice, the perturbative expansion generates loops over quantum fluctuations. This leads to sums over spinor and colour structures as well as integrals over internal loop momenta. As a consequence two kinds of divergences may arise. UV divergences occur

when the loop integrals diverge for internal momenta going to infinity. These divergences can be removed by renormalisation, which will be discussed in the next sections.

In contrast, IR divergences occur due to massless propagators when integrals diverge as loop momenta go to zero (soft divergence) or become collinear with one of the external momenta [42]. This is particularly relevant for massless particles, such as gluons and light quarks. Massive propagators are protected from such divergences by the mass term. One has to include diagrams containing unresolved or very soft radiation to cancel IR divergences.

2.1.3 Dimensional Regularisation

In order to remove UV divergences we first have to parametrise them using a regularisation technique. In this thesis we will employ dimensional regularisation [43], as it is compatible with the symmetries of QCD. This means that we work in $D = 4 - 2\epsilon$ dimensions, where ϵ is a small parameter. Hence, the mass dimensions of the fields and couplings become

$$\begin{aligned} [q] &= \frac{D-1}{2}, \\ [A^\mu] &= \frac{D-2}{2}, \\ [\mathcal{L}_{QCD}] &= D, \\ [g_s] &= \epsilon, \\ [\xi] &= 0. \end{aligned} \tag{2.12}$$

It is convenient to re-express the coupling g_s as a dimensionless quantity

$$g_s \rightarrow g_s \nu^\epsilon, \tag{2.13}$$

where ν is an arbitrary scale parameter. This results in an effective shift of each momentum k integral $d^4k \rightarrow \nu^{4-D} d^Dk$.

Hence, we can now write Green's functions G as Laurent series in ϵ , giving

$$G = \frac{1}{\epsilon^N} G^{(-N)} + \frac{1}{\epsilon^{N-1}} G^{(-N+1)} + \dots + G^{(0)} + \mathcal{O}(\epsilon), \tag{2.14}$$

where $N \leq L$ for L -loop integrals with UV divergences. After regularisation we can proceed to cancel the UV poles using renormalisation, such that $G^{\text{ren}} = G^{(0),\text{ren}} + \mathcal{O}(\epsilon)$.

2.1.4 Renormalisation

In order to obtain finite Green's functions we have to renormalise the bare fields and couplings appearing in the Lagrangian Eq.(2.9) via

$$\begin{aligned} A_{0\mu} &= Z_A^{1/2} A_\mu(\mu), & q_0 &= Z_q^{1/2} q(\mu), & \xi_0 &= Z_\xi \xi(\mu), \\ g_{0,s} &= Z_g g_s(\mu) \nu^\epsilon, & m_{0,q} &= Z_m m_q(\mu), & \chi_0 &= Z_\chi \chi(\mu), \end{aligned} \quad (2.15)$$

where we have indicated the bare fields and couplings with the “0” subscript. The renormalised quantities are finite, but depend on a renormalisation scale μ , which is, in general, not related to the dimensional regularisation scale ν . The renormalisation constants Z contain poles which cancel the UV divergences. The $Z - 1$ are also referred to as counterterms.

The Z -factors may contain arbitrary finite parts which correspond to different renormalisation schemes. In the following, we will review two types of renormalisation schemes - minimal subtraction and momentum subtraction.

Minimal Subtraction Schemes

The minimal subtraction (MS) scheme removes only the poles, thus the counterterms do not contain finite parts [43]. In this thesis we will be using the modified minimal subtraction ($\overline{\text{MS}}$) scheme. In this scheme the scale ν is identified as

$$\nu = \mu \left(\frac{e^{\gamma_E}}{4\pi} \right)^{\frac{1}{2}}, \quad (2.16)$$

prior to performing the minimal subtraction. This is equivalent to defining the renormalised gauge coupling as

$$g_{0,s} = Z_g g_s(\mu) \mu^\epsilon \left(\frac{e^{\gamma_E}}{4\pi} \right)^{\frac{\epsilon}{2}}, \quad (2.17)$$

where γ_E is the Euler-Mascheroni constant.

The renormalisation scale dependence of the strong coupling is encoded by the β_s function [44, 45]

$$\beta_s(\mu) = \mu \frac{d}{d\mu} \left(\frac{\alpha_s(\mu)}{4\pi} \right) = -2\epsilon \frac{\alpha_s(\mu)}{4\pi} - 2\beta_0 \left(\frac{\alpha_s(\mu)}{4\pi} \right)^2 + \mathcal{O} \left(\frac{\alpha_s(\mu)}{4\pi} \right)^3, \quad (2.18)$$

where β_0 is its one-loop coefficient, given as

$$\beta_0 = \frac{11}{3} N_c - \frac{2}{3} N_f, \quad (2.19)$$

and $\alpha_s(\mu) = g_s(\mu)^2/(4\pi)$ is the fine structure constant of QCD. N_c is the number of colours and N_f is the number of active quark flavours. Due to $\beta_0 > 0$ in QCD the coupling becomes perturbative in the high energy regime (asymptotic freedom) [46, 47]. For low energies, however, the theory is strongly interacting and confining. Similarly, the mass and field anomalous dimensions γ can be similarly inferred from Z_m and Z_q .

For minimal subtraction, renormalisation constants $Z(\mu)$ can be written as

$$Z(\mu) = 1 + Z^{(1)} \frac{\alpha(\mu)}{4\pi} + Z^{(2)} \left(\frac{\alpha(\mu)}{4\pi} \right)^2 + \mathcal{O} \left(\frac{\alpha(\mu)}{4\pi} \right)^3, \quad (2.20)$$

where each perturbative order $Z^{(n)}$ is expanded in powers of ϵ

$$Z^{(n)} = \sum_{m=0}^n Z^{(n,m)} \frac{1}{\epsilon^m}. \quad (2.21)$$

The particular $\overline{\text{MS}}$ Z -factors, relevant for this thesis, are the wavefunction renormalisation constants [48], given by

$$\begin{aligned} Z_q^{(1)} &= -\frac{C_F}{\epsilon} \xi, \\ Z_q^{(2,2)} &= \frac{C_F}{4N_c} \xi (-\xi + 3N_c^2 + 2\xi N_c^2), \\ Z_q^{(2,1)} &= \frac{C_F}{8N_c} (-3 - 2\xi^2 - 22N_c^2 - 8\xi N_c^2 + \xi^2 N_c^2 + 4N_c N_f) - \frac{C_F^2}{2} \xi^2, \end{aligned} \quad (2.22)$$

where $C_F = (N_c^2 - 1)/(2N_c)$ is the quadratic Casimir invariant for the defining representation of $SU(N_c)$. In addition, we will need the gauge renormalisation constant [49]

$$Z_g^{(1)} = -\frac{\beta_0}{\epsilon}, \quad (2.23)$$

and the gauge parameter Z -factor

$$Z_\xi^{(1)} = \left(N_c \left(\frac{5}{3} + \frac{1}{2}(1 - \xi) \right) - \frac{2}{3} N_f \right) \frac{1}{\epsilon}. \quad (2.24)$$

Before we can discuss the momentum subtraction schemes, we have to introduce the notion of renormalisation of amputated Green's functions.

Renormalised Green's Functions

In a similar fashion to Eq.(2.10) we can define a renormalised connected Green's function in momentum space

$$G_{\text{ren}}^{ijk}(g_s(\mu), m_q(\mu), p_i^q, p_j^{\bar{q}}, p_k^A, \xi(\mu), \mu) \times (2\pi)^4 \delta^4 \left(\sum_{n=1}^i p_n^q + \sum_{m=1}^j p_m^{\bar{q}} + \sum_{l=1}^k p_l^A \right) \quad (2.25)$$

$$= \langle 0 | T q_1(p_1^q) \dots q_i(p_i^q) \bar{q}_1(p_1^{\bar{q}}) \dots \bar{q}_j(p_j^{\bar{q}}) A_1^{\mu_1}(p_1^A) \dots A_k^{\mu_k}(p_k^A) | 0 \rangle_{\text{conn}},$$

where the fields on the right-hand-side are renormalised. The corresponding connected amputated Green's function $\Lambda_{\text{ren}}^{ijk}$, which is known as the scattering amplitude, is given by

$$\Lambda_{\text{ren}}^{ijk} = \frac{G_{\text{ren}}^{ijk}}{\prod_{i,j} G_{\text{ren}}^{110} \prod_k G_{\text{ren}}^{002}}. \quad (2.26)$$

This expression is only schematic, the factors in the denominator mean the (matrix) inverse of 'dressed' propagators which, in general, involve various index contractions. The equivalent can also be defined for the bare Green's functions. Both are then related via

$$\Lambda_{\text{ren}}^{ijk}(g_s, m_q, p_l, \xi, \mu) = Z_q^{(i+j)/2} Z_A^{k/2} \Lambda_0^{ijk}(g_{0,s}, m_{0,q}, p_l, \xi_0). \quad (2.27)$$

Later, we will also be using the "bracket" notation to denote operator \mathcal{O} insertions into amputated Green's functions as $\Lambda(\mathcal{O}) = \langle \mathcal{O} \rangle$. In particular, for our operator Q defined in Eq.(2.1) the four-point amputated Green's function is given by

$$\Lambda_{\alpha\beta\gamma\delta}^{ijkl}(p_1, p_2, p_3, p_4) = \langle d_\alpha^i(p_1) \bar{s}_\beta^j(-p_2) d_\gamma^k(p_3) \bar{s}_\delta^l(-p_4) Q(p_1 + p_3 - p_2 - p_4) \rangle_{\text{conn}} \quad (2.28)$$

$$= \langle Q \rangle,$$

where i, j, k, l are colour and $\alpha, \beta, \gamma, \delta$ are Dirac indices, and p_1, p_3 are incoming and p_2, p_4 outgoing momenta, subject to the constraint $p_1 + p_3 = p_2 + p_4$. Once the renormalisation is performed, we can take the limit $\epsilon \rightarrow 0$ and obtain a finite scattering amplitude.

Momentum Subtraction Schemes

As opposed to minimal subtraction, where the dimensional regularisation scale is translated into the renormalisation scale, momentum subtraction schemes (MOM) are regularisation invariant (RI) and instead the renormalisation scale corresponds to a momentum. In general, these schemes are specified by renormalisation conditions which are fixed such that at a subtraction point the renormalised Green's functions are satisfied by their tree-

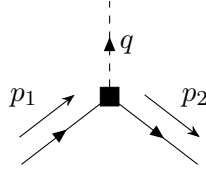


Figure 2.1: Momentum subtraction point, where $q = p_1 - p_2$ and the square corresponds to insertion of an operator. Solid lines denote fermions and dashed line momentum transfer.

level expressions.

The subtraction point is defined through different momentum configurations of an operator \hat{O} insertion between two external quark lines at fixed gauge, for which the momentum flow is illustrated in Figure 2.1. There are two choices for the momentum configuration: exceptional and non-exceptional. The exceptional momentum configuration involves

$$p_1^2 = p_2^2 = p^2 = -\mu^2 \quad \text{and} \quad q = 0, \quad (2.29)$$

where $\mu^2 > 0$ is the renormalisation scale. This is known as the RI-MOM scheme, which was introduced in the context of non-perturbative renormalisation of lattice operators in [50]. On the other hand, the non-exceptional point, which is often called symmetric or RI-SMOM, is defined with all non-zero channels, as

$$p_1^2 = p_2^2 = q^2 = p^2 = -\mu^2 \quad \text{and} \quad q = p_1 - p_2. \quad (2.30)$$

RI-SMOM was introduced in [51]. In both cases p is the Euclidean momentum, hence $p^2 < 0$. The symmetric configuration is usually preferred, due to better convergence of the perturbative expansion, decrease in chiral symmetry breaking and other infrared effects [51].

The renormalisation constants for the RI-MOM and RI-SMOM schemes are obtained as follows. Consider a Green's function $G_{\hat{O}}$, given by

$$G_{\hat{O}} = i \int d^4x e^{ipx} \langle 0 | T \hat{O}(x) | 0 \rangle, \quad (2.31)$$

which is equivalent to Eq.(2.10). Then the amputated Greens function, as in Eq.(2.26), can be defined as

$$\Lambda_{\hat{O}} = S^{-1}(p_2) G_{\hat{O}} S^{-1}(p_1), \quad (2.32)$$

where $S(p)$ is the ‘dressed’ quark propagator

$$S(p) = G^{110} = i \int d^4x e^{ipx} \langle 0 | T q(x) \bar{q}(0) | 0 \rangle. \quad (2.33)$$

The wavefunction renormalisation constants Z_q , defined in Eq.(2.15), can be obtained from the following conditions

$$\lim_{m_q \rightarrow 0} \frac{1}{48} \text{Tr} \left[\gamma^\mu \frac{\partial S_R^{-1}(p)}{\partial p^\mu} \right] \Big|_{p^2 = -\mu^2} = -1, \quad \text{RI-(S)MOM}, \quad (2.34)$$

$$\lim_{m_q \rightarrow 0} \frac{1}{12p^2} \text{Tr}[S_R^{-1}(p) \not{p}] \Big|_{p^2 = -\mu^2} = -1, \quad \text{RI-SMOM}, \quad (2.35)$$

imposed on a renormalised quark propagator $S_R^{-1} = Z_q^{-1} S_0^{-1}$, where the bare propagators is defined as

$$S_0(p) = \frac{-1}{\not{p} - m_{0,q} + i0 - \Sigma(p)}, \quad (2.36)$$

and $\Sigma(p)$ denotes the higher order corrections to the quark self-energy. The quarks are treated as massless and the trace is defined over both colour and spin. There are further renormalisation conditions defined for the quark masses and different operator insertions into vertex itself, which can be found in [51]. Before we can discuss the renormalisation of four-quark operators, we have to comment on the non-renormalisable couplings of higher dimensional operators.

Non-renormalisable Couplings

The renormalisation procedure is applicable to all loop orders in theories containing couplings with non-negative mass dimensions. Generally, higher order operators, giving rise to couplings with negative mass dimensions, are considered non-renormalisable. However, they can be renormalised order by order in perturbation theory, provided an increasingly large set of operators is considered.

2.2 Operator Renormalisation and Matching

In this thesis, we will only consider the four-quark operator which represents the low-energy approximation to the strong interaction. Hence, these operators are not treated as independent interactions that would enter loop integrals. Instead, only renormalisable QCD interactions are considered, as they represent the high-energy formulation of the theory. As a result, the four-fermion operators introduce counterterms and are renormalised

by dimension four interactions, while operators with even higher mass dimension are not required. As the light quark mass is neglected, the renormalisation remains proportional four-quark operators, and a Z factor can be introduced. In general, this will be a matrix of renormalisation constants.

In this section we will review the renormalisation of four-quark operators in $\overline{\text{MS}}$ NDR and momentum subtraction schemes. We will also discuss the evanescent operators, the matching between the two types of schemes and derive the anomalous dimension matrix for the renormalised operators. The latter allows us to obtain the two-loop renormalisation constants in terms of one-loop poles and anomalous dimensions. For a comprehensive introduction to the treatment of four-quark operators we refer to [31, 41] and references therein.

2.2.1 $\overline{\text{MS}}$ NDR Scheme and Evanescent Operators

$\overline{\text{MS}}$ schemes, within the context of dimensional regularisation, are constructed explicitly out of the bare operators. In general, the renormalised operators involve several bare operators, which would lead to a renormalisation

$$Q_i^{\text{ren}}(\mu) = \sum_j Z_{ij}(\mu) Q_j^{\text{bare}}, \quad (2.37)$$

where $Z_{ij}(\mu)$ is a matrix of renormalisation constants. In our case, we have only one physical bare operator Q^B and a single renormalisation constant Z_{QQ} . In dimensional regularisation there are additional operators E_i^B , as a consequence of the larger Dirac algebra in $D \neq 4$ compared to $D = 4$. They can be chosen such that they vanish at tree-level in $D = 4$ and are known as evanescent operators. For the renormalised four-quark operator Q defined in Eq.(2.1), we have

$$Q^{\text{NDR}} = Z_{QQ} Q^B + \sum_i Z_{QE_i} E_i^B, \quad (2.38)$$

where ‘NDR’ specifies anti-commuting γ^5 and Z_{QQ} and Z_{QE_i} are renormalisation constants. Defining the renormalised coupling through Eq.(2.15), the Z -factors are defined such that $g_s(\mu)$ and $\langle Q^{\text{NDR}} \rangle$ (for renormalised quark fields) have a finite limit $\epsilon \rightarrow 0$. The Z factors are singular as $\epsilon \rightarrow 0$ and, for $\overline{\text{MS}}$, are taken equal to the principal parts of their Laurent expansions (i.e. containing only poles in ϵ).

Up to two-loop order the following basis of evanescent operators suffices:

$$\begin{aligned}
E_F &= (\bar{s}^i \gamma^\mu P_L d^l) (\bar{s}^k \gamma_\mu P_L d^j) - Q, \\
E_1 &= (\bar{s}^i \gamma^{\mu_1 \mu_2 \mu_3} P_L d^j) (\bar{s}^k \gamma_{\mu_1 \mu_2 \mu_3} P_L d^l) - (16 - 4\epsilon - 4\epsilon^2)Q, \\
E_2 &= (\bar{s}^i \gamma^{\mu_1 \mu_2 \mu_3} P_L d^l) (\bar{s}^k \gamma_{\mu_1 \mu_2 \mu_3} P_L d^j) - (16 - 4\epsilon - 4\epsilon^2)(Q + E_F), \\
E_3 &= (\bar{s}^i \gamma^{\mu_1 \mu_2 \mu_3 \mu_4 \mu_5} P_L d^j) (\bar{s}^k \gamma_{\mu_1 \mu_2 \mu_3 \mu_4 \mu_5} P_L d^l) - (256 - 224\epsilon - 144\epsilon^2)Q, \\
E_4 &= (\bar{s}^i \gamma^{\mu_1 \mu_2 \mu_3 \mu_4 \mu_5} P_L d^l) (\bar{s}^k \gamma_{\mu_1 \mu_2 \mu_3 \mu_4 \mu_5} P_L d^j) - (256 - 224\epsilon - 144\epsilon^2)(Q + E_F),
\end{aligned} \tag{2.39}$$

where $\gamma^{\mu_1 \mu_2 \mu_3} = \gamma^{\mu_1} \gamma^{\mu_2} \gamma^{\mu_3}$ etc. We use a different definition from the Brod–Gorbahn basis [52], which we will explain in more detail in Section 3.7. The E_i are chosen to vanish at $\epsilon = 0$ ($D = 4$) at tree level. At loop level, E_i require renormalisation just like the physical operators

$$E_i^{\text{NDR}} = Z_{E_i E_j} E_j^B + Z_{E_i Q} Q^B. \tag{2.40}$$

While the $Z_{E_i E_j}$ can again be chosen to be the principal parts of their Laurent series, a finite $Z_{E_i Q}$ is generally required in order to have $\langle E_i^{\text{NDR}} \rangle = 0$ also at loop level. The E_i^{NDR} renormalised in such a fashion are known as evanescent operators, and in particular give vanishing contributions to physical matrix elements. The $\mathcal{O}(\epsilon)$ and $\mathcal{O}(\epsilon^2)$ terms are chosen for convenience.

2.2.2 Four-quark Operators in MOM Schemes

Similarly to the QCD renormalisation, operator Z -factors can be alternatively fixed by momentum space conditions. This is attractive from a lattice perspective. Calculations on the lattice are done numerically, where the lattice spacing, renormalisation scale and gauge are fixed and the external states are off-shell (as this is how the non-perturbative lattice renormalisation scheme is defined, in order to reduce the systematic errors [50]). Once computed, the bare matrix element is then renormalised in terms of some intermediate scheme. It has to be possible to implement this scheme both numerically on the lattice as well as in perturbation theory. This is because we want to combine the matrix element with the Wilson coefficients, which are usually computed in $\overline{\text{MS}}$ NDR scheme. In order to achieve that goal, both the matrix elements and the Wilson coefficients are renormalised in the same scheme. One type of schemes, that are viable for such conversion, are the RI-(S)MOM schemes.

Originally, RI-MOM and RI-SMOM schemes were applied to four-quark operators in [53] and [4] respectively. For our operator defined in Eq.(2.1), a typical momentum

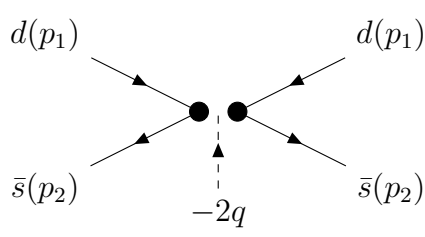


Figure 2.2: Momentum subtraction point for a four-quark operator: $p_1^2 = p_2^2 = (p_1 - p_2)^2$ and $q = p_1 - p_2$. The solid black lines with arrows indicate fermion and momentum flow, the dashed line with arrow indicates momentum flow into the vertex.

flow is shown in Figure 2.2, with the same kinematics as given in Eqs.(2.29, 2.30). The vertex renormalisation condition is defined such that at the subtraction point the four-point amputated Green's function Λ , given in Eq.(2.28), is equal to the tree-level Green's function. The projection operators, which facilitate this, can be written as

$$P_{(\gamma_\mu),\alpha\beta,\gamma\delta}^{ij,kl} = \frac{(\gamma^\nu)_{\beta\alpha}(\gamma_\nu)_{\delta\gamma} + (\gamma^\nu\gamma^5)_{\beta\alpha}(\gamma_\nu\gamma^5)_{\delta\gamma}}{256N_c(N_c + 1)} \delta_{ij}\delta_{kl}, \quad \text{RI-(S)MOM}, \quad (2.41)$$

$$P_{(\not{q}),\alpha\beta,\gamma\delta}^{ij,kl} = \frac{(\not{q})_{\beta\alpha}(\not{q})_{\delta\gamma} + (\not{q}\gamma^5)_{\beta\alpha}(\not{q}\gamma^5)_{\delta\gamma}}{64q^2N_c(N_c + 1)} \delta_{ij}\delta_{kl}, \quad \text{RI-SMOM}, \quad (2.42)$$

where N_c is the number of colours, i, j, k, l colour and $\alpha, \beta, \gamma, \delta$ spinor indices [4]. These projection operators are normalised in such a way that $\text{Tr}(P\Lambda^{tree}) = 1$. Having multiple projectors allows us to assess the systematic uncertainties resulting from the choice of scheme.

Given the two projectors in Eqs.(2.41, 2.42) and the two conditions on the quark propagator that specify $Z_q^{(\gamma_\mu)}$ in Eq.(2.34) and $Z_q^{(\not{q})}$ in Eq.(2.35), we can define four renormalisation schemes as

$$Q_R^{(\gamma_\mu, \gamma_\mu)} = Z_Q^{(\gamma_\mu, \gamma_\mu)} Q_B, \quad (2.43)$$

$$Q_R^{(\gamma_\mu, \not{q})} = Z_Q^{(\gamma_\mu, \not{q})} Q_B, \quad (2.44)$$

$$Q_R^{(\not{q}, \gamma_\mu)} = Z_Q^{(\not{q}, \gamma_\mu)} Q_B, \quad (2.45)$$

$$Q_R^{(\not{q}, \not{q})} = Z_Q^{(\not{q}, \not{q})} Q_B, \quad (2.46)$$

where ‘ R ’ stands for renormalised and ‘ B ’ for bare. The Z -factors here are given by

$$Z_Q^{(\gamma_\mu, \gamma_\mu)} = \left(Z_q^{(\gamma_\mu)} \right)^2 \frac{1}{P_{(\gamma_\mu)}(\Lambda_B)}, \quad (2.47)$$

$$Z_Q^{(\gamma_\mu, \not{q})} = \left(Z_q^{(\not{q})} \right)^2 \frac{1}{P_{(\gamma_\mu)}(\Lambda_B)}, \quad (2.48)$$

$$Z_Q^{(\not{q}, \gamma_\mu)} = \left(Z_q^{(\gamma_\mu)} \right)^2 \frac{1}{P_{(\not{q})}(\Lambda_B)}, \quad (2.49)$$

$$Z_Q^{(\not{q}, \not{q})} = \left(Z_q^{(\not{q})} \right)^2 \frac{1}{P_{(\not{q})}(\Lambda_B)}, \quad (2.50)$$

where $P_{(X)}(\Lambda) = P_{(X)\alpha\beta, \gamma\delta}^{ij, kl} \Lambda_{\alpha\beta, \gamma\delta}^{ij, kl}$ [4]. We can now proceed to derive the conversion factors for the operators between the $\overline{\text{MS}}$ and RI-(S)MOM schemes.

2.2.3 Matching between $\overline{\text{MS}}$ and RI-(S)MOM schemes

In this thesis we will be matching our operator Q between $\overline{\text{MS}}$ and RI-(S)MOM schemes, as mentioned in Eq.(2.2). Generally, a relation between two schemes A and B for such operator is itself a finite renormalisation

$$Q^B = C_Q^{A \rightarrow B} Q^A, \quad (2.51)$$

where $C_Q^{A \rightarrow B} = Z_Q^A / Z_Q^B$. Likewise, for the quark field we have

$$\psi^B = (C_q^{A \rightarrow B})^{1/2} \psi^A, \quad (2.52)$$

and similar for the gluon field. The Green’s functions in both schemes are related as

$$\Lambda^B = (C_q^{A \rightarrow B})^2 C_Q^{A \rightarrow B} \Lambda^A, \quad (2.53)$$

where dependence on colour, Dirac indices, and momenta has been suppressed. Consider now any linear functional $P(\Lambda)$, in practice a combined Lorentz-colour-tensor which contracts with the Green’s function to a scalar. Then, for any kinematics for which $P(\Lambda)$ does not vanish, the scheme conversion factor can be evaluated as

$$C_Q^{A \rightarrow B} = \frac{1}{(C_q^{A \rightarrow B})^2} \frac{P(\Lambda^B)}{P(\Lambda^A)}, \quad (2.54)$$

in terms of the Green’s functions and the wave function conversion factors.

Hence, for the conversion factors defined as the ratio between the four-quark operator

in the NDR scheme and in the RI-SMOM scheme

$$Q_{VV+AA}^{\text{NDR}}(\mu) = C_{B_K}^{\text{SMOM}}(p^2/\mu^2)Q_{VV+AA}^{\text{SMOM}}(p), \quad (2.55)$$

where p is the renormalisation scale of the SMOM scheme and μ is renormalisation scale of the NDR scheme, the factors are given by

$$C_{B_K}^{(X,Y)} = (C_q^{(Y)})^2 P_{(X)\alpha\beta,\gamma\delta}^{ij,kl} \Lambda_{\alpha\beta,\gamma\delta}^{ij,kl}, \quad (2.56)$$

where $C_q^{(Y)} = Z_q^{\overline{\text{MS}}}/Z_q^{(Y)}$ is the conversion factor for the wave-function renormalisation. P are the projectors, defined in Eqs.(2.41, 2.42) with (X,Y) corresponding to different RI-SMOM schemes. $\Lambda_{\alpha\beta,\gamma\delta}^{ij,kl}$ is the amputated four-point Green's function computed in the $\overline{\text{MS}}$ -NDR renormalisation and at the RI-SMOM point.

2.2.4 Operator Anomalous Dimensions

In order to perform the conversion between the two schemes at two-loop order, we will need two-loop $\overline{\text{MS}}$ renormalisation constants. These can usually be extracted from the computation of the amplitude (or at least its poles). Alternatively, they enter the computation of the two-loop anomalous dimensions. Several such computations have been performed specifically for operator Q and can be found in [52, 54]. In this section we provide the derivation of the anomalous dimensions in our conventions.

In general, renormalised operators Q_i^{ren} can be expressed in terms of bare operators Q_i^{bare} , which have a well-defined meaning during the calculation, as defined in Eq.(2.37). The renormalisation group equations of the operators

$$\mu \frac{d}{d\mu} Q_i^{\text{ren}}(\mu) = \gamma_{ij} Q_j^{\text{ren}}(\mu), \quad (2.57)$$

are determined by the anomalous dimension matrix (ADM) γ_{ij} , defined via

$$\gamma_{ij} = \mu \frac{dZ_{ik}}{d\mu} Z_{kj}^{-1}. \quad (2.58)$$

Using the beta function of α_s Eq.(2.18) together with Eqs.(2.20, 2.21), we can compute

the ADM as

$$\begin{aligned}
\gamma &= -2Z^{(1,1)}\frac{\alpha_s(\mu)}{4\pi} + \left(\frac{1}{\epsilon}(-2\beta_0 Z^{(1,1)} - 4Z^{(2,2)} + 2Z^{(1,1)}Z^{(1,1)})\right. \\
&\quad \left.+ (-2\beta_0 Z^{(1,0)} - 4Z^{(2,1)} + 2Z^{(1,0)}Z^{(1,1)} + 2Z^{(1,1)}Z^{(1,0)})\right) \left(\frac{\alpha_s(\mu)}{4\pi}\right)^2 \\
&\quad + \mathcal{O}\left(\frac{\alpha_s(\mu)}{4\pi}\right)^3.
\end{aligned} \tag{2.59}$$

Hence, the one-loop ADM is given by

$$\gamma^{(0)} = -2Z^{(1,1)}. \tag{2.60}$$

The coefficient in front of the $1/\epsilon$ pole has to vanish as the ADM has to be finite since it encodes the change of operators with the renormalisation scale. Hence, one can obtain an ADM finiteness (or renormalisability) condition as

$$-2\beta_0 Z^{(1,1)} - 4Z^{(2,2)} + 2Z^{(1,1)}Z^{(1,1)} = 0. \tag{2.61}$$

Finally, the two-loop ADM is given by

$$\gamma^{(1)} = (-2\beta_0 Z^{(1,0)} - 4Z^{(2,1)} + 2Z^{(1,0)}Z^{(1,1)} + 2Z^{(1,1)}Z^{(1,0)}). \tag{2.62}$$

As long as $\gamma^{(0)}$ arises at one-loop, as is the case in our investigation, it is scheme-independent. The $\gamma^{(1)}$ generally depend on the renormalisation scheme as $Z^{(1,0)}$ and $Z^{(2,1)}$ usually depend on the choice of the evanescent operators, conventionally chosen such that their Green's functions vanish in four dimensions.

2.3 Technical Aspects of Loop Integrals

In Chapter 3, we will encounter loop integrals when computing the one and two-loop radiative corrections to the vertex shown in Figure 2.2. A detailed introduction to loop integrals can be found in [42, 55]. The Feynman rules, defined in Section 2.1.2, can be used to translate the contributing diagrams into expressions for the amputated Green's functions. At two-loop in particular, these expressions contain a large variety of tensor integrals over internal loop momenta. Contracting with the (S)MOM projectors allows us to express the tensors in terms of scalar products. Hence we only need to deal with scalar integrals. A generic scalar one-loop integral I_n , with p_n external momenta, can be defined

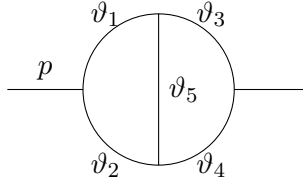


Figure 2.3: The massless two-loop bubble with a vertical line, $I(\vartheta_1, \vartheta_2, \vartheta_3, \vartheta_4, \vartheta_5)$, with p external momentum and the ϑ 's corresponding to the powers of the propagators.

as

$$I_n(\vartheta_1, \dots, \vartheta_n) = \nu^{4-D} \int \frac{d^D k}{i\pi^{\frac{D}{2}}} \prod_{i=1}^n \frac{1}{(q_i^2 - m_i^2 + i0)^{\vartheta_i}}, \quad (2.63)$$

where ν is the dimensional regularisation scale, k is the loop momentum, $i\pi^{\frac{D}{2}}$ is a normalisation factor, $q_i = k + \sum_{j=0}^i p_j$ are the momenta of all the propagators with masses m_i , $i0$ is the Feynman prescription and ϑ_i are the integer powers of n propagators. The integral is defined in Minkowski space with D dimensions and metric $\eta_{\mu\nu}$ follows the Bjorken-Drell convention. Momentum conservation implies $\sum_{i=1}^n p_i = 0$. The subscript n is used to indicate the number of different propagators corresponding to the integral.

Generally, the initial diagrams that we get from the Feynman rules have $\vartheta_i = 1$ (or 2 depending on gauge). The transition from tensors to scalars as well as any other factors of loop momenta in the numerator generate a range of integrals with additional positive or negative powers of propagators $|\vartheta_i| > 1$. These integrals can be reduced via the integration by parts (IBP) method [56] to a particular choice of master integrals. An introduction to the IBP method can be found in [55, 57]. To facilitate this reduction at two-loop we have to define auxiliary topologies. In this section we will review these techniques.

Integration by Parts

One-loop and many two-loop integrals by now are very well known and solutions for all of them can be found in the literature. Instead of attempting to derive analytic solutions ourselves, we will focus on expressing the diagrams we want to compute in terms of integrals that are mostly already known. Hence, integration by parts (IBP) method is an invaluable tool as it allows us to obtain linear relations between loop integrals.

Take the two-loop two-point function as an example, given in Figure 2.3. This diagram is too complicated to be solved using the standard Feynman parametrisation, hence we need a more advanced approach. Our aim here is to relate the physical integral $I(1, 1, 1, 1, 1)$ to simpler integrals, corresponding to the same diagram, but with differ-

ent powers of propagators. We can write I as

$$I(\vartheta_1, \dots, \vartheta_5) = \int \frac{d^D k}{i\pi^{D/2}} \int \frac{d^D l}{i\pi^{D/2}} \frac{1}{(k^2)^{\vartheta_1} ((k+p)^2)^{\vartheta_2} (l^2)^{\vartheta_3} ((l+p)^2)^{\vartheta_4} ((k-l)^2)^{\vartheta_5}}, \quad (2.64)$$

where k and l are the loop-momenta, p is external momentum, ϑ 's corresponding to arbitrary powers of the propagators. Next, we can take a total derivative, with respect to one of the loop momenta, giving us

$$\int \frac{d^D k}{i\pi^{D/2}} \int \frac{d^D l}{i\pi^{D/2}} \frac{\partial}{\partial k^\mu} \left(\frac{v^\mu}{(k^2)^{\vartheta_1} ((k+p)^2)^{\vartheta_2} (l^2)^{\vartheta_3} ((l+p)^2)^{\vartheta_4} ((k-l)^2)^{\vartheta_5}} \right) = 0, \quad (2.65)$$

where v^μ is just an arbitrary 4-vector. Taking the derivative gives

$$\begin{aligned} & \int \frac{d^D k}{i\pi^{D/2}} \int \frac{d^D l}{i\pi^{D/2}} \frac{1}{(k^2)^{\vartheta_1} ((k+p)^2)^{\vartheta_2} (l^2)^{\vartheta_3} ((l+p)^2)^{\vartheta_4} ((k-l)^2)^{\vartheta_5}} \\ & \times \left(\frac{\partial v^\mu}{\partial k^\mu} - \frac{\vartheta_1}{k^2} 2k^\mu v_\mu - \frac{\vartheta_2}{(k+p)^2} 2(k+p)^\mu v_\mu - \frac{\vartheta_5}{(k-l)^2} 2(k-l)^\mu v_\mu \right) = 0. \end{aligned} \quad (2.66)$$

We can already see that most of the terms come with an extra propagator. In addition, depending on what v^μ is chosen to be, we can get a scalar product that can be expressed in terms of inverse propagators. For instance, if we take $v^\mu = k^\mu$ and the third term, we can get $2(k+p) \cdot k = 2k^2 + 2k \cdot p = (k+p)^2 + k^2 - p^2$, which lowers the powers of the second and the first propagators respectively. We proceed by choosing $v^\mu = (k-l)^\mu$ for convenience. We denote the change in propagator powers by raising or lowering operators as \mathbf{n}^\pm , where \mathbf{n} is the index corresponding to the ϑ_n and \pm refers to $\vartheta_n \pm 1$. We get

$$(D - \vartheta_1 - \vartheta_2 - 2\vartheta_5)I + \vartheta_1 \mathbf{1}^+ (\mathbf{3}^- - \mathbf{5}^-)I + \vartheta_2 \mathbf{2}^+ (\mathbf{4}^- - \mathbf{5}^-)I = 0. \quad (2.67)$$

Setting $\vartheta_n = 1$ and using the symmetries of the integrals gives

$$I(1, 1, 1, 1, 1) = \frac{2}{D-4} [I(2, 1, 1, 1, 0) - I(2, 1, 0, 1, 1)], \quad (2.68)$$

where the $\vartheta_n = 0$ refers to an effectively pinched propagator. We have expressed the integral in terms of the diagrams, shown in Figure 2.4, which are much easier to compute.

We can see that with 2 loop momenta and 1 external momentum, we have two choices for the derivatives and 3 for v^ν , giving us 6 coupled linear equations. These can then be solved, to find the solution in terms of a preferred basis of integrals. It can indeed be very convenient to reduce all integrals in terms of a small basis, for which we already know the solutions. Such basis is also known as the master integrals. However, to fully exploit this

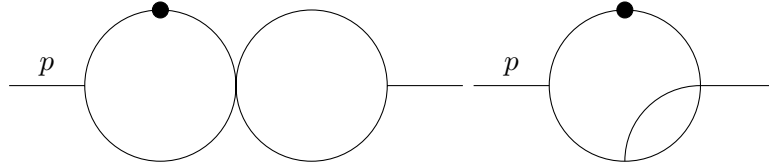


Figure 2.4: Two diagrams corresponding to $I(2, 1, 1, 1, 0)$ and $I(2, 1, 0, 1, 1)$. Dot represents propagator squared.

at two-loop order, we need to also introduce auxiliary topologies.

IBP at Two-loop Order: Auxiliary Topologies

A two-loop diagram with two independent external momenta can have at most 7 linearly independent propagators. This number is based on the possible scalar products between the loop and external momenta. For example, if we have k_1, k_2 as our loop and p_1, p_2 as external momenta, we can have 3 combinations of k_1, k_2 and 4 combinations of k_1, k_2 with p_1, p_2 . We know how scalar products are related to the propagators from the previous section. Hence, 7 combinations of scalar products lead to 7 linearly independent propagators.

The example shown in Figure 2.3 had 2 loop and 1 external momentum. Therefore, we could have had at most 5 propagators. Hence, during the reduction, we could express all the scalar products in terms of the propagators. This is, however, not always the case. For diagrams with fewer than the maximum number of propagators, applying the IBP method on such diagrams, could result in irreducible numerators. This means that these numerators can not be expressed in terms of the inverse propagators. This is also the reason why Passarino-Veltman technique can not be used beyond one loop [55].

The corrections to the aforementioned vertex are going to come with at most 6 propagators. In order to reduce all these diagrams systematically and to not run into irreducible numerators, we have to define our diagrams in terms of topologies, with a full set of 7 propagators. As shown in Figure 2.5, we can do this by simply adding extra linearly independent propagator to one of the existing diagrams. This also allows us to express any other terms in the numerators coming from the propagators in the full Feynman diagrams, in terms of the inverse propagators of the auxiliary topology. As a result, if we map all the diagrams onto a small set of topologies, we only need one set of IBP identities per each topology, and this can be used to reduce all the integrals belonging to that topology into a small set of masters.

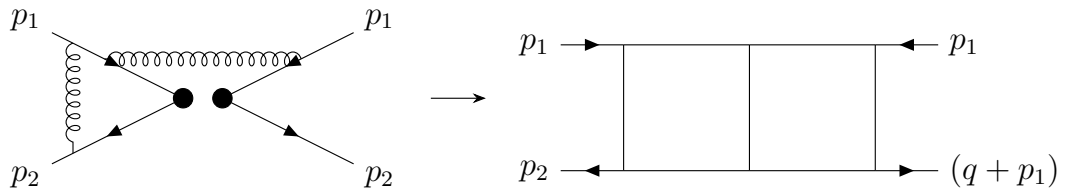


Figure 2.5: Obtaining an auxiliary topology based on one of the diagrams.

2.4 Summary

In this chapter we have covered the basic aspects of renormalisation in QCD and defined our notation and conventions. In particular we have reviewed the computation of amputated Green's functions and their renormalisation in minimal subtraction as well as momentum subtraction schemes. In addition, we have discussed the renormalisation of four-quark operators in both kinds of schemes along with conversion between them. We have also derived the anomalous dimensions of the operators in our conventions, which will be very useful in extracting the two-loop counter-terms in the next chapter. Finally, we reviewed the integration by parts method and its application at two-loop order, which is an essential tool in computation of one and two-loop amplitudes.

Chapter 3

NNLO Matching of RI/(S)MOM Schemes to $\overline{\text{MS}}$ for B_K

In this chapter, we present the first two-loop calculation of the conversion factor for the kaon bag parameter, required for the matching between lattice RI/SMOM scheme to $\overline{\text{MS}}$ scheme. In addition, we provide the conversion factors to translate the result to Brod–Gorbahn scheme. This calculation is an extension to the one-loop conversion factors obtained in [4].

The chapter is organised as follows. In Section 3.1 we review the diagrams that comprise the bare two-loop amputated Greens functions. We discuss the structure of these diagrams and the issues with tensor reduction and γ_5 at two-loop order. This provides us with the motivation to take a different approach to computing the amplitude to that of [4], presented in Section 3.2. Our method involves computing only part of the diagrams using Greek projections and obtaining the rest by inspecting the aforementioned structures. We then proceed to validate this technique by computing the the one-loop amplitude and counterterms in Section 3.3 as well as reproduce the one-loop result for the conversion factors of [4] in Section 3.4. Furthermore, we calculate the additional one- and two-loop counterterms and the renormalised amplitude in Section 3.5. We present the first results for the two-loop conversion factors in Section 3.6. In Section 3.7 we compute the conversion factors necessary to translate our results to the Brod–Gorbahn basis of evanescent operators. This means that our conversion factors can be used in conjunction with the Wilson coefficients and anomalous dimensions in [52]. Finally, in Section 3.8 we present a result for B_K in the two $\overline{\text{MS}}$ schemes and summarise this chapter in Section 3.9.

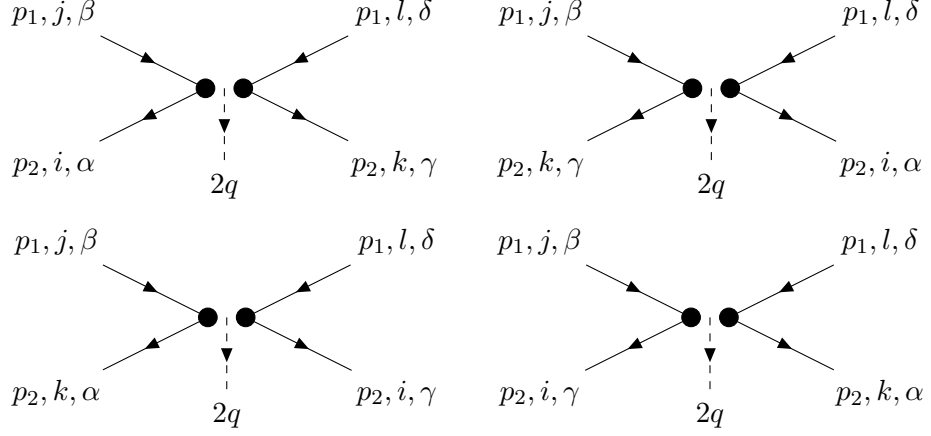


Figure 3.1: The four configurations of the external indices, corresponding to the following structures described in the text: $(\Gamma \otimes \Gamma 1 \otimes 1)$, $(\Gamma \tilde{\otimes} \Gamma 1 \tilde{\otimes} 1)$, $(\Gamma \otimes \Gamma 1 \tilde{\otimes} 1)$, $(\Gamma \tilde{\otimes} \Gamma 1 \otimes 1)$ (left to right, top to bottom). Each dot corresponds to an insertion of a current Γ and arrows indicate fermion and momentum flow.

3.1 Four-quark Amplitude in Perturbation Theory

The key ingredient in computing the conversion factor in Eq.(2.2) is the perturbative calculation of projected amplitudes $P_{(X)\alpha\beta,\gamma\delta}^{ij,kl} \Lambda_{\alpha\beta,\gamma\delta}^{ij,kl}$, as defined in Eq.(2.56). The amplitude corresponds to an insertion of the operator Q in Eq.(2.1) into the vertex of transition $d(p_1)\bar{s}(-p_2) \rightarrow \bar{d}(p_1)s(-p_2)$ computed at RI-(S)MOM subtraction point, given in Fig.(2.2).

In this section we will examine the structure of $\Lambda_{\alpha\beta,\gamma\delta}^{ij,kl}$, including the quantum corrections up to two-loop order. We will also discuss the issues with tensor reduction at two-loop order and the ambiguities arising in traces over γ_5 in D dimensions.

3.1.1 Amplitude at Leading Order

Let us explicitly write the tree-level matrix element (four-fermion Green's functions) corresponding to the insertion of operator Q at RI-(S)MOM kinematics as

$$\begin{aligned}
\langle Q \rangle &\equiv \Lambda_{\alpha\beta\gamma\delta}^{ijkl}(Q) = 2 \left((\gamma^\mu P_L)_{\alpha\beta} (\gamma_\mu P_L)_{\gamma\delta} \delta^{ij} \delta^{kl} - (\gamma^\mu P_L)_{\alpha\delta} (\gamma_\mu P_L)_{\gamma\beta} \delta^{il} \delta^{kj} \right) \\
&\equiv 2\gamma^\mu P_L \otimes \gamma_\mu P_L 1 \otimes 1 - 2\gamma^\mu P_L \tilde{\otimes} \gamma_\mu P_L 1 \tilde{\otimes} 1 \\
&\equiv 2Q^s 1 \otimes 1 - 2\tilde{Q}^s 1 \tilde{\otimes} 1,
\end{aligned} \tag{3.1}$$

where we use the superscript 's' to denote the Dirac structures defined above. The factor of 2 comes from the fact that we can interchange the two currents. The pictorial representation of the two structures is given in the top row of Fig.(3.1). A further operator \tilde{Q} ,

corresponding the bottom two diagrams in Fig.(3.1) can be defined as

$$\tilde{Q} = (\bar{s}^i \gamma^\mu P_L d^l) (\bar{s}^k \gamma_\mu P_L d^j), \quad (3.2)$$

with the matrix element given by

$$\langle \tilde{Q} \rangle = 2 Q^s 1 \tilde{\otimes} 1 - 2 \tilde{Q}^s 1 \otimes 1. \quad (3.3)$$

The Greens functions $\langle \tilde{Q} \rangle$ differ from those of $\langle Q \rangle$ only by interchange of the two colour structures.

The expressions for the matrix elements can be split into two parts

$$\langle Q \rangle = \langle Q \rangle_1 + \langle Q \rangle_2, \quad (3.4)$$

where $\langle Q \rangle_1 = -2(\gamma^\mu P_L)_{\alpha\delta}(\gamma_\mu P_L)_{\gamma\beta} \delta^{il} \delta^{kj}$ and $\langle Q \rangle_2 = 2(\gamma^\mu P_L)_{\alpha\beta}(\gamma_\mu P_L)_{\gamma\delta} \delta^{ij} \delta^{kl}$. Next, we recall that our projectors, defined in Eqs.(2.41, 2.42) are of the form

$$P_{\alpha\beta,\gamma\delta} \propto X_{\beta\alpha} Y_{\delta\gamma} \delta_{ij} \delta_{kl}. \quad (3.5)$$

Projecting the two structures in Eq.(3.4) results in two types of spinor index contractions

$$P\langle Q \rangle_1 \propto \text{Tr}(X \gamma^\mu P_L Y \gamma_\mu P_L), \quad (3.6)$$

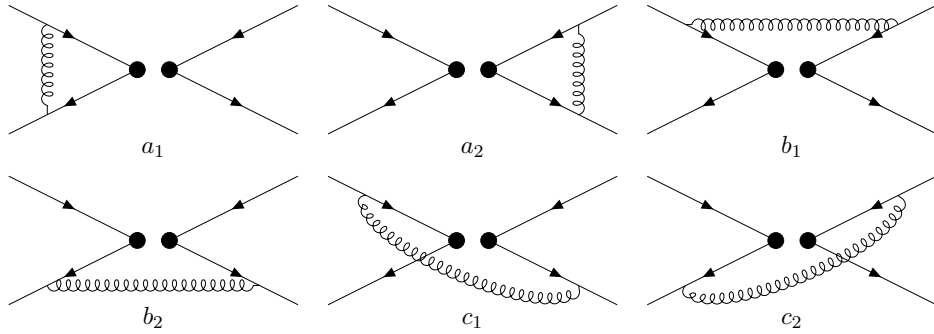
$$P\langle Q \rangle_2 \propto \text{Tr}(X \gamma^\mu P_L) \text{Tr}(Y \gamma_\mu P_L). \quad (3.7)$$

The same traces can be obtained for $\langle \tilde{Q} \rangle$, but with different colour contractions. In this thesis, we will be denoting the structures that result in double traces, like in Eq.(3.7) as “crossed”, corresponding to diagrams on the LHS of Figure 3.1. The structures that lead to single traced contractions as in Eq.(3.6) and the related diagrams on the RHS of Figure 3.1 we will call “direct”. We will be referring to this later in this section, when we talk about tracing over γ_5 .

3.1.2 Amplitude at Next-to-Leading Order

The one-loop amplitude can be obtained from the sum of the following 6 diagrams and their permutations of external legs (corresponding to Fig.(3.1)) and exchange of the two currents:

The computation of this amplitude can be found in [4], where it was done with open



indices, by employing the Passarino-Veltmann technique and performing the projections in 4 dimensions. In this thesis, we will reproduce these results using a different technique as part of the validation.

3.1.3 Amplitude at NNLO

The direct part of the two-loop amplitude is comprised of 103 diagrams. 36 of these are recursively one-loop, i.e. they involve insertions of self-energies into the propagators of one-loop diagrams. The remaining 67 diagrams are the true two-loop diagrams. In Figure 3.2 we give the pictorial representation of the unique 28 diagrams. The rest of the diagrams can be obtained by exchanging the external legs and the currents.

Two types of exchanges can be performed: exchange of bilinears, i.e. $(i, \alpha) \leftrightarrow (k, \gamma)$ and $(j, \beta) \leftrightarrow (l, \delta)$, or exchange of external momenta, meaning $(i, \alpha) \leftrightarrow (j, \beta)$ and $(k, \gamma) \leftrightarrow (l, \delta)$. The number of diagrams corresponding to each diagram given in Figure 3.2 can be determined from the symmetries of each diagram. For instance diagrams A2, A5 and C2 are symmetric under both types of exchanges, hence only one of these diagrams enters the two-loop amplitude. Diagrams C1, D1 and OL5 are symmetric under the exchange of bilinears, hence corresponding diagrams with momentum exchange have to be computed. Similarly for diagrams A1, A4, D2, D3, OL4 and OL6 only the corresponding diagrams with exchanged bilinears have to be computed. For the remaining diagrams all four permutations enter the amplitude. The equivalent holds for the crossed structures as well.

Tensor Reduction at NNLO

While the one-loop calculation of the conversion factor exists [4], it is not a trivial task to extend it to two-loop order. The first complication is the reduction of the tensor integrals in the two-loop amplitude $\Lambda_{\alpha\beta,\gamma\delta}^{ij,kl}$. The Passarino-Veltmann technique cannot be used for two-loop integrals, as not every scalar product of the external and internal

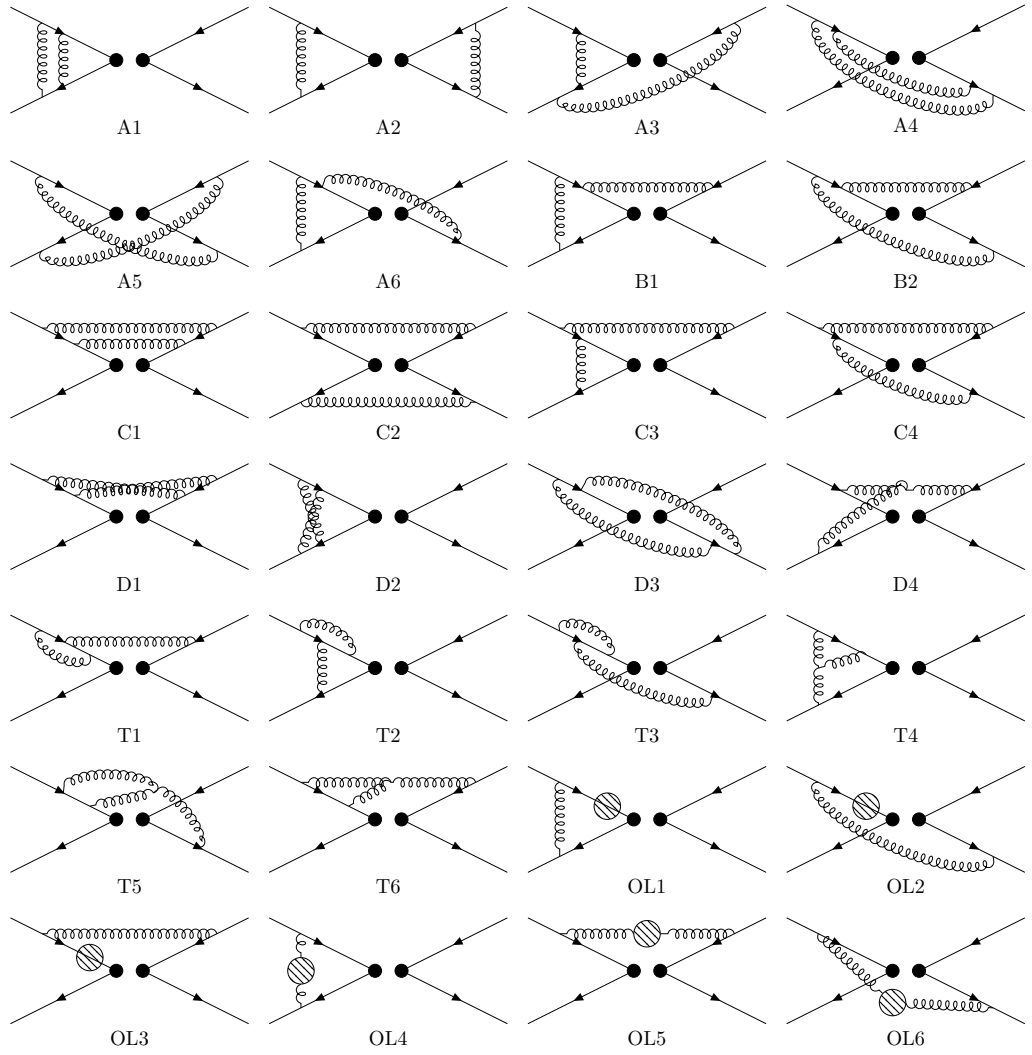


Figure 3.2: 28 classes of diagrams corresponding to the two-loop radiative corrections to the $\Lambda_{\alpha\beta,\gamma\delta}^{ij,kl}$. The hatched blobs correspond to the sum of one-loop insertions into the propagators. Kinematics are defined in Figure 2.2.

momenta can be expressed in terms of the inverse propagators [55]. Hence, more advanced methods are required, such as dimensional shift [58]. However, this would bring yet another complication: we would need solutions to these integrals in other than $D = 4$ dimensions, which can also be difficult to obtain. A workaround this issue is to apply projectors first, turning tensors into scalar products and hence allowing us to express these products in terms of propagators of scalar two-loop integrals. These extra negative powers of propagators can then be reduced via the IBP relations to a small set of master integrals. The downside is that special care needs to be taken as tracing over the spinor indices first means that it has to be done in D instead of 4 dimensions and that can lead to inconsistencies when evaluating traces with γ_5 .

Traces over γ_5 in D Dimensions

The use of the projectors $P_{(1)}$ and $P_{(2)}$, defined in Eqs.(2.41, 2.42), gives rise to closed Dirac traces involving γ^5 . It is well known that such traces cannot in general be continued away from $D = 4$ in a manner consistent with γ^5 being anti-commuting [59]. This is not a problem for the renormalisation conditions, which are imposed on renormalised Green's functions after the limit $D \rightarrow 4$ has been taken. However, it does require care to be taken in the perturbative evaluation of $\Lambda_{\alpha\beta,\gamma\delta}^{ij,kl}$.

There is no way to define the double traces consistently in this case. For the single trace, however, as long as the evanescent operators are defined such that their ‘Greek projections’ [60, 61] $\Gamma\gamma^T\Gamma' = 0$ vanish in D dimensions, we can consistently use anti-commuting γ^5 . Together with $\gamma^\mu P_L \gamma^\tau \gamma_\mu P_L = (2-d)\gamma^\tau P_L$, this can be used, for a general loop diagram, to obtain the coefficient of $\langle Q \rangle^{\text{tree}}$.

In addition, even though traces such as $\text{Tr}(\not{p}_1 \not{p}_2 \not{k}_1 \not{k}_2 \gamma_5)$, may be encountered in the two-loop calculation, where k_i are loop momenta, reducing terms like $k_1^\mu k_2^\nu$ will lead to $g^{\mu\nu}$ and $p_1^\mu p_2^\nu$. This follows from performing tensor reduction via dimensional shift method [58]. Hence, the longest irreducible Dirac structure remaining after the tensor reduction would be $\text{Tr}(\not{p}_1 \not{p}_2 \gamma_5)$, which is consistently equal to zero in 4 and in D dimensions. Therefore, all direct traces can be evaluated in D dimensions by anti-commuting each γ_5 to the right and dropping the terms containing it without introducing ambiguities. In the following sections we will present a way to compute the full amplitude using only the direct diagrams.

Two-loop Calculation and Renormalisation

The final hurdles of this calculation involve computing the projected diagrams themselves and obtaining the renormalised amplitude, which is finite in $D = 4$ dimensions. In Section 3.1.3, we have noted that the two-loop amplitude consists of 103 diagrams. The general procedure for solving loop integrals involves first reducing them into a set of master integrals, which can then be evaluated. This is achieved using the IBP method, discussed in Section 2.3. The procedure minimises the overall uncertainty of the amplitude. While one could apply IBP relations to every single diagram separately, it is more efficient to consider symmetries and group them into topologies. In the end we will find that all of the diagrams will reduce to around 30 masters. The resulting diagrams can then in principle be evaluated numerically, however it is always beneficial to use as many analytic results as there are available for better precision.

Once the amplitude is computed its poles have to cancel against the counterterms. The computation of counterterms themselves involves one-loop calculations as well as extractions of two-loop renormalisation constants from the anomalous dimensions. All poles must cancel in the final result, which is non-trivial for the entirety of 103 diagrams. In the following sections we will give explicit details on the choice of topologies and master integrals, their evaluation as well as computation of the counterterms and their structure.

3.2 Full Amplitude from Direct Diagrams

In this section, we present a method to obtain the RI-(S)MOM projections of the full amplitude up to two-loop order by computing only projections of direct diagrams. The reason for this is that we would like to avoid performing tensor reduction at two-loop order by contracting spinor indices in the beginning. This means, however, that the γ_5 can be treated without ambiguities only for the direct diagrams.

The section is organised as follows. In Section 3.2.1 we investigate what Lorentz structures are going to appear in the two-loop calculation. Since we are computing only direct diagrams, there are additional Lorentz structures involving external momenta that need to be considered in order to reconstruct the full amplitude. Hence, in Section 3.2.2 we define further tree-level matrix elements corresponding to the additional structures. We also write down the amplitude in terms of the matrix elements. As we introduce new operators we need a way to disentangle them, therefore, in Section 3.2.3 we define a new set of projectors. Along with those, we present an extended basis of evanescent operators.

In Section 3.2.4, we then proceed to write down the direct amplitude and explain how we obtain the coefficients in front of the tree-level matrix elements. In Section 3.2.5 we discuss how to extract the projections $P_{(1)}$ and $P_{(2)}$ of the full amplitude from these coefficients. Finally, in Section 3.2.6 we present an alternative minimal basis of operators.

3.2.1 Bilinears and Invariants

In a computation with open indices, after carrying out the loop integrals, all our Dirac strings can be written as a single P_L at the right end, preceded by an odd number n of Dirac matrices, where some of these may be contracted with p_1 or p_2 , with \not{p}_1 and \not{p}_2 appearing at most once. At one loop, $n = 1$ or 3 , at two loops $n = 1, 3$ or 5 .

A complete set of bilinears can be chosen to be:

$$\begin{aligned} \not{p}_i P_L, \quad \gamma^\mu P_L, \quad \not{p}_1 \not{p}_2 \gamma^\mu P_L, \quad \not{p}_i \gamma^\mu \gamma^\nu P_L, \quad \gamma^\mu \gamma^\nu \gamma^\rho P_L, \\ \not{p}_1 \not{p}_2 \gamma^\mu \gamma^\nu \gamma^\rho P_L, \quad \not{p}_i \gamma^\mu \gamma^\nu \gamma^\rho \gamma^\sigma P_L, \quad \gamma^\mu \gamma^\nu \gamma^\rho \gamma^\sigma \gamma^\tau P_L. \end{aligned}$$

Wherever convenient, the elements in each bilinear can be permuted (except P_L), the difference is always expressible in terms of shorter bilinears (P_L can also be moved around, but may turn into P_R).

Out of the bilinears on each of the first five lines, 3 four-fermion-invariants can be constructed (6 if also counting colour), noting that invariants can be chosen to be symmetric under exchange of the two bilinears, because any operator matrix element automatically is symmetric after summing over all Wick contractions (Feynman diagrams). This gives 16 Lorentz structures, and 32 structures once taking into account colour.

However, most of these are evanescent. By anti-symmetrising in Dirac indices (if needed after taking p_i^α outside the bilinears), any structure involving a bilinear of length three or more can be reduced, in four dimensions, to structures expressible in terms of the first three bilinears. Consequently, in D dimensions, any Dirac structure can be written as a linear combination of evanescent structures E_i^s and the following four structures

$$Q^s = \gamma^\mu P_L \otimes \gamma_\mu P_L,$$

$$M_{11}^s = \not{p}_1 P_L \otimes \not{p}_1 P_L, \quad M_{12}^s = \frac{1}{2} (\not{p}_1 P_L \otimes \not{p}_2 P_L + \not{p}_2 P_L \otimes \not{p}_1 P_L), \quad M_{22}^s = \not{p}_2 P_L \otimes \not{p}_2 P_L.$$

3.2.2 Matrix Elements Entering the Total Amplitude

Analogously to Section 3.1.1, let us define the tree-level matrix elements (four-fermion Green's functions), corresponding to the structures above, at generalised MOM kinematics as

$$\langle Q_1 \rangle = 2 Q^s 1 \otimes 1 - 2 \tilde{Q}^s 1 \tilde{\otimes} 1, \quad (3.8)$$

$$\langle Q_2 \rangle = 2 M_{11}^s 1 \otimes 1 - 2 \tilde{M}_{11}^s 1 \tilde{\otimes} 1, \quad (3.9)$$

$$\langle Q_3 \rangle = 2 M_{12}^s 1 \otimes 1 - 2 \tilde{M}_{12}^s 1 \tilde{\otimes} 1, \quad (3.10)$$

$$\langle Q_4 \rangle = 2 M_{22}^s 1 \otimes 1 - 2 \tilde{M}_{22}^s 1 \tilde{\otimes} 1, \quad (3.11)$$

We can also define the four further matrix elements $\langle \tilde{Q}_i \rangle$, $i = 1, \dots, 4$, with identical Lorentz structures but $\otimes \leftrightarrow \tilde{\otimes}$ for the colour contractions.

The total amplitude up to two loops can then be written in the form

$$\Lambda = \sum_{i=1}^4 (A_i \langle Q_i \rangle + \tilde{A}_i \langle \tilde{Q}_i \rangle) \quad (3.12)$$

+ linear combinations of evanescent Lorentz structures,

where A_i and \tilde{A}_i denote the coefficients in front of the tree-level matrix elements, obtained after reducing the structures appearing in the diagrams that make up the amplitude. The full set of diagrams contains both direct and crossed diagrams, such that the full Λ satisfies $\Lambda_{\alpha\beta\gamma\delta}^{ijkl} = -\Lambda_{\alpha\delta\gamma\beta}^{ilkj}$, as required by Fermi statistics, and accounted for by the form of $\langle Q_i \rangle$ and $\langle \tilde{Q}_i \rangle$.

3.2.3 Projectors and Evanescent Structures

When including all counterterm diagrams the coefficients are all finite, such that the projectors $P_{(i)}$ can be directly applied to Λ . However, we will not compute all the counterterms (renormalisation constants) required to obtain finite coefficients for all the evanescent operators and therefore need a method of removing them in the presence of UV poles. In addition, we would like to use trace techniques to evaluate individual diagrams, which may be divergent. We are able to achieve both aims by choosing a set of projectors which are unambiguous in D dimensions and a set of evanescent operators which is projected to zero by all projectors.

We choose as projectors

$$\Pi_\mu(\Gamma_1 P_L \otimes \Gamma_2 P_L) = \text{tr } \gamma^\mu \Gamma_1 \gamma_\mu \Gamma_2, \quad (3.13)$$

$$\Pi_{11}(\Gamma_1 P_L \otimes \Gamma_2 P_L) = \text{tr } \not{p}_1 \Gamma_1 \not{p}_1 \Gamma_2, \quad (3.14)$$

$$\Pi_{12}(\Gamma_1 P_L \otimes \Gamma_2 P_L) = \text{tr } \not{p}_1 \Gamma_1 \not{p}_2 \Gamma_2, \quad (3.15)$$

$$\Pi_{22}(\Gamma_1 P_L \otimes \Gamma_2 P_L) = \text{tr } \not{p}_2 \Gamma_1 \not{p}_2 \Gamma_2, \quad (3.16)$$

with no trace over colour is understood. We have defined them only for the direct diagrams, specified in Section 3.1.1, because this is sufficient to reconstruct the entire result. To evaluate them, any chiral projector or γ_5 in any Dirac line should first be moved to the right end of that line. The traces are unambiguous in D dimensions because no Levi-Civita symbols are generated by them, nor by the tensor loop integrals we encounter.

We then define evanescent structures E_j^s such that $\Pi_i(E_j^s) = 0$ for all projectors Π_i . In Eq.(2.39) we have previously defined

$$E_1^s = \gamma^\mu \gamma^\nu \gamma^\rho P_L \otimes \gamma_\mu \gamma_\nu \gamma_\rho P_L - ((D-10)D + 8)Q^s, \quad (3.17)$$

$$E_3^s = \gamma^\mu \gamma^\nu \gamma^\rho \gamma^\sigma \gamma^\tau P_L \otimes \gamma_\mu \gamma_\nu \gamma_\rho \gamma_\sigma \gamma_\tau P_L \\ - (D-2)(D((D-26)D + 152) - 128)Q^s, \quad (3.18)$$

which project to zero under all Π_i . A further independent 10 structures meeting this condition are

$$F_{ij}^s = \frac{1}{2} (\not{p}_i \gamma^\mu \gamma^\nu P_L \otimes \not{p}_j \gamma_\mu \gamma_\nu P_L + (i \leftrightarrow j)) + (D-2)(D-4)M_{ij}^s \\ - 4p_i \cdot p_j Q^s, \quad (3.19)$$

$$H_{ij}^s = \frac{1}{2} (\not{p}_i \gamma^\mu \gamma^\nu \gamma^\rho \gamma^\sigma P_L \otimes \gamma_\mu \gamma_\nu \gamma_\rho \gamma_\sigma \not{p}_j P_L + (i \leftrightarrow j)) \\ - (D(D-14) + 32)(D-2)(D-4)M_{ij}^s + 8(D-8)(D-2)p_i \cdot p_j Q^s, \quad (3.20)$$

$$G_1^s = \frac{1}{2} (\not{p}_1 \not{p}_2 \gamma^\mu P_L \otimes \gamma_\mu P_L + \gamma^\mu P_L \otimes \not{p}_1 \not{p}_2 \gamma_\mu P_L) - p_1 \cdot p_2 Q^s, \quad (3.21)$$

$$G_2^s = \not{p}_1 \not{p}_2 \gamma^\mu \gamma^\nu \gamma^\rho P_L \otimes \not{p}_1 \not{p}_2 \gamma_\mu \gamma_\nu \gamma_\rho P_L \\ - (D-4)(D(D-14) + 32) (p_2^2 M_{11}^s + p_1^2 M_{22}^s - 2p_1 \cdot p_2 M_{12}^s) \\ + (D(D-10) + 8)p_1^2 p_2^2 Q^s, \quad (3.22)$$

$$G_3^s = \frac{1}{2} (\not{p}_1 \not{p}_2 \gamma^\mu \gamma^\nu \gamma^\rho P_L \otimes \gamma_\mu \gamma_\nu \gamma_\rho P_L + \gamma^\mu \gamma^\nu \gamma^\rho P_L \otimes \not{p}_1 \not{p}_2 \gamma_\mu \gamma_\nu \gamma_\rho P_L) \\ + (D(D-10) + 8)p_1 \cdot p_2 Q^s, \quad (3.23)$$

$$\begin{aligned}
G_4^s &= \not{p}_1 \not{p}_2 \gamma^\mu P_L \otimes \not{p}_1 \not{p}_2 \gamma_\mu P_L \\
&+ (D-4) (p_2^2 M_{11}^s + p_1^2 M_{22}^s - 2p_1 \cdot p_2 M_{12}^s) - p_1^2 p_2^2 Q^s.
\end{aligned} \tag{3.24}$$

All 12 evanescent structures (24 when including colour) are symmetric under the exchange of both bilinears and therefore (upon adding the piece required by Fermi symmetry) are the matrix elements of suitably chosen operators.

3.2.4 Obtaining Coefficients A_i and \tilde{A}_i

Similarly to Section 3.1.1, let us split $\langle Q_i \rangle = \langle Q_i \rangle_1 + \langle Q_i \rangle_2$, where $\langle Q_i \rangle_1$ denotes the second term on the r.h.s. of each of (3.8)–(3.11), which is due to the “direct” Feynman diagram. Moreover, we apply the same procedure to $\langle \tilde{Q}_i \rangle$. The entire amplitude Λ then splits in a similar manner into a direct and a crossed contribution. The direct contribution is due to all the direct diagrams, and has the form

$$\Lambda_1 = \sum_{i=1}^4 (A_i \langle Q_i \rangle_1 + \tilde{A}_i \langle \tilde{Q}_i \rangle_1) \tag{3.25}$$

+ linear combinations of evanescent Lorentz structures.

Λ_1 enjoys the property that our projectors Π_i are defined on it, on a diagram-by-diagram basis. We can therefore compute

$$\begin{aligned}
\Pi_i(\Lambda_1) &= \sum_{j=1}^4 \left(A_j \Pi_i(\langle Q_j \rangle_1) + \tilde{A}_j \Pi_i(\langle \tilde{Q}_j \rangle_1) \right) \\
&= \sum_{j=1}^4 B_{ij} \left(A_j 1 \tilde{\otimes} 1 + \tilde{A}_j 1 \otimes 1 \right) \\
&= \sum_{j=1}^4 \left(C_i 1 \tilde{\otimes} 1 + \tilde{C}_i 1 \otimes 1 \right),
\end{aligned} \tag{3.26}$$

wherein contributions proportional to the tree-level matrix elements of the evanescent operators have disappeared, and the matrix B is readily found by applying the projectors Π_i to the basis Dirac structures Q^s , M_{11}^s , M_{12}^s and M_{22}^s . After summing over diagrams and counter-diagrams, we should find explicitly that C_i and \tilde{C}_i are finite, and can compute A_i and \tilde{A}_i via the inverse of B . B is nonsingular except for $q^2 = 0$; if we want a result directly at $q^2 = 0$ we need to redo the procedure with a subset of basis structures and a 2×2 B -matrix which then should be nonsingular.

Computation of the $B_{ij} = \Pi_i Q_j^s$ for our choice of projectors and operators is given in Table 3.1. One can make B dimensionless by rescaling the momentum-dependent basis

	Π_μ	Π_{11}	Π_{12}	Π_{22}
Q^s	$-2(D-2)D$	$-2(D-2)p_1^2$	$-2(D-2)(p_1 \cdot p_2)$	$-2(D-2)p_2^2$
M_{11}^s	$-2(D-2)p_1^2$	$2p_1^4$	$2p_1^2(p_1 \cdot p_2)$	$4(p_1 \cdot p_2)^2 - 2p_1^2p_2^2$
M_{12}^s	$-2(D-2)(p_1 \cdot p_2)$	$2p_1^2(p_1 \cdot p_2)$	$2p_1^2p_2^2$	$2p_2^2(p_1 \cdot p_2)$
M_{22}^s	$-2(D-2)p_2^2$	$4(p_1 \cdot p_2)^2 - 2p_1^2p_2^2$	$2p_2^2(p_1 \cdot p_2)$	$2p_2^4$

Table 3.1: $B_{ij} = \Pi_i Q_j^s$ for projectors, defined in Eqs.(2.41-2.42), and the structures, given in Sec.(3.2.1).

structures and projectors by some scalar product(s) of momenta.

3.2.5 Obtaining the (S)MOM Projections

Once the A_i and \tilde{A}_i are found, calculating the projections $P_{(\gamma\mu)}(\Lambda)$ and $P_{(\not{g})}(\Lambda)$ (or any other projections) amounts to simply computing

$$P_{(i)}(\Lambda) = \sum_{j=1}^4 \left(\sum A_j P_{(i)}(\langle Q_j \rangle) + \sum \tilde{A}_j P_{(i)}(\langle \tilde{Q}_j \rangle) \right), \quad (3.27)$$

which is a $D = 4$ exercise. Here one needs to include both direct and crossed part and colour. The projections of the tree-level basis structures are given by

$$P_{(\gamma\mu)}(\langle Q_i \rangle) = \left\{ \frac{1}{4} - \frac{3\epsilon}{16} + \frac{\epsilon^2}{32}, -\frac{\mu^2}{16} \left(1 - \frac{\epsilon}{4}\right), \frac{\mu^2}{32}(\omega - 2) \left(1 - \frac{\epsilon}{4}\right), -\frac{\mu^2}{16} \left(1 - \frac{\epsilon}{4}\right) \right\}, \quad (3.28)$$

$$P_{(\not{g})}(\langle Q_i \rangle) = \left\{ \frac{1}{4} - \frac{\epsilon}{16}, -\frac{\mu^2}{32}(\omega + 1), \frac{\mu^2}{64}(3\omega - 2), -\frac{\mu^2}{32}(\omega + 1) \right\}, \quad (3.29)$$

$$P_{(\gamma\mu)}(\langle \tilde{Q}_i \rangle) = \left\{ \frac{1}{4} - \frac{5\epsilon}{16} + \frac{3\epsilon^2}{32}, -\frac{\mu^2}{16} \left(1 - \frac{3\epsilon}{4}\right), \frac{\mu^2}{32}(\omega - 2) \left(1 - \frac{3\epsilon}{4}\right), -\frac{\mu^2}{16} \left(1 - \frac{3\epsilon}{4}\right) \right\}, \quad (3.30)$$

$$P_{(\not{g})}(\langle \tilde{Q}_i \rangle) = \left\{ \frac{1}{4} - \frac{3\epsilon}{16}, \frac{\mu^2}{32}(\omega - 3), \frac{\mu^2}{64}(\omega - 6), \frac{\mu^2}{32}(\omega - 3) \right\}. \quad (3.31)$$

where $p_1^2 = p_2^2 = -\mu^2$, $q^2 = -\omega\mu^2$. For RI-MOM $\omega = 0$ and for RI-SMOM $\omega = 1$. These expressions are exact, i.e. they include all orders of ϵ .

3.2.6 Fierz-evanescent Operators

One can present the results in a slightly different manner, by trading the \tilde{Q}_i for Fierz-evanescent operators such that only a minimal number of operators contribute to the renormalised Green's function at $D \rightarrow 4$ (and hence to the SMOM projections). We find

that the following operators are evanescent, including the first one which we already had:

$$E_{1F} = \tilde{Q}_1 - Q_1, \quad (3.32)$$

$$E_{2F} = Q_2 + \tilde{Q}_2 - \frac{p_1^2}{2}(Q_1 + E_{1F}), \quad (3.33)$$

$$E_{3F} = Q_3 + \tilde{Q}_3 - \frac{p_1 \cdot p_2}{2}(Q_1 + E_{1F}), \quad (3.34)$$

$$E_{4F} = Q_4 + \tilde{Q}_4 - \frac{p_2^2}{2}(Q_1 + E_{1F}). \quad (3.35)$$

One can then rearrange e.g. Eq.(3.12) in terms of the (direct parts of the) matrix elements of Q_i and E_{iF} , which gives the new coefficients

$$A'_1 = A_1 + \tilde{A}_1 + \frac{p_1^2}{2}\tilde{A}_2 + \frac{p_1 \cdot p_2}{2}\tilde{A}_3 + \frac{p_2^2}{2}\tilde{A}_4, \quad (3.36)$$

$$A'_2 = A_2 - \tilde{A}_2, \quad (3.37)$$

$$A'_3 = A_3 - \tilde{A}_3, \quad (3.38)$$

$$A'_4 = A_4 - \tilde{A}_4. \quad (3.39)$$

The second sum in Eq.(3.27) then disappears without replacement, as the evanescent operators have zero tree-level matrix elements. Both methods give the same result.

3.3 One-loop Amplitude and Counterterms

In order to obtain finite C_i and \tilde{C}_i we have to renormalise the amplitude Λ_1 . The procedure outlined in the previous section is applicable to the computation of both one and two-loop amplitudes. In this section, we focus on the one-loop amplitude and counterterms, both of which also enter the two-loop amplitude. The section is organised as follows, we start by discussing the relations that hold between the different diagrams and projections. Next, we perform an open-index calculation of the one-loop amplitudes, including amplitudes with insertions of evanescent operators, in order to obtain the one-loop counterterms. Finally, we discuss the counterterm structure of the one-loop renormalised amplitude.

3.3.1 Projected Diagrams

The following relations between the different projections, defined in Eqs.(3.13-3.16), of the diagrams, given in Section 3.1.2, in SMOM scheme hold:

$$\begin{aligned}
\Pi_\mu a_1 &= \Pi_\mu a_2, & \Pi_\mu b_1 &= \Pi_\mu b_2, & \Pi_\mu c_1 &= \Pi_\mu c_2, \\
\Pi_{12} a_i &= \Pi_{21} a_j, \quad i \neq j, & \Pi_{12} b_i &= \Pi_{21} b_j, & \Pi_{12} c_i &= \Pi_{21} c_j, \\
\Pi_{11} a_i &= \Pi_{22} a_j, & \Pi_{11} b_i &= \Pi_{22} b_j, \quad i \neq j, & \Pi_{11} c_i &= \Pi_{22} c_j, \\
\Pi_{kk} a_1 &= \Pi_{kk} a_2, & & & \Pi_{kk} c_1 &= \Pi_{kk} c_2,
\end{aligned} \tag{3.40}$$

where $\Pi_{21}(\Gamma_1 P_L \otimes \Gamma_2 P_L) = \text{tr} \not{p}_2 \Gamma_1 \not{p}_1 \Gamma_2$ and $i, j, k = 1, 2$. We can see from the relations that it is sufficient to compute one of each a, b, c diagrams and the other ones can be obtained by interchanging the Π_{12} with Π_{21} for a and c diagrams and Π_{11} with Π_{22} for b type diagrams. We will see that similar relations hold between the two-loop diagrams as well.

3.3.2 Counterterms

Adding all 6 diagrams, for the one-loop amplitude we obtain

$$\begin{aligned}
\langle Q \rangle^{1\text{-loop}} &= \frac{\alpha_s}{4\pi \epsilon} \left\{ \left(2C_F \xi - 3 \left(1 - \frac{1}{N_c} \right) \right) \langle Q \rangle - 3 \langle E_F \rangle + \frac{1}{2N_c} \langle E_1 \rangle - \frac{1}{2} \langle E_2 \rangle \right\} \\
&+ \mathcal{O}(\epsilon^0).
\end{aligned} \tag{3.41}$$

From the requirement $Z_q^2 \langle Q^{\overline{\text{MS}}} \rangle = \text{finite}$, where $Z_q = 1 - C_F \xi \alpha_s / (4\pi \epsilon)$ is the 1-loop $\overline{\text{MS}}$ field renormalisation constant in a general covariant gauge [4], the $\alpha_s / (4\pi)$ coefficients in the Z -factors can then be read-off as

$$Z_{QQ}^{(1)} = \frac{3}{\epsilon} \left(1 - \frac{1}{N_c} \right), \tag{3.42} \quad Z_{QE_2}^{(1)} = \frac{1}{2\epsilon}, \tag{3.45}$$

$$Z_{QE_F}^{(1)} = \frac{3}{\epsilon}, \tag{3.43} \quad Z_{QE_3}^{(1)} = 0, \tag{3.46}$$

$$Z_{QE_1}^{(1)} = -\frac{1}{2N_c \epsilon}, \tag{3.44} \quad Z_{QE_4}^{(1)} = 0. \tag{3.47}$$

3.3.3 Renormalised Amplitude

In order to obtain finite C_i and \tilde{C}_i we have to renormalise the amplitude Λ_1 . Renormalised amplitude is given by

$$\Lambda_{\text{ren}} = Z_q^2 (Z_{QQ} \langle Q \rangle + Z_{QE_n} \langle E_n \rangle), \tag{3.48}$$

where $\langle Q \rangle$ and $\langle E_n \rangle$ are the bare matrix elements, which can be expanded in α_s^{bare} as

$$\langle Q \rangle = \langle Q \rangle^{\text{tree}} + \frac{\alpha_s^{\text{bare}}}{4\pi} \langle Q \rangle^{1\text{-loop}} + \left(\frac{\alpha_s^{\text{bare}}}{4\pi} \right)^2 \langle Q \rangle^{2\text{-loop}}, \quad (3.49)$$

and similarly for $\langle E_n \rangle$. The one-loop renormalised amplitude is given by

$$\Lambda_{\text{ren}}^{(1)} = \langle Q \rangle^{1\text{-loop}} + (2Z_q^{(1)} + Z_{QQ}^{(1)}) \langle Q \rangle^{\text{tree}} + Z_{QE_F}^{(1)} \langle E_F \rangle^{\text{tree}}. \quad (3.50)$$

where $\langle Q \rangle^{1\text{-loop}}$ is the one-loop matrix element, obtained from the sum of the six diagrams and the wave function renormalisation constant is given in Eq.(2.22). The rest of the evanescent operators do not enter this amplitude as by definition their tree-level matrix elements project to zero.

3.4 Validation against C_{B_K} at Next-to-Leading Order

We are now in a position to reproduce the one-loop results for the conversion factors C_{B_K} from [4]. This serves as a validation for our way of calculating the amplitude.

The conversion factors are given by Eq.(2.56), which we repeat here

$$C_{B_K}^{(X,Y)} = (C_q^{(Y)})^2 P_{(X)\alpha\beta,\gamma\delta}^{ij,kl} \Lambda_{\alpha\beta,\gamma\delta}^{ij,kl}. \quad (3.51)$$

The one-loop RI-SMOM conversion factors for the wavefunction are given by

$$C_q^{(\not{d})} = 1 + \frac{\alpha_s}{4\pi} C_F \xi \left(\log \left(\frac{-p^2}{\mu^2} \right) - 1 \right) + \mathcal{O}(\alpha_s^2), \quad (3.52)$$

$$C_q^{(\gamma\mu)} = 1 + \frac{\alpha_s}{4\pi} C_F \left(1 - \frac{\xi}{2} \left(3 - 2 \log \left(\frac{-p^2}{\mu^2} \right) - C_0 \right) \right) + \mathcal{O}(\alpha_s^2), \quad (3.53)$$

which are taken from [4]. Here $C_0 \simeq 2.34391$ is the coefficient of the one-loop triangle diagram $J(D, 1, 1, 1) = -i\pi^{-\frac{D}{2}} C_0 / (p^2)^{(1+\epsilon)}$ from [62] and we keep the $p^2 = p_1^2 = p_2^2 = q^2 = -\mu^2$ Euclidean.

Next, we compute the projected one-loop amplitudes $P_{(i)}(\Lambda)$, as outlined in Section 3.2. Using these amplitudes together with the counterterms, given in Section 3.3, we can obtain the projected renormalised four-point amputated Green's functions $P_{(X)\alpha\beta,\gamma\delta}^{ij,kl} \Lambda_{\alpha\beta,\gamma\delta}^{ij,kl} =$

Scheme	$\xi = 0$	$\xi = 1$
(γ_μ, \not{q})	$1 + \frac{\alpha_s}{4\pi}(-2.45482\dots) + \mathcal{O}(\alpha_s^2)$	$1 + \frac{\alpha_s}{4\pi}(-3.51294\dots) + \mathcal{O}(\alpha_s^2)$
(γ_μ, γ_μ)	$1 + \frac{\alpha_s}{4\pi}(0.211844\dots) + \mathcal{O}(\alpha_s^2)$	$1 + \frac{\alpha_s}{4\pi}(0.945601\dots) + \mathcal{O}(\alpha_s^2)$
(\not{q}, \not{q})	$1 + \frac{\alpha_s}{4\pi}(-0.454823\dots) + \mathcal{O}(\alpha_s^2)$	$1 + \frac{\alpha_s}{4\pi}(-0.169035\dots) + \mathcal{O}(\alpha_s^2)$
(\not{q}, γ_μ)	$1 + \frac{\alpha_s}{4\pi}(2.21184\dots) + \mathcal{O}(\alpha_s^2)$	$1 + \frac{\alpha_s}{4\pi}(4.28951\dots) + \mathcal{O}(\alpha_s^2)$

Table 3.2: Conversion factors $C_{B_K}^{(X,Y)}$ in Landau ($\xi = 0$) and Feynman ($\xi = 1$) gauges from four RI-SMOM schemes, where $X = \gamma_\mu, \not{q}$ and $Y = \gamma_\mu, \not{q}$, to $\overline{\text{MS}}$. The factors are in agreement with [4].

$P_{(i)}(\Lambda_{\text{ren}}^{(1)})$. Hence, combining this with the C_q we get

$$C_{B_K}^{(\gamma_\mu, \not{q})} = 1 + \frac{\alpha_s}{4\pi} \left(2 \log \left(\frac{-p^2}{\mu^2} \right) + 8 \log 2 - 8 + \xi \left(1 - \frac{5}{3} C_0 + \frac{8}{3} \log 2 \right) \right), \quad (3.54)$$

$$C_{B_K}^{(\gamma_\mu, \gamma_\mu)} = 1 + \frac{\alpha_s}{4\pi} \left(2 \log \left(\frac{-p^2}{\mu^2} \right) + 8 \log 2 - \frac{16}{3} - \xi \left(1 + \frac{1}{3} C_0 - \frac{8}{3} \log 2 \right) \right), \quad (3.55)$$

$$C_{B_K}^{(\not{q}, \not{q})} = 1 + \frac{\alpha_s}{4\pi} \left(2 \log \left(\frac{-p^2}{\mu^2} \right) + 8 \log 2 - 6 - \xi \left(-\frac{2}{3} C_0 + \frac{8}{3} \log 2 \right) \right), \quad (3.56)$$

$$C_{B_K}^{(\not{q}, \gamma_\mu)} = 1 + \frac{\alpha_s}{4\pi} \left(2 \log \left(\frac{-p^2}{\mu^2} \right) + 8 \log 2 - \frac{10}{3} - \xi \left(-\frac{4}{3} + \frac{2}{3} C_0 + \frac{8}{3} \log 2 \right) \right), \quad (3.57)$$

where we have set $N_c = 3$. These conversion factors are in agreement with [4].

The one-loop conversion factors depend on the renormalisation scale only through the running of the strong coupling. Hence, we provide the numerical results as expansion in α_s for both Landau ($\xi = 0$) and Feynman ($\xi = 1$) gauges in Table 3.2. Now that we have validated our method, we can proceed to compute the two-loop amplitude and conversion factors.

3.5 Two-loop Amplitude and Counterterms

Similarly to one-loop, the calculation at two-loop order involves renormalisation of the two-loop amplitude which allows us to obtain finite C_i and \tilde{C}_i . The section starts with the discussion of the relations between the projections, defined in Eqs.(2.41-2.42), of two-loop diagrams, given in Figure 3.2. As the two-loop calculation is much more involved, we give further details on how we define the topologies and evaluate the master integrals. Next, we compute further one-loop counterterms which enter the two-loop amplitude in addition to already computed one-loop counterterms and amplitude. We then show how to obtain the two-loop counterterms from one-loop poles and the two-loop anomalous dimension. Finally, we present the counterterm structure of the two-loop renormalised amplitude.

3.5.1 Projected Diagrams

As detailed in Section 3.1.3, the full list of diagrams entering the amplitude can be obtained by considering the permutations of external legs for the 28 graphs given in Figure 3.2. Similar to the one-loop case, we compute all diagrams in SMOM kinematics and find that certain relations hold between the five projections of them. In particular, bilinear exchange corresponds to interchanging Π_{12} and Π_{21} . On the other hand, exchange of external momenta corresponds to the interchange of Π_{11} and Π_{22} projections. Hence, one can obtain the full direct amplitude from the 28 diagrams, given in Figure 3.2.

3.5.2 Defining Topologies

As detailed before, our tensor integrals can be reduced into scalar ones. Thus, in this section we focus on the scalar part of our 4-point function $\Lambda_{\alpha\beta,\gamma\delta}^{ij,kl}$. At tree level, this amplitude can be pictured as shown in Figure 2.2: we have two particles with momentum p_1 going into the vertex and two particles with momentum p_2 , as well as $q = p_2 - p_1$, that ensures momentum conservation in the case of $p_1 \neq p_2$, going out of the vertex.

In order to compute the NNLO corrections for this diagram, we have to consider all of the possible two-loop radiative corrections, given in Figure 3.2. The diagrams can be divided into six groups: A, B, C, D, T and OL. Diagrams A, B and D correspond to the topologies with the same name, which can be obtained and reduced straightforwardly, following Section 2.3. The “topology” of the diagrams C has linearly dependent propagators. We will discuss how to express its integrals in terms of proper topologies in the following section. T stands for the remaining triangle integrals and OL for the integrals with one-loop insertions, both of which can be expressed in terms of topology A, B, C and D integrals. These are shown in Figure 3.3 and the propagators are given by

	Top A	Top B	“Top” C	Top D	
1.	$k_1,$	$k_1,$	$k_1,$	$k_1,$	
2.	$k_2,$	$k_2,$	$k_2,$	$k_2,$	
3.	$k_1 - k_2,$	$k_1 - k_2,$	$k_1 - k_2,$	$k_1 - k_2,$	
4.	$k_1 + p_1,$	$k_1 - p_1,$	$k_1 + p_2,$	$k_1 - p_1,$	
5.	$k_2 + p_2,$	$k_2 + p_1,$	$k_2 + p_1,$	$k_1 - k_2 - p_2,$	
6.	$k_1 - q,$	$k_1 + q,$	$k_1 + 2p_1,$	$k_1 + q,$	
7.	$k_2 - q,$	$k_2 + q,$	$k_2 + 2p_1,$	$k_2 + p_1,$	(3.58)

where the numbers correspond to the numbering of propagators in Figure 3.3.

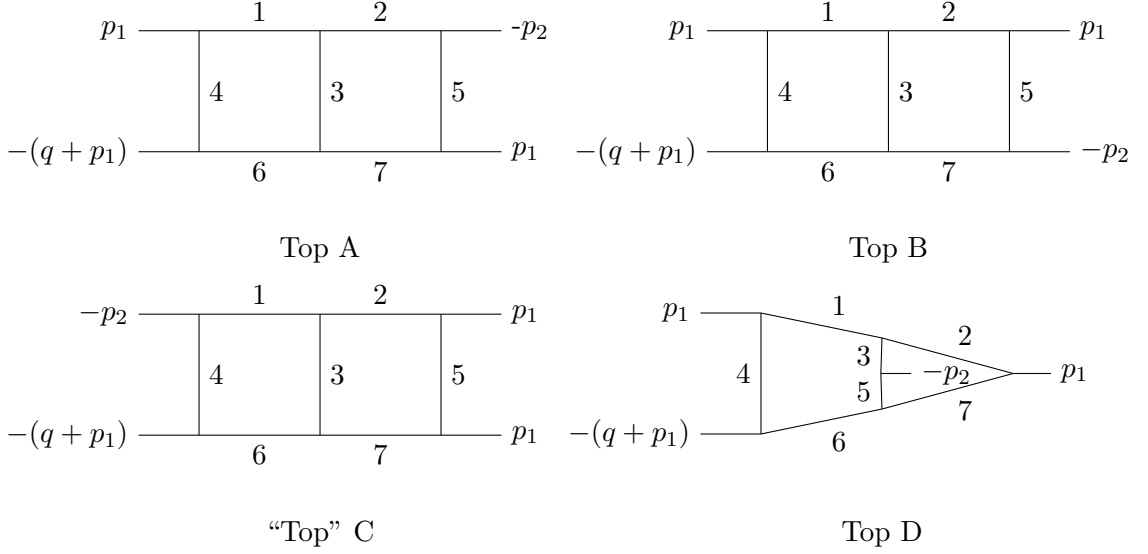


Figure 3.3: Topologies A, B, C and D. “Top” indicates that the diagram has linearly dependent propagators. All external momenta are defined as incoming. Numbers correspond to propagator labels, as defined in Section 3.5.2.

Linearly Dependent Propagators

In the previous section we have introduced “topology” C, displayed in Figure 3.3. It is obtained in the same manner as topologies A, B and D, however, there is no way to add an auxiliary propagator such that all of the propagators would be linearly independent. Not having all of the possible linearly independent propagators in the topology results in irreducible numerators. These numerators interfere with the IBP algorithm, as they cannot be expressed in terms of the propagators.

To mitigate this issue, we first have to remove the linear dependences and then map the resulting integrals onto proper auxiliary topologies. Hence, for “topology” C, we obtain a linear relationship between the propagators, given by

$$k_2^2 - 2(k_2 + p_1)^2 + (k_2 + 2p_1)^2 = 2p_1^2, \quad (3.59)$$

where k_2 is the loop momentum. We can then turn this into an identity operator, written as

$$\mathcal{I}_C = \frac{1}{2p_1^2} (\mathbf{2}^- - 2 \times \mathbf{5}^- + \mathbf{7}^-), \quad (3.60)$$

where $\mathbf{2}^-$, $\mathbf{5}^-$ and $\mathbf{7}^-$ correspond to reducing the power of the second, fifth and seventh propagators by one. In addition, “topology” C integrals always contain at most 6 propagators. Using this together with the identity operator \mathcal{I}_C , we can express some of the integrals in terms of topology A and B integrals. For the rest of the integrals we define

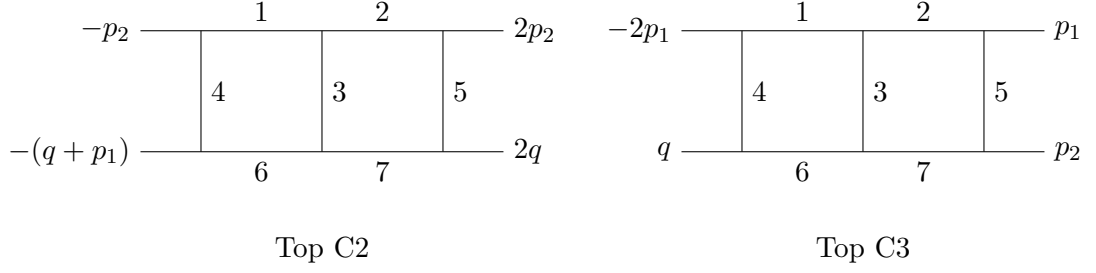


Figure 3.4: Two additional topologies. All external momenta are defined as incoming. Numbers correspond to propagator labels, as defined in Section 3.5.2.

two additional topologies: C2 and C3, shown in Figure 3.4, with propagators given by

	Top C2	Top C3	
1.	$k_1,$	$k_1,$	
2.	$k_2,$	$k_2,$	
3.	$k_1 - k_2,$	$k_1 - k_2,$	
4.	$k_1 + p_2,$	$k_1 + 2p_1,$	
5.	$k_2 + 2p_2,$	$k_2 + p_1,$	
6.	$k_1 + 2p_1,$	$k_1 + p_1 + p_2,$	
7.	$k_2 + 2p_1,$	$k_2 + p_1 + p_2,$	

(3.61)

where the numbers correspond to the numbering of propagators in Figure 3.4. The remaining triangles and one-loop insertions can be solved using the \mathcal{I}_C in Eq.(3.60) and existing topologies. In Figure 3.2 we also have one non-planar triangle D1, which can be written as topology D integral without the fourth propagator. A different identity can be used for this integral, given by

$$k_1^2 - (k_1 + 2p_1)^2 - 2(k_1 - k_2)^2 + 2(k_2 + p_1)^2 - 2k_2^2 + 2(k_1 - k_2 + p_1)^2 = 0, \quad (3.62)$$

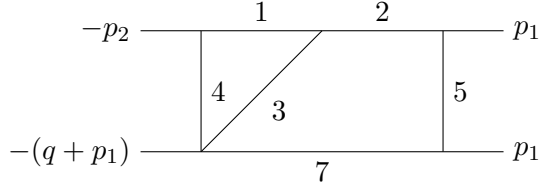
resulting in projection

$$\mathcal{I}_D = \mathbf{1}^+ \mathbf{6}^- + 2 \times \mathbf{1}^+ \mathbf{3}^- - 2 \times \mathbf{1}^+ \mathbf{7}^- + 2 \times \mathbf{1}^+ \mathbf{2}^- + 2 \times \mathbf{1}^+ \mathbf{5}^-, \quad (3.63)$$

where the numbers correspond to topology D propagator labels defined in the previous section.

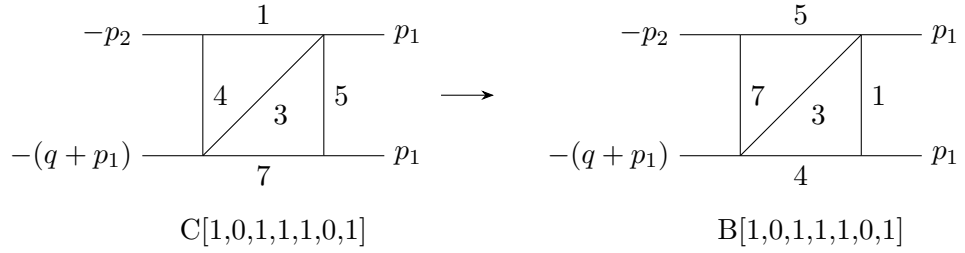
Example: Mapping Diagrams onto Topologies

We are now going to illustrate, what we mean by mapping diagrams onto topologies and using the identity projections, in more detail. We can write down diagram C3 in terms of “topology” C as follows



C[1,1,1,1,1,0,1]

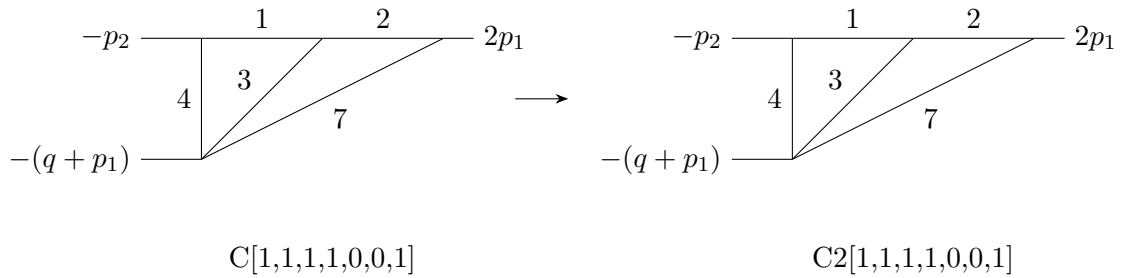
where $C[1, 1, 1, 1, 1, 0, 1]$ refers to “topology” C and the numbers - to the powers of the propagators. We can see that this diagram is the same as “topology” C in Figure 3.3 but with 6th propagator pinched. Applying Eq.(3.60) gives us three diagrams: with 2nd, 5th and 7th propagators removed. Hence, we can remove one of the linearly dependent propagators and map these onto proper topologies. This can be depicted diagrammatically as



C[1,0,1,1,1,0,1]

B[1,0,1,1,1,0,1]

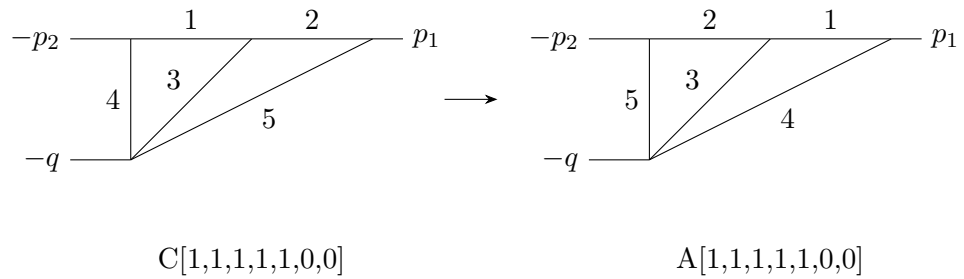
where the loop momenta has to be shifted by $k_1 \rightarrow -k_2 - p_1$ and $k_2 \rightarrow -k_1 - p_1$,



C[1,1,1,1,0,0,1]

C2[1,1,1,1,0,0,1]

which does not require any shifts and



C[1,1,1,1,1,0,0]

A[1,1,1,1,1,0,0]

where the loop momenta have to be shifted by $k_1 \rightarrow k_2$ and $k_2 \rightarrow k_1$. In some cases the

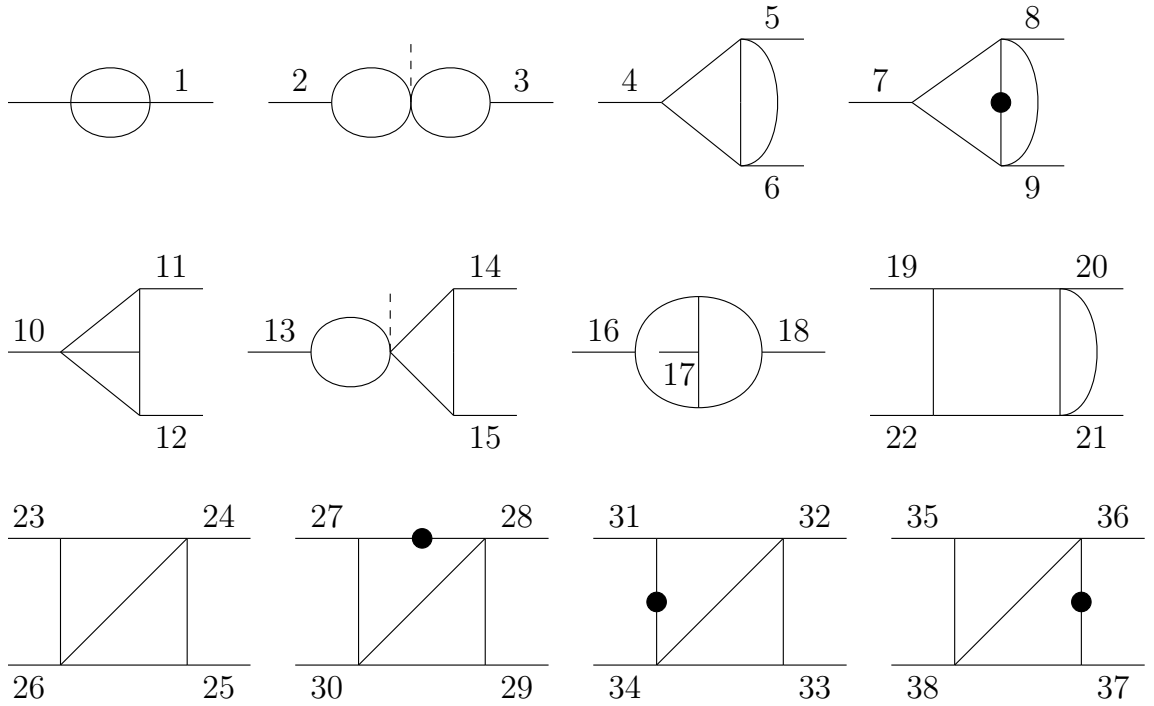


Figure 3.5: Two-loop master integrals. Black dots represent squared propagators. All of the momentum configurations of these diagrams can be found in Table 3.3. Dashed lines indicate external legs that do not appear in all momentum configurations of a particular diagram and are chosen such that momentum conservation holds.

propagators have to be remapped as well. This procedure can be carried out for all the C, T and OL integrals that have linearly dependent propagators. It may even be implemented iteratively for multiple powers of propagators, until all the propagators in a diagram are linearly independent. At that point, the diagrams are ready for the IBP reduction.

3.5.3 Master Integrals

After expressing all the integrals in terms of the five topologies we can proceed to calculate the IBP identities, using `Reduze 2` [63, 64]. This framework maps each topology to a linear combination of master integrals. We can then identify the masters that are the same for several topologies and simplify the set further. This allows us to express the results in terms of the minimal set. It is important to note, that the set of the master integrals is not unique and therefore a different basis can be chosen. In particular, it is convenient to choose masters for which we have analytic solutions. Moreover, choosing master integrals with positive powers of the propagators makes it easier to match between different topologies. We find that our set contains 15 unique two-loop diagrams, shown in Figure 3.5, with various external momentum configurations for SMOM schemes, given in Table 3.3. In SMOM schemes, for bubbles and triangles it is sufficient to give the external

index	c. 1	c. 2	c. 3	c. 4	c. 5	c. 6	index	c. 1	c. 2	index	c. 1	c. 2
1	p^2	$3p^2$	$4p^2$				16	p^2		31	p^2	p^2
2	p^2	$4p^2$	p^2				17	p^2		32	\tilde{p}^2	p^2
3	p^2	$4p^2$	$4p^2$				18	p^2		33	p^2	\tilde{p}^2
4	p^2	p^2	p^2	$4p^2$	p^2	$4p^2$	19	\tilde{p}^2	p^2	34	$3p^2$	$3p^2$
5	p^2	p^2	$4p^2$	p^2	p^2	p^2	20	p^2	p^2	35	p^2	
6	p^2	$3p^2$	$3p^2$	$3p^2$	$4p^2$	p^2	21	$3p^2$	$3p^2$	36	p^2	
7	p^2	p^2	p^2	$4p^2$			22	p^2	\tilde{p}^2	37	\tilde{p}^2	
8	p^2	p^2	$4p^2$	p^2			23	p^2	p^2	38	$3p^2$	
9	p^2	$3p^2$	$3p^2$	$3p^2$			24	\tilde{p}^2	p^2			
10	p^2	$3p^2$	$3p^2$				25	p^2	\tilde{p}^2			
11	p^2	p^2	p^2				26	$3p^2$	$3p^2$			
12	p^2	p^2	$4p^2$				27	p^2	p^2			
13	p^2	$4p^2$					28	\tilde{p}^2	p^2			
14	p^2	p^2					29	p^2	\tilde{p}^2			
15	p^2	p^2					30	$3p^2$	$3p^2$			

Table 3.3: Momentum configurations, denoted as ‘c. number’, of the diagrams in Figure 3.5 for SMOM scheme. The ‘index’ corresponds to external leg labels in aforementioned figure. For the box diagrams tilde indicates one of p^2 that is linearly independent from the other two.

legs in terms of p^2 as it does not matter how the p_1^2 , p_2^2 and q^2 are arranged. Where this does matter is for the box diagrams as they generally have configurations with $p_1^2 = p^2$, $p_1^2 = p^2$, $p_2^2 = p^2$ and $(q + p_1)^2 = 3p^2$, or the same but with $p_1 \leftrightarrow p_2$ external legs. In these cases it matters which two of the p^2 legs are the same and which one is the different one. Hence, we use the $\tilde{p}^2 = p^2$ to indicate this. We also note that some of the diagrams appear multiple times but with different powers of propagators, meaning that such diagrams are linearly independent from each other.

Dependence on the Kinematics of the Scheme

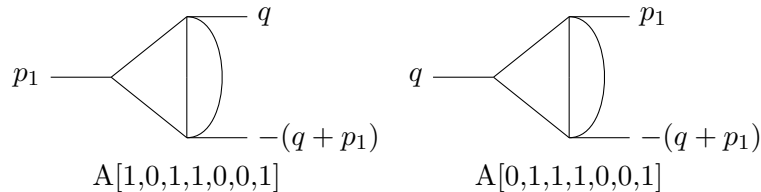
The set of the master integrals also depends on the kinematics which differ with the renormalisation scheme. Hence, when changing from one scheme to another

1. different diagrams may become the same,
2. master integrals can be reduced to simpler diagrams,
3. linearly independent diagrams may become linearly dependent,

or the other way around. For example, let us take two topology A masters

index	1	2	4	7	10	13	16	19	23	27	31	35
order	ϵ^2	ϵ	ϵ	ϵ	1	ϵ	1	ϵ	1	ϵ	ϵ	ϵ

Table 3.4: Required order of ϵ for each of the diagrams in Figure 3.5. Diagrams are indicated by their first index.



where two external legs are interchanged. We recall that our integrals depend on external momentum squared. Hence, in SMOM schemes we have $p_1^2 = q^2 = p^2$ and $(q + p_1)^2 = 3p^2$. In a MOM scheme we have $p_1^2 = (q + p_1)^2 = p^2$ and $q^2 = 0$ instead. If we consider all three external momenta to be independent, we have two distinct master integrals which are the same for SMOM schemes and can be reduced further for MOM scheme.

Evaluation

The computation on the lattice is done at a fixed renormalisation scale, hence it is sufficient to obtain the matching coefficient numerically at the corresponding scale. From the IBPs we can obtain the prefactors each master integral comes with and hence determine to which order in ϵ we need to evaluate the particular master integral. In Table 3.4 we give explicitly up to which order in ϵ each of the diagrams in Figure 3.5 are required for this calculation.

All of the necessary bubble diagrams are available up to any order in ϵ . The two-loop triangle diagrams have been calculated analytically up to finite order in the literature, whereas the results for the one-loop triangle are available to $\mathcal{O}(\epsilon)$ [62, 65]. In addition to these we also need the one-loop triangle up to $\mathcal{O}(\epsilon^2)$ for the one-loop matrix elements. There are no analytic results for the box diagrams with four off-shell legs available.

We calculate the missing pieces and the box diagrams using sector decomposition method. The formalism works by factorising the integrals in a way that separates out overlapping divergences into sectors, which are then integrated numerically. The whole procedure involves various complex algorithms which are possible to implement in a computer program. Hence, we use PySecDec [66] to facilitate the evaluation of two-loop off-shell box diagrams as well as obtain the missing $\mathcal{O}(\epsilon)$ and $\mathcal{O}(\epsilon^2)$ of triangle diagrams.

3.5.4 One-loop Counterterms

In addition to the one-loop amplitude and counterterms introduced in the previous section, for the two-loop renormalisation we also require additional one-loop Z factors corresponding to the evanescent operators E_F , E_1 and E_2 . We obtain them via insertions of the evanescent operators into the vertices of the one-loop diagrams. Inserting E_F into the vertex yields

$$\begin{aligned} \langle E_F \rangle^{1-loop} = & \frac{\alpha_s}{4\pi} \frac{1}{\epsilon} \left\{ \left(2C_F \xi + 3 \left(1 + \frac{1}{N_c} \right) \right) \langle E_F \rangle \right. \\ & \left. - \left(\frac{1}{4} + \frac{1}{2N_c} \right) \langle E_1 \rangle + \left(\frac{1-C_F}{2} + \frac{1}{4N_c} \right) \langle E_2 \rangle \right\} + \mathcal{O}(\epsilon^0), \end{aligned} \quad (3.64)$$

giving the constants

$$Z_{E_F Q}^{(1)} = 0, \quad (3.65) \quad Z_{E_F E_2}^{(1)} = \frac{1}{\epsilon} \left(\frac{C_F - 1}{2} - \frac{1}{4N_c} \right), \quad (3.68)$$

$$Z_{E_F E_F}^{(1)} = -\frac{3}{\epsilon} \left(1 + \frac{1}{N_c} \right), \quad (3.66) \quad Z_{E_F E_3}^{(1)} = 0, \quad (3.69)$$

$$Z_{E_F E_1}^{(1)} = \frac{1}{\epsilon} \left(\frac{1}{4} + \frac{1}{2N_c} \right), \quad (3.67) \quad Z_{E_F E_4}^{(1)} = 0. \quad (3.70)$$

Similarly, the remaining Z factors have been obtained from the corresponding insertions into the one-loop amplitudes

$$\begin{aligned} \langle E_1 \rangle^{1-loop} = & \frac{\alpha_s}{4\pi} \frac{1}{\epsilon} \left\{ \left(2C_F \xi - \frac{13}{N_c} \right) \langle E_1 \rangle + 13 \langle E_2 \rangle + \frac{1}{2N_c} \langle E_3 \rangle - \frac{1}{2} \langle E_4 \rangle \right\} \\ & + 24 \left(2C_F + 1 - \frac{1}{N_c} \right) \langle Q \rangle + \text{evanescent}, \end{aligned} \quad (3.71)$$

$$\begin{aligned} \langle E_2 \rangle^{1-loop} = & \frac{\alpha_s}{4\pi} \frac{1}{\epsilon} \left\{ 5 \langle E_1 \rangle + \left(2C_F \xi + 16C_F - \frac{5}{N_c} \right) \langle E_2 \rangle - \frac{1}{4} \langle E_3 \rangle \right. \\ & \left. + \frac{1}{4} \left(\frac{1}{N_c} - 2C_F \right) \langle E_4 \rangle \right\} + 48 \left(1 - \frac{1}{N_c} \right) \langle Q \rangle + \text{evanescent}, \end{aligned} \quad (3.72)$$

where ‘‘evanescent’’ denotes terms that vanish as $D \rightarrow 4$. The renormalisation constants can then be read-off as

$$Z_{E_1 E_F}^{(1)} = 0, \quad (3.73) \quad Z_{E_2 E_F}^{(1)} = 0, \quad (3.77)$$

$$Z_{E_1 E_1}^{(1)} = \frac{13}{N_c \epsilon}, \quad (3.74) \quad Z_{E_2 E_1}^{(1)} = -\frac{5}{\epsilon}, \quad (3.78)$$

$$Z_{E_1 E_2}^{(1)} = -\frac{13}{\epsilon}, \quad (3.75) \quad Z_{E_2 E_2}^{(1)} = \frac{1}{\epsilon} \left(\frac{5}{N_c} - 16C_F \right), \quad (3.79)$$

$$Z_{E_1 E_3}^{(1)} = -\frac{1}{2N_c \epsilon}, \quad (3.76) \quad Z_{E_2 E_3}^{(1)} = \frac{1}{4\epsilon}, \quad (3.80)$$

$$Z_{E_1 E_4}^{(1)} = \frac{1}{2\epsilon}, \quad (3.81) \quad Z_{E_2 E_4}^{(1)} = \frac{1}{4\epsilon} \left(2C_F - \frac{1}{N_c} \right). \quad (3.82)$$

The properly renormalised evanescent operators also require a subtraction of the finite constants multiplying $\langle Q \rangle$, giving

$$Z_{E_1 Q}^{(1)} = 24 \left(2C_F + 1 - \frac{1}{N_c} \right), \quad (3.83) \quad Z_{E_2 Q}^{(1)} = 48 \left(1 - \frac{1}{N_c} \right). \quad (3.84)$$

3.5.5 Two-loop Counterterms

Two-loop Z factors can be extracted from the 2-loop ADM. The Z factor can be expanded as

$$Z^{(2)} = \left(\frac{1}{\epsilon} Z^{(2,1)} + \frac{1}{\epsilon^2} Z^{(2,2)} \right), \quad (3.85)$$

Recalling the ADM finiteness limit in Eq.(2.61), given by

$$4Z^{(2,2)} + 2\beta_0 Z^{(1,1)} - 2Z^{(1,1)} Z^{(1,1)} = 0, \quad (3.86)$$

where $\beta_0 = (11N_c - 2N_f)/3$, we get

$$Z_{QQ}^{(2,2)} = \frac{1}{2} (Z_{QQ}^{(1,1)})^2 - \frac{1}{2} Z_{QQ}^{(1,1)} \beta_0 = -\frac{(N_c - 1)(N_c(-2N_f + 11N_c - 9) + 9)}{2N_c^2}, \quad (3.87)$$

$$Z_{QE_F}^{(2,2)} = \frac{1}{2} (Z_{QQ}^{(1,1)} Z_{QE_F}^{(1,1)} + Z_{E_F E_F}^{(1,1)} Z_{QE_F}^{(1,1)}) - \frac{1}{2} Z_{QE_F}^{(1,1)} \beta_0 = N_f - \frac{11N_c}{2} - \frac{9}{N_c}. \quad (3.88)$$

Using Eq.(5.2) of [54], which translated to our conventions is written as

$$\gamma_{QQ}^{(1)} = \frac{(N_c - 1)}{2N_c} \left(21 - \frac{57}{N_c} + \frac{19}{3} N_c - \frac{4}{3} N_f \right), \quad (3.89)$$

and Eq.(2.62), given by

$$\gamma_{QQ}^{(1)} = -4Z_{QQ}^{(2,1)} + 2Z_{QE_1}^{(1,1)} Z_{E_1 Q}^{(1,0)}, \quad (3.90)$$

we get

$$Z_{QQ}^{(2,1)} = \frac{N_c(-288C_F + N_c(19N_c - 4N_f + 44) + 4N_f - 378) + 315}{24N_c^2}. \quad (3.91)$$

Technically, $Z_{QE_F}^{(2,1)}$ also enters the two-loop amplitude, however, we find that it drops out of the computation of A' , hence it is not essential.

3.5.6 Renormalised Amplitude

The renormalized two-loop amplitude can be written as

$$\begin{aligned} \Lambda_{\text{ren}}^{(2)} = & \langle Q \rangle^{2\text{-loop}} + 2Z_q^{(1)} \Lambda_{\text{ren}}^{(1)} + \left(Z_g^{(1)} + Z_\xi^{(1)} \xi \frac{\partial}{\partial \xi} + Z_{QQ}^{(1)} \right) \langle Q \rangle^{1\text{-loop}} \\ & + Z_{QE_n}^{(1)} \langle E_n \rangle^{1\text{-loop}} + (-3(Z_q^{(1)})^2 + 2Z_q^{(2)} + Z_{QQ}^{(2)}) \langle Q \rangle^{\text{tree}} + Z_{QE_n}^{(2)} \langle E_n \rangle^{\text{tree}}. \end{aligned} \quad (3.92)$$

where $n = \{F, 1, 2\}$. $\langle Q \rangle^{2\text{-loop}}$ is the two-loop matrix element, obtained from the sum of all diagrams, discussed in Section 3.1.3. $\Lambda_{\text{ren}}^{(1)}$ is the renormalised one-loop amplitude, defined in Eq.(3.50). $Z_{QQ}^{(1)}$ is the one-loop counterterm given in Eq.(3.42). The one- and two-loop wave function renormalisation constants $Z_q^{(1)}$ and $Z_q^{(2)}$ are listed in Eq.(2.22). The gauge and gauge parameter Z -factors $Z_g^{(1)}$ and $Z_\xi^{(1)}$ are provided in Eqs.(2.23, 2.24) respectively.

3.6 C_{B_K} at NNLO

In this section we present the first results for the conversion factor C_{B_K} to SMOM schemes at two-loop order. The computation is analogous to the one given for the one-loop order result in Section 3.4. We take the NNLO coefficients of the $C_q^{(\not{d})}$ and $C_q^{(\gamma\mu)}$ from [67](setting $C_A = N_c, T_F = 1/2$) and [68](setting $w = 1, r = 1$). In addition, to the one-loop amplitude and counterterms we also use additional one and two-loop Z -factors and compute the NNLO renormalised Green's function as discussed in Section 3.5.

The numerical results for the C_{B_K} are presented as an expansion in α_s

$$C_{B_K}^{(X,Y)} = 1 + \frac{\alpha_s}{4\pi} C_{B_K,\text{NLO}}^{(X,Y)} + \frac{\alpha_s^2}{16\pi^2} C_{B_K,\text{NNLO}}^{(X,Y)} + \dots, \quad (3.93)$$

where the NLO result has been given in Table 3.2. The coefficients $C_{B_K,\text{NNLO}}$ are presented in Table 3.5, where they have been computed for Landau and Feynman gauges, $N_c = 3$, $N_f = 3$ and three scales $\nu^2 = \mu^2 = -p^2 = \{2, 3, 4\}$ GeV at SMOM subtraction point.

The main uncertainties in these results arise from the numerical evaluation of the integrals using Sector Decomposition. We have checked that the coefficients of all of the poles in the calculation are consistent with zero within the uncertainties, hence they have been dropped.

We use the world average of $\alpha_s(M_Z) = 0.1180 \pm 0.0007$ [38], which is evolved to GeV scales using 4-loop QCD β function and threshold corrections available in RunDec [69]. We give the values for the LO+NLO and LO+NLO+NNLO conversion factors (LO=1), as

Scheme	$\xi = 0$		
	$\mu = 2 \text{ GeV}$	$\mu = 3 \text{ GeV}$	$\mu = 4 \text{ GeV}$
(γ_μ, \not{q})	-36.2 ± 0.1	-36.2 ± 0.1	-36.1 ± 0.1
(γ_μ, γ_μ)	16.2 ± 0.1	16.2 ± 0.1	16.3 ± 0.1
(\not{q}, \not{q})	-13.45 ± 0.02	-13.42 ± 0.02	-13.31 ± 0.02
(\not{q}, γ_μ)	44.35 ± 0.02	44.38 ± 0.02	44.48 ± 0.02
	$\xi = 1$		
	$\mu = 2 \text{ GeV}$	$\mu = 3 \text{ GeV}$	$\mu = 4 \text{ GeV}$
(γ_μ, \not{q})	-40.23 ± 0.05	-40.20 ± 0.06	-40.09 ± 0.07
(γ_μ, γ_μ)	31.33 ± 0.05	31.37 ± 0.06	31.48 ± 0.07
(\not{q}, \not{q})	-15.05 ± 0.03	-15.03 ± 0.02	-14.93 ± 0.02
(\not{q}, γ_μ)	71.42 ± 0.03	71.45 ± 0.02	71.55 ± 0.02

Table 3.5: NNLO coefficient of conversion factors $C_{B_K}^{(X,Y)}$ in Landau and Feynman gauges with $\nu = \mu$ for four RI-SMOM schemes, where $X = \gamma_\mu, \not{q}$ and $Y = \gamma_\mu, \not{q}$, to $\overline{\text{MS}}$. The prefactor $\frac{\alpha_s^2}{16\pi^2}$ is omitted.

well as the difference between the NNLO and NLO corrections in Table 3.6. We find the perturbative series exhibits excellent convergence as the NNLO corrections give relative contributions below 4% for all schemes. For the (γ_μ, γ_μ) with $\xi = 0$ and (\not{q}, \not{q}) with $\xi = 1$ schemes, the NNLO contributions are larger than the NLO ones. However, the relative NLO corrections to the series are significantly smaller compared to other schemes, while the NNLO contributions are of comparable size. Hence we do not consider the perturbative behaviour in these cases to be abnormal. In addition, there is a mild dependence on the renormalisation scale (0.5 – 3% between $\mu = 2 \text{ GeV}$ and $\mu = 4 \text{ GeV}$) as well as a larger dependence on the gauge choice (ranging between 1 – 5 %). The dominant uncertainty here comes from the error on $\alpha_s(\mu)$ at NLO and NNLO respectively.

Scheme	$\xi = 0$								
	$\mu = 2 \text{ GeV}$			$\mu = 3 \text{ GeV}$			$\mu = 4 \text{ GeV}$		
	NLO	NNLO	diff.	NLO	NNLO	diff.	NLO	NNLO	diff.
(γ_μ, \not{d})	0.9425(9)	0.923(2)	0.0195	0.9523(6)	0.939(1)	0.0133	0.9573(5)	0.9463(7)	0.011
(γ_μ, γ_μ)	1.00496(8)	1.0139(4)	0.00894	1.00412(5)	1.0103(2)	0.00618	1.0037(4)	1.0086(2)	0.0049
(\not{d}, \not{d})	0.9893(2)	0.9820(4)	0.0073	0.9912(1)	0.9861(2)	0.0051	0.99208(9)	0.9880(2)	0.00408
(\not{d}, γ_μ)	1.0518(8)	1.076(2)	0.0242	1.0430(6)	1.060(1)	0.017	1.0385(4)	1.0520(7)	0.0135
	$\xi = 1$								
	$\mu = 2 \text{ GeV}$			$\mu = 3 \text{ GeV}$			$\mu = 4 \text{ GeV}$		
	NLO	NNLO	diff.	NLO	NNLO	diff.	NLO	NNLO	diff.
(γ_μ, \not{d})	0.917(1)	0.896(2)	0.021	0.9317(9)	0.916(1)	0.0157	0.9388(7)	0.927(1)	0.0118
(γ_μ, γ_μ)	1.0222(4)	1.0394(9)	0.0172	1.01839(2)	1.0303(6)	0.01191	1.0165(2)	1.0260(4)	0.0095
(\not{d}, \not{d})	0.99604(6)	0.9878(3)	0.00824	0.99671(4)	0.9910(2)	0.00571	0.99706(3)	0.9925(1)	0.00456
(\not{d}, γ_μ)	1.100(2)	1.139(3)	0.039	1.083(1)	1.110(2)	0.027	1.075(9)	1.096(1)	0.021

Table 3.6: Conversion factors $C_{BK}^{(X,Y)}$ evaluated with $\alpha_s(\mu)$ including NLO (i.e. 1+NLO) and NNLO (i.e. 1+NLO+NNLO) corrections, as well as the difference |diff. | between the two (i.e. NNLO) in Landau and Feynman gauges from four RI-SMOM schemes, where $X = \gamma_\mu, \not{d}$ and $Y = \gamma_\mu, \not{d}$, to $\overline{\text{MS}}$. The results are computed at three different scales $\nu = \mu$.

3.7 Conversion factors to Brod–Gorbahn Basis

Our choice of evanescent operators differs from the ones used by J. Brod and M. Gorbahn [52] for the Wilson coefficients. They are given by

$$\begin{aligned}
E_F^{\text{BG}} &= (\bar{s}^i \gamma^\mu P_L d^l) (\bar{s}^k \gamma_\mu P_L d^j) - Q, \\
E_1^{(1),\text{BG}} &= (\bar{s}^i \gamma^{\mu_1 \mu_2 \mu_3} P_L d^j) (\bar{s}^k \gamma_{\mu_1 \mu_2 \mu_3} P_L d^l) - (16 - 4\epsilon - 4\epsilon^2) Q, \\
E_2^{(1),\text{BG}} &= (\bar{s}^i \gamma^{\mu_1 \mu_2 \mu_3} P_L d^l) (\bar{s}^k \gamma_{\mu_1 \mu_2 \mu_3} P_L d^j) - (16 - 4\epsilon - 4\epsilon^2) (Q + E_F), \\
E_1^{(2),\text{BG}} &= (\bar{s}^i \gamma^{\mu_1 \mu_2 \mu_3 \mu_4 \mu_5} P_L d^j) (\bar{s}^k \gamma_{\mu_1 \mu_2 \mu_3 \mu_4 \mu_5} P_L d^l) - \left(256 - 224\epsilon - \frac{108816}{325} \epsilon^2 \right) Q, \\
E_2^{(2),\text{BG}} &= (\bar{s}^i \gamma^{\mu_1 \mu_2 \mu_3 \mu_4 \mu_5} P_L d^l) (\bar{s}^k \gamma_{\mu_1 \mu_2 \mu_3 \mu_4 \mu_5} P_L d^j) - \left(256 - 224\epsilon - \frac{108816}{325} \epsilon^2 \right) (Q + E_F),
\end{aligned} \tag{3.94}$$

where $\gamma^{\mu_1 \mu_2 \mu_3} = \gamma^{\mu_1} \gamma^{\mu_2} \gamma^{\mu_3}$ etc. Comparing with Eq.(2.39), we can see that the difference is in the ϵ^2 parts of E_3 and E_4 . Our choice of evanescent operators can be translated to the ones in which Brod and Gorbahn have obtained the NNLO Wilson coefficients and anomalous dimension matrices as follows:

$$E_3 = E_1^{(2),\text{BG}} + \kappa \epsilon^2 Q, \tag{3.95}$$

$$E_4 = E_2^{(2),\text{BG}} + \kappa \epsilon^2 (Q + E_F), \tag{3.96}$$

where $\kappa = -62\,016/325$. As a result, the renormalised Green's functions of Q to NNLO differs between the two schemes as

$$\begin{aligned} \langle Q^{\overline{\text{MS}}} \rangle &= \langle Q^{\overline{\text{MS}},\text{BG}} \rangle + \kappa Z_{QE_3}^{(2,2)} \left(\frac{\alpha_s(\mu)}{4\pi} \right)^2 \langle Q \rangle^{\text{tree}} \\ &+ \kappa Z_{QE_4}^{(2,2)} \left(\frac{\alpha_s(\mu)}{4\pi} \right)^2 (\langle Q \rangle^{\text{tree}} + \langle E_F \rangle^{\text{tree}}). \end{aligned} \quad (3.97)$$

The change of basis can be obtained in terms of $1/\epsilon^2$ parts of renormalisation constants. To convert to the BG scheme, we require two two-loop $1/\epsilon^2$ pole coefficients in the evanescent sector. They can be inferred from the Eq.(2.61) as

$$Z_{QE_3}^{(2,2)} = Z_{QE_1}^{(1)} Z_{E_1E_3}^{(1)} + Z_{QE_2}^{(1)} Z_{E_2E_3}^{(1)} = \frac{1}{4N_c^2} + \frac{1}{8}, \quad (3.98)$$

$$Z_{QE_4}^{(2,2)} = Z_{QE_1}^{(1)} Z_{E_1E_4}^{(1)} + Z_{QE_2}^{(1)} Z_{E_2E_4}^{(1)} = \frac{C_F}{4} - \frac{3}{8N_c}. \quad (3.99)$$

Hence, we can obtain the conversion of B_K from SMOM to BG in two steps, by first translating to our scheme and then further to BG by means of the Eq.(3.97). The full expression can be written as

$$B_K^{\overline{\text{MS}},\text{BG}} = C_1^{\text{SMOM} \rightarrow \text{MS}} C_2^{\text{MS} \rightarrow \text{MS},\text{BG}} B_K^{\text{SMOM}}, \quad (3.100)$$

where C_1 corresponds to the C_{B_K} we have computed in Sections 3.4 and 3.6. C_2 can be obtained from Eq.(3.97) for Landau gauge as

$$C_{2, \xi=0}^{\text{MS} \rightarrow \text{MS},\text{BG}} = \frac{P\langle Q^{\overline{\text{MS}},\text{BG}} \rangle}{P\langle Q^{\overline{\text{MS}}} \rangle} = 1 + (0.4 \pm 0.2)\alpha_s^2, \quad \text{for } P_{(\gamma_\mu)}, \quad (3.101)$$

$$= 1 + (0.44 \pm 0.03)\alpha_s^2, \quad \text{for } P_{(\not{e})}. \quad (3.102)$$

Similarly, for Feynman gauge we have

$$C_{2, \xi=1}^{\text{MS} \rightarrow \text{MS},\text{BG}} = 1 + (0.44 \pm 0.08)\alpha_s^2, \quad \text{for } P_{(\gamma_\mu)}, \quad (3.103)$$

$$= 1 + (0.44 \pm 0.04)\alpha_s^2, \quad \text{for } P_{(\not{e})} \text{ and } \mu = 2 \text{ GeV}, \quad (3.104)$$

$$= 1 + (0.44 \pm 0.03)\alpha_s^2, \quad \text{for } P_{(\not{e})} \text{ and } \mu > 2 \text{ GeV}. \quad (3.105)$$

Where not indicated otherwise the results are the same for all three renormalisation scales. In Table 3.7 we give C_2 evaluated at $\alpha_s(\mu)$ at the three renormalisation scales. The dominant uncertainty here comes from the numerical integration of the loop-integrals.

Proj.	$\xi = 0$			$\xi = 1$		
	$\mu = 2$ GeV	$\mu = 3$ GeV	$\mu = 4$ GeV	$\mu = 2$ GeV	$\mu = 3$ GeV	$\mu = 4$ GeV
$P_{(\gamma_\mu)}$	1.04(2)	1.03(1)	1.020(8)	1.038(7)	1.026(5)	1.020(4)
$P_{(\not{q})}$	1.038(3)	1.026(2)	1.020(1)	1.038(4)	1.026(2)	1.020(1)

Table 3.7: $C_2^{MS \rightarrow MS, BG}$ for the two projectors $P_{(\gamma_\mu)}$ and $P_{(\not{q})}$, evaluated at $\alpha_s(\mu)$.

3.8 B_K in $\overline{\text{MS}}$ Scheme

Taking our results for the conversion factors we can perform a matching calculation using Eq.(3.100) at 3 GeV from the lattice estimate of B_K [70]. We quote the lattice result as well as present our computed values of $B_K(\overline{\text{MS}})$ using one-loop and two-loop matching in Table 3.8. We also give a combined estimate following the approach outlined in the aforementioned paper. For comparison, the one-loop matching yields

$$B_K(\overline{\text{MS}}, 3 \text{ GeV}) = 0.5294(18)(107), \quad (3.106)$$

which is in agreement with [70]. The first error accounts for the systematic uncertainties, while the second estimates the error from truncating the α_s expansion. The latter is obtained by taking the difference between the matching results in the two schemes (\not{q}, \not{q}) and (γ_μ, γ_μ) , the central value corresponds to the (\not{q}, \not{q}) result. At two-loop we obtain

$$B_K(\overline{\text{MS}}, 3 \text{ GeV}) = 0.5267(18)(48), \quad (3.107)$$

$$B_K(\overline{\text{MS}}, \text{BG}, 3 \text{ GeV}) = 0.5404(21)(28), \quad (3.108)$$

for ours as well as the BG scheme. The increase in the systematic error in the latter result with respect to [70] is a direct consequence of the uncertainties discussed in the previous section. The reduction of this error is the subject of future work. We observe that the two-loop matching yields 2 to 5 times smaller truncation errors and reduces the overall uncertainties to 1.25% and 0.91% for our and BG scheme respectively.

Scheme	Lattice	NLO	NNLO	BG NNLO
$B_K(\not{q}, \not{q})$	0.5341(18)	0.5294(18)	0.5267(18)	0.5404(21)
$B_K(\gamma_\mu, \gamma_\mu)$	0.5166(18)	0.5187(18)	0.5219(18)	0.5376(55)

Table 3.8: Bag parameter B_K from the (\not{q}, \not{q}) and (γ_μ, γ_μ) schemes for $\mu = 3$ GeV and $\xi = 0$. Lattice results are taken from [70]. The remaining columns correspond to the SMOM to $\overline{\text{MS}}$ one-loop, two-loop and two-loop Brod–Gorbahn (BG) matching respectively.

3.9 Summary

In this chapter, we have presented the first results for the NNLO conversion factors between $\overline{\text{MS}}$ and RI-SMOM schemes for the kaon bag parameter. This is an extension to the one-loop conversion factors in [4]. We found the NNLO contributions lead to 0.4% to 4% corrections with respect to the tree-level. Furthermore, the perturbative series in α_s are stable. The dominant errors on the results stem from uncertainty in α_s . In addition we have given the conversion factors necessary for translating our results to the Brod–Gorbahn basis, for which the Wilson coefficients and anomalous dimensions have been computed. During this calculation, we have developed our technique for obtaining the full two-loop amplitude from only part of diagrams and circumventing the tensor reduction and γ_5 ambiguities at two-loop order. Furthermore we have validated our method and correctly reproduced the one-loop results in [4]. Finally, we have performed the matching for B_K at $\mu = 3$ GeV and found roughly a factor of 2 increase in precision, with the dominant uncertainty still coming from the truncation of the perturbative series.

Preface to Chapter 4

The Chapter 4 presents a journal paper [1] verbatim. The sections of this chapter map directly to the ones in the publication and are preceded by the abstract. The appendix of the paper is included in App.(A).

In the previous chapters we have concerned ourselves with precision calculations within the SM context. These efforts can be utilised to probe observables that are sensitive to new physics in a “bottom-up” approach. In the same spirit, we can look for BSM physics at colliders by studying signatures of some generic particles. In the following chapter we look at the bounds on the masses of stable multiply charged particles. As such particles are predicted by composite Higgs models, this chapter bridges the gap towards explicit studies of these models at colliders.

Chapter 4

Bounds and Prospects for Stable Multiply Charged Particles at the LHC

Colored and colorless particles that are stable on collider scales and carry exotic electric charges, so-called MCHSPs, exist in extensions of the Standard Model, and can include the top partner(s) in solutions of the hierarchy problem. To obtain bounds on color-triplets and color-singlets of charges up to $|Q| = 8$, we recast searches for signatures of two production channels: the “open” channel – where the particles are pair-produced above threshold, and are detectable in dedicated LHC searches for stable multiply charged leptons, and the “closed” channel – where a particle-antiparticle pair is produced as a bound state, detectable in searches for a diphoton resonance. We recast the open lepton searches by incorporating the relevant strong-interaction effects for color-triplets. In both open and closed production, we provide a careful assessment of photon-induced processes using the accurate LUXqed PDF, resulting in substantially weaker bounds than previously claimed in the literature for the colorless case. Our bounds for colored MCHSPs are shown for the first time, as the LHC experiments have not searched for them directly. Generally, we obtain nearly charge-independent lower mass limits of around 970 GeV (color-triplet scalar), 1200 GeV (color-triplet fermion), and 880 – 900 GeV (color-singlet fermion) from open production, and strongly charge-dependent limits from closed production. In all cases there is a cross-over between dominance by open and closed searches at some charge. We provide prospective bounds for $\sqrt{s} = 13$ TeV LHC searches at integrated luminosities of 39.5 fb^{-1} , 100 fb^{-1} , and 300 fb^{-1} . Moreover, we show that a joint observation in the open and the closed channels allows to determine the mass, spin, color, and electric charge of

the particle.

4.1 Introduction

Extensions of the Standard Model (SM) often contain particles that are stable, or sufficiently long-lived to be effectively stable on the time and distance scales relevant to collider experiments. Examples include the lightest supersymmetric particle if R -parity is approximately or exactly conserved (see [71] for a review) and particles in certain composite Higgs models [72]. It is possible that such a particle has exotic and possibly large electric charge; we will refer to this as a Multiply-Charged Heavy Stable Particle (MCHSP).

Within the context of the naturalness problem (see e.g [73]), such MCHSP can cure the quadratic divergence in the Higgs mass parameter; this has recently been realized in the framework of Colorful Twisted Top Partners (CTTPs) [6]. The CTTP can take the form of a spin-0 or spin-1/2 color-triplet of arbitrary electric charge. The divergence cancellation occurs between the top loop in Fig. 4.1(a), and a scalar CTTP loop (Fig. 4.1(b)) or a fermion loop (Fig. 4.1(c)). The CTTP is stable either due to an (approximate) accidental $U(1)$ symmetry, conserving partner-number, or due to an (approximate) Z_2 symmetry, under which the CTTP is odd and all SM particles are even. In fact, CTTPs of charges different from $Q = 2/3 + n$ or $Q = -(1/3 + n)$, where n is a non-negative integer, are not allowed to decay to SM particles altogether [33]. Consequently, exotically charged top partners are likely to be stable or long lived.

Motivated by the above, we will consider color-triplet particles with arbitrary electric charges, and refer to them as CTTPs, or “partners”, irrespective of whether they are connected to naturalness or not. An important implication of their long lifetime is the presence of a near-threshold, positronium-like bound state. In the top partner case, this is known as the partnerium [6], and we will use this term to denote the bound state

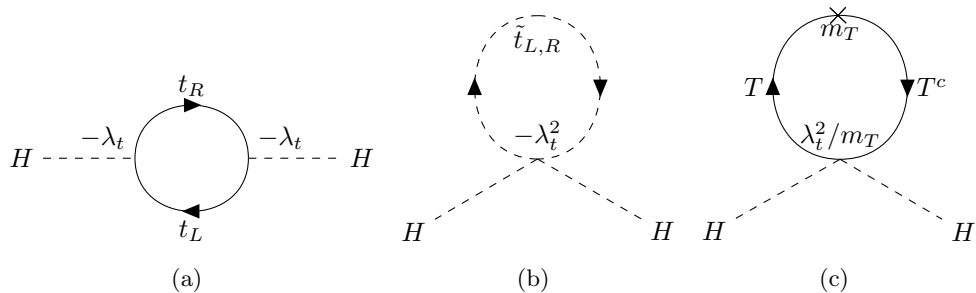


Figure 4.1: (a) Divergent top loop correction to the Higgs mass. (b) Loop contribution of a scalar top-partner. (c) Loop contribution of a fermion top-partner. The diagrams are taken from [6].

in the generic case. The colored particle-antiparticle pair is bound by both a Coulomb-like Quantum Chromodynamics (QCD) potential and by Electromagnetism (EM), with the latter becoming important for large charges. Since partnerium carries no conserved charge, it is free to annihilate into SM particles, leaving potentially detectable signatures, the most relevant of which, for our purposes, is a diphoton resonance.

In addition to the bound-state production (referred to as “closed”), the stable (or long-lived) partner can be pair-produced above threshold (referred to as “open”), leaving tracks in all detector layers and eventually escaping without an observed decay. Color-triplet top partners with charges different than $2/3$ have not been directly searched for at the LHC, and are largely unconstrained. In this work, we obtain current bounds on exotically-charged scalar and fermion CTPs, considering both open pair production and partnerium signatures. We also obtain prospective bounds, for future LHC searches, at several integrated luminosities and Center of Mass (COM) energy of 13 TeV. We choose to focus on multiply-charged ($|Q| > 1$) color-triplet top partners, which are expected to exhibit an interesting interplay between the two channels, especially given their sizable partnerium-annihilation to a pair of photons. In addition, we consider color-singlet fermion MCHSPs, referred to as lepton-like particles. In this case, the bound state is purely EM, referred to as “leptonium”. We restrict ourselves to $SU(2)_{\text{weak}}$ singlets, both for colored and colorless MCHSPs.

The remainder of the paper is organized as follows. In Section 4.2 we discuss the open-production signatures of MCHSPs, and consider the existing run-I ($\sqrt{s} = 8$ TeV) LHC searches for color-neutral stable particles with large electric charges. In order to recast these searches for colored particles, and to update their results for colorless particles, we compute the production cross sections and the detection efficiencies for both spinless and spin-1/2 color-triplets, and for colorless fermions, all with charges Q in the range $1 \leq |Q| \leq 8$ and masses m in the range $100 \text{ GeV} \leq m \leq 3 \text{ TeV}$. We validate our methodology against the published efficiencies in the colorless case. We also obtain the required components for the prospective $\sqrt{s} = 13$ TeV searches. Section 4.3 reviews the pertinent aspects of the bound state signatures, in particular the resonant-production cross section of a diphoton final state. Section 4.4 contains our main findings, in the form of current lower limits on the masses of colored and color-neutral particles. For the color-neutral case, we obtain weaker constraints than a recent paper, albeit stronger than the bounds originally obtained by CMS; we trace these discrepancies to the photon-induced component of the signal and stress the importance of an appropriate choice of the

photon Parton Distribution Function (PDF). In Section 4.5, we present projected bounds for LHC searches at $\sqrt{s} = 13$ TeV, for integrated luminosities of 39.5 fb^{-1} , 100 fb^{-1} , and 300 fb^{-1} , taking into account the scaling of pileup. We briefly discuss how by combining an open-production effective cross section measurement and a diphoton resonance observation one can determine the mass, spin, electric charge and color charge of the particle. Our conclusions can be found in Section 4.6.

4.2 Stable Multiply-Charged Particles at the LHC

Our first goal is to obtain constraints on CTTPs from their signatures as stable particles, produced above threshold. So far, there have been no LHC searches designated for color-triplet MCHSPs. However, there have been experimental searches for other kinds of heavy stable charged particles, which could be potentially recast to apply to CTTPs.

The stable fermion and scalar color-triplet partners are expected to hadronize to form "R-hadrons", similarly to quarks and squarks [32]. Searches for stable R-hadrons have been carried out both in ATLAS [74–76], and in CMS [9, 77, 78] for COM energies of 7, 8 and 13 TeV. However, these searches are designated for stops and gluinos, and thus optimized for unit-charged R-hadrons. Applying such searches for multiply-charged R-hadrons could bear a significant loss of the discovery potential.

Searches for multiply-charged color-singlet fermions account for the difficulties concerning the detection of MCHSPs. These searches were conducted by ATLAS for particles with charges of 2-6 [79], and conducted by CMS for particles with charges of 1-8 [9]. Both searches were analyzed for $\sqrt{s} = 8$ TeV, but have yet to be updated for $\sqrt{s} = 13$ TeV. Results for a $Q = 2$ lepton-like particle have been published by CMS for $\sqrt{s} = 13$ TeV, following an analysis that uses the same discriminators as for R-hadrons [77]. However, the resulting bound was less stringent than the one derived from the designated search for multiply-charged lepton-like particles, carried out for $\sqrt{s} = 8$ TeV.

As the aforementioned searches were carried out for colorless fermions only, heavy stable CTTPs are still essentially unconstrained. While multiply-charged scalar and fermion CTTPs are expected to share a lot of phenomenological traits with multiply-charged leptons, QCD-induced processes for color-triplets still need to be accounted for. First, one should consider the appropriate production mechanism, both for cross section and for efficiency calculations. Second, the hadronization of the colored particle-pair might yield two differently charged R-hadrons, and thus change the event acceptance. Moreover, nuclear energy loss and charge-changing effects [32] might further reduce the efficiency of the

search. Therefore, the existing analyses are not sufficient for obtaining bounds on stable CTTs.

Furthermore, the previous analyses for colorless fermions might be lacking. As shown in the re-analyses of the ATLAS search [79] in [11], the bounds on multiply-charged particles are sensitive to the treatment of photo-induced processes, which were not included in the original LHC analyses. However, the PDF used in [11] has been shown to have large uncertainties for the photon PDF and thus also for the photon luminosity [80–82]. This translates into large uncertainties on the previously obtained bounds. A more accurate determination of the photon PDF using ep scattering data was proposed in ref. [80, 83], resulting in significantly smaller errors, which are at the 1% level over a large range of momentum fractions. For these reasons, we would like to reanalyze the signatures of MCHSPs using the resulting LUXqed PDF [80].

This motivates us to recast a search for lepton-like MCHSPs, in order to apply its observations to fermion and scalar CTTs, and to update the bounds on lepton-like particles. The rest of this section is dedicated to describing our recast procedure.

We chose to recast the most recent CMS search for lepton-like particles with charges of 1-8 [9]¹. Since the search is a counting experiment, essentially blind to mass and charge, it is imposing a universal upper limit on the product of the cross section and the efficiency, $\sigma \cdot \epsilon$. This “effective cross section” upper limit is then compared to its theoretical prediction for each signal benchmark, described below, to obtain the upper bounds on the signal mass. In the next sections, we discuss our calculations of the cross sections and efficiencies separately, which are later combined to obtain the theoretical effective cross sections. As the search is only available for $\sqrt{s} = 7\&8$ TeV, we calculate the bounds based on the observed result at $\sqrt{s} = 8$ TeV, and estimate the expected bounds for $\sqrt{s} = 13$ TeV.

For convenience, our signal benchmarks are based on the charges already considered in the original search. Namely, color-singlets with integer charges $|Q_{\text{LLP}}| = 1 - 8$ and color-triplets that hadronize to acquire such charges, initially charged as: $5/3 \leq Q_{\text{CTTP}} \leq 23/3$ and $-22/3 \leq Q_{\text{CTTP}} \leq -4/3$, in increments of one. We did not include charges of $-1/3$ and $2/3$ in our analysis, as those were better studied in stable R-hadrons searches. Charges of $26/3$ and $-25/3$ were disregarded due to their sizable hadronization fraction to $|Q_{\text{R-hadron}}| = 9$ particles, that were not included in the original search. It has been shown in [11, 33] that particles with such large charges can still be treated perturbatively as long as the coupling is sufficiently small and the energy domain is well below the Landau pole.

¹The corresponding ATLAS search [79] resulted in similar bounds, and should have the same qualitative efficiency behavior, however it was only applied to $Q \leq 6$.

This is ensured when $\alpha Q^2 \lesssim \mathcal{O}(1)$. As the theory loses perturbativity for $\alpha Q^2 \gtrsim \mathcal{O}(1)$, our predictions could not be straightforwardly extrapolated for $Q \gtrsim 10$. Since both the observations and the selections of the search are common to all masses and charges, one can easily interpolate our results for any intermediate charge.

The masses of the signal benchmarks were determined in a similar fashion. Since the original search considered masses of 100 – 1000 GeV, lepton-like particles of the same masses were generated in a Monte-Carlo simulation, described in the following, in order to estimate the accuracy of the efficiency calculation. Bounds were calculated for particles of masses 500 – 3000 GeV.

4.2.1 Recalculating Production Cross Sections

The pair-production cross section of CTPs is calculated by summing the contributions from the gg , $g\gamma$ and $\gamma\gamma$ Vector Boson Fusion (VBF) production channels, as well as from the $q\bar{q}$ Drell-Yan (DY) production channel, mediated by g , γ or Z . The calculation of the pair-production cross section of lepton-like particles accounts for production both by photon-fusion and by a DY process mediated by γ or Z . In contrast to both the original search [9] and to a re-interpretation of the ATLAS search [79] in [11], all cross sections below are calculated with the LUXqed PDF set (LUXqed17_plus_PDF4LHC15_nnlo_100) [80, 83]. We use MadGraph5 [84] to calculate the parton-level cross section at LO. The resulting cross sections are presented in Appendix A.1.

The relative importance of the different production channels is highly affected by the PDF of the incoming partons. Photon-induced charge-dependent VBF processes are suppressed by the smallness of the photon PDF, while charge-independent gluon-fusion processes benefit from the large PDF of the gluon. Since the ratio between the gluon PDF and the photon PDF is slightly smaller at higher energies, a large charge-dependent contribution could eventually overcome the PDFs imbalance. Thus, as shown in Fig 4.2, heavier particles with large charges will mostly be produced by photon-inclusive, highly charge-dependent processes, and lighter particles with small charges will mostly be produced by charge-independent processes.

We use Pythia8 [85, 86] to perform showering and hadronization. As can be seen in Table 4.1, hadronized partners mainly have charges of $\pm(Q + 1/3)$ and $\pm(Q - 2/3)$, with only a negligible fraction of $\pm(Q + 4/3)$ R-hadrons. Since hadronization of the heavy partner and anti-partner takes place mostly independently, they may hadronize into two differently charged R-hadrons.

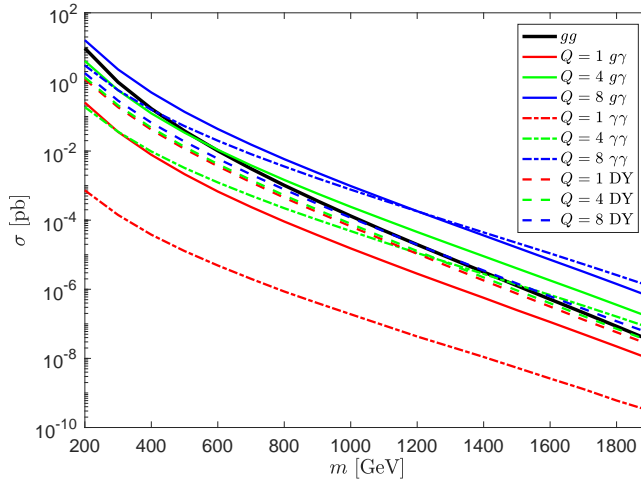


Figure 4.2: Different subprocesses for pair-production of a scalar CTPP with charges of $Q = 1, 4, 8$.

4.2.2 Efficiency Calculation

Since we do not have access to the full CMS detector simulation, we defined a set of selection criteria to account for detection efficiencies. Using our efficiency calculation, with the production mechanism described in [9], we aim to reproduce the mass bounds obtained by CMS for lepton-like particles within 15% accuracy. A similar accuracy should be maintained as we calculate the bounds on the masses of CTPPs, and of lepton-like particles produced as in Section 4.2.1. We account for the online, offline and final selections criteria, as will be explained in the following paragraphs. Even though our treatment is somewhat rough, we will see it is more than satisfactory for obtaining mass bounds, as they are only weakly affected by efficiencies.

Procedure

The online selection for the search [9] consists of an E_T^{miss} trigger and/or a muon trigger. To pass the E_T^{miss} trigger, an event should be assigned $E_T^{\text{miss}} \geq 150$ GeV as measured

R-hadron	Fraction (%)
$R^{Q+1/3}$	28.25
$R^{Q-2/3}$	21.50
$R^{Q+4/3}$	0.25
$\bar{R}^{-(Q+1/3)}$	26.75
$\bar{R}^{-(Q-2/3)}$	23.00
$\bar{R}^{-(Q+4/3)}$	0.25

Table 4.1: Fractions of produced R-hadrons with specific charges, obtained using MadGraph and Pythia simulation of partner pair-production and hadronization.

in the calorimeter. This criterion is useful to some extent for particles that were not reconstructed as muons, but we expect it to have a negligible contribution to the overall efficiency, since the offline and final selections essentially require a muon candidate.

We therefore focus on simulating the muon trigger as our online selection. To pass the muon trigger requirements, an event must have at least one particle reconstructed as a muon. The muon candidate must have $\eta \leq 2.1$, and $p_{T_{\text{meas}}} \geq 40$ GeV as measured in the Inner Detector (ID). The transverse momentum is measured from the curvature radius of the particle's track, r , under a magnetic field, B , which follows

$$r = \frac{p_T}{0.3 \cdot Q \cdot B}. \quad (4.1)$$

However, the reconstruction algorithm assumes $Q = 1$, and so the measured p_T is $p_{T_{\text{meas}}} = p_{T_{\text{truth}}}/Q$. This effectively requires the truth-level transverse momentum to satisfy $p_{T_{\text{truth}}} \geq Q \cdot (40 \text{ GeV})$, thus reducing the efficiency for large charges and small masses.

In addition, triggering particles must be fast enough to have both their ID and Muon System (MS) tracks in the same bunch crossing [87]. Since the LHC collisions were planned to occur every 25 ns, slow particles that reach the MS more than 25 ns after a $\beta = 1$ particle, will be associated with the wrong bunch crossing and thus will not have a matching ID track [5]. An additional Resistive Plate Chamber (RPC) muon trigger was applied for $\eta \leq 1.6$, allowing candidates to reach the MS up to 50 ns later than a $\beta = 1$ particle [88].

RPC-triggered particles must have a minimum of four RPC hits (three if not geometrically possible) within the trigger time window [88, 89]. A similar requirement also holds for particles triggered by the Cathode Strip Chambers (CSCs) positioned at $\eta \geq 1.6$, as the CSC trigger relies on three different track segments to reconstruct p_T [90]. These constraints effectively define a minimal distance, denoted as x_{trigger} , that candidates must travel within the trigger time window, as function of η .

In order to calculate the time required for a candidate to travel the distance necessary for triggering, denoted as t_{TOF} , one must account for the ionization energy loss in the Hadronic Calorimeter (HCAL) and in the MS. Following the Bethe-Bloch formula [35], the ionization energy loss rate decreases with the velocity of the particle and quadratically increases with its charge. Therefore, the timing requirement is expected to be crucial for MCHSPs, that are both produced with smaller velocities and significantly slowed down, or even stopped, by ionization energy loss.

Heavy R-hadrons may also undergo nuclear interactions with matter, causing addi-

tional energy loss and potentially altering the quark content of the R-hadron, resulting in a charge change [32]. However, as can be seen in Fig. 4.3, for slow particles with large charges, nuclear energy loss is quite negligible compared to ionization energy loss, and hence could be ignored. Since we did not have access to a reliable simulation of charge-changing processes, we could not account for them in our analysis. As we would expect these processes to cause some efficiency loss, it would be desirable to include them in a full experimental study. The calculation of t_{TOF} is further explained in Appendix. A.1.2.

Candidates in events passing the online selection are subject to an offline selection specified in Tables 1-2 of [9], applied at particle level. Our offline efficiency calculation is rather limited, and only explicitly includes p_T and isolation criteria, as described in lines 4-5 of Table 4.2. An additional selection requires the particle to be reconstructed as a global muon [91], filtering out particles that were not identified as muons at the muon trigger level. Therefore, we replaced the global muon selection by only accepting candidates that individually satisfy the online muon trigger requirements, as defined above. This assumption is further justified in Appendix A.1.2. Since we cannot account for the remaining criteria without a full detector simulation, we use the values quoted in Tables C1-C16 of [5] as multiplicative factors for the offline efficiency calculation. A factor for each signal mass and charge is calculated by

$$\epsilon_{\text{offline}}^{\text{sim}} = \frac{\epsilon_{\text{offline}}}{\epsilon_{\text{global muon}} \cdot \epsilon_{p_T} \cdot \epsilon_{\text{isolation}}}, \quad (4.2)$$

where $\epsilon_{\text{offline}}$ is the fraction of particles passing the offline selection, out of all particles

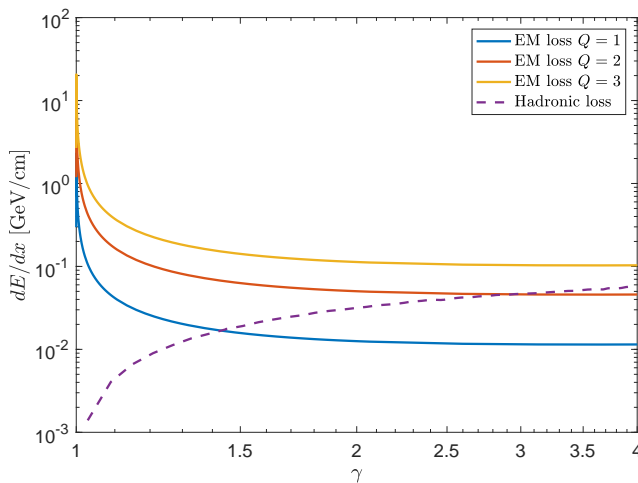


Figure 4.3: Energy loss per distance traveled in iron as a function of γ . *Solid* - ionization energy loss for $Q = 1, 2, 3$ [7]. *Dashed* - average nuclear energy loss for a hadronized stable stop [8].

from events that passed the online selection. The efficiencies $\epsilon_{\text{global muon}}$, ϵ_{p_T} , $\epsilon_{\text{isolation}}$ correspond to the fractions of particles passing the global muon, p_T and $\sum_{R \leq 0.3} p_T$ requirements, respectively, out of the particles passing all selections imposed prior to them (online selection included). The aforementioned values were given in [5] for lepton-like particles of charges 1-8 and masses of 100-1000 GeV. Since they vary weakly with mass, we use $m = 1000$ GeV efficiencies for all $m \geq 1000$ GeV particles.

Lastly, the signal region is determined by the final selection criteria, presented in Table 3 (line 4) of [9]. We include the $1/\beta \geq 1.2$ selection in our criteria, designed to identify slow particles, and calculate it using the Time of Flight (TOF) defined in Eq. A.1. Since we cannot recreate the I_{as} selection, we expect our efficiency to be overestimated for unit-charge particles. However, particles with larger charges are not affected [5].

Our efficiency calculation may require adjustment for $\sqrt{s} = 13$ TeV. In the absence of MCHSPs searches at $\sqrt{s} = 13$ TeV, we have to make certain assumptions about how the selection criteria will change. The choice of p_T thresholds is taken from the $\sqrt{s} = 13$ TeV search for unit-charged heavy stable charged particles [77], since the corresponding $\sqrt{s} = 8$ TeV searches for multiply-charged and unit-charged particles had the same p_T requirements. We had no reliable estimate of how the offline and the final selections might be modified for 13 TeV. We therefore kept them the same as in 8 TeV searches, noting that the offline efficiencies given in [5] for the 7 TeV and the 8 TeV runs show only a weak dependence on the masses and COM energies.

The efficiency calculation steps and criteria are summarized in Table 4.2. Events that pass those criteria are assumed 100% efficiency, as our calculation does not account for trigger inefficiencies and other hardware effects. The final efficiencies for the signal benchmarks mentioned above are given in Appendix A.1.2.

Validation

We compare the overall efficiencies, obtained by our simplified calculation, to the total efficiencies given in [5, 9]. For this purpose, we follow the production prescription in the original analysis by CMS, and generate lepton-like particles by DY processes with CTEQ6L1 PDFs [92]. The ratio of the efficiencies is presented in Fig. 4.4(a) for 8 TeV, and a relatively good agreement is established. We find that our efficiency and the results by CMS are less than 40% apart, for all charges for masses larger than 300 GeV.

As the cross sections for pair-produced MCHSPs drop sharply with their mass, the final mass bounds are only weakly sensitive to the exact upper limits on the effective cross

	8 TeV	13 TeV
Online	$p_T \geq Q \cdot 40 \text{ GeV}$	$p_T \geq Q \cdot 50 \text{ GeV}$
	$ \eta \leq 2.1$	
	$t_{\text{TOF}} - \frac{x_{\text{trigger}}}{c} \leq 50 \text{ ns (25 ns)}$	
Offline	$p_T \geq Q \cdot 45 \text{ GeV}$	$p_T \geq Q \cdot 55 \text{ GeV}$
	$\sum_{R \leq 0.3} p_T \leq 50 \text{ GeV}$	
Final	$\frac{c \cdot t_{\text{TOF}}}{x_{\text{trigger}}} \geq 1.2$	
Multiplicative Factor	$\epsilon_{\text{offline}}^{\text{sim}}(Q, m), m \leq 1000 \text{ GeV}$	
	$\epsilon_{\text{offline}}^{\text{sim}}(Q, 1000), m > 1000 \text{ GeV}$	

Table 4.2: Simplified efficiency calculation steps and criteria used in this analysis. Each step is applied only to candidates passing the selections in the steps above it. The online timing requirement is 50 ns for $|\eta| \leq 1.6$ and 25 ns for $|\eta| > 1.6$. The multiplicative factor accounts for the offline selection criteria, which are not explicitly simulated, and instead the efficiencies associated with them are taken from [5]. More details in text.

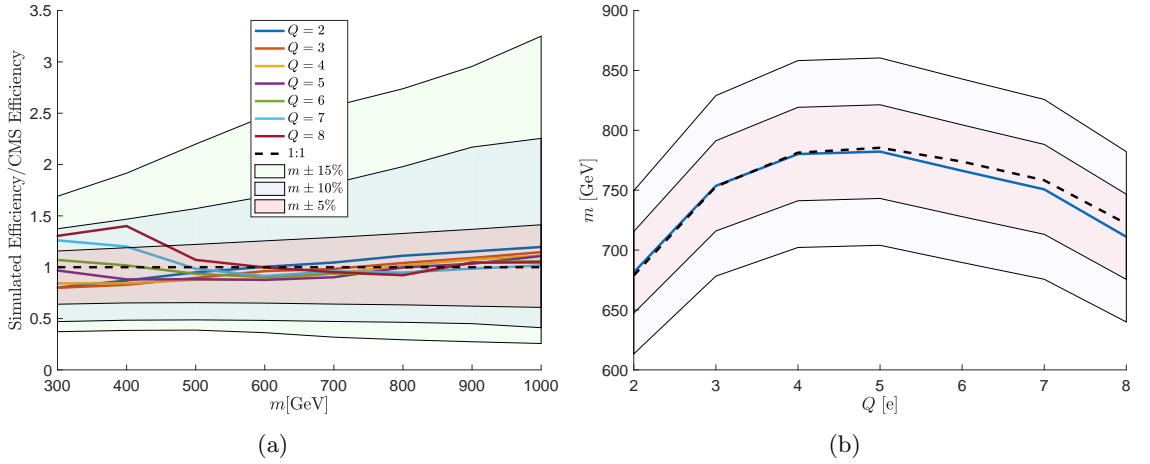


Figure 4.4: Simplified efficiency calculation validation. (a) The ratio between our resulting efficiencies and the respective CMS efficiencies for $\sqrt{s} = 8 \text{ TeV}$ [9], [5]. Indicated as well are the efficiency deviation bands corresponding to less than 5% (red), 10% (light blue) and 15% (light green) deviation in the mass bound. (b) Reproduced mass bounds for lepton-like particles, following the production mechanism used by CMS. *Dashed* – the bounds published by CMS [9], using a full detector simulation. *Solid* – our results using the simplified efficiency calculation. Indicated as well are the 5% (red) and 10% (light blue) mass deviation bands, around the our final mass bounds plot.

section. Therefore, inaccuracies in the efficiency estimation would result in much smaller deviations in the mass bounds. The mass bounds resulting from our efficiency calculation are expected to differ from the corresponding bounds calculated with the full detector

simulation by less than 10% for smaller masses, and by much less than 5% for masses larger than 500 GeV. Indeed, as shown in Fig. 4.4(b), we were able to reproduce the mass bounds for lepton-like particles with excellent accuracy.

When comparing the efficiencies at the muon trigger level with the values given in [5], we find that other than for $m = 100$ GeV, we overestimate the intermediate efficiency by 5% – 40%. There are additional effects, not included in our calculation, that might reduce the number of events passing the muon trigger selection. One such effect is the track reconstruction and matching. Heavy particles with large charges experience large ionization energy loss, and as a result are expected to be less compatible with a global muon pattern. Second, the trigger response and the gaps in the RPC and CSC coverage may increase the distance a candidate must travel to have a sufficient number of hits. Moreover, we do not consider background effects, both from pileup and from hard particles produced in the interaction, that could affect reconstruction. It may also be that we somewhat underestimate the material budget. However, the final selection filters out particles that are too fast, which are favored by the muon trigger. As a result, the overestimation of the muon trigger efficiency could be compensated, and the total efficiency is therefore in agreement with CMS. Even had these effects not canceled out, the final error for the mass bounds would still be smaller than 15% for masses larger than 500 GeV.

4.3 Bound State Signal at the LHC

Our second goal is to obtain mass bounds on CTPPs from their signatures as partnerium bound states. In this section, we will discuss the salient features of the partnerium resonance, and introduce our recast procedure, which will be centered around diphoton channel.

The partnerium is unstable due to the annihilation of its constituents, and can be detected as a resonance, with invariant-mass peak at $M \approx 2m_{\text{partner}}$. A $J = 0$ or $J = 2$ partnerium state, made of EM-charged constituents, can always decay through annihilation into $\gamma\gamma, \gamma Z$ and ZZ . In the case of the color-triplet CTPPs, it may also decay into a pair of gluons. A $J = 1$ partnerium, consisting of fermions, can annihilate into W^+W^- [11], or to any SM fermion - anti-fermion pair, through s -channel γ/Z exchange [33]. Moreover, if the constituent is a top partner, its large coupling to the Higgs implies significant annihilation rates into Higgs pairs and longitudinally polarized Electroweak (EW) gauge bosons (for $J = 0$ or 2 partnerium made of scalars), or to hZ (for $J = 1$ fermion bound states) [6]. Out of these search channels, the diphoton signal is by far the most sensitive [6, 33], especially for the large electric charges we consider. We will thus solely focus on this final

state.

Several authors have recast LHC resonance searches to obtain bounds on CTPPs. Mass bounds for scalar and fermion CTPPs of charges $-1/3, 2/3, -4/3, 5/3$ can be inferred from the plots presented in ref. [6]. In addition, the authors of [93] obtained bounds for colored scalars with charges $-7/3, 8/3, -10/3$ and of different $SU(2)_{\text{weak}}$ representations. However, these analyses attributed the dominant partnerium production, binding and decay mechanisms to QCD. This is not necessarily the case for partners with larger charges, as we will see. Ref. [11] contains the only available resonance analysis for charges 1-8, but is limited to colorless fermions bound in a ‘‘Leptonium’’ [11]. As the leptonium diphoton signal is highly sensitive to the photon PDF, we will also see that a more accurate PDF choice can lead to significantly different conclusions. Thus, similarly to the open-production case, the existing analyses of partnerium-like signatures are insufficient for constraining the parameter space of MCHSPs. We therefore recast a diphoton resonance search, to obtain bounds on the masses of CTPPs and to update the corresponding bounds for lepton-like particles.

Our recast is based on the latest diphoton search, at $\sqrt{s} = 13$ TeV and an integrated luminosity of 35.9 fb^{-1} , published by CMS [10]. As the efficiency of diphoton detection at a given invariant mass is mostly independent of the signal model, we kept it unmodified. We therefore only compute the diphoton production cross section, resulting from a partnerium or a leptonium resonance, accounting for both QCD and EM effects, and using the more precise LUXqed PDF set [80] (see also Section 4.2). The rest of this section is dedicated to the cross section calculation method.

The diphoton resonant production cross section is calculated using the full Breit-Wigner formula [35]. Thus, we are interested in both the production and the decay channels of the intermediate bound state. The partnerium can be produced by photon-fusion and gluon-fusion (projected onto a color-singlet), regardless of the partner’s spin. A leptonium, consisting of color-singlet fermions, can be produced via photon-fusion. A fermion-based bound state can also be produced via DY processes, mediated by a photon or a Z boson [33], however it may not decay into a diphoton final state. The allowed decay channels of a diphoton resonance are those of a $J = 0, 2$ resonance, discussed above. The resulting diphoton cross section would therefore follow

$$\begin{aligned} \sigma_{pp \rightarrow B \rightarrow \gamma\gamma} &= 8\pi \int_0^1 \left[\frac{1}{64} \mathcal{L}_{gg}(\tau) \Gamma_{B \rightarrow gg} + \mathcal{L}_{\gamma\gamma}(\tau) \Gamma_{B \rightarrow \gamma\gamma} \right] \\ &\times \frac{\Gamma_{B \rightarrow \gamma\gamma}}{(\hat{s} - 4m^2)^2 + \hat{s}(\Gamma_{B \rightarrow \gamma\gamma}(1 + 2 \tan^2 \theta_W + \tan^4 \theta_W) + \Gamma_{B \rightarrow gg})^2} \frac{d\tau}{\tau}, \end{aligned} \quad (4.3)$$

where $\tau = \hat{s}/s$, with $\sqrt{\hat{s}}$ being the total partonic COM energy, and θ_W is the weak angle. The parton luminosity for a pair of partons a, b is

$$\mathcal{L}_{ab}(\tau) = \tau \int_{\tau}^1 \frac{dx}{x} f_a(x) f_b\left(\frac{\tau}{x}\right) \quad (4.4)$$

where x is the fraction of the proton momentum carried by the parton and f_a is the PDF of the parton, which we evaluate at the factorization scale m . For colorless fermions, the diphoton cross section is the same, excluding QCD contributions [11]. The relevant decay widths for scalar CTTPs are given by [33, 94]

$$\Gamma_{B \rightarrow \gamma\gamma} = \frac{24\pi\alpha^2 Q^4}{M^2} |\Psi(0)|^2 \quad (\times 2 \text{ for fermions, } \times 1/3 \text{ for color-singlets}), \quad (4.5)$$

$$\Gamma_{B \rightarrow gg} = \frac{16}{3} \frac{\pi\alpha_s^2}{M^2} |\Psi(0)|^2 \quad (\times 2 \text{ for fermions}), \quad (4.6)$$

where M is the mass of the resonance, and modification factors for fermions and for color-singlet particles are given in parentheses. The naturalness-enhanced decays of the partnerium were found to be negligible when calculating the total decay width.

Colored particles of large charges could have a non-negligible contribution to their binding coming from the EM force

$$V(r) = -\frac{C\bar{\alpha}_s + Q^2\alpha}{r}, \quad (4.7)$$

where C is the Casimir of $SU(3)_c$, $C_3 = 4/3$ for a color-triplet and $C_0 = 0$ for a color-singlet. The wavefunction at the origin is

$$|\psi(0)|^2 = \frac{(C\bar{\alpha}_s + Q^2\alpha)^3 M^3}{8\pi n}, \quad (4.8)$$

where n is the radial excitation level. Since the contributions from $n \geq 2$ states are negligible, we keep only the ground state contribution [33]. In addition, we only consider the LO effects in the binding potential. The higher order effects have been studied in [33, 95, 96]. They find a noticeable though not dramatic enhancement of the signal cross section. Therefore, our bounds are somewhat conservative. One should note that in the decay rates and in the wavefunction $M^2 \rightarrow \hat{s}$, as \hat{s} is the mass of the resonance [97].

The decay rates of the partnerium and the leptonium grow significantly with the charge of the constituents. For lepton-like particles, and for CTTPs with large charges, the bound state annihilation rate approaches a Q^{10} -dependence, as a result of the dominant EM contributions. Therefore, the diphoton cross section will exhibit high charge sensitivity.

The signal benchmarks are as described for the open-production channel recast. A resonance treatment is indeed appropriate for all the charges we consider, since $\Gamma/M \lesssim 10^{-1}$ for constituents with $Q \lesssim 8$. For CTTPs and lepton-like particles with $Q \leq 4$, we have found that the narrow width approximation is more stable numerically. The production cross section for a narrow $\gamma\gamma$ resonance, via the decay of spin-0 partnerium bound state B , is given by

$$\begin{aligned} \sigma_{pp \rightarrow B \rightarrow \gamma\gamma} &= \sigma_{pp \rightarrow B} Br_{B \rightarrow \gamma\gamma} \\ &= \frac{\pi^2}{m^3} \left[\frac{1}{64} \mathcal{L}_{gg} \left(\frac{4m^2}{s} \right) \Gamma_{B \rightarrow gg} + \mathcal{L}_{\gamma\gamma} \left(\frac{4m^2}{s} \right) \Gamma_{B \rightarrow \gamma\gamma} \right] \\ &\times \frac{\Gamma_{B \rightarrow \gamma\gamma}}{\Gamma_{B \rightarrow \gamma\gamma} (1 + 2 \tan^2 \theta_W + \tan^4 \theta_W) + \Gamma_{B \rightarrow gg}}, \end{aligned} \quad (4.9)$$

and in the decay rates and wavefunctions $M^2 \rightarrow 4m^2$, where m is the mass of the partner.

Following the calculation above, using Mathematica package ManeParse 2.0 [98] with LUXqed PDFs [80] and performing numerical integration using Mathematica, we obtain the diphoton cross sections for differently charged MCHSPs, which can be found in Appendix A.2. The resulting current and future-projected bounds are discussed in Sections 4.4 and 4.5.

4.4 Current Status – Recast Bounds

We are now in a position to obtain and compare lower bounds on the masses of Multiply-Charged Heavy Stable Particles (MCHSPs) from the (recast) searches for their open-production and closed-production signatures. We begin by describing the current mass bounds, corresponding to the latest observations. Our bounds from the most recently published searches are presented in Table 4.3 and compared in Figure 4.5. Conservatively combining the bounds by taking the stricter one for each signal benchmark, we obtain the current mass bounds at a minimal CL of 95%, highlighted in the table.

To obtain current constraints on MCHSPs from the open channel, we utilize the most recent search for above-threshold MCHSPs, conducted by CMS at $\sqrt{s} = 8$ TeV [9]. The limits on particle masses, in a given signal model, are derived by first obtaining a 95%-Confidence Level (CL) upper limit on the effective cross section, and then choosing the mass such that the theoretical effective cross section saturates this limit. Following CMS, we apply a hybrid Bayesian-frequentist p-value computation [99], with the relevant parameters given in the original analysis. Our resulting upper limit is consistent with that inferred from CMS results. The theoretical effective cross sections are calculated by mul-

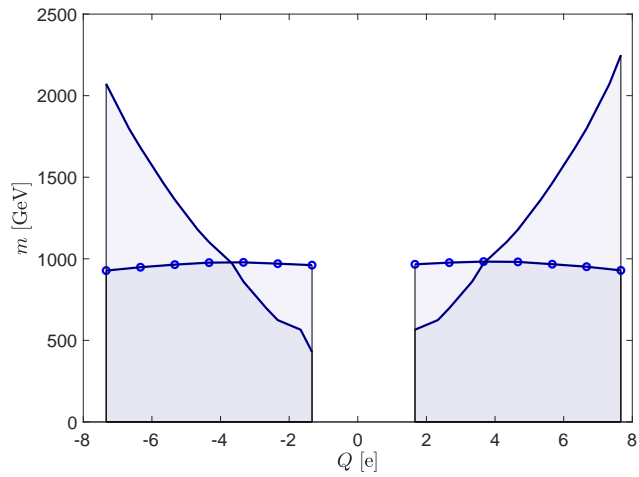
tipling the cross sections and the efficiencies, as explained in Sections 4.2.1, 4.2.2, and can be found in Appendix A.1.3.

Analogously to the open channel, we derive mass bounds for MCHSPs from their bound state signatures as well. For the closed production case, we require the theoretical diphoton production cross section, induced by the bound state resonance, as explained in Section 4.3, to saturate the upper limits at 95%-CL. For the current bound, we employ the CMS limit given in [10] for $\sqrt{s} = 13$ TeV at $\mathcal{L} = 35.9 \text{ fb}^{-1}$. It should be noted the signal efficiency in [10] was calculated for gluon-fusion production, and could be slightly different for photon-produced resonances. The experimental bounds on a diphoton resonance in [10] were given for three resonance-width benchmarks: $\Gamma/M = 1.4 \cdot 10^{-4}$ (narrow), $\Gamma/M = 1.4 \cdot 10^{-2}$ (mid-width) and $\Gamma/M = 5.6 \cdot 10^{-2}$ (wide). Therefore, when available, we use narrow resonance bounds for $\Gamma/M \lesssim 5 \cdot 10^{-3}$ ($Q \lesssim 5$ for color-triplets, $Q \lesssim 6$ for color-singlets), mid-width resonance bounds for $5 \cdot 10^{-3} \lesssim \Gamma/M \lesssim 3 \cdot 10^{-2}$ ($5 \lesssim Q \lesssim 6$ for color-triplets, $6 \lesssim Q \lesssim 7$ for color-singlets) and wide resonance bounds for $\Gamma/M \gtrsim 3 \cdot 10^{-2}$ ($6 \lesssim Q$ for color-triplets, $7 \lesssim Q$ for color-singlets).

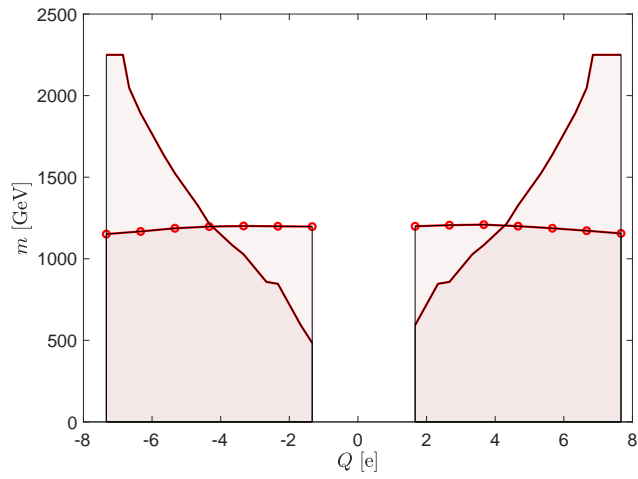
The diphoton cross section limit observed in the search was given up to resonance masses of 4500 GeV. However, for colored fermions with $Q > 6.9$ the corresponding $\gamma\gamma$ cross section is larger than the observed limit throughout the available mass range. They are thus excluded below $m = 2250$ GeV, but their exact mass bound can not be explicitly inferred from this search.

4.4.1 Bounds from Open Signatures of MCHSPs

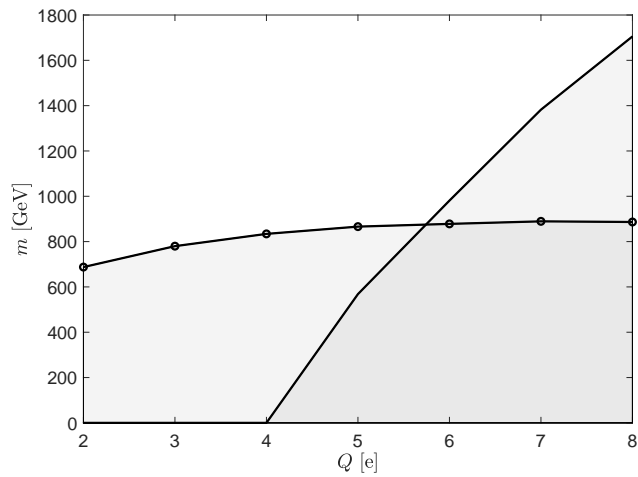
We find that scalar and fermion CTTs are excluded below masses of roughly 1 TeV and 1.2 TeV, respectively. Interestingly, the bounds are almost charge independent both for scalar and fermion CTTs. As can be seen in Fig. 4.6, this is a result of a coincidental balance between the production cross sections and the efficiencies at which color-triplet MCHSPs could be directly observed. On the one hand, the search becomes less efficient as the charge of the particle increases. For smaller masses, this is mainly a result of the p_T/Q selection, while for larger masses, the timing requirement, imposed by the muon trigger, becomes more important, due to the particle's large ionization energy loss. On the other hand, the cross sections grow with the charge of the particle. The production rate consists of the Q-independent QCD processes, the Q^2 -dependent $g\gamma$ -fusion and EW-mediated Drell-Yan (DY) processes, and the Q^4 -dependent photon-fusion. As we have shown in Sec. 4.2.1, each subprocess becomes dominant at a different mass scale, resulting



(a) Colored scalars.



(b) Colored fermions.



(c) Colorless fermions.

Figure 4.5: Lower mass bounds, as given by the most recent searches. *Solid* – a diphoton resonance search at $\sqrt{s} = 13$ TeV, $\mathcal{L} = 35.9 \text{ fb}^{-1}$ [10] (closed-production channel). *Round markers* – a search for MCHSP tracks at $\sqrt{s} = 8$ TeV, $\mathcal{L} = 18.8 \text{ fb}^{-1}$ [9] (open-production channel). *Shaded* – regions excluded by each channel. More details in text.

Q[e]	5/3	8/3	11/3	14/3	17/3	20/3	23/3	channel
color-triplet scalar	970	980	980	980	970	950	930	open
scalar	570	700	970	1180	1460	1800	2250	closed
color-triplet fermion	1200	1200	1210	1200	1190	1170	1160	open
fermion	590	860	1080	1330	1640	2050	2250*	closed
Q[e]	-4/3	-7/3	-10/3	-13/3	-16/3	-19/3	-22/3	channel
color-triplet scalar	960	970	980	980	960	950	930	open
scalar	430	620	860	1100	1360	1680	2070	closed
color-triplet fermion	1200	1200	1200	1200	1190	1170	1150	open
fermion	480	850	1030	1210	1520	1890	2250*	closed
Q[e]	2	3	4	5	6	7	8	channel
color-singlet fermion	690	780	840	870	890	890	890	open
fermion	-	-	-	570	980	1380	1710	closed

Table 4.3: Current lower bounds on the masses of MCHSPs. The bounds were obtained from the diphoton resonance signatures at $\sqrt{s} = 13$ TeV, $\mathcal{L} = 35.9 \text{ fb}^{-1}$ (closed-production channel) and from the MCHSPs signatures at $\sqrt{s} = 8$ TeV, $\mathcal{L} = 18.8 \text{ fb}^{-1}$ (open-production channel). The colored cells are the corresponding combined bounds, given by naively taking the stricter bound of the two searches. *Blue* – scalar CTTs, *red* – fermion CTTs and *black* – lepton-like particles. Mass bounds are given in GeV. *Fermion CTTs with $Q = 23/3, -22/3$, are excluded below 2250 GeV, however the exact bound could not be inferred from the search. More details in text.

in a rather strong charge-dependence for the production rates of heavy partners. The bounds on the masses of lepton-like particles are slightly more charge dependent. We find colorless fermions to be excluded below a mass of 690 GeV for $Q = 2$, and below 890 GeV for $Q = 8$. This is a result of the larger charge dependence of the production cross section of lepton-like particles, in the absence of the charge-independent QCD production.

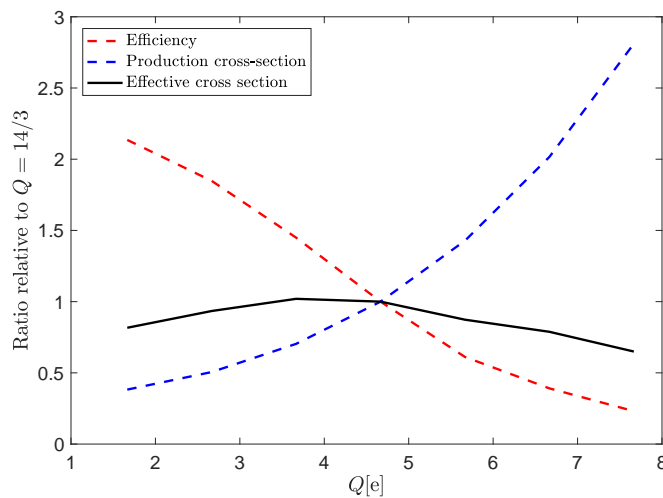


Figure 4.6: Detection efficiency, production cross section and the resulting effective cross section $\sigma \cdot \epsilon$ for a color-triplet scalar of $m = 1000$ GeV, at $\sqrt{s} = 8$ TeV. All are presented relative to their value for a color-triplet scalar of $Q = 14/3$.

Due to hadronization, the bounds in the open channel are asymmetric for positively and negatively charged color-triplets.

4.4.2 Bounds from Closed Signatures of MCHSPs

The diphoton data excludes color-triplet MCHSPs of charges larger than ~ 4 (~ 7) at masses below 1 TeV (2 TeV). Due to the smaller production and decay rates of bound states consisting of color-singlets, the bounds placed on lepton-like particles are somewhat weaker. Lepton-like particles of charges larger than 5 (8) are excluded below masses of 0.5 TeV (1.7 TeV). The charge dependence of the mass bounds coming from the closed-production signatures is understandably large, due to the dominant EM effects contributing to production, binding and decay, as explained in Section 4.3. These result in a significant charge dependence of the diphoton resonant cross section, that can be as much as Q^{10} -dependent for lepton-like particles. In addition, the efficiency for the diphoton search is not directly related to the bounded constituents charges. The bounds are symmetric for negative and positive charges, as the diphoton cross section in the Sec. 4.3 is an even function of the Q .

4.4.3 Combined Bounds

Combining the searches in the open and the closed channels provides powerful constraints on MCHSPs models. As shown above, the current limits derived from the direct search for MCHSPs are stronger for charges smaller than ~ 4 for scalar and fermion color-triplets, and for charges smaller than ~ 6 for colorless fermions, while for larger charges the diphoton exclusion bounds dominate. Therefore, we benefit from considering both searches, even by naively setting the bound at the larger of the two. Upon further statistical analysis, one should be able to combine the searches as the two channels must be explained simultaneously for stable particles, and thus obtain even stronger mass bounds at 95% CL.

4.4.4 The Leptonic Case – Comparison to the Literature

Since lepton-like particles have been studied in the past, we may now compare our new bounds for lepton-like particles to those found in the literature. As we will see, the bounds we have obtained are in disagreement with the existing results. These differences are mainly a result of our new cross section calculations, which are more exhaustive and reliable, compared to previous analyses.

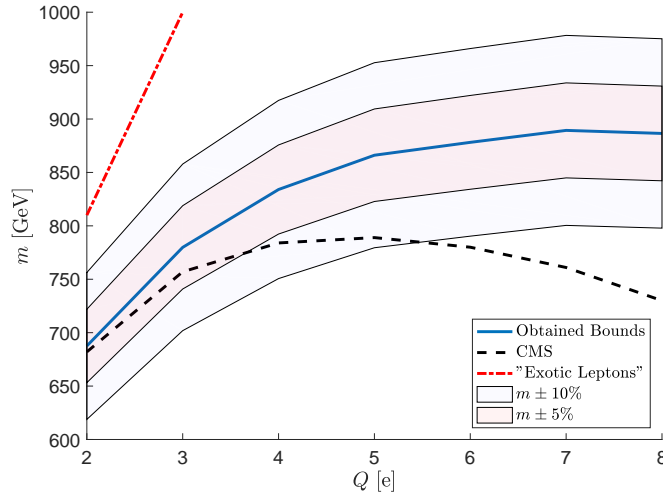


Figure 4.7: Comparing the lower mass bounds on multiply-charged lepton-like particles, coming from the different analyses of the open-production signature. *Dashed* – results published by CMS [9]. *Dash-dotted red* – bounds for $Q = 2, 3$ given in [11]. *Solid blue* – mass bounds calculated in this study with 5% (*Red*) and 10% (*Light blue*) deviation bands.

As shown in Fig. 4.7, the mass bounds we have obtained from the open-production signature are stricter than those published by CMS [9]. While the analysis by CMS considered DY-production exclusively, we also include photon-fusion production. Similarly to [11], we find that photo-production processes significantly enhance the cross sections for particles with large charges, and therefore the bounds have strengthened.

The choice of the PDF plays an essential role in calculating the production cross sections, and is particularly important when considering photo-production processes. This can be inferred by comparing our mass bounds, obtained using LUXqed PDFs set, to the bounds presented in [11], derived using NNPDF2.3QED [81], as both analyses considered the same production processes. As can be seen in Fig. 4.7, the mass bounds for colorless fermions, derived from our analysis of the open-production channel, are much weaker than the bounds set by the corresponding analysis in [11]. The same trend emerges when comparing the closed-production signature analyses, and we find our bounds to be less stringent than those previously obtained in [11]. The origin of these differences can be traced to the choice of the photon PDF. As discussed in [80] (see also [82]), the way the photon PDF is obtained in the NNPDFx.yQED sets is afflicted by large uncertainties. For the $\gamma\gamma$ parton luminosity at invariant masses of 1-3 TeV, as relevant to our analysis, the resultant uncertainty can be more than an order of magnitude. The precise extraction of the photon PDF via the method of [80, 83], using ep data, implies, via the resulting LUXqed PDF set, a photon luminosity which is as much as a factor of 60 lower than that obtained for central values of the NNPDF2.3QED set. As a result, the cross section

calculations in ref. [11], which are based on those central values, substantially overestimate the contributions coming from photon fusion (as well as other photon-induced components) to the cross section. Consequently, the bounds in [11] need to be corrected down to those derived and presented here.

4.5 Future Scenarios – Discovery and Exclusion

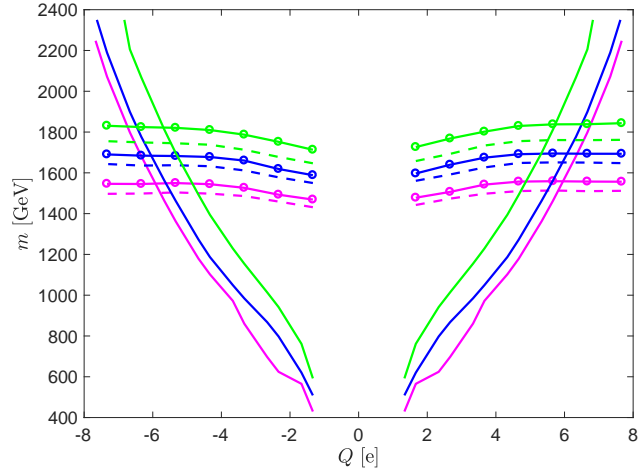
In order to obtain the prospective mass bounds from LHC searches at $\sqrt{s} = 13$ TeV, we consider integrated luminosities of 36 fb^{-1} , 100 fb^{-1} (current – July 2018) and 300 fb^{-1} (future). Our projected mass bounds from the two kinds of searches are presented in Figure 4.8.

For the closed-production signatures, projected bounds for integrated luminosities of 100 fb^{-1} and 300 fb^{-1} , are calculated using the expected upper limits for ATLAS searches of a photo-produced $J = 0$ resonance, as given in [13].

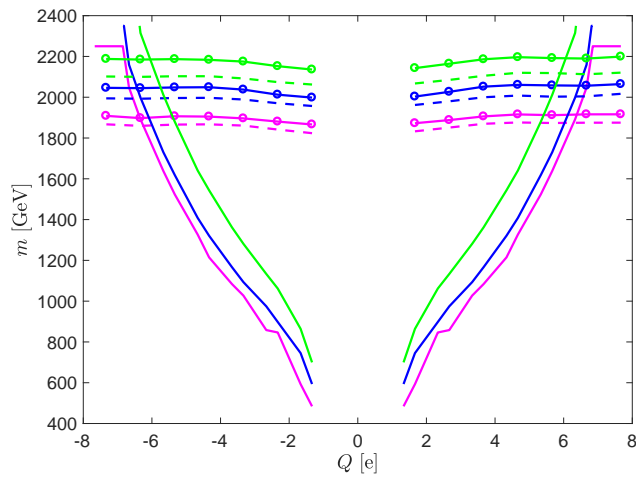
Although the LHC has been running in Center of Mass (COM) energy of 13 TeV since 2015, MCHSPs search results have yet to be updated. Therefore, for the open-production searches, we calculate the expected effective cross section upper limit at 95%-CL, under the background hypothesis. The expected number of background events is calculated by scaling the corresponding $\sqrt{s} = 8$ TeV estimate [9] in two ways – by the luminosity ratio and by the luminosity ratio times the pileup ratio. The latter is more conservative, and perhaps more realistic, as some of the selections and the backgrounds involved may depend not only on the luminosity, but also on the amount of pileup in each run.

Following our analysis, we expect the mass bounds from the open-production searches to improve dramatically with COM energy. For $\sqrt{s} = 13$ TeV, the bounds could reach about 1-1.5 TeV for lepton-like particles, 1.5 TeV for scalar CTTPs, and just under 2 TeV for fermion CTTPs, even when only considering an integrated luminosity of 36 fb^{-1} . We therefore believe that a dedicated experimental search for MCHSPs, accounting for the additional properties of colored particles, such as nuclear energy loss and charge change, is very much in need.

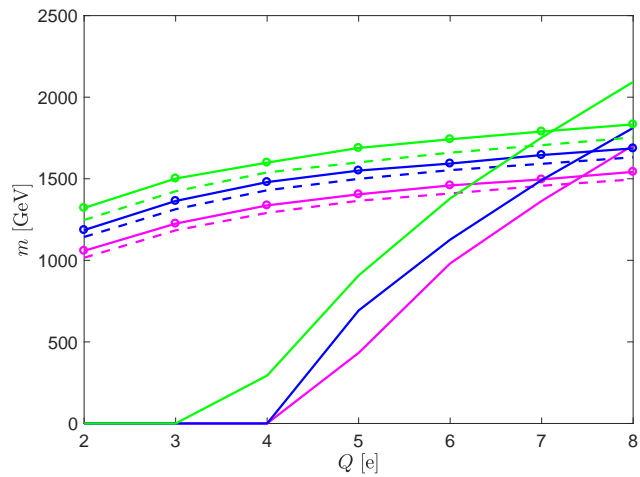
We find that the interplay between the searches for MCHSP tracks and the searches for diphoton resonances leads to an effective way to probe the parameter space of these models. We will now present how the searches in the open and the closed channels could be combined to better study MCHSPs in the future.



(a) Colored scalars.



(b) Colored fermions.



(c) Colorless fermions.

Figure 4.8: Expected lower mass bounds at $\sqrt{s} = 13$ TeV, $\mathcal{L} = 35.9$ fb $^{-1}$ (magenta), 100 fb $^{-1}$ (blue), and 300 fb $^{-1}$ (green). *Solid* – diphoton resonance searches (closed-production channel). *Round markers* – searches for MCHSP tracks with luminosity-scaling (open-production channel). *Dashed* – searches for MCHSP tracks with luminosity and pileup scaling (open-production channel).

In the case where no excess is observed in both channels, one can combine their results to set upper limits that are significantly stricter than the ones obtained by each search individually. Comparing the two channels assuming the same energy and luminosity, we find that open-production searches are expected to become stronger, and dominate up to charges of about ~ 6 for CTTPs, and ~ 7 for lepton-like particles. Therefore, these searches are also more likely to carry a potential for discovery. However, in the case of a discovery in the open channel, its analysis might not be able to determine the charge of the observed MCHSP, as we have already established. In addition, the measured kinematics of the particle is different from the truth-level kinematics, due to its unknown charge and ionization energy loss, and will thus be difficult to interpret with good accuracy. On the other hand, given its strong charge-dependence, the diphoton search, although typically less sensitive, can be very useful in breaking the charge degeneracy, or at least in narrowing down the range of allowed charges. The situation could be reversed for very large charges, and the diphoton search could become the discovery channel. In the transition region, correlated excesses in both channels, even if insignificant for each one, may be sufficiently significant to point to a discovery of an MCHSP when combined.

In case of a discovery in both channels, not only would one be able to claim an observation of an MCHSP with higher significance, but also to better study its properties, as we will now demonstrate. First, the mass of the particle could be determined from the diphoton resonance peak. Given the measured mass, one could calculate the theoretical effective cross section, relevant for the open search, and the theoretical diphoton cross section, relevant for the closed search, for MCHSPs of different spins, charges and color representations. As demonstrated for $m = 1500$ GeV in Fig. 4.9, the measurements in both channels would mark a specific point, which could then be related to a specific choice of the particle's quantum numbers. This is true for most of the parameter space, except for the crossing point between a highly charged lepton-like particle and a colored scalar, corresponding to two different choices of quantum numbers. Although measurement uncertainties could make the model distinction less sharp, the appropriate parameter space would be substantially narrowed given the combination of the two measurements.

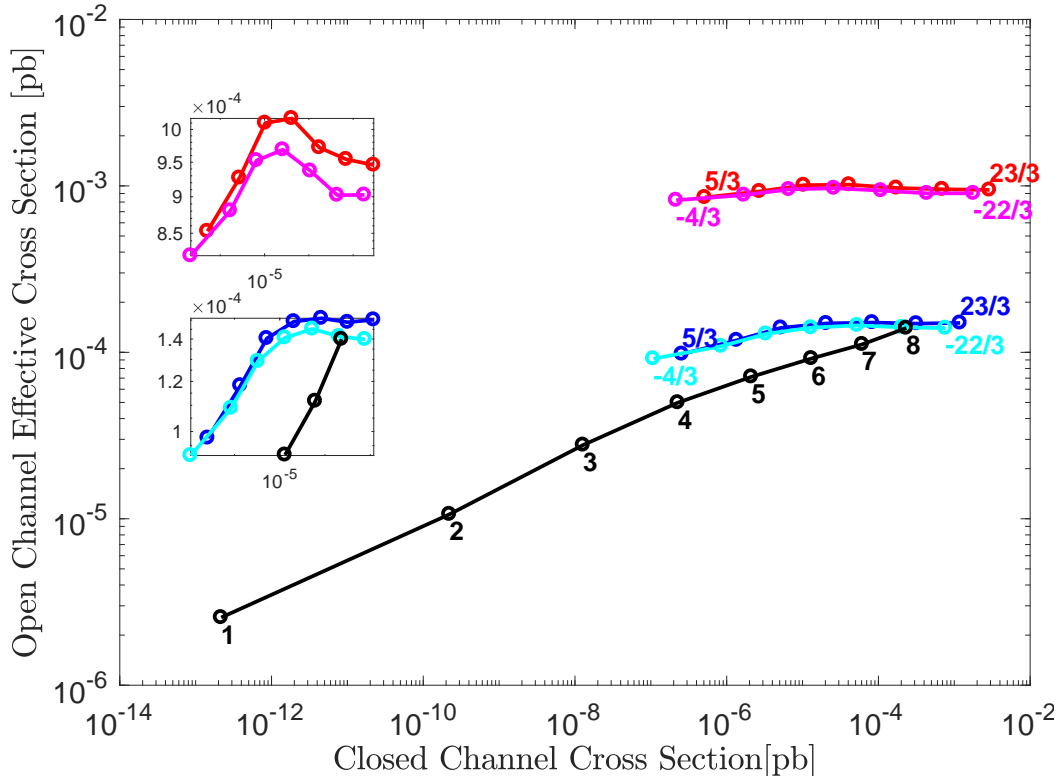


Figure 4.9: The combined signatures of a hypothetical MCHSP with $m = 1500$ GeV, for different choices of its quantum numbers. In case of a discovery in both channels, combining the observables measured in the two searches could be used to determine the quantum numbers of the newly discovered particle. The lines correspond to different spin-color combinations studied in this work. *Black* – color-singlet fermions. *Blue* – color-triplet scalars with positive charges. *Cyan* – color-triplet scalars with negative charges. *Red* – color-triplet spin-1/2 fermions with positive charges. *Magenta* – color-triplet spin-1/2 fermions with negative charges. *Round markers* indicate charges spaced by one unit, colored labels indicate the charges. The two subplots on the top-left are magnified views. *Top box* – negatively-charged and positively-charged color-triplet fermions. *Bottom box* – negatively-charged and positively-charged color-triplet scalars.

4.6 Conclusions and Outlook

We have studied the LHC phenomenology of Multiply-Charged Heavy Stable Particles (MCHSPs). Such particles, that are stable on collider scales and carry exotic electric charges, exist in various extensions of the SM. We introduced the signatures of color-triplet MCHSPs, referred to as Colorful Twisted Top Partners (CTTPs), which were proposed as a solution to the hierarchy problem [6]. In addition, we reanalyzed the signatures of colorless fermion MCHSPs, referred to as lepton-like particles. We considered both the “closed” channel – where the MCHSP and its anti-particle form a bound state (partnerium/leptonium), detectable as a diphoton resonance, and the “open” channel – where each of the MCHSPs propagates approximately independently, detectable in designated searches. For this purpose, we have recast existing analyses, including QCD effects

and an updated treatment of EM effects.

For MCHSPs with relatively small charges, the open-production searches are more important, albeit with only little sensitivity to the charge of the particle. This is in contrast to the diphoton channel, which is more sensitive to MCHSPs with large charges, and exhibits a strong charge-dependence. Thus, a combined search is useful both for the exclusion and for the discovery of MCHSPs. We have obtained bounds on MCHSPs from both production channels, and combined them by taking the more stringent bound for each signal model. We find lower bounds on CTTP masses, that are nearly constant at about 1 TeV for charges $|Q| \leq 4$, then raising to 2.3 TeV at $|Q| = 8$. This behavior is due to the closed (diphoton resonance) signature becoming more constraining than open pair production for $|Q| \geq 4$. The bounds on lepton-like particles display an analogous behavior, beginning at about 0.8 TeV and starting to rise at $|Q| = 6$, to about 1.7 TeV at $|Q| = 8$. The bounds we obtained for lepton-like particles are significantly weaker than those given in [11], but are stronger than the bounds given in [9]. The differences stem from our cross section calculation, which accounts for photo-production processes using LUXqed PDFs set, which is more precise for the photon PDF.

In addition, we have presented two future scenarios: exclusion and discovery. In the exclusion scenario, where no signal is observed, we have projected the bounds to 13 TeV, three integrated luminosities and with or without the pileup scaling. In all cases we find that the bounds become stricter. We therefore strongly encourage a dedicated experimental analysis for MCHSPs, which includes colored particles, and which should combine open production and diphoton resonance signals². In the event of a discovery, we have shown how combining the measurements at both channels will allow to determine the mass, spin, color, and charge of the observed particle.

In light of our findings, let us briefly comment on the future of open-production searches of MCHSPs. In order to reduce the impact of pileup, both ATLAS and CMS are considering installing a new timing sub-detector, that is capable of measuring Time of Flight (TOF) at 30 ps resolution [101]. These timing detectors might improve the discovery reach for

²After completing and posting the manuscript, the results of a Run-II ATLAS search for open-production lepton-like particles [100] became publicly available. This is the first LHC analysis corresponding to the $\sqrt{s} = 13$ TeV, $\mathcal{L} = 36 \text{ fb}^{-1}$ data in the context of $|Q| > 2$ MCHSPs. Similarly to the run-I CMS analysis [9] discussed above, this new ATLAS analysis did not account for photo-production processes. A rough estimate of these effects can be given by recalculating the theoretical production cross sections, as described in our analysis, and comparing them to the cross section upper limits observed by ATLAS to obtain mass bounds. This leads to mass bounds of 1.02 TeV ($Q = 2$), 1.36 TeV ($Q = 5$) and 1.32 TeV ($Q = 7$), which are in good agreement with our future-projected bounds for the same energy and luminosity. A more precise treatment requires a dedicated efficiency computation, considering the relevant aspects of the ATLAS detector and signal selections, and should be addressed through a reanalysis by ATLAS.

MCHSPs, by providing an additional, more accurate, discriminator for slow particles. Moreover, they may be able to measure the TOF of a particle prior to its interactions with the material in the calorimeters and in the Muon System (MS), which are the main cause of ionization energy loss, thus improving detection efficiencies. We leave a dedicated study of the implications of incorporating the information collected by the timing detectors in searches for MCHSPs for future work.

Chapter 5

Composite Higgs Models

The composite Higgs models are known to be able to solve the hierarchy problem by generating the Higgs mass and EWSB scale in line with the naturalness paradigm. In the previous chapter we have studied the collider phenomenology of the multiply charged top partners that could potentially come from composite Higgs models. In this chapter we will delve deeper into these theories, with particular focus on pseudo-Nambu-Goldstone boson Higgs. In Section 5.1 we review the salient features of such models and in particular look at a few simplified examples in more detail. In Section 5.2 we discuss the existing collider constraints and present a collider study which aims to look for specific signatures of CH models that could help differentiate between them. This section contains novel results from our publication [2]. Finally, to pave way towards the model building efforts in Chapter 6, we review the electro-weak corrections in Section 5.3 and include a brief summary of the chapter in Section 5.4.

5.1 The PNGB Higgs

In this section we will cover the salient features of composite Higgs models, with a particular focus on the ones with pseudo-Nambu-Goldstone Higgs and partial compositeness in the fermion sector. We will also review the CCWZ formalism and the three versions of the minimal composite Higgs models. In addition, we will discuss the computation of mass matrices and the mass spectrum of the composite partners for a set of models with fully-composite right-handed top. The concepts introduced in this section will be used extensively in the next chapter. Some of the more comprehensive reviews on the subject can be found in [37, 102–107].

5.1.1 Salient Features

The main motivation behind composite Higgs models is to address the naturalness problem. As discussed in the introduction, the issue arises if the Higgs boson is truly an elementary particle, its mass receives large radiative corrections proportional to the high-energy cut-off scale Λ_{UV} of the Standard Model. In composite Higgs models the Higgs arises as a bound state of a new strongly coupled sector. Hence, its mass only receives corrections of the order of the compositeness scale, where the new strong sector confines. This allows for a UV cut-off parametrically larger than the weak scale without introducing an associated large tuning. In order to avoid another naturalness problem the new strong sector has to be connected to a UV fixed point. Thus, its only scale is the compositeness one, which is generated dynamically.

The ‘elementary’ sector, which comprises of the remaining SM fields, does not directly interact with the composite gauge bosons. Instead, SM fermions may couple to the composite fields via linear mixing terms. This is known as partial compositeness. The interaction Lagrangian can take the form

$$\mathcal{L}_{\text{Int}} = \frac{\lambda_{t_L}}{\Lambda_{UV}^{D_L-5/2}} \bar{q}_L \mathcal{O}^L + \frac{\lambda_{t_R}}{\Lambda_{UV}^{D_R-5/2}} \bar{t}_R \mathcal{O}^R + \dots, \quad (5.1)$$

where q_L and t_R are the elementary quarks, $\mathcal{O}^{L,R}$ are the strong sector operators with $D_{L,R}$ scaling dimensions and $\lambda_{t_{L,R}}$ are the corresponding dimensionless couplings. Λ_{UV} is the UV cut-off of the theory. The hierarchy of scaling dimensions of the composite operators translates to a hierarchy of the mixings at the composite scale via the renormalisation group

$$\lambda_{t_{L,R}}(m_*) = \lambda_{t_{L,R}}(\Lambda_{UV}) \left(\frac{m_*}{\Lambda_{UV}} \right)^{D_{L,R}-5/2}, \quad (5.2)$$

where $m_* \ll \Lambda_{UV}$ is the compositeness scale. Hence, if the operators have $D_{L,R} > 5/2$, some of the λ 's can receive a sizeable suppression due to a large scale separation. This, in turn, can be used to explain why the top quark is much heavier than other quarks as the top Yukawa $y_t \propto \lambda_{t_L} \lambda_{t_R}$. In addition, the small elementary composite mixings along with the m_* suppression are sufficient to bring the dimension-six operators that mediate flavour-changing neutral currents (FCNC) to phenomenologically acceptable values.

Of special interest are models in which the compositeness scale can be large compared to the electro-weak (EW) scale. That is the case if the Higgs is a pseudo-Nambu-Goldstone boson (pNGB). This assumes that the gauge group \mathcal{G} of the UV theory is spontaneously broken at the compositeness scale to a symmetry \mathcal{H} , which contains the SM gauge group.

In the next section we will review the CCWZ formalism which provides the standard parametrisation of such breaking for arbitrary \mathcal{G} and \mathcal{H} . The hierarchy between the Higgs mass and m_* is then generated by a small explicit breaking of the quotient symmetry \mathcal{G}/\mathcal{H} . Hence, this reduces the ‘little’ hierarchy problem between the Higgs vacuum expectation value (VEV) v and m_* to v and f , where $f \ll m_*$ is the pNGB decay constant. Moreover, pNGB Higgs suppresses the $H \rightarrow \gamma\gamma$ coupling [103], because of residual shift symmetry [37].

Generally, the $O(4) = (SU(2)_L \times SU(2)_R) \rtimes Z_2$ symmetry is necessary in CH models to prevent tree-level contributions to the T -parameter [108], which is one of the oblique corrections that we will discuss later in this chapter. In addition, the relationship between the $SU(2)$ fundamental generators $T_{3L} = T_{3R}$ must hold for any sizeable composite admixture to b_L , as it forbids the tree-level corrections to the $Z \rightarrow b_L b_L$ process [109]. This also ensures that b_L is an eigenstate of the Z_2 projections $P_{L,R}$. Hence, any large admixtures are allowed only with the Higgs, which transforms as (2,2) of $SU(2)_L \times SU(2)_R$.

The minimal composite Higgs model (MCHM) provides the smallest sector \mathcal{G} which is compatible with the SM Higgs and can generate a viable electro-weak symmetry breaking (EWSB). This will be reviewed in the following sections.

5.1.2 CCWZ Formalism

The Callan–Coleman–Wess–Zumino (CCWZ) formalism [110, 111] is one of the ways of choosing a field basis for the parametrisation of pNGBs. In this section we follow the presentation of [37]. First, let us explore the idea behind the CCWZ formalism. We would like to write a general low-energy effective Lagrangian for a strongly (or weakly) coupled theory, which describes the Goldstone bosons and heavy resonances, for a particular symmetry breaking pattern $\mathcal{G} \rightarrow \mathcal{H}$. A group element can be defined as

$$g = e^{i\omega_A T^A} = e^{i\eta_{\hat{a}} T^{\hat{a}}} e^{i\eta_a T^a}, \quad (5.3)$$

where T^A are the generators of \mathcal{G} . This can then be factorised into unbroken generators T^a , corresponding to \mathcal{H} , and the broken generators $T^{\hat{a}}$. The CCWZ field can be expressed in terms of the broken generators as

$$U[\Pi] = e^{i\frac{\sqrt{2}}{f}\Pi_{\hat{a}} T^{\hat{a}}}, \quad (5.4)$$

where $\Pi_{\hat{a}}$ are the scalar NGB fields, one for each broken generator. The $U[\Pi]$ transforms under \mathcal{G} as

$$U[\Pi] \rightarrow g \cdot U[\Pi] \cdot h^{-1}(g), \quad (5.5)$$

where $h(g)$ is the group element of \mathcal{H} . As CCWZ fields are non-linear, the group \mathcal{H} is said to be non-linearly realised. If we have two fields that transform as

$$\Psi \rightarrow g\Psi, \quad (5.6)$$

$$\psi \rightarrow h(g)\psi, \quad (5.7)$$

we can write an invariant

$$\bar{\Psi}U\psi \rightarrow \bar{\Psi}g^\dagger g U h^{-1}(g)h(g)\psi = \bar{\Psi}U\psi. \quad (5.8)$$

Hence, $U[\Pi]$ can then be used together with fields that transform under the unbroken group \mathcal{H} to form invariants under \mathcal{G} .

5.1.3 Minimal Composite Higgs Models

The starting point in writing down the MCHM is the assumption that the strongly coupled gauge theory underlying the composite dynamics has a global $SO(5) \times U(1)_X$ symmetry, which at the confinement scale f is spontaneously broken to $SO(4) \times U(1)_X$. The four Goldstone bosons arising from this symmetry breaking pattern form an $SO(4)$ fourplet in the $SO(5)/SO(4)$ coset which we identify with the Higgs field. The fact that this breaking preserves the custodial symmetry has important consequences for the phenomenological bounds on the model [109]. The SM fields enter as elementary particles. The gauge fields are coupled to the strong sector through the gauging of the $SU(2)_L \times U(1)_Y$ subset of $SO(4) \times U(1)_X$ symmetry, with the hypercharge generator being associated with the diagonal generator of $SU(2)_R$ plus the X generator, i.e. $Y = T_R^3 + X$. The SM fermions are coupled to the strong sector through the partial compositeness mechanism, where operators containing SM quarks are coupled to operators of the strong sector. The SM quark doublet cannot fill a complete $SO(4)$ multiplet without the introduction of additional external states while the states in the strong sector can, thus some of the components of this multiplet will be spurious and lead to explicit breaking of the $SO(5)$ symmetry.

We use the standard CCWZ toolkit to determine the structure of our top-partner effective field theory (EFT) given the $SO(5)/SO(4)$ coset. The applications of this form-

top-partners in **4** and **1** representations of $SO(4)$ can be embedded in $SO(5)$ fiveplets as

$$\psi_4 = \frac{1}{\sqrt{2}} \begin{pmatrix} iB - iX_{5/3} \\ B + X_{5/3} \\ iT + iX_{2/3} \\ -T + X_{2/3} \\ 0 \end{pmatrix}, \quad \psi_1 = \begin{pmatrix} 0 \\ 0 \\ 0 \\ 0 \\ \tilde{T} \end{pmatrix}, \quad (5.12)$$

respectively. Embeddings in a **14** of $SO(5)$ follow similarly. The embedding of the SM quarks ensures that the theory includes the SM $q_L = (b_L, t_L)$ doublet with $Y = 1/6$ hypercharge and a right-handed top quark with $Y = X = 2/3$. In fact the hypercharge of the right-handed top quark fixes the $U(1)_X$ charge assignments of all the fermionic fields described above, and the singlet top-partner has the same SM charges as the SM right-handed top quark. However the quarks from the fourplet form two $SU(2)_L$ doublets, $Q = (T, B)$, has the same SM charge assignment as the SM quark doublet and $(X_{5/3}, X_{2/3})$ is an exotic doublet where the subscript denotes the electromagnetic charge.

SO(5)/SO(4) Models for Top Partners

In this section we review the three versions of MCHM, denoted as $q_L + t_R$ embedding: the **5+5**, **5+1** and **14+1** of $SO(5)$, presented in [37]. In particular, we will be making comparisons between the former two models and our models in next chapter.

The effective Lagrangian consists of three parts: the elementary sector, the composite one and the mixing terms

$$\mathcal{L} = \mathcal{L}_{\text{elem}} + \mathcal{L}_{\text{comp}} + \mathcal{L}_{\text{mix}}, \quad (5.13)$$

where for the elementary sector we have the standard canonical kinetic terms

$$\mathcal{L}_{\text{elem}} = i\bar{q}_L \not{D} q_L + i\bar{t}_R \not{D} t_R. \quad (5.14)$$

Here \not{D} denotes the covariant derivative. The composite sector Lagrangian is given by

$$\begin{aligned} \mathcal{L}_{\text{comp}} = & i\bar{\psi}_4 \not{D} \psi_4 + i\bar{\psi}_1 \not{D} \psi_1 - m_4 \bar{\psi}_4 \psi_4 - m_1 \bar{\psi}_1 \psi_1 \\ & - (ic_L \bar{\psi}_{4L} \gamma^\mu d_\mu \psi_{1L} + ic_R \bar{\psi}_{4R} \gamma^\mu d_\mu \psi_{1R} + \text{h.c.}) \\ & - (ic_t \bar{\psi}_{4R} \gamma^\mu d_\mu t_R + \text{h.c.}), \end{aligned} \quad (5.15)$$

where c_L, c_R, c_t are the coefficients in front of the d -terms. The $c_t \neq 0$ only for models with

fully-composite t_R , i.e. we assume the right-handed top quark to be a chiral bound state of the strong sector. These couplings are phenomenologically preferred to be non-zero as they can suppress certain oblique corrections, which we will introduce of the following sections. Finally, the mixing terms can be written as

$$\mathcal{L}_{\text{mix}}^{\mathbf{5}+\mathbf{5}} = y_{L4} f \bar{q}_L^{\mathbf{5}} U \psi_4 + y_{L1} f \bar{q}_L^{\mathbf{5}} U \psi_1 + y_{R4} f \bar{t}_R^{\mathbf{5}} U \psi_4 + y_{R1} f \bar{t}_R^{\mathbf{5}} U \psi_1 + \text{h.c.}, \quad (5.16)$$

$$\mathcal{L}_{\text{mix}}^{\mathbf{5}+\mathbf{1}} = y_t f \bar{q}_L^{\mathbf{5}} U t_R^{\mathbf{1}} + y_{L4} f \bar{q}_L^{\mathbf{5}} U \psi_4 + y_{L1} f \bar{q}_L^{\mathbf{5}} U \psi_1 + \text{h.c.}, \quad (5.17)$$

$$\mathcal{L}_{\text{mix}}^{\mathbf{14}+\mathbf{1}} = \frac{y_{Lt}}{2} f (U^\top \bar{q}_L^{\mathbf{14}} U)_{55} t_R + y_{L4} f (U^\top \bar{q}_L^{\mathbf{14}} U)_{i5} \psi_4^i + \frac{y_{L1}}{2} f (U^\top \bar{q}_L^{\mathbf{14}} U)_{55} \psi_1^5 + \text{h.c.}, \quad (5.18)$$

here y 's are the elementary-composite mixings and $i = 1..4$. As $\mathbf{14}$ can be decomposed into $\mathbf{9} \oplus \mathbf{4} \oplus \mathbf{1}$ under $SO(4)$, similar composite and mixing terms can be derived for the nineplet as well, however these will not be discussed any further in this thesis. The $\mathbf{5}+\mathbf{1}$ and $\mathbf{14}+\mathbf{1}$ cases have a fully-composite top. This means that the top mass is generated directly via q_L - t_R coupling as opposed to indirectly through the elementary-composite couplings like in the $\mathbf{5}+\mathbf{5}$ case. In the next section we examine in more detail simplified versions of the two models with fully-composite top.

Simplified Models

In this section we employ simplified models, as outlined in [104], which serve to capture the features of light top-partner states relevant for phenomenological purposes. These models are not complete realisations and there is not enough structure to compute a finite Higgs potential or determine the level of fine-tuning present in it. Due to this we will assume that the Higgs mass takes its observed value and that the fine-tuning in the Higgs potential is smaller for smaller top-partner masses. We will however be able to calculate the top quark mass from the mixing between the SM top quark and top-partners and this will serve as a constraint on the parameters of the Lagrangian.

Composite Higgs models predict many new composite resonances of differing spin with masses near the compositeness scale, which we define as m_* . If m_* is sufficiently large one can write down an effective field theory where states above that mass scale have been integrated out. However, in order to obtain a natural EWSB scenario we know that light top-partners are required, therefore it would be natural to suspect that the lightest top-partners have masses which lay below the scale m_* and cannot be integrated out. The approach taken in [104] and in other simplified models, including those used by the ATLAS and CMS collaborations, assumes that only one top-partner lays below

the scale m_* . Allowing more than one light top-partner could drastically change the collider phenomenology as the possibility of additional cascade decays opens up and the relationship between the top-partner masses, couplings, and f changes.

The effective field theory for the models we use here are constructed using the same power counting rules as in [104] which in turn follows the ‘SILH’ approach [103]. As in [104], we will study top-partners in either the $\mathbf{1}_{2/3}$ or $\mathbf{4}_{2/3}$ representations of $SO(4) \times U(1)_X$, while the SM doublet quarks will be embedded in either a $\mathbf{5}_{2/3}$ or $\mathbf{14}_{2/3}$ of $SO(5) \times U(1)_X$. The right-handed top quark will always be defined as a $\mathbf{1}_{2/3}$ of $SO(4) \times U(1)_X$, since it is being treated as a composite chiral state. Given the choices of top-partner states and SM quark embeddings we see that there are four top-partner models to study: $\mathbf{M4}_5$, $\mathbf{M4}_{14}$, $\mathbf{M1}_5$, and $\mathbf{M1}_{14}$.

$\mathbf{M4}_5$

With a light top-partner transforming as a $\mathbf{4}_{2/3}$ of $SO(4)$ and the SM left-handed top-bottom doublet embedded in a $\mathbf{5}$ of $SO(5)$ the relevant effective action for the SM plus the top-partner, after the states heavier than m_* have been integrated out, is

$$\begin{aligned} \mathcal{L}_{\mathbf{M4}_5} = & i\bar{q}_L \not{D} q_L + i\bar{t}_R \not{D} t_R + i\bar{\psi}_4 \not{D} \psi_4 - m_\psi \bar{\psi}_4 \psi_4 + ic_1 \bar{\psi}_4 d_\mu \gamma^\mu t_R \\ & + yf \bar{q}_L^5 U \psi_{4R} + yfc_2 \bar{q}_L^5 U t_R^1 + \text{h.c.}, \end{aligned} \quad (5.19)$$

where the $SO(5)$ embedding of the top-partner states is assumed. The y in Eq.(5.19) is the coupling that mixes the elementary and strong sectors, and $c_{1,2}$ are expected to be $\mathcal{O}(1)$ coefficients arising from integrating out the heavier states. Notice that the coupling proportional to c_1 does not carry a y dependence since t_R is treated as a composite state. Fixing to unitary gauge and expanding the Higgs field around its vacuum expectation value the following mass matrix is found for the top and top-partners

$$\begin{pmatrix} \bar{t}_L \\ \bar{T}_L \\ \bar{X}_{2/3,L} \end{pmatrix}^\top \begin{pmatrix} -\frac{yf c_2}{\sqrt{2}} s_\epsilon & \frac{y}{2} f(1 + c_\epsilon) & \frac{y}{2} f(1 - c_\epsilon) \\ 0 & -m_\psi & 0 \\ 0 & 0 & -m_\psi \end{pmatrix} \begin{pmatrix} t_R \\ T_R \\ X_{2/3,R} \end{pmatrix}. \quad (5.20)$$

An orthogonal rotation of the T and $X_{2/3}$ states reduces the above mass matrix to a mixing between just one linear combination of the top-partners, and leaves the kinetic and vector-like mass terms invariant. If we had not performed this rotation now then it would simply be part of the mass matrix diagonalization required later. This transformation can be

written as

$$\begin{pmatrix} t \\ T \\ X_{2/3} \end{pmatrix} \rightarrow \frac{1}{N} \begin{pmatrix} N & 0 & 0 \\ 0 & 1 + c_\epsilon & 1 - c_\epsilon \\ 0 & -1 + c_\epsilon & 1 + c_\epsilon \end{pmatrix} \begin{pmatrix} t \\ T \\ X_{2/3} \end{pmatrix}, \quad N = \sqrt{2 + 2c_\epsilon^2}, \quad (5.21)$$

and the resultant mass matrix is

$$\begin{pmatrix} \bar{t}_L \\ \bar{T}_L \end{pmatrix}^\top \begin{pmatrix} -\frac{yf c_2}{\sqrt{2}} s_\epsilon & \frac{y}{2} f \sqrt{3 + c_{2\epsilon}} \\ 0 & -m_\psi \end{pmatrix} \begin{pmatrix} t_R \\ T_R \end{pmatrix}, \quad (5.22)$$

with the $X_{2/3}$ state now being decoupled from the top quark and the Higgs. Upon diagonalising this mass matrix the mass of the T top-partner gets shifted away from the vector-like mass, however the masses of both the $X_{2/3}$ and $X_{5/3}$ state remain degenerate at m_Ψ .

M4₁₄

The effective action for a light top-partner transforming as a $\mathbf{4}_{2/3}$ of $SO(4)$ and the SM left-handed top-bottom doublet embedded in a $\mathbf{14}$ of $SO(5)$ is obtained as

$$\begin{aligned} \mathcal{L}_{\mathbf{M4}_{14}} &= i\bar{q}_L \not{D} q_L + i\bar{t}_R \not{D} t_R + i\bar{\psi}_4 \not{D} \psi_4 - m_\psi \bar{\psi}_4 \psi_4 + ic_1 \bar{\psi}_4 d_\mu \gamma^\mu t_R \\ &+ yf \text{Tr} \left(\bar{q}_L^{\mathbf{14}} U \psi'_{4R} U^\top \right) + yf \text{Tr} \left(\bar{q}_L^{\mathbf{14}} U t_R^{\mathbf{1}'} U^\top \right), \end{aligned} \quad (5.23)$$

where ψ'_4 is defined as the direct product of the $SO(5)$ breaking VEV, $\Sigma_0 = (0, 0, 0, 0, 1)$, and ψ_4 . In this way the invariant in the Lagrangian can be written as

$$(\bar{q}_L^{\mathbf{14}})^{IJ} U_{IM} U_{JN} \Sigma_0^N (\psi_4)^M, \quad (5.24)$$

in accordance with [104]. We also use an analogous definition of $t_R^{\mathbf{1}'}$. Because the top-partners transform in a $\mathbf{4}$ of $SO(4)$ the particle content here is the same as in the $\mathbf{M4}_5$ model, however the mass matrix differs slightly due to the embedding of the SM doublet,

$$\begin{pmatrix} \bar{t}_L \\ \bar{T}_L \\ \bar{X}_{2/3L} \end{pmatrix}^\top \begin{pmatrix} -\frac{yf c_2}{2\sqrt{2}} s_{2\epsilon} & \frac{yf}{2} (c_\epsilon + c_{2\epsilon}) & \frac{yf}{2} (c_\epsilon - c_{2\epsilon}) \\ 0 & -m_\psi & 0 \\ 0 & 0 & -m_\psi \end{pmatrix} \begin{pmatrix} t_R \\ T_R \\ X_{2/3R} \end{pmatrix}. \quad (5.25)$$

Analogously to the previous model we can also rotate the top-partner states such that only one of the top-partners couples to the SM doublet and the Higgs, with the transformation being

$$\begin{pmatrix} t \\ T \\ X_{2/3} \end{pmatrix} \rightarrow \frac{1}{N} \begin{pmatrix} N & 0 & 0 \\ 0 & c_\epsilon + c_{2\epsilon} & c_\epsilon - c_{2\epsilon} \\ 0 & -c_\epsilon + c_{2\epsilon} & c_\epsilon + c_{2\epsilon} \end{pmatrix} \begin{pmatrix} t \\ T \\ X_{2/3} \end{pmatrix}, \quad N = \sqrt{2 + c_{2\epsilon} + c_{4\epsilon}}, \quad (5.26)$$

leaving the resultant mass matrix as

$$\begin{pmatrix} \bar{t}_L \\ \bar{T}_L \end{pmatrix}^\top \begin{pmatrix} -\frac{yfc_2}{2\sqrt{2}}s_{2\epsilon} & \frac{yf}{2}\sqrt{2 + c_{2\epsilon} + c_{4\epsilon}} \\ 0 & -m_\psi \end{pmatrix} \begin{pmatrix} t_R \\ T_R \end{pmatrix}. \quad (5.27)$$

The $X_{2/3}$ state has decoupled in the same way as in the **M4₅** model and has a mass degenerate with the exotic $X_{5/3}$ top-partner.

M1₅

For a light top-partner transforming as a $\mathbf{1}_{2/3}$ of $SO(4)$ and the SM left-handed top-bottom doublet embedded in a $\mathbf{5}$ of $SO(5)$ the relevant effective action is

$$\begin{aligned} \mathcal{L}_{\mathbf{M1}_5} = & i\bar{q}_L \not{D} q_L + i\bar{t}_R \not{D} t_R + i\bar{\psi}_1 \not{D} \psi_1 - m_\psi \bar{\psi}_1 \psi_1 \\ & + yf \bar{q}_L^{\mathbf{5}} U \psi_{1R} + yf c_2 \bar{q}_L^{\mathbf{5}} U t_R^{\mathbf{1}} + \text{h.c.} \end{aligned} \quad (5.28)$$

where the term proportional to c_1 is now absent. With singlet top-partners we only have one top-partner state with charges equal to that of the right-handed top quark. The mass matrix in this case is simpler than with fourplet top-partners, and is written as

$$\begin{pmatrix} \bar{t}_L \\ \bar{T}_L \end{pmatrix}^\top \begin{pmatrix} -\frac{yfc_2}{\sqrt{2}}s_\epsilon & \frac{yf}{\sqrt{2}}s_\epsilon \\ 0 & -m_\psi \end{pmatrix} \begin{pmatrix} t_R \\ T_R \end{pmatrix}. \quad (5.29)$$

M1₁₄

For a light top-partner transforming as a $\mathbf{1}_{2/3}$ of $SO(4)$ and the SM left-handed top-bottom doublet embedded in a $\mathbf{14}$ of $SO(5)$ the relevant effective action is

$$\begin{aligned} \mathcal{L}_{\mathbf{M1}_{14}} = & i\bar{q}_L \not{D} q_L + i\bar{t}_R \not{D} t_R + i\bar{\psi}_1 \not{D} \psi_1 - m_\psi \bar{\psi}_1 \psi_1 \\ & + yf \text{Tr} \left(\bar{q}_L^{\mathbf{14}} U \psi'_{1R} U^\top \right) + yf c_2 \text{Tr} \left(\bar{q}_L^{\mathbf{14}} U t_R^{\mathbf{1}'} U^\top \right) + \text{h.c.} \end{aligned} \quad (5.30)$$

where the singlet composite states are embedded in **14** representations of $SO(5)$ when coupled to the SM doublet. The mass matrix is similar to the $\mathbf{M1}_5$ case,

$$\begin{pmatrix} \bar{t}_L \\ \bar{T}_L \end{pmatrix}^\top \begin{pmatrix} -\frac{yf c_2}{2\sqrt{2}} s_{2\epsilon} & \frac{yf}{2\sqrt{2}} s_{2\epsilon} \\ 0 & -m_{\psi} \end{pmatrix} \begin{pmatrix} t_R \\ T_R \end{pmatrix}. \quad (5.31)$$

Additional light top-partner multiplets

Introducing additional light top-partner multiplets can be done in a straightforward way. To keep the models simple we will assume that all top-partner states couple to the SM with the same strength, with their masses determining their influence on the top mass and Yukawa coupling. We label our top-partner multiplets as $\psi_{4,i}$ and $\psi_{1,i}$, and their masses as M_{Ψ_i} , whereas the components of these multiplets are denoted by T^i , B^i , $X_{2/3}^i$, $X_{5/3}^i$.

Introducing additional multiplets in the $\mathbf{M1}_5$ and $\mathbf{M1}_{14}$ is straightforward since we are dealing with singlet top-partners. For example the mass matrices for these models with one additional singlet each can be written as

$$\begin{pmatrix} \bar{t}_L \\ \bar{T}_L^1 \\ \bar{T}_L^2 \end{pmatrix}^\top \begin{pmatrix} -\frac{yf c_2}{\sqrt{2}} s_\epsilon & \frac{yf}{\sqrt{2}} s_\epsilon & \frac{yf}{\sqrt{2}} s_\epsilon \\ 0 & -m_{\psi_1} & 0 \\ 0 & 0 & -m_{\psi_2} \end{pmatrix} \begin{pmatrix} t_R \\ T_R^1 \\ T_R^2 \end{pmatrix} \quad \text{for } \mathbf{M1}_5 \text{ and} \\ \begin{pmatrix} \bar{t}_L \\ \bar{T}_L^1 \\ \bar{T}_L^2 \end{pmatrix}^\top \begin{pmatrix} -\frac{yf c_2}{2\sqrt{2}} s_{2\epsilon} & \frac{yf}{2\sqrt{2}} s_{2\epsilon} & \frac{yf}{2\sqrt{2}} s_{2\epsilon} \\ 0 & -m_{\psi_1} & 0 \\ 0 & 0 & -m_{\psi_2} \end{pmatrix} \begin{pmatrix} t_R \\ T_R^1 \\ T_R^2 \end{pmatrix} \quad \text{for } \mathbf{M1}_{14}. \quad (5.32)$$

When the top partners are in fourplets all we need to do is to rotate each $(T^i, X_{2/3}^i)$ pair separately such that only one linear combination of quarks from each multiplet couples to the top quark and the Higgs. For one additional top-partner in the fourplet models this can be done using the orthogonal transformations

$$\begin{pmatrix} t \\ T^1 \\ X_{2/3}^1 \\ T^2 \\ X_{2/3}^2 \end{pmatrix} \rightarrow \frac{1}{N} \begin{pmatrix} N & 0 & 0 & 0 & 0 \\ 0 & 1 + c_\epsilon & 1 - c_\epsilon & 0 & 0 \\ 0 & -1 + c_\epsilon & 1 + c_\epsilon & 0 & 0 \\ 0 & 0 & 0 & 1 + c_\epsilon & 1 - c_\epsilon \\ 0 & 0 & 0 & -1 + c_\epsilon & 1 + c_\epsilon \end{pmatrix} \begin{pmatrix} t \\ T^1 \\ X_{2/3}^1 \\ T^2 \\ X_{2/3}^2 \end{pmatrix} \quad (5.33)$$

for $\mathbf{M4}_5$ with $N = \sqrt{2 + 2c_\epsilon^2}$, and

$$\begin{pmatrix} t \\ T^1 \\ X_{2/3}^1 \\ T^2 \\ X_{2/3}^2 \end{pmatrix} \rightarrow \frac{1}{N} \begin{pmatrix} N & 0 & 0 & 0 & 0 \\ 0 & c_\epsilon + c_{2\epsilon} & c_\epsilon - c_{2\epsilon} & 0 & 0 \\ 0 & -c_\epsilon + c_{2\epsilon} & c_\epsilon + c_{2\epsilon} & 0 & 0 \\ 0 & 0 & 0 & c_\epsilon + c_{2\epsilon} & c_\epsilon - c_{2\epsilon} \\ 0 & 0 & 0 & -c_\epsilon + c_{2\epsilon} & c_\epsilon + c_{2\epsilon} \end{pmatrix} \begin{pmatrix} t \\ T^1 \\ X_{2/3}^1 \\ T^2 \\ X_{2/3}^2 \end{pmatrix} \quad (5.34)$$

for $\mathbf{M4}_{14}$ with $N = \sqrt{2 + c_{2\epsilon} + c_{4\epsilon}}$. Adding more top-partners requires analogous rotations of the form above. The important point is that we can completely decouple the $X_{2/3}$ states from the top quark and the Higgs irrespective of how many top-partners we have. The mass matrices for these models with one additional light top-partner can then be written as

$$\begin{pmatrix} \bar{t}_L \\ \bar{T}_L^1 \\ \bar{T}_L^2 \end{pmatrix}^T \begin{pmatrix} -\frac{yf c_2}{\sqrt{2}} s_\epsilon & \frac{yf}{2} \sqrt{3 + c_{2\epsilon}} & \frac{yf}{2} \sqrt{3 + c_{2\epsilon}} \\ 0 & -m_{\psi_1} & 0 \\ 0 & 0 & -m_{\psi_2} \end{pmatrix} \begin{pmatrix} t_R \\ T_R^1 \\ T_R^2 \end{pmatrix} \quad \text{for } \mathbf{M4}_5 \text{ and} \\ \begin{pmatrix} \bar{t}_L \\ \bar{T}_L^1 \\ \bar{T}_L^2 \end{pmatrix}^T \begin{pmatrix} -\frac{yf c_2}{2\sqrt{2}} s_{2\epsilon} & \frac{yf}{2} \sqrt{2 + c_{2\epsilon} + c_{4\epsilon}} & \frac{yf}{2} \sqrt{2 + c_{2\epsilon} + c_{4\epsilon}} \\ 0 & -m_{\psi_1} & 0 \\ 0 & 0 & -m_{\psi_2} \end{pmatrix} \begin{pmatrix} t_R \\ T_R^1 \\ T_R^2 \end{pmatrix} \quad \text{for } \mathbf{M4}_{14}. \quad (5.35)$$

One can see from this construction that adding an arbitrary number of light top-partners can be implemented in a straightforward way. There is also no need for the light top-partners to be in the same $SO(4)$ representation as each other, one could just as well have a light singlet and fourplet in the spectrum and there would be no extra complication.

5.1.4 Mass spectrum

The purpose of this section is to study how the masses vary with the input parameters for scenarios with both one and two light top-partner multiplets in each of the simplified models discussed in the previous section.

The first thing to discuss is the effect of the operators in Eq.(5.19) and Eq.(5.23) which are preceded by the c_1 coefficients. After writing the d_μ term in unitary gauge we have

$$d_\mu^i = \delta^{i4} \sqrt{2} \frac{\partial_\mu \rho}{f} + \dots, \quad (5.36)$$

and thus the top-partners have a derivative coupling with the Higgs boson. Via a field re-definition we can recast this derivative coupling to a CP-odd Yukawa term, which scales as $\text{Im}(c_1)$, plus operators that involve higher powers of the Higgs boson field, or different fermionic fields, and hence are not relevant for single-Higgs production.

The general EFT Lagrangian that contains the interactions between the top quark $t_{L,R}$ and the charge 2/3 top-partners $T_{L,R}$ mixing with it is

$$\begin{aligned} \mathcal{L}_{\text{EFT}} \supset & -m_t \bar{t}t - m_b \bar{b}b - m_T^j \bar{T}_j T_j - \kappa_t \frac{m_t}{v} \bar{t}th - \kappa_b \frac{m_b}{v} \bar{b}bh \\ & + \kappa_T^j \frac{m_T^j}{v} \bar{T}_j T_j h + i\tilde{\kappa}_t \frac{m_t}{v} \bar{t}\gamma_5 th + i\tilde{\kappa}_T^j \frac{m_T^j}{v} \bar{T}_j \gamma_5 T_j h, \end{aligned} \quad (5.37)$$

where the sums over j indicate sums over top-partner multiplets. In this work we will consider at most two multiplets. The mixing of the bottom quark with the composite sector is assumed to be small, therefore we do not include the bottom partners in the EFT. The κ_i 's are defined such that in the SM we have $\kappa_{b,t} = 1$, and $\kappa_T = \tilde{\kappa}_{t,T} = 0$. The CP-odd couplings in the second line of Eq.(5.37) will only exist for the **M4₅** and **M4₁₄** models as they arise from the d -terms, and will be functions of the mixing angles and $\text{Im}(c_1)$.

One light top-partner multiplet

In the case where we have only one light top-partner multiplet the Yukawa couplings in the mass eigenbasis can be written down analytically. In general, the mass-mixing matrix can be written in the form

$$- \begin{pmatrix} \bar{t}_L \\ \bar{T}_L \end{pmatrix}^T \begin{pmatrix} m & \Delta \\ 0 & m_\psi \end{pmatrix} \begin{pmatrix} t_R \\ T_R \end{pmatrix}. \quad (5.38)$$

diagonalization of the matrix is achieved via a double rotation with left-handed and right-handed mixing angles θ_L and θ_R respectively. This gives us the mass eigenstates with top mass m_t and top-partner mass m_T , and consequently a relation between m, Δ, m_ψ and the parameters $m_t, m_T, \theta_L, \theta_R$:

$$\begin{aligned} m &= \frac{\cos \theta_R}{\cos \theta_L} m_t = \frac{\sin \theta_R}{\sin \theta_L} m_T, & m_\psi &= \frac{\sin \theta_L}{\sin \theta_R} m_t = \frac{\cos \theta_L}{\cos \theta_R} m_T, \\ \Delta &= \frac{\sin^2 \theta_L - \sin^2 \theta_R}{\sin \theta_L \sin \theta_R} \tan \theta_L m_t = \frac{\sin^2 \theta_L - \sin^2 \theta_R}{\sin \theta_L \sin \theta_R} \tan \theta_R m_T, \end{aligned} \quad (5.39)$$

where the two mixing angles are related through

$$\tan \theta_L = \frac{m_T}{m_t} \tan \theta_R. \quad (5.40)$$

The Yukawa terms derived in a similar fashion along with a discussion on perturbativity and the relevant limits of these models can be found in [2].

The bottom quark mass is also generated via partial compositeness, although the mixing of the bottom quark with the composite sector is much milder and the right-handed bottom is certainly not composite. Given that the CP-odd terms are also proportional to the mixing with the composite sector, these can also be taken to be absent for the bottom quark.

Two light top-partner multiplets

In the case of two top partners T^1 and T^2 , we take a different approach with respect to the single top-partner case, in that we study the relationship between the fundamental parameters of each model (i.e. the vector-like masses, the couplings and the decay constant f) and the physical top-partner masses. In particular, we take as free parameters $y, f, m_{\psi_1}, m_{\psi_2}$, as well as the CP-odd couplings, with c_2 being used to fix the top quark mass to ~ 173 GeV.

In Figure 5.1 we plot the masses of T^1 or T^2 as a function of the heavier vector-like mass for $m_{\psi_1} = 1200$ GeV, $y = 1$, and $f = 600/1000$ GeV. We also show the mass of a single top partner (labelled T^1 only), corresponding to the same values of y and f , and $m_{\psi} = m_{\psi_1}$. We stress that T^1 is the lighter top partner everywhere. The first thing we notice when looking at Figure 5.1 is that, in the singlet top-partner models, there is almost a degeneracy between the vector-like mass m_{ψ_2} and the mass of the T^2 state. There is also no difference between the $f = 600$ GeV and $f = 1000$ GeV scenarios for the singlet models, this is because in these models the mass matrix is largely insensitive to f , a feature not shared by the fourplet models. In fourplet models instead, this occurs only as one of the vector-like masses is made much larger than the other. Also, when considering fourplet models, we should keep in mind that $m_{\psi_{1,2}}$ are in fact the masses of the $X_{2/3}^{1,2}$ and $X_{5/3}^{1,2}$ states. Therefore, for $m_{\psi_2} \gg m_{\psi_1}$, T^2 has the same mass as $X_{2/3}^2$ and $X_{5/3}^2$. A further discussion on the various relationships between couplings, masses and f in these models is presented in [2].

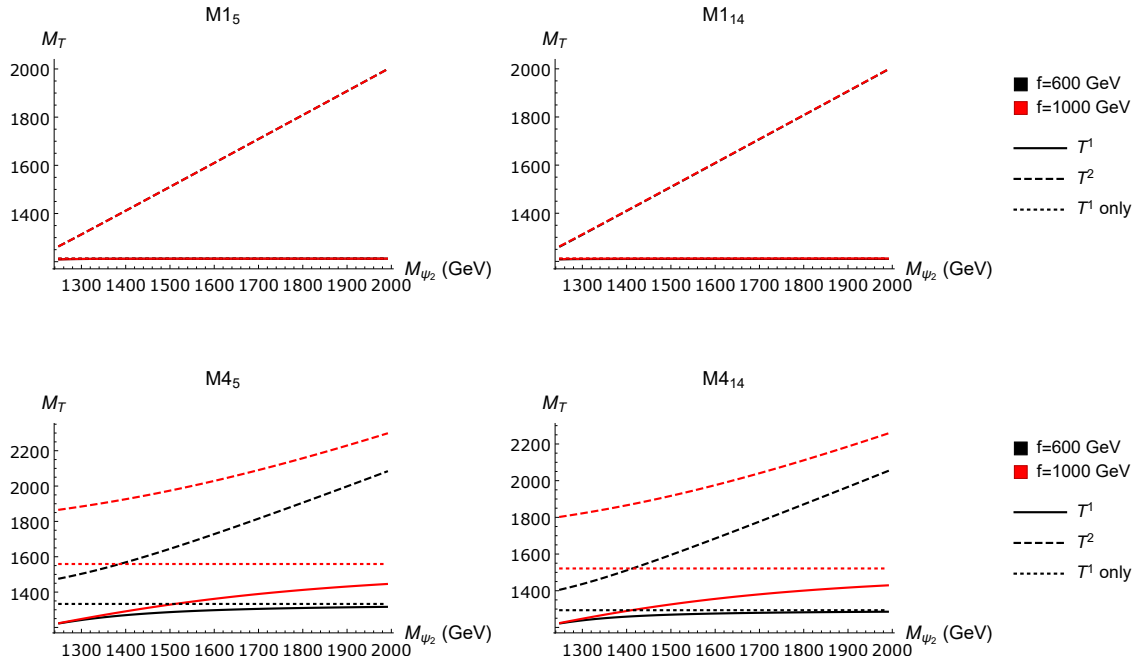


Figure 5.1: The masses of the two light top-partners T^1 or T^2 as functions of the heavier vector-like mass, for $m_{\psi_1} = 1200$ GeV, $y = 1$, and $f = 600/1000$ GeV. The figure is taken from [2].

5.2 PNCB Higgs at Colliders

The effects of top-partner states on single-Higgs production via gluon fusion have been studied in detail, however in this case the pNGB nature of the Higgs boson leads to a cancellation of new physics effects dependent on the top-partner masses in the production cross-section [112–114]. To probe the top-partners in gluon initiated Higgs production the produced Higgs must be allowed to recoil off a gluon, and for this the study of Higgs production in association with a jet is useful. This process has been explored in some detail already [115–117].

This section is organised as follows. In Section 5.2.1 we cover the relevant experimental bounds on the masses of top partners and coloured pNGBs. In Section 5.2.2 we aim to summarise the main results of [2] on the study of Higgs+Jet production. Finally, in Appendix B.1 we give the expressions for the **CP**-odd contribution to Higgs+Jet in decoupling, soft and collinear limits. Section 5.2.2 and Appendix B.1 contain novel results.

5.2.1 Brief Summary of Experimental Bounds

The first experimental constraint to mention is that on the decay constant f , which through the analysis in [118] is constrained to be larger than ~ 600 GeV. These bounds are derived

from Higgs decays to vector bosons and Higgs production. Recent limits on top-partner masses have been obtained through analyses at $\sqrt{s} = 13$ TeV by the ATLAS collaboration [119–132]. The first point to note is that these analyses only consider the presence of one light top-partner state, and thus these bounds are relevant to our lightest state. Including heavier states opens up possibilities for much more intricate signatures involving cascade decays. The lower mass bounds on the T and $X_{2/3}$ partners from the fourplet models are quoted at 1350 GeV, and the lower mass bound on T for singlet models are 1170 GeV. However, the latter assumes that $\text{Br}(T \rightarrow Wb) = 100\%$. These bounds are weakened if one considers sizeable branching ratios into multiple channels. More interesting and intricate signatures arise in twin Higgs models [133–135] which have QCD-like dark sectors with Higgs portal couplings to the SM. Much work has been done in developing these models [136–142] and studying their phenomenology [143–147]. Translating these collider constraints into bounds on the top-partner models presented in the previous sections is beyond the scope of this work, and in our analysis we will use a lower limit of 1200 GeV for the lightest vector-like mass.

Constraints on the $c_{1,1}$ and $c_{1,2}$ parameters have been derived from electron and neutron Electric Dipole Moment (EDM) experiments [148]. These results indicate that with the top-partner masses at the TeV scale, the imaginary values of these parameters are constrained to $\lesssim 0.2$. It is not the goal of the thesis to study the effects of these parameters on the EDMs, therefore we will simply constrain $\text{Re}(c_{1,1}), \text{Re}(c_{1,1}), \text{Im}(c_{1,2}), \text{Im}(c_{1,2}) < 0.2$ in our work. Future electron EDM experiments will introduce much more stringent bounds on these parameters. The remaining parameter space that we wish to study here is summarised by $1.2 \text{ TeV} < m_T < 2.2 \text{ TeV}$, $600 \text{ GeV} < f < 1.2 \text{ TeV}$, and $y < 3$.

In Chapter 6, in addition to the top partners, we will also consider colour-triplet pNGBs with $U(1)_X$ charge of $\pm 1/3$. Because of a non-trivial charge and particle number conservation, these pNGBs can be approximated as heavy stable charged particles. Hence, its constraints mostly come from long-lived R -hadron (stop) searches at the LHC. The current bound is 1.34 TeV [149]. The main difference from the long-lived R -hadron (stop) is minor: there would be a 4-point interaction involving two colour-triplet pNGBs with either hh^\dagger or WW . However, the QCD pair-production via gluons is the dominant channel in the hadron collider experiments such as LHC

5.2.2 Higgs plus One Jet

It is well known that the production cross-section of the Higgs boson via gluon fusion is insensitive to the mass spectrum of top-partners in composite Higgs models [112–114]. This low-energy theorem arises due to the pseudo-Goldstone boson origin of the Higgs field in composite Higgs models. In [114], the effects from new coloured fermions in composite Higgs models to gluon fusion Higgs production, along with other less transparent phenomena from new physics, were studied by means of an effective Lagrangian. These investigations were conducted by analysing the following higher dimensional operators constructed from SM fields:

$$\mathcal{O}_H = \partial^\mu(H^\dagger H)\partial_\mu(H^\dagger H), \quad \mathcal{O}_y = H^\dagger H\bar{\psi}_L H\psi_R, \quad \mathcal{O}_g = H^\dagger H G_{\mu\nu}^a G_a^{\mu\nu}. \quad (5.41)$$

Through an explicit calculation, the authors of [114] showed that the gluon fusion production rate of the composite Higgs depended only on the decay constant f of the model, not on the top-partners mass spectrum.

In contrast to the case of single-Higgs production from gluon fusion, Higgs production with an additional jet $pp \rightarrow h + j$ has been shown to have some dependence on the mass of a top partner in composite Higgs models. In [115] it was demonstrated how the low-energy theorem rendering the cross section insensitive to the masses of fermions in the loop no longer holds when the transverse momentum of one of the final states is large. For Higgs plus one extra parton (quark or gluons), this happens at high p_T , i.e. the transverse momentum of either the Higgs or the jet. Let us consider one of the partonic subprocesses contributing to $pp \rightarrow h + j$, namely $gg \rightarrow h + g$. The $gg \rightarrow h + g$ matrix element $\mathcal{M}_{\lambda_1\lambda_2\lambda_3}$, where $\lambda_i = \pm$ denotes the helicities of the 3 gluons, for one fermion species in the loop with mass m_f and Yukawa coupling $\frac{m_f}{v}\kappa_f$ will have a different behaviour according to the size of p_T . For instance, for the amplitude \mathcal{M}_{+++} , in the limit $p_T \gg m_f, m_H$ we have [115]

$$\mathcal{M}_{+++} \propto \frac{m_f^2 \kappa_f}{p_T} \left(A_0 + A_1 \ln \left(\frac{p_T^2}{m_f^2} \right) + A_2 \ln^2 \left(\frac{p_T^2}{m_f^2} \right) \right), \quad (5.42)$$

where A_0, A_1, A_2 are combinations of constants and logarithms that are independent of m_f . On the other hand, for low p_T we have [115]

$$\mathcal{M}_{+++} \propto \kappa_f p_T. \quad (5.43)$$

where there is no dependence on the fermion mass, and the result is proportional to what

would be obtained for $gg \rightarrow h$. If we now consider a top quark, with mass m_t and Yukawa coupling $\frac{m_t}{v}\kappa_t$, and a top partner with mass m_T and Yukawa coupling $\frac{m_T}{v}\kappa_T$, the dependencies on the top partner mass will be present if we increase p_T further to the region $p_T \gg m_t, m_H, m_T$, where both the top quark and top partner contributions will approximately be in the high- p_T limit form given in Eq.(5.42). This behaviour of the matrix element was also confirmed numerically [115].

Definition of the p_T Spectrum Observable

The difference between the differential cross section $d\sigma/dp_T$ of a SM Higgs and that of a composite Higgs is certainly a very useful probe of the compositeness of the Higgs. This was the observable considered in [115]. Here we employ a net Higgs plus jet efficiency, i.e. the fraction of events for which the Higgs (or at least one jet) has a transverse momentum larger than p_T^{cut}

$$\epsilon(p_T > p_T^{\text{cut}}) = \frac{1}{\sigma} \int_{p_T^{\text{cut}}} dp_T \frac{d\sigma}{dp_T}. \quad (5.44)$$

In this case, an overall normalisation of the cross section cancels between numerator and denominator in Eq.(5.44), so that this quantity is most sensitive to the mass of top-partner and the corresponding Yukawa couplings. We now assess the deviation of the one-jet efficiency from its SM value using the variable

$$\delta(p_T^{\text{cut}}) \equiv \frac{\epsilon_{\text{BSM}}(p_T > p_T^{\text{cut}})}{\epsilon_{\text{SM}}(p_T > p_T^{\text{cut}})} - 1. \quad (5.45)$$

In the above definition, ϵ_{SM} denotes the SM efficiency, while ϵ_{BSM} is the efficiency of any of the composite Higgs models studied in this work.

Results

The full presentation and discussion of the results of this study can be found in [2]. In particular this work highlights how at high transverse momentum the Higgs+Jet process could be used to study the top-partner spectrum in composite Higgs models, and how the results could provide insight as to the embedding of these states in the global symmetries of the strong sector. Here we provide a short summary.

With one top-partner we see a variety of deviations from the SM, reflecting the different ways in which the Yukawa couplings are modified according to the fundamental parameter of each model. In Figures 5.2 and 5.3, we show contour plots of $\delta(p_T^{\text{cut}})$ for $p_T^{\text{cut}} = 200$ GeV and $\sin^2\theta_L = 0.1$ for singlet and fourplet models respectively. The $\kappa_t \leq 0.8$ here is

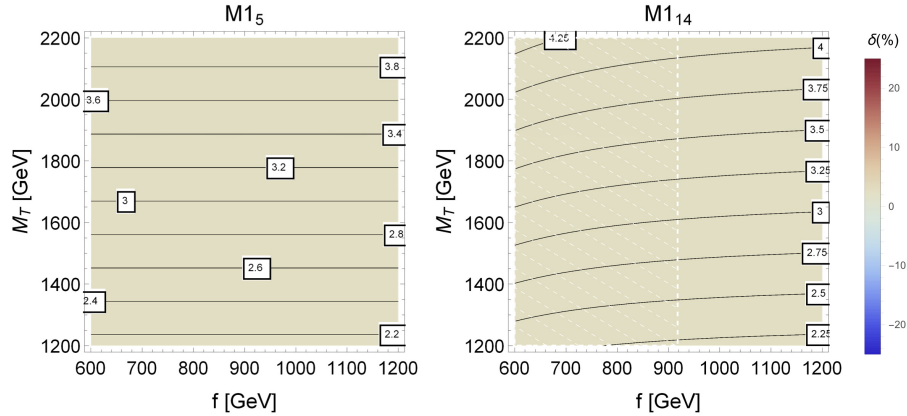


Figure 5.2: The contour plots of $\delta(p_T^{\text{cut}})$ with $\sin^2 \theta_L = 0.1$ and $p_T^{\text{cut}} = 200$ GeV for each of the singlet models with one top partner multiplet. The solid lines correspond to constant values of the coupling y . The region marked by dashed white lines indicates when $\kappa_t \leq 0.8$. The figure is taken from [2].

excluded by the recent observation of Higgs production in association with a top-antitop pair by the ATLAS experiment [150] at 2σ . First, we observe that the deviation from the SM is not large. This is due to the fact that the integrated transverse momentum spectrum is dominated by the lowest values of p_T . There, the top still behaves as a heavy particle in loops, therefore the cancellation between top and top-partner contributions is still at work. Nevertheless, there is a very different behaviour for singlet (Fig. 5.2) and fourplet (Fig. 5.3) models. For singlet models, the deviation from the SM mildly increases as M_T is increased. For fourplet models the deviations increases with increasing f . This behaviour arises since negative contributions from the Yukawa coupling due to $\sin^2 \theta_L$ and $\cos^2 \theta_L$ become smaller as f is increased. Note that, for **M4**₁₄, these negative contributions dominate for small values of f , and one gets negative interference between the contribution of the top and the top partner.

We now keep the values $\sin^2 \theta_{L,R} = 0.1$ and increase p_T^{cut} to 600 GeV. The corresponding contour plots are shown in Figures 5.4 and 5.5, again as a function of M_T and f . The p_T values probed here are high enough to break the cancellation between the contribution of a top and a top-partner in loops. This is why, for singlet models, we observe huge deviations from the SM. For fourplet models, we note, again, that the deviation decreases with decreasing f . This is again due to the fact that for smaller f , the negative contribution to the Yukawa couplings due to $\sin^2 \theta_L$ and $\cos^2 \theta_L$ becomes more important, and vanishes for $f \rightarrow \infty$. The most striking feature occurs for **M4**₁₄ at small values of f , where one sees a large negative interference between top and top-partner contributions.

In addition, we find that for singlet models, even a mild mixing of right-handed fermions

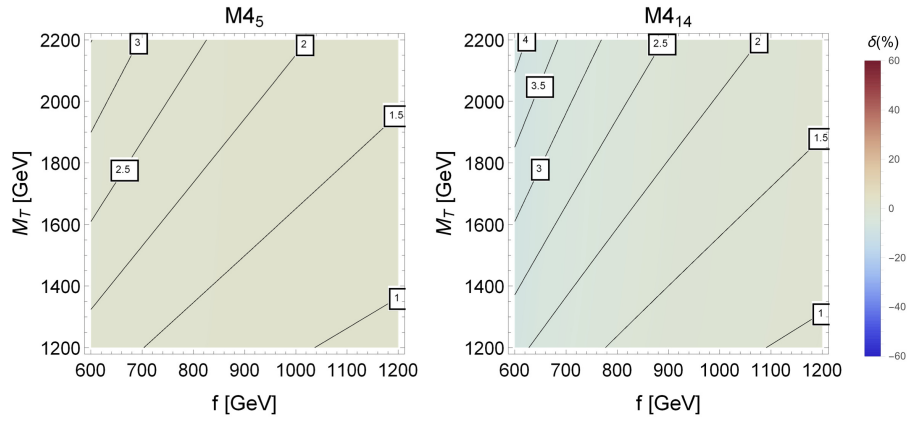


Figure 5.3: The contour plots of $\delta(p_T^{\text{cut}})$ with $\sin^2 \theta_R = 0.1$ and $p_T^{\text{cut}} = 200$ GeV for each of the fourplet models with one top partner multiplet. The solid lines correspond to constant values of the coupling y . None of the parameter space on these plots result in $\kappa_t \leq 0.8$. The figure is taken from [2].

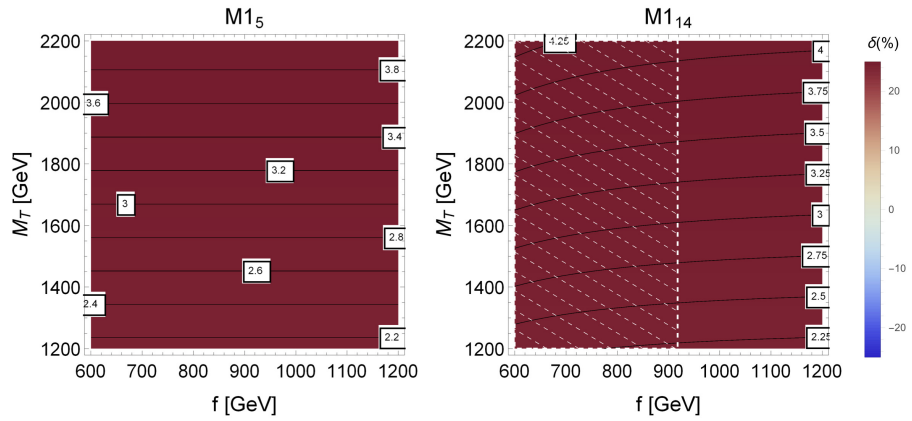


Figure 5.4: The contour plots of $\delta(p_T^{\text{cut}})$ with $\sin^2 \theta_L = 0.1$ and $p_T^{\text{cut}} = 600$ GeV for each of the singlet models with one top partner multiplet. The corresponding values of y are indicated by the solid lines. The region marked by dashed white lines indicates when $\kappa_t \leq 0.8$. The figure is taken from [2].

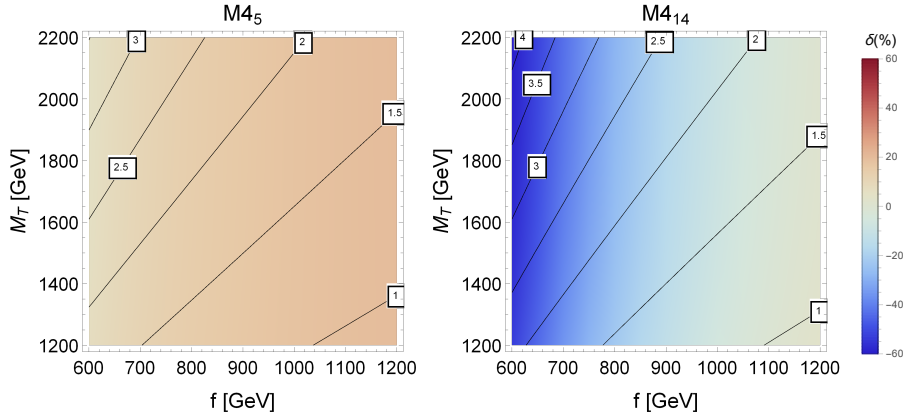


Figure 5.5: The contour plots of $\delta(p_T^{\text{cut}})$ with $\sin^2 \theta_R = 0.1$ and $p_T^{\text{cut}} = 600$ GeV for each of the fourplet models with one top partner multiplet. The corresponding values of y are indicated by the solid lines. None of the parameter space on these plots result in $\kappa_t \leq 0.8$. The figure is taken from [2].

leads to huge deviations from the SM, as can be seen in Figure 5.6. Therefore, the parameters of these models will be the easiest to access through Higgs production plus one jet. For fourplet models, the most promising situation occurs for large mixings which prevent the negative contributions from taking over. Hence, using high values of $p_T^{\text{cut}} = 600$ GeV, and $\sin^2 \theta_R = 0.4$, one expects to see sizeable deviations from the SM, as shown in Figure 5.7.

With an additional light top-partner the deviations from the SM can be much larger than with just a single top-partner, and the best way to probe the parameter space of the model using the Higgs+Jet signal would be through a shape analysis of the p_T distribution of the Higgs, or better the corresponding efficiency. In one of the scenarios, we investigate the effect of increasing the vector-like mass M_{Ψ_2} , from the case in which it is quasi degenerate with M_{Ψ_1} to the case in which the second top partner decouples, i.e. $M_{\Psi_2} \gg M_{\Psi_1}$. The compositeness scale is set to $f = 800$ GeV, an intermediate value with respect to the two shown in Figure 5.1. The relative deviation from the SM $\delta(p_T^{\text{cut}})$ is plotted in Fig. 5.8, as a function of p_T^{cut} , for selected values of M_{Ψ_2} (the solid curves), and for the case with one top partner (the dashed curve), with the same value of y and $M_{\Psi} = M_{\Psi_1}$. This benchmark scenario does not present any unexpected features. For singlet models we have an enhancement with respect to the SM, and for fourplet models we have a depletion due to negative interference. We notice that there is an appreciable dependence on the vector-like quark mass M_{Ψ_2} . Also, when M_{Ψ_2} gets bigger, the heavier top-partner decouples, and the deviation tends to that with a single top partner. Again, this is expected from Fig. 5.1, where we see that the masses of the lighter top-partner

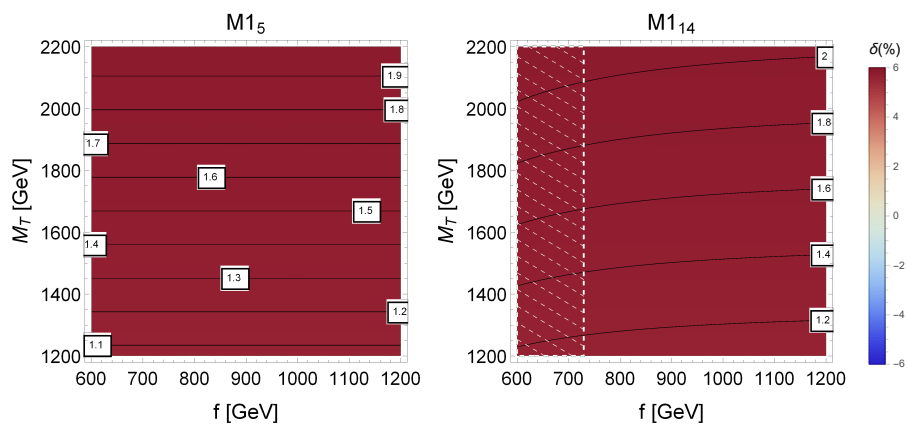


Figure 5.6: The contour plots of $\delta(p_T^{\text{cut}})$ with $\sin^2 \theta_L = 0.025$ and $p_T^{\text{cut}} = 600$ GeV for the singlet models with one top partner multiplet. The corresponding values of y are indicated by the solid lines. The region marked by dashed white lines indicates when $\kappa_t \leq 0.8$. The figure is taken from [2].

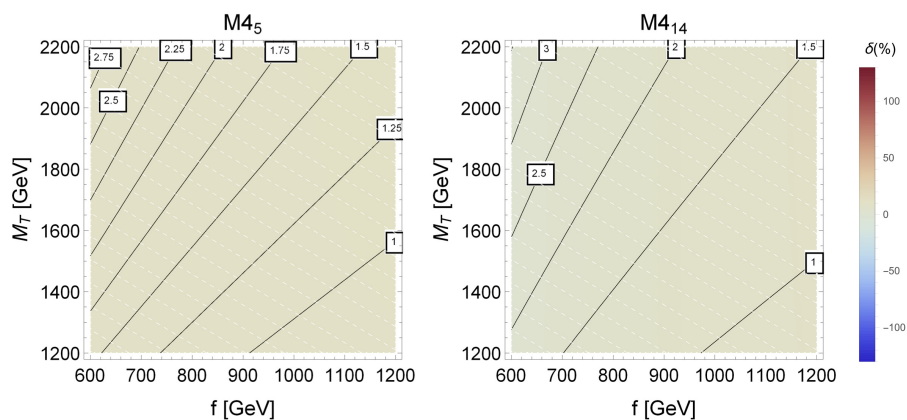


Figure 5.7: The contour plots for δ with $\sin^2 \theta_R = 0.4$ and $p_T^{\text{cut}} = 600$ GeV for each of the fourplet models with one top partner multiplet. The corresponding values of y are indicated by the solid lines. As indicated by the dashed white lines, all points on these plots result in $\kappa_t \leq 0.8$. The figure is taken from [2].

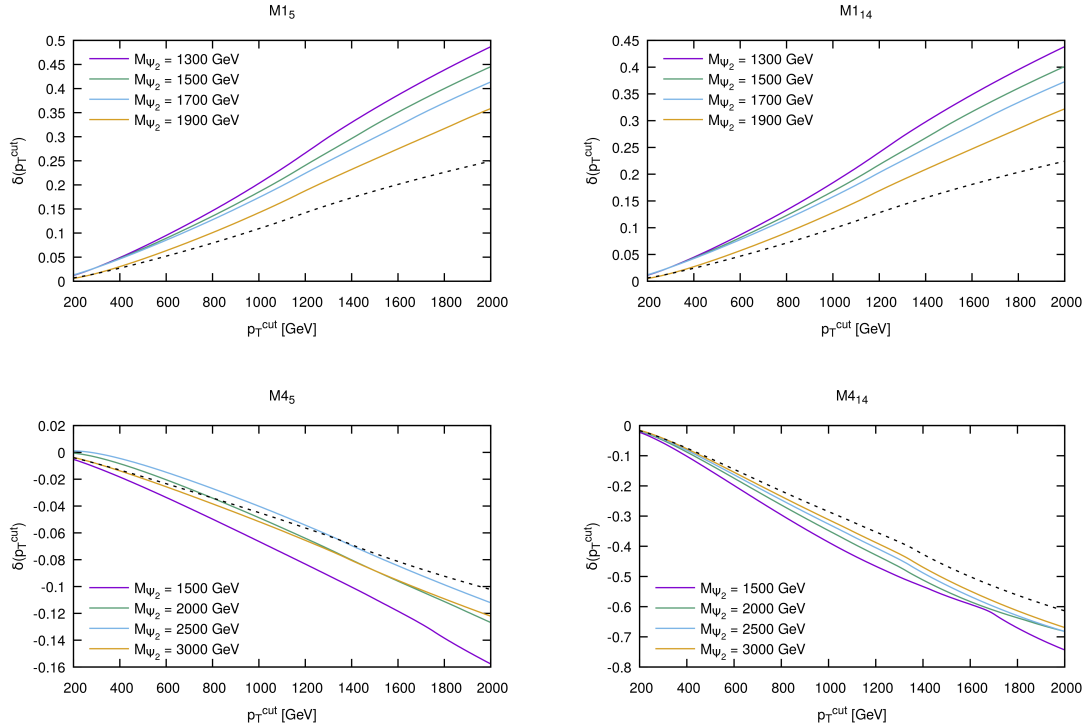


Figure 5.8: The distribution $\delta(p_T^{\text{cut}})$ for benchmark scenario with $y = 1$, $M_{\Psi_1} = 1200$ GeV, $1300 \text{ GeV} < M_{\Psi_2} < 3000$ GeV, $f = 800$ GeV (see Figs. 5.1) and the four models considered in Section 5.1.4. The figure is taken from [2].

approach those of the single top-partner scenario.

In both cases, we find that the contributions of the CP-odd couplings to the Higgs+Jet rate are typically small. One aspect of the calculation of the CP-odd contribution that needs to be checked is the certain QCD limits. We present this in the Appendix B.

5.3 Electro-weak Observables

We conclude this chapter by reviewing the main EW observables that constrain composite Higgs models, namely the Higgs mass and the oblique corrections. In Chapter 6 we will be deriving the Higgs potential explicitly for our models and computing the contributions to the T parameter. These along with the bounds on fermion and coloured NGB masses are some of the tightest phenomenological constraints on a variety of composite Higgs models, hence it is presented here. A comprehensive review on EW constraints can be found in [38].

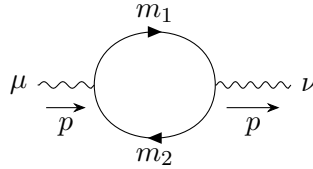


Figure 5.9: Vacuum-polarization amplitude with two different fermions.

5.3.1 Higgs Potential

In Section 5.1.3 we have introduced the composite sector which is made of $SO(4)$ fields. We have seen that even though these fields themselves do not transform under $SO(5)$, the combinations of them along with the NGB matrix can be used to form $SO(5)$ invariants. Hence, such spontaneous symmetry breaking does not explicitly violate the symmetry, it is merely realised in a non-linear way. We have also introduced elementary-composite mixings that break the $SO(5)$ symmetry of the Lagrangian. This breaking generates a Higgs potential, the minima of which correspond to the VEV of EWSB, giving masses for gauge bosons and the Higgs itself [37].

The Higgs potential is generated by the Coleman-Weinberg mechanism [151]. The main contributions come from the top quark and the gauge bosons. The potential can be expanded in trigonometric functions of Higgs field as

$$V[H] = -\alpha f^2 \sin^2 \frac{H}{f} + \beta f^2 \sin^4 \frac{H}{f}, \quad (5.46)$$

where coefficients α and β contain the strong sector dynamics. Minimising Eq.(5.46) for a realistic EWSB gives

$$m_h^2 = 8\xi(1 - \xi)\beta, \quad (5.47)$$

$$\alpha = 2\beta\xi, \quad (5.48)$$

where the Higgs VEV is $\xi = \sin^2 \langle H \rangle / f \ll 1$ and Higgs mass is $m_h = 126$ GeV [37]. We will be discussing more explicit calculations of the potential in Chapter 3.

5.3.2 Oblique Corrections

The oblique parameters are defined in terms of the gauge boson vacuum-polarisation function

$$\Pi_{ij}^{\mu\nu}(p^2) = -ig^{\mu\nu} A_{ij}(p^2) + iB_{ij}(p^2)p^\mu p^\nu, \quad (5.49)$$

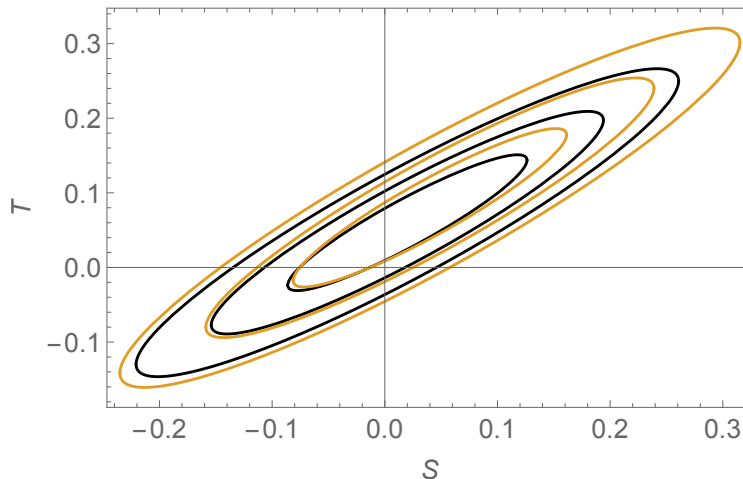


Figure 5.10: 1, 2 and 3 σ $S - T$ ellipse comparison of PDG (black) and Gfitter (yellow).

where A_{ij} and B_{ij} are the form factors encoding dynamics of the model. The oblique parameters are defined as

$$\hat{S} = -\frac{16\pi}{m_z}(A_{3Y}(m_Z^2) - A_{3Y}(0)), \quad (5.50)$$

$$\hat{T} = \frac{4\pi}{m_Z^2 \sin^2 \theta_W \cos^2 \theta_W}(A_{11}(0) - A_{33}(0)), \quad (5.51)$$

with $Y = Q - T_3$, $A_{11} = A_{22} = A_{W+W-}/2$, $\hat{S} = \alpha S$, $\hat{T} = \alpha T$ and the fine structure constant at Z mass $\alpha = 1/128$ [152, 153]. We will discuss the calculation of A_{ij} in the next subsection. The two more recent constraints on the values of S and T are given by

$$S = 0.04 \pm 0.08, \quad T = 0.08 \pm 0.07, \quad \text{Gfitter [154]}, \quad (5.52)$$

$$S = 0.02 \pm 0.07, \quad T = 0.06 \pm 0.06, \quad \text{PDG [38]}. \quad (5.53)$$

The correlation coefficients for both PDG and Gfitter parameters are 92%. The resulting plots of 1, 2 and 3 σ contours can be found in Figure 5.10.

In this thesis, we will focus mostly on the fermion contribution to T , which tends to be the dominant one, however, S and T can also get contributions coming from IR and vector resonances. IR corrections are given by

$$\Delta \hat{S}_{IR} = \frac{g^2}{192\pi^2} \xi \log \left(\frac{m_\rho^2}{m_h^2} \right), \quad (5.54)$$

$$\Delta \hat{T}_{IR} = -\frac{3g'^2}{64\pi^2} \xi \log \left(\frac{m_\rho^2}{m_h^2} \right). \quad (5.55)$$

\hat{S} also receives sizeable contributions from vector resonances, which can be written as

$$\Delta\hat{S}_V \approx \frac{m_W^2}{m_\rho^2}, \quad (5.56)$$

and fermions, given by

$$\Delta\hat{S}_{ferm} = \frac{g^2}{8\pi^2} \xi \log \left(\frac{m_\rho^2}{m_\Psi^2} \right). \quad (5.57)$$

Here $g = 2m_W/v$ and $g' = 2m_Z \sin \theta_W/v$, with $v = 246$ GeV. All of these relations have been taken from [37] and will be valid for our model in Chapter 6.

SU(2)_L Amplitudes and Currents

The vacuum polarisation amplitude can be obtained by applying a transverse projector to Eq.(5.49) as

$$P_{\mu\nu}\Pi_{ij}^{\mu\nu}(p^2) = i(p^2 g_{\mu\nu} - p_\mu p_\nu)\Pi_{ij}^{\mu\nu}(p^2) = (D-1)p^2 A_{ij}(p^2), \quad (5.58)$$

where D is the number of dimensions. The vacuum polarisation is related to the $SU(2)_L$ currents j_i^μ as

$$i\Pi_{ij}^{\mu\nu}(p^2) = \text{FT} \langle 0|T j_i^\mu(x) j_j^\nu(0)|0\rangle, \quad (5.59)$$

where FT stands for the Fourier transform and $i, j = 1..3$ are the $SU(2)_L$ indices. This is essentially a computation of the diagram in Figure 5.9 with the currents j_i^μ inserted at the vertices. The SM currents are given by

$$j_{+SM}^\mu = (j_-^\mu)^\dagger = \bar{t}\gamma^\mu P_L b, \quad (5.60)$$

$$j_{3,SM}^\mu = \frac{1}{2}(\bar{t}\gamma^\mu P_L t - \bar{b}\gamma^\mu P_L b), \quad (5.61)$$

where t and b are the top and bottom quarks respectively and $j_\pm^\mu = j_1^\mu \pm j_2^\mu$. The contributions from the composite sector can be obtained as follows. Using the field definitions in Section 5.1.3 and denoting $\Psi = \psi_4$ and $\psi = \psi_1$, we can write the relevant terms in the Lagrangian as

$$\mathcal{L}_{comp} = i\bar{\Psi}\not{D}\Psi + i\bar{\psi}\not{D}\psi + (ic\bar{\Psi}\gamma^\mu d_\mu\psi + \text{h.c.}) + \dots, \quad (5.62)$$

with the covariant derivative for Ψ given by

$$D_\mu\Psi = (\partial_\mu - iA_\mu + ie_\mu). \quad (5.63)$$

We can perform a field redefinition, such that

$$\begin{aligned}\Phi^T &= (U\Psi)^T \\ &= \frac{1}{2}(iX_{5/3} - iB, -B - X_{5/3}, -iT - iX_{2/3}, (T - X_{2/3})c_\xi, -(T - X_{2/3})s_\xi),\end{aligned}\quad (5.64)$$

$$\phi^T = (U\psi)^T = (0, 0, 0, \tilde{T}s_\xi, \tilde{T}c_\xi), \quad (5.65)$$

using $c_\xi = \cos \xi$ and $s_\xi = \sin \xi$. With this redefinition Lagrangian becomes

$$\mathcal{L}_{comp} = i\bar{\Phi}\not{D}\Phi + i\bar{\phi}\not{D}\phi = i\bar{\Psi}U^\dagger\not{D}U\Psi + i\bar{\psi}U^\dagger\not{D}U\psi. \quad (5.66)$$

In the convention $U^\dagger(i\partial_\mu + A_\mu)U = -d_\mu - e_\mu$ we can write

$$i(\bar{\Psi}U^\dagger)\not{D}(U\Psi) = i\bar{\Psi}\gamma^\mu\partial_\mu\Psi - \bar{\Psi}\gamma^\mu(d_\mu + e_\mu)\Psi = i\bar{\Psi}(\partial_\mu + ie_\mu)\Psi, \quad (5.67)$$

as well as a similar relation for ψ . Hence Eq.(5.67) contains all the terms necessary to obtain the Noether current, given by

$$j_\mu^i = \frac{\partial\mathcal{L}}{\partial(\partial_\mu\Phi)}\partial^i\Phi + \frac{\partial\mathcal{L}}{\partial(\partial_\mu\phi)}\partial^i\phi. \quad (5.68)$$

The singlet field ϕ will not contribute to the current so we ignore it. In this basis the current is particularly simple and given by

$$j_\mu^i = \bar{\Phi}\gamma_\mu t^i\Phi, \quad (5.69)$$

where t^i are the $SU(2)$ generators of fundamental representation. We can write $\tau^+ = t^1 + it^2$ and $\tau^- = t^1 - it^2$, which, together with our embeddings in Eqs.(5.64, 5.65), gives

$$\begin{aligned}j_\mu^+ &= (j_\mu^-)^\dagger = \frac{1}{2}((1 + c_\xi)\bar{T}\gamma_\mu B + (1 - c_\xi)\bar{X}_{2/3}\gamma_\mu B + (1 + c_\xi)\bar{X}_{5/3}\gamma_\mu X_{2/3} \\ &\quad + (1 - c_\xi)\bar{X}_{5/3}\gamma_\mu T),\end{aligned}\quad (5.70)$$

$$j_\mu^3 = \frac{1}{2}(c_\xi\bar{T}\gamma_\mu T + \bar{X}_{5/3}\gamma_\mu X_{5/3} - \bar{B}\gamma_\mu B - c_\xi\bar{X}_{2/3}\gamma_\mu X_{2/3}). \quad (5.71)$$

If we had instead redefined $\tilde{\Phi} = (U\Psi + U\psi)$, we would have also obtained a cross term

$$\frac{i}{\sqrt{2}}\bar{\Psi}\gamma^\mu d_\mu\psi - \frac{i}{\sqrt{2}}\bar{\psi}\gamma^\mu(d_\mu)^T\Psi, \quad (5.72)$$

which yields the d_μ term with $c = 1/\sqrt{2}$. Hence, the additional terms to the current are given by

$$\begin{aligned} \tilde{j}_\mu^+ &= j_\mu^+ + c(s_\xi \bar{\tilde{T}} \gamma_\mu B - s_\xi \bar{X}_{5/3} \gamma_\mu \tilde{T}), \\ \tilde{j}_\mu^3 &= j_\mu^3 + \frac{c}{2} s_\xi (\bar{\tilde{T}} \gamma_\mu T + \bar{\tilde{T}} \gamma_\mu X_{2/3} + \bar{\tilde{T}} \gamma_\mu \tilde{T} + \bar{X}_{2/3} \gamma_\mu \tilde{T}). \end{aligned}$$

5.4 Summary

In this chapter we have reviewed models with pNGB Higgs and its QCD as well as EW observables. In particular, we have discussed the unique features of these theories and performed diagonalization of the mass matrices for a few simplified cases. We have also provided an overview of the current EW and collider constraints and discussed how p_T spectra of the Higgs+Jet processes could be used to differentiate various CH models at colliders. Along with this we have also presented the calculation of CP-odd contributions to the Higgs+Jet in decoupling, soft and collinear limits. The latter two have appeared in our publication [2]. Finally, we have reviewed the Higgs potential and the calculation of oblique corrections including the derivation of the $SU(2)_L$ currents. Everything discussed in this chapter serves as a basis for model building that will be presented in Chapter 6.

Chapter 6

Gauge and Matter Unification in Composite Higgs Models

In this chapter, we aim to construct a composite Higgs model consistent with grand unification. In particular, we focus on partially composite models with custodial symmetry, which can achieve a natural electroweak scale, are compatible with the oblique corrections, provide an explanation for the fermion mass hierarchies, satisfy the constraints on the Z couplings to quarks and leptons and can accommodate current flavour data – constraints as well as the apparent anomalies in $b \rightarrow c\tau\nu$ and $b \rightarrow s\ell^+\ell^-$ transitions. The work presented in this chapter is part of an ongoing project.

This chapter is organised as follows. In Section 6.1 we present the salient features of our model. We specialise the CCWZ formalism for $SO(11)/SO(10)$ to include coloured NGBs in Section 6.2. Embeddings into $SO(11)/SO(10)$ are discussed and the Lagrangian as well as mass matrices are derived in Section 6.3. As it is imperative for any composite Higgs model to reproduce the correct Higgs mass, we compute the Higgs potential in Section 6.4. Since our model has a unique fermion embedding, it has to be ensured that the T parameter adheres to experimental bounds. Therefore, we discuss the computation of it in Section 6.5. Finally, in Section 6.6 we present how well our models satisfy Higgs mass, EW constraints and collider.

6.1 The Model Setup

In this section we present the setup for our model. In addition to the various salient features already mentioned in Chapter 5, our model aims to achieve gauge and matter unification, hence the MCHM has to be extended. There have been attempts to build

such models in the past, for which details can be found in [155–157].

We start with a partially composite pNGB Higgs model. The gauge invariance of linear mixings requires the strong sector symmetry to be at least $SU(3) \times SU(2)_L \times SU(2)_R \times U(1)_X$. The extra $U(1)$ factor is necessary to accommodate the SM hypercharges, with $Q = T_{3L} + T_{3R} + X$. The partial compositeness alone cannot achieve gauge unification. This imposes further restrictions on our composite sector, namely that the corresponding states must come in complete multiplets of a simple group S with a suitable hypercharge embedding. We discuss the latter in Section 6.1.1.

With the $SU(4)$ adjoint representation, we can have quarks and leptons coupling through a single vector leptoquark, which could help explain the R_D and R_{D^*} anomalies [158]. More generally, one may attempt to make partially composite quarks and leptons with a single multiplet of a composite sector. An immediate obstacle any such attempt must confront is guaranteeing that the proton remains stable on the timescales of order of inverse GUT scale. Imposing baryon and lepton number conservation prevents this along with heavy neutrino masses as discussed further in Section 6.1.2.

We have already seen that small elementary-composite mixings are enough to suppress the FCNCs. However, explicit computations of the vector-meson contributions to the CP-violating parameter ϵ_K require a scale $m_* \gg 10$ TeV if an anarchic, CP-nonsymmetric strong sector is assumed. If a lower scale is demanded in order to reduce EW fine-tuning or accommodate B -physics anomalies, then the strong-sector symmetry needs to be enhanced. Many authors have considered $U(2)^n$ or $SU(3)^n$ flavour symmetries [108, 159–161]. A more minimal solution may be to impose CP symmetry on the strong sector, as explored in [162]. The CP violation then originates from the elementary-composite couplings. Reproducing the large CKM phase, while maintaining consistency with FCNC including ϵ_K , requires a larger number of composite partners of the elementary quark doublets. Hence, we are considering a pair of bi-doublets.

Given the mentioned constraints, we attempt to build a composite Higgs model with an $SO(11) \rightarrow SO(10) \times U(1) \cong SO(6) \times SO(4) \times U(1)$ gauge symmetry. Here $SO(6) \sim SU(4)$ and $SO(4) \sim SU(2)_L \times SU(2)_R$. We give the most minimal set of viable embeddings for the elementary and composite fermions in our model in Table 6.1.

Comp field	SM field	$SU(4)_c \sim SU(3)_C \times U(1)_X$	$SU(2)_L$	$SU(2)_R$
Ψ	$(u, d)_L, (\nu^l, l)_L$	$\mathbf{15} \sim \mathbf{3}_{2/3}, \mathbf{1}_0, \dots$	$\mathbf{2}$	$\mathbf{2}$
$\tilde{\Psi}$	$(u, d)_L, (\nu^l, l)_L$	$\mathbf{15} \sim \mathbf{3}_{2/3}, \mathbf{1}_0, \dots$	$\mathbf{2}$	$\mathbf{2}$
ψ_u	u_R, ν_R^c	$\mathbf{15} \sim \mathbf{3}_{2/3}, \mathbf{1}_0, \dots$	$\mathbf{1}$	$\mathbf{1}$
ψ_d	d_R, e_R	$\mathbf{15} \sim \mathbf{3}_{2/3}, \mathbf{1}_0, \dots$	$\mathbf{1}$	$\mathbf{3}$
\mathcal{H}		$\mathbf{1}_0$	$\mathbf{2}$	$\mathbf{2}$

Table 6.1: Embeddings of $\{d, s, b\}_L, \{e, \mu, \tau\}_L, \nu_R^{e, \mu, \tau}, \{u, c, t\}_R$ and the Higgs \mathcal{H} for our partially composite Higgs model with custodial symmetry, which result in full unification with $Y = T_{3R} + X$. The subscripts denote the $U(1)_X$ charge. The branching rule for $SU(4) \supset SU(3) \times U(1)$ relevant here is: $(101) = \mathbf{15} = \mathbf{1}_0 \oplus \mathbf{3}_{2/3} \oplus \bar{\mathbf{3}}_{-2/3} \oplus \mathbf{8}_0$.

6.1.1 Embedding of the Hypercharge

The hypercharge Y must be embedded in S such that, for each S -multiplet,

$$\frac{3}{5} \text{tr}(Y^2) = \text{tr}(T_W^2) = \text{tr}(T_G^2), \quad (6.1)$$

where T_W is any of the weak $SU(2)_L$ generators, and T_G is any gluon generator. If this is true for one multiplet, then it is true for all multiplets, as all the traces are proportional to the index of that multiplet, up to universal normalisations. If we have a $P_{L,R}$ symmetry, then

$$\text{tr}(Y^2) = \text{tr}(X^2) + \text{tr}(T_L^2), \quad (6.2)$$

follows automatically for each irreducible representation, where we have used $\text{tr}(XT_R^a) = 0$, etc. This implies

$$\text{tr}(X^2) = \frac{2}{3} \text{tr}(T^2). \quad (6.3)$$

The condition is satisfied for the X -generator in $SU(4)$ in the normalisation where the $SU(3)$ singlet has $X = -1/3$, i.e.

$$X|_{SU(4)} = \sqrt{\frac{2}{3}} T_{15}. \quad (6.4)$$

In this normalisation, the colour-triplet of $SU(4)$ generators has $Y = X = 2/3$, and the corresponding Noether currents can annihilate spin-1 $(3, 1)_{2/3}$ states.

If we embed t_R in a $(n, 1, 1)$, then we require n to contain a colour triplet with $X = 2/3$. The smallest possible choices are $n = \mathbf{15}$ (adjoint), $n = \overline{\mathbf{45}}$, and $n = \mathbf{84}$. The left-handed quarks in $(n, 2, 2)$ require the same n . If the Higgs is a singlet under $SU(4)$ then the right-handed down-type quarks must also have $X = 2/3$, i.e. the possible $SU(4)$ representations

are again the same.

6.1.2 Baryon and Lepton Number

To achieve a baryon number conservation, one needs a generator distinguishing different components of a candidate unified $SU(4)$ multiplet. This is X , up to a normalisation and the addition of an arbitrary generator commuting with $SU(4)$ which will act on the composite partners of the elementary states as a multiple of ‘particle number’ $3B + L$.

Remarkably, X coincides with $2B$ if composite quarks and leptons are in the adjoint of $SU(4)$. This provides an essentially unique way to achieve quark-lepton unification, which is generically not possible [155]. Hence we can take the particle number to be a $U(1)$ factor outside S , with $SU(4) \times SU(2) \times SU(2) \subset S$. If all composites mixing with the elementary fields have the same particle number, we have separate B and L conservation, preventing proton decay and TeV-scale neutrino masses.

6.2 CCWZ for $SO(11)/SO(10)$

In a first step of our model building efforts we have to choose a basis for the pNGB fields. Hence, we are specialising the CCWZ formalism, defined in Section 5.1.2, to the $SO(11) \rightarrow SO(10) \times U(1) \cong SO(6) \times SO(4) \times U(1)$ gauge symmetry, with $SO(6) \sim SU(4)$ and $SO(4) \sim SU(2)_L \times SU(2)_R$. Let us first define the indices that we use to decompose fields with respect to these subgroups. With capital letters $A, B, ..$ we denote fundamental $SO(11)$ indices running between 1 and 11. We choose Greek letters $\alpha, \beta, ...$ to mark $SO(10)$ indices in the range 1..10. Small Latin letters $a, b, ...$ indicate $SU(4)$ indices between 1 and 6. We use $i, j, ..$ for indices 7 to 10 of $SO(11)$ corresponding to $SO(4)$, and x for index 11. For convenience, this decomposition can be summarised as

$$\begin{aligned}
 A &= \{\alpha, x\} = \{a, i, x\}, \\
 B &= \{\beta, x\} = \{b, j, x\}, \\
 C &= \{\gamma, x\} = \{c, k, x\}, \\
 D &= \{\delta, x\} = \{d, l, x\}, \\
 E &= \{\epsilon, x\} = \{e, m, x\}.
 \end{aligned}
 \tag{6.5}$$

The symmetry breaking pattern $SO(11) \rightarrow SO(10)$ results in 10 broken generators, meaning that we have 10 NGB fields. We can define an NGB vector field as

$$\tilde{\Pi}^\tau = (\tilde{\phi}^a, \tilde{h}^i). \quad (6.6)$$

Here, in addition to the Higgs NGB \tilde{h} , which is the usual $SU(2)_L \times SU(2)_R$ bi-doublet, we also have 6 coloured NGBs $\tilde{\phi}^a$. They form a complex triplet \mathcal{T} and its conjugate \mathcal{T}^* , corresponding to $\mathbf{3} + \bar{\mathbf{3}}$ of $SU(3)_c$. In unitary gauge (UG), the NGB vector can be parametrised as

$$\vec{\Pi}^\tau = \left(\frac{1}{\sqrt{2}}(\mathcal{T}^{a'} + \mathcal{T}^{*a'}), -\frac{i}{\sqrt{2}}(\mathcal{T}^{a'} - \mathcal{T}^{*a'}), 0_3, h \right), \quad (6.7)$$

where a', b' are the $SU(3)$ colour indices. The U matrix is given by

$$U = e^{i\frac{\sqrt{2}}{f}\tilde{\Pi}_a X^{\hat{a}}} = \begin{bmatrix} \mathbb{1} - \left(1 - \cos \frac{\tilde{\Pi}}{f}\right) \frac{\tilde{\Pi}\tilde{\Pi}^\tau}{\tilde{\Pi}^2} & \sin \frac{\tilde{\Pi}}{f} \frac{\tilde{\Pi}}{\tilde{\Pi}} \\ -\sin \frac{\tilde{\Pi}}{f} \frac{\tilde{\Pi}^\tau}{\tilde{\Pi}} & \cos \frac{\tilde{\Pi}}{f} \end{bmatrix}, \quad (6.8)$$

where the broken generators can be written

$$X_{IJ}^{\hat{a}} = \frac{i}{\sqrt{2}}(\delta_I^{\hat{a}}\delta_J^{11} - \delta_J^{\hat{a}}\delta_I^{11}). \quad (6.9)$$

Since $\tilde{\Pi}$ involves both Higgs and coloured NGBs, an expression in UG is rather complicated. Instead, we perform a field redefinition $\sin(\tilde{\Pi}/f)\tilde{\Pi}/\tilde{\Pi} = \vec{\Pi}$ [163], which allows us to write U in UG as

$$U = \begin{bmatrix} \mathbb{1} - \frac{\vec{\Pi}\vec{\Pi}^\tau}{1+\Omega} & \vec{\Pi} \\ -\vec{\Pi}^\tau & \Omega \end{bmatrix} = \begin{pmatrix} \mathbb{1}_{6 \times 6} - \frac{\vec{\phi}\vec{\phi}^\tau}{1+\Omega} & 0_{4 \times 3} & -\frac{\vec{\phi}h}{1+\Omega} & \vec{\phi} \\ 0_3 & \mathbb{1}_{3 \times 3} & 0_3 & 0_3 \\ -\frac{h^3\vec{\phi}^\tau}{1+\Omega} & 0_3^\tau & 1 - \frac{h^2}{1+\Omega} & h \\ -\vec{\phi} & 0_3^\tau & h & \Omega \end{pmatrix}, \quad (6.10)$$

where $\phi^a = ((\mathcal{T}^{a'} + \mathcal{T}^{*a'}), -i(\mathcal{T}^{a'} - \mathcal{T}^{*a'}))^T/\sqrt{2}$ and $\Omega = \sqrt{1 - \Pi^2} = \sqrt{1 - h^2 - 2|\mathcal{T}|^2}$. With this we can now proceed to derive the Lagrangian.

6.3 Lagrangian and Mass Matrices

Similarly to Section 5.1.3, we are going to derive the Lagrangian and the mass matrices for our fields, given in Table 6.1. We will use this Lagrangian for calculations of the T -

parameter, defined in Section 5.3.2. As the $SO(6)$ (colour) does not get broken by the SSB, the coloured NGBs will not contribute, hence in this derivation we set them to zero.

6.3.1 Embedding into Anti-symmetric Tensors

We are going to embed our elementary and composite fields into anti-symmetric representations of $SO(11)$ and $SO(10)$ respectively. We denote an anti-symmetric (AS) n -index representation of $SO(N)$ as $[n]_N$ and the corresponding tensor as $T^{A_1 A_2 \dots A_n}$. Moreover, we fix the tensor by specifying only the $A_1 < A_2 < \dots < A_n$ components as $T^{A_2 A_1 \dots A_n} = -T^{A_1 A_2 \dots A_n}$, etc. The product of two such tensors can be written as the sum

$$\bar{T}T = \sum_{A_1, A_2, \dots, A_n} \bar{T}^{A_1 A_2 \dots A_n} T^{A_1 A_2 \dots A_n} = \mathcal{N} \sum_{A_1 < A_2 < \dots < A_n} \bar{T}^{A_1 A_2 \dots A_n} T^{A_1 A_2 \dots A_n}, \quad (6.11)$$

where $\mathcal{N} = n!$ as it corresponds to the number of possible permutations of the indices.

In Table 6.2 we give the embeddings of elementary and composite fields into AS tensors of $SO(11)$ and $SO(10)$ respectively. Analogously to MCHM the SM fields form incomplete multiplets of $SO(11)$. We use the indices to indicate this as A, B, \dots lie in the range 1..6, K, L, \dots in 7..10 and X stands for 11. These index ranges follow from the embeddings. For instance, to embed b_R in the (15,1,3) of $SU(4) \times SU(2)_L \times SU(2)_R$ we need 2 $SO(6)$ and 2 $SO(4)$ indices. Hence we need a tensor with at least four indices to embed this. The composite fields form complete multiplets of $SO(10)$, however we use the $SO(6)$, $SO(4)$ and x indices to indicate the relevant parts that contract with the elementary fields.

6.3.2 Mass Terms

The mass terms entering a Lagrangian with an $SO(11)$ symmetry are given by

$$\mathcal{L}_{mass} = m_T \bar{T}T, \quad (6.12)$$

where T is a fermion in some $SO(11)$ representation. Let us start by embedding t_R in $[2]_{11}$. We can decompose the tensor product into $SO(10)$ and then into $SO(6)$ and $SO(4)$ as

$$\begin{aligned} \bar{T}T &= 2 \sum_{A < B} \bar{T}^{AB} T^{AB} = 2 \left(\sum_{\alpha < \beta} \bar{T}^{\alpha\beta} T^{\alpha\beta} + \sum_{\alpha, x} \bar{T}^{\alpha x} T^{\alpha x} \right) \\ &= 2 \left(\sum_{a < b} \bar{T}^{ab} T^{ab} + \sum_{a, j} \bar{T}^{aj} T^{aj} + \sum_{a, x} \bar{T}^{ax} T^{ax} + \sum_{i < j} \bar{T}^{ij} T^{ij} + \sum_{i, x} \bar{T}^{ix} T^{ix} \right), \end{aligned} \quad (6.13)$$

Tensor	SM field	$SO(11)$ field	Composite field(s)	$SO(10)$ field
[5]	q_L	T^{ABCDM}	$\Psi, \tilde{\Psi}$	Ψ^{abcdm}
		T^{ABKLM}	$\Psi, \tilde{\Psi}$	Ψ^{abklm}
	t_R	T^{ABCDX}		
	b_R	T^{ABKLX}		
[4]	t_R	T^{ABCD}	ψ_u	ψ^{abcd}
		T^{ABKL}	ψ_d	ψ^{abkl}
		T^{ABKX}		
[3]	q_L	T^{ABK}	$\Psi, \tilde{\Psi}$	Ψ^{abk}
		T^{ABX}		
[2]	t_R	T^{AB}	ψ_u	ψ^{ab}

Table 6.2: Elementary and composite fermion embeddings into $SO(11)$ and $SO(10)$ anti-symmetric tensors (AS) respectively. $[n]$ denotes the n -index AS tensor. $A, B..$ and $a, b..$ correspond to indices in range 1..6 and $K, L..$ with $k, l..$ - 7..10 of $SO(11)$ and $SO(10)$ respectively.

where the underline marks the relevant term in our expansion for the embedding of t_R . Therein, we use the components T^{ab} , which are identified as the adjoint representation $\mathbf{15}$ of $SU(4)$, to embed the t_R into the $[2]_{11}$. By decomposing our fields in this way, the embedding is straightforward to obtain.

We can follow an analogue of this procedure to embed b_R $[4]_{11}$ as

$$\begin{aligned}
\bar{T}T &= 4! \sum_{A<B<C<D} \bar{T}^{ABCD} T^{ABCD} \\
&= 4! \left(\sum_{\alpha<\beta<\gamma<\delta} \bar{T}^{\alpha\beta\gamma\delta} T^{\alpha\beta\gamma\delta} + \sum_{\alpha<\beta<\gamma,x} \bar{T}^{\alpha\beta\gamma x} T^{\alpha\beta\gamma x} \right) \\
&= 4! \left(\underline{\sum_{a<b<c<d} \bar{T}^{abcd} T^{abcd}} + \sum_{a<b<c,l} \bar{T}^{abcl} T^{abcl} + \sum_{a<b<c,x} \bar{T}^{abcx} T^{abcx} \right. \\
&\quad + \sum_{a<b,k<l} \bar{T}^{abkl} T^{abkl} + \sum_{a<b,k,x} \bar{T}^{abkx} T^{abkx} + \sum_{a,j<k<l} \bar{T}^{ajkl} T^{ajkl} \\
&\quad \left. + \sum_{a,j<k,x} \bar{T}^{ajkx} T^{ajkx} + \sum_{i<j<k<l} \bar{T}^{ijkl} T^{ijkl} + \sum_{i<j<k,x} \bar{T}^{ijkx} T^{ijkx} \right), \tag{6.14}
\end{aligned}$$

where we have denoted the components of T^{ABCD} suitable for embedding b_R by dashed underline. We even find a few more viable embeddings in this representation. The top quark t_R can be embedded into T^{abcd} (marked by solid underline), which is a $SO(6)$ -dual

of T^{ab} via the relation

$$T^{abcd} = \epsilon_{abcdef} T^{ef}, \quad (6.15)$$

where ϵ is an $SO(6)$ Levi-civita tensor. There is also a viable opportunity to embed q_L (marked by wavy underline), which requires two $SO(6)$ and one $SO(4)$ index. Hence, it is actually possible to embed all of the elementary quarks into $[4]_{11}$. As q_L and t_R with b_R belong to 4 and 3 index representations of $SO(10)$ respectively, they could also have different masses associated with them.

Following this approach even tensors with a larger number of indices are feasible. Using the relations between duals we could again find suitable embeddings. In particular, multiple versions of a single fermion can be embedded into a single $SO(11)$ representation, as we will see later. Composite partners are embeddable in the same way into appropriate $SO(10)$ multiplets.

6.3.3 Mixing Terms

Mixing terms can be decomposed in exactly the same way as the mass terms discussed in the previous section. Generally, they can be written as

$$\mathcal{L}_{mix} = \lambda T \mathcal{O}, \quad (6.16)$$

where \mathcal{O} is the composite operator in an AS tensor representation of $SO(N)$ and λ the coupling constant. \mathcal{O} can be decomposed in terms of $SO(N-1)$ representations as

$$\begin{pmatrix} [k]_N \\ \mathcal{O} \end{pmatrix} \rightarrow \begin{pmatrix} [k]_{N-1} \\ \Psi \end{pmatrix} + \begin{pmatrix} [k-1]_{N-1} \\ \psi \end{pmatrix}, \quad (6.17)$$

where we denote the composite in $[k]_{N-1}$ representation as Ψ and the one in $[k-1]_{N-1}$ as ψ . Recalling the invariant in Eq.(5.1.2), the mixing term for the $[2]_{11}$ can be written as

$$\mathcal{L}_{mix}^{[2]} \propto \bar{T}^{AB} U^{A\gamma} (U^{B\delta} \Psi^{\gamma\delta} + U^{Bx} \psi^\gamma), \quad (6.18)$$

where U is our 11×11 NGB matrix, given in Eq.(6.10). As before, decomposing this in terms of $SO(10)$ indices gives

$$\begin{aligned} \sum_{A,B} \sum_{\gamma,\delta} \bar{T}^{AB} U^{A\gamma} (U^{B\delta} \Psi^{\gamma\delta} + U^{Bx} \psi^\gamma) &= \sum_{\alpha,\beta} \sum_{\gamma,\delta} \bar{T}^{\alpha\beta} U^{\alpha\gamma} (U^{\beta\delta} \Psi^{\gamma\delta} + U^{\beta x} \psi^\gamma) \\ &+ \sum_{\alpha,x} \sum_{\gamma,\delta} \bar{T}^{\alpha x} U^{\alpha\gamma} (U^{x\delta} \Psi^{\gamma\delta} + U^{xx} \psi^\gamma) + \sum_{x,\beta} \sum_{\gamma,\delta} \bar{T}^{x\beta} U^{x\gamma} (U^{\beta\delta} \Psi^{\gamma\delta} + U^{\beta x} \psi^\gamma), \end{aligned} \quad (6.19)$$

where we have again marked the relevant term for t_R by underline. As mentioned in the beginning of this section, in this particular derivation of the Lagrangian we set the colour NGBs to zero, yielding a mostly diagonal U matrix. The $SO(10)$ part of U is completely diagonal, hence we can proceed to decompose as follows

$$\begin{aligned}
& \sum_{\alpha,\beta} \sum_{\gamma,\delta} \bar{T}^{\alpha\beta} U^{\alpha\gamma} (U^{\beta\delta} \Psi^{\gamma\delta} + U^{\beta x} \psi^{\gamma}) = \sum_{\alpha,\beta} \bar{T}^{\alpha\beta} U^{\alpha\alpha} (U^{\beta\beta} \Psi^{\alpha\beta} + U^{\beta x} \psi^{\alpha}) \\
& = 2 \sum_{\substack{a<b \\ \underline{a,b}}} \bar{T}^{ab} U^{aa} (U^{bb} \Psi^{ab} + U^{bx} \psi^a) + \sum_{a,j} \bar{T}^{aj} U^{aa} (U^{jj} \Psi^{aj} + U^{jx} \psi^a) \\
& + \sum_{i,b} \bar{T}^{ib} U^{ii} (U^{bb} \Psi^{ib} + U^{bx} \psi^i) + 2 \sum_{i<j} \bar{T}^{ij} U^{ii} (U^{jj} \Psi^{ij} + U^{jx} \psi^i).
\end{aligned} \tag{6.20}$$

This can be simplified further as U is just an identity matrix for $SO(6)$, giving

$$2 \sum_{a<b} \bar{T}^{ab} U^{aa} (U^{bb} \Psi^{ab} + U^{bx} \psi^a) = 2 \sum_{a<b} \bar{T}^{ab} \Psi^{ab}, \tag{6.21}$$

where the second term vanishes because $U^{bx} = 0$ for all $b = 1..6$. Hence, we have simplified the mixing term to the point where it can be written in terms of $\mathbf{15}$'s of $SO(6)$.

We can now follow the same steps and derive the mixing terms for $[4]_{11}$. It can be written as

$$\begin{aligned}
\mathcal{L}_{mix}^{[4]} & \propto \sum_{A,B,C,D} \sum_{\epsilon,\zeta,\eta,\phi} \bar{T}^{ABCD} U^A \epsilon U^B \zeta U^C \eta (U^{D\phi} \Psi^{\epsilon\zeta\eta\phi} + U^{Dx} \psi^{\epsilon\zeta\eta}) \\
& = \sum_{\alpha,\beta,\gamma,\delta} \sum_{\epsilon,\zeta,\eta,\phi} \bar{T}^{\alpha\beta\gamma\delta} U^{\alpha\epsilon} U^{\beta\zeta} U^{\gamma\eta} (U^{\delta\phi} \Psi^{\epsilon\zeta\eta\phi} + U^{\delta x} \psi^{\epsilon\zeta\eta}) \\
& + \sum_{\alpha,\beta,\gamma,x} \sum_{\epsilon,\zeta,\eta,\phi} \bar{T}^{\alpha\beta\gamma x} U^{\alpha\epsilon} U^{\beta\zeta} U^{\gamma\eta} (U^{x\phi} \Psi^{\epsilon\zeta\eta\phi} + U^{xx} \psi^{\epsilon\zeta\eta}) \\
& + \sum_{\alpha,\beta,x,\delta} \sum_{\epsilon,\zeta,\eta,\phi} \bar{T}^{\alpha\beta x\delta} U^{\alpha\epsilon} U^{\beta\zeta} U^{x\eta} (U^{\delta\phi} \Psi^{\epsilon\zeta\eta\phi} + U^{\delta x} \psi^{\epsilon\zeta\eta}) \\
& + \sum_{\alpha,x,\gamma,\delta} \sum_{\epsilon,\zeta,\eta,\phi} \bar{T}^{\alpha x\gamma\delta} U^{\alpha\epsilon} U^{x\zeta} U^{\gamma\eta} (U^{\delta\phi} \Psi^{\epsilon\zeta\eta\phi} + U^{\delta x} \psi^{\epsilon\zeta\eta}) \\
& + \sum_{x,\beta,\gamma,\delta} \sum_{\epsilon,\zeta,\eta,\phi} \bar{T}^{x\beta\gamma\delta} U^{x\epsilon} U^{\beta\zeta} U^{\gamma\eta} (U^{\delta\phi} \Psi^{\epsilon\zeta\eta\phi} + U^{\delta x} \psi^{\epsilon\zeta\eta}).
\end{aligned} \tag{6.22}$$

At this point, all of these terms are relevant for our embeddings, hence we will focus on each term one at a time. Keeping the same underlines as in the previous section, the first

term gives

$$\begin{aligned}
& \sum_{\alpha,\beta,\gamma,\delta} \sum_{\epsilon,\zeta,\eta,\phi} \bar{T}^{\alpha\beta\gamma\delta} U^{\alpha\epsilon} U^{\beta\zeta} U^{\gamma\eta} (U^{\delta\phi} \Psi^{\epsilon\zeta\eta\phi} + U^{\delta x} \psi^{\epsilon\zeta\eta}) \\
&= \sum_{\alpha,\beta,\gamma,\delta} \bar{T}^{\alpha\beta\gamma\delta} U^{\alpha\alpha} U^{\beta\beta} U^{\gamma\gamma} (U^{\delta\delta} \Psi^{\alpha\beta\gamma\delta} + U^{\delta x} \psi^{\alpha\beta\gamma}) \\
&= 4! \sum_{a<b<c<d} \bar{T}^{abcd} U^{aa} U^{bb} U^{cc} (U^{dd} \Psi^{abcd} + U^{dx} \psi^{abc}) \\
&\quad \text{-----} \\
&+ 3! \sum_{a<b,k<l} \bar{T}^{abkl} U^{aa} U^{bb} U^{kk} (U^{ll} \Psi^{abkl} + U^{lx} \psi^{abk}) \\
&\quad \text{-----} \\
&+ 3! \sum_{a<b,k<l} \bar{T}^{klab} U^{kk} U^{ll} U^{aa} (U^{bb} \Psi^{klab} + U^{bx} \psi^{kla}) + \dots, \\
&\quad \text{-----}
\end{aligned} \tag{6.23}$$

where we have kept only the relevant parts. We can write the underlined sum as

$$4! \sum_{a<b<c<d} \bar{T}^{abcd} U^{aa} U^{bb} U^{cc} (U^{dd} \Psi^{abcd} + U^{dx} \psi^{abc}) = 4! \sum_{a<b<c<d} \bar{T}^{abcd} \Psi^{abcd}, \tag{6.24}$$

the first dashed term as

$$\begin{aligned}
& 3! \times 2 \sum_{a<b,k<l} \bar{T}^{abkl} U^{aa} U^{bb} U^{kk} (U^{ll} \Psi^{abkl} + U^{lx} \psi^{abk}) \\
&= 3! \times 2 \sum_{a<b,k<l} \bar{T}^{abkl} \left(U^{ll} \Psi^{abkl} + \underbrace{\frac{1}{2} U^{lx} \psi^{abk}} \right), \\
&\quad \text{-----}
\end{aligned} \tag{6.25}$$

where we get coupling to the q_L composite counterpart, and the second dashed term as

$$3! \times 2 \sum_{a<b,k<l} \bar{T}^{klab} U^{kk} U^{ll} U^{aa} (U^{bb} \Psi^{klab} + U^{bx} \psi^{kla}) = 3! \times 2 \sum_{a<b,k<l} \bar{T}^{abkl} U^{ll} \Psi^{abkl}. \tag{6.26}$$

The dashed terms (which are just index permutations of one another) are not equal. The 4-index parts match forming 4! permutations, however the 3-index composite field appears only when the last index is l , hence we have merely 3! of such terms.

For the second term keeping in mind that the x is fixed, we can write

$$\begin{aligned}
& \sum_{\alpha,\beta,\gamma,x} \sum_{\epsilon,\zeta,\eta,\phi} \bar{T}^{\alpha\beta\gamma x} U^{\alpha\epsilon} U^{\beta\zeta} U^{\gamma\eta} (U^{x\phi} \Psi^{\epsilon\zeta\eta\phi} + U^{xx} \psi^{\epsilon\zeta\eta}) \\
&= \sum_{\alpha,\beta,\gamma,x} \sum_{\phi} \bar{T}^{\alpha\beta\gamma x} U^{\alpha\alpha} U^{\beta\beta} U^{\gamma\gamma} (U^{x\phi} \Psi^{\alpha\beta\gamma\phi} + U^{xx} \psi^{\alpha\beta\gamma}) \\
&= 3! \sum_{a<b<c,x} \bar{T}^{abcx} U^{aa} U^{bb} U^{cc} \left(\sum_p U^{xp} \Psi^{abcp} + U^{xx} \psi^{abc} \right) \\
&\quad + 3! \sum_{a<b,k,x} \bar{T}^{abkx} U^{aa} U^{bb} U^{kk} \left(\sum_p U^{xp} \Psi^{abkp} + U^{xx} \psi^{abk} \right) \\
&\quad + 3! \sum_{a,j<k,x} \bar{T}^{ajkx} U^{aa} U^{jj} U^{kk} \left(\sum_p U^{xp} \Psi^{ajkp} + U^{xx} \psi^{ajk} \right) \\
&\quad + 3! \sum_{i<j<k,x} \bar{T}^{ijkx} U^{ii} U^{jj} U^{kk} \left(\sum_p U^{xp} \Psi^{ijkp} + U^{xx} \psi^{ijk} \right).
\end{aligned} \tag{6.27}$$

For the wavy part we get

$$\begin{aligned}
& 3! \sum_{a<b,k,x} \bar{T}^{abkx} U^{aa} U^{bb} U^{kk} \left(\sum_p U^{xp} \Psi^{abkp} + U^{xx} \psi^{abk} \right) \\
&= 3! \sum_{a<b,k,x} \bar{T}^{abkx} U^{kk} \left(\sum_p U^{xp} \Psi^{abkp} + U^{xx} \psi^{abk} \right).
\end{aligned} \tag{6.28}$$

The third term in Eq.(6.22) can be simplified as follows

$$\begin{aligned}
& \sum_{\alpha,\beta,x,\delta} \sum_{\epsilon,\zeta,\eta,\phi} \bar{T}^{\alpha\beta x\delta} U^{\alpha\epsilon} U^{\beta\zeta} U^{x\eta} (U^{\delta\phi} \Psi^{\epsilon\zeta\eta\phi} + U^{\delta x} \psi^{\epsilon\zeta\eta}) \\
&= \sum_{\alpha,\beta,x,\delta} \sum_{\eta} \bar{T}^{\alpha\beta x\delta} U^{\alpha\alpha} U^{\beta\beta} U^{x\eta} (U^{\delta\delta} \Psi^{\alpha\beta\eta\delta} + U^{\delta x} \psi^{\alpha\beta\eta}) \\
&\Rightarrow 3! \sum_{a<b,x,l} \sum_o \bar{T}^{abxl} U^{xo} \left(U^{ll} \Psi^{abol} + \frac{1}{3} U^{lx} \psi^{abo} \right),
\end{aligned} \tag{6.29}$$

where we once more retain only the relevant parts. Again, the last index has to be fixed to l in order to get the 3-index term. The fourth and the fifth terms in Eq.(6.22) are the same as the third one.

In summary, our elementary-composite mixing terms read

$$\begin{aligned}
\mathcal{L}_{mix}^{[4]} \propto & 4! \sum_{a<b<c<d} \bar{T}^{abcd} \Psi^{abcd} + 4! \sum_{a<b,k<l} \bar{T}^{abkl} U^{ll} \Psi^{abkl} + 3! \sum_{a<b,k<l} \bar{T}^{abkl} U^{lx} \psi^{abk} \\
& + 4! \sum_{a<b,k,x} \sum_p \bar{T}^{abkx} U^{kk} U^{xp} \Psi^{abkp} + 3! \sum_{a<b,k,x} \bar{T}^{abkx} U^{kk} U^{xx} \psi^{abk} \\
& + 3! \sum_{a<b,x,l} \sum_o \bar{T}^{abxl} U^{xo} U^{lx} \psi^{abo},
\end{aligned} \tag{6.30}$$

and

$$\mathcal{L}_{mix}^{[2]} \propto 2 \sum_{a<b} \bar{T}^{ab} \Psi^{ab}. \tag{6.31}$$

The main problem with these embeddings is that there is no way to produce top quark mass as t_R and q_L cannot couple via the same composite fermion. We find that an odd number of indices for the t_R representation is required to generate a top mass.

In Table 6.3 we explore more options for the quark and lepton embeddings. As we have already mentioned the U matrix in Eq.(6.10) is mostly diagonal. The non-diagonal bits can be written as power series in Higgs fields. This specifies the number of Higgs bosons coupling to a specific vertex and it contains all higher order terms. We refer to the vertices containing odd powers of Higgs $h + h^3 + \dots$ as odd and to the even $1 + h^2 + \dots$ as even.

The composites that are identical can be used to couple two elementary fermions to generate quark masses. However, this can only happen if one Higgs coupling is even and the other one is odd. Hence, we can identify two of the most minimal viable models: 2-3-4-5 and 3-3-5-5, where the numbers $n = 2, 3, 4, 5$ refer to embedding t_R, q_L, q'_L, b_R in an n -index anti-symmetric representation of $SO(11)$. For both of these we have feasible $q_L - t_R$ and $q_L - b_R$ couplings, which are independent of each other. This can be used to explain the mass difference between the top and bottom quarks. In addition, we show that it is also possible to embed the elementary and composite leptons in the $SO(11)/SO(10)$ GUT group.

Tensor	SM field	$SO(11)$ field	Composite 1	Composite 2	H1	H2
5	q_L	T^{ABCDM}	Ψ^{abcdm}	ψ^{abcd}	even	odd
		T^{ABKLM}	Ψ^{abklm}	ψ^{abkl}	even	odd
	t_R	T^{ABCDX}	Ψ^{abcdm}	ψ^{abcd}	odd	even
	b_R	$T^{ABK LX}$	Ψ^{abklm}	ψ^{abkl}	odd	even
4	t_R	T^{ABCD}	ψ^{abcd}		even	odd
	b_R	T^{ABKL}	ψ^{abkl}	Ψ^{abk}	even	odd
	q_L	$T^{ABK X}$	ψ^{abkl}	Ψ^{abk}	odd	even
3	q_L	T^{ABK}	Ψ^{abk}	ψ^{ab}	even	odd
	t_R	T^{ABX}	Ψ^{abk}	ψ^{ab}	odd	even
2	t_R	T^{AB}	ψ^{ab}		even	odd

Tensor	SM field	$SO(11)$ field	Composite 1	Composite 2	H1	H2
3	l_L	T^{KLM}	Ψ^{klm}	ψ^{kl}	even	odd
	τ_R	$T^{K LX}$	Ψ^{klm}	ψ^{kl}	odd	even
2	τ_R	T^{KL}	ψ^{kl}	Ψ^k	even	odd
	l_L	$T^{K X}$	ψ^{kl}	Ψ^k	odd	even
1	l_L	T^K	Ψ^k		even	odd
	ν_R	T^X	Ψ^k		odd	even

Table 6.3: Embedding options for elementary and composite quarks and leptons in $SO(11)$. Composites that are the same can be used to get contributions to the top or bottom mass. H1 and H2 stand for Higgs coupling at the elementary-composite vertex corresponding to composite 1 or 2. Even and odd indicate powers of the Higgs. More details are given in the main text.

6.3.4 The Two Models: 2-3-4-5 and 3-3-5-5

We will now summarise the two viable models 2-3-4-5 and 3-3-5-5 and derive the mass matrices. The composite mass terms are the same for both of them, given by

$$\begin{aligned} \mathcal{L}_{mass} = & -m_\Psi \sum_{a<b,k} \bar{\Psi}^{abk} \Psi^{abk} - m_{\tilde{\Psi}} \sum_{a<b,k} \bar{\tilde{\Psi}}^{abk} \tilde{\Psi}^{abk} \\ & - m_{\psi_t} \sum_{a<b} \bar{\psi}^{ab} \psi^{ab} - m_{\psi_b} \sum_{a<b,k<l} \bar{\psi}^{abkl} \psi^{abkl}. \end{aligned} \quad (6.32)$$

The mixing terms for the 2-3-4-5 model are

$$\begin{aligned} \mathcal{L}_{mix}^{2345} = & \lambda_R^\psi f \sum_{A<B} \bar{T}^{AB} \psi^{ab} + \lambda_L^\Psi f \sum_{A<B,K} T^{ABK} U^{Kk} \Psi^{abk} \\ & + \frac{1}{\sqrt{3}} \lambda_L^\psi f \sum_{A<B,K} T^{ABK} U^{Kx} \psi^{ab} \\ & + \frac{1}{2} \tilde{\lambda}_L^\Psi f \sum_{A<B,K,X} \bar{T}^{ABKX} (U^{Kk} U^{Xx} - U^{Xk} U^{Kx}) \Psi^{abk} \\ & + \tilde{\lambda}_L^\psi f \sum_{A<B,K<L,X} \bar{T}^{ABKX} U^{Xl} \psi^{abkl} + 2\tilde{\lambda}_R^\Psi f \sum_{A<B,K<L,X} \bar{T}^{ABKLX} U^{LX} \tilde{\Psi}^{abk} \\ & + \frac{1}{\sqrt{5}} \tilde{\lambda}_R^\psi f \sum_{A<B,K<L,X} \bar{T}^{ABKLX} (U^{Ll} U^{Xx} - U^{Xl} U^{Lx}) \psi^{abkl}, \end{aligned} \quad (6.33)$$

and for the 3-3-5-5 we have

$$\begin{aligned} \mathcal{L}_{mix}^{3355} = & \lambda_R^\Psi f \sum_{A<B,K,X} T^{ABX} U^{Xk} \Psi^{abk} + \frac{1}{\sqrt{3}} \lambda_R^\psi f \sum_{A<B,X} T^{ABX} U^{Xx} \psi^{ab} \\ & + \lambda_L^\Psi f \sum_{A<B,K} T^{ABK} U^{Kk} \Psi^{abk} + \frac{1}{\sqrt{3}} \lambda_L^\psi f \sum_{A<B,K} T^{ABK} U^{Kx} \psi^{ab} \\ & + \tilde{\lambda}_L^\Psi f \sum_{A<B,K<L<M} \bar{T}^{ABKLM} U^{Mm} \Psi^{abklm} \\ & + \frac{1}{\sqrt{5}} \tilde{\lambda}_L^\psi f \sum_{A<B,K<L<M} \bar{T}^{ABKLM} U^{Mx} \psi^{abkl} \\ & + \tilde{\lambda}_R^\Psi f \sum_{A<B,K<L<M,X} \bar{T}^{ABKLX} U^{Xm} \Psi^{abklm} \\ & + \frac{1}{\sqrt{5}} \tilde{\lambda}_R^\psi f \sum_{A<B,K<L,X} \bar{T}^{ABKLX} (U^{Ll} U^{Xx} - U^{Xl} U^{Lx}) \psi^{abkl}. \end{aligned} \quad (6.34)$$

Here the fields are canonically normalised and we have indicated the $SO(11)$ indices by capital letters. For colour parts of the U matrix we have $U^{Aa} = \delta^{Aa}$, hence they have been omitted. The colour contraction leads to $\sum_{A<B} \bar{T}^{AB} T^{AB} = \bar{T}^1 T^1 + \bar{T}^2 T^2 + \bar{T}^3 T^3$, where 1, 2, 3 are colour labels. This contraction is identical for all quarks and their partners,

therefore a coefficient 3 can be factored out to account for this contraction.

For the remaining $SO(4)$ indices, just like for MCHM in Section 5.1.3, we can write the elementary and composite fields in terms of their components as

$$q_L^{SO(4)} = \frac{1}{\sqrt{2}}(-ib_L, -b_L, -it_L, t_L)^\top, \quad (6.35)$$

$$\Psi_q = \frac{1}{\sqrt{2}}(-iB + iX_{5/3}, -B - X_{5/3}, -iT - iX_{2/3}, T - X_{2/3})^\top, \quad (6.36)$$

$$t_R^{SO(4)} = t_R, \quad (6.37)$$

$$\psi_t = \tilde{T}, \quad (6.38)$$

where the 4 component vector is the fundamental representation of $SO(4)$. For b_R a $\mathbf{6}$ of $SO(4)$ is required. Since $SO(4) \simeq SU(2)_L \times SU(2)_R$, the six generators can be split into two sets as discussed in [37]. The three generators in the defining representation of $SO(4)$ and corresponding to $SU(2)_R$ are given by

$$T_R^1 = -\frac{i}{2} \begin{pmatrix} 0 & 0 & 0 & 1 \\ 0 & 0 & 1 & 0 \\ 0 & -1 & 0 & 0 \\ -1 & 0 & 0 & 0 \end{pmatrix}, \quad T_R^2 = -\frac{i}{2} \begin{pmatrix} 0 & 0 & -1 & 0 \\ 0 & 0 & 0 & -1 \\ 1 & 0 & 0 & 0 \\ 0 & 1 & 0 & 0 \end{pmatrix}, \quad (6.39)$$

$$T_R^3 = -\frac{i}{2} \begin{pmatrix} 0 & 1 & 0 & 0 \\ -1 & 0 & 0 & 0 \\ 0 & 0 & 0 & -1 \\ 0 & 0 & 1 & 0 \end{pmatrix}.$$

We can define these generators in terms of raising and lowering operators using

$$\tau^+ = T_R^1 + iT_R^2, \quad \tau^- = T_R^1 - iT_R^2, \quad \tau^0 = T^3. \quad (6.40)$$

This allows us to write b_R in terms of τ^-

$$b_R^{SO(4)} = b_R \tau^- = \frac{b_R}{2} \begin{pmatrix} 0 & 0 & 1 & i \\ 0 & 0 & -i & 1 \\ -1 & i & 0 & 0 \\ -i & -1 & 0 & 0 \end{pmatrix}, \quad (6.41)$$

and embed its composite partners using all three generators as

$$\begin{aligned} \psi_b &= X_+ \tau^+ + \sqrt{2} X_0 \tau^0 + \tilde{B} \tau^- \\ &= \frac{1}{2} \begin{pmatrix} 0 & -i\sqrt{2} X_0 & \tilde{B} - X_+ & i\tilde{B} + iX_+ \\ i\sqrt{2} X_0 & 0 & -i\tilde{B} - iX_+ & \tilde{B} - X_+ \\ -\tilde{B} + X_+ & i\tilde{B} + iX_+ & 0 & i\sqrt{2} X_0 \\ -i\tilde{B} - iX_+ & -\tilde{B} + X_+ & -i\sqrt{2} X_0 & 0 \end{pmatrix}, \end{aligned} \quad (6.42)$$

where the triplet is (X_+, X_0, \tilde{B}) . The normalisation here is such that $\sum_{K<L} \bar{b}_R^{KL} \bar{b}_R^{KL} = \bar{b}_R b_R$ and so on. We will now proceed to write down the mass matrices.

6.3.5 Mass Matrices: 2-3-4-5 Model

Combining Eq.(6.33) with the field embeddings in the previous section, we can formulate three mass matrices for each isospin.

Isospin 5/3:

$$\begin{pmatrix} \bar{X}_{5/3} \\ \bar{X}'_{5/3} \\ \bar{X}_+ \end{pmatrix}^T \begin{pmatrix} -m_\Psi & 0 & 0 \\ 0 & -m_{\tilde{\Psi}} & 0 \\ 0 & 0 & -m_{\psi_b} \end{pmatrix} \begin{pmatrix} X_{5/3} \\ X'_{5/3} \\ X_+ \end{pmatrix} \quad (6.43)$$

Isospin 2/3:

$$\begin{pmatrix} \bar{t}_L \\ \bar{t}'_L \\ \bar{T}_L \\ \bar{T}'_L \\ \bar{X}_L^{2/3} \\ \bar{X}_L'^{2/3} \\ \bar{X}_L^0 \\ \bar{\tilde{T}}_L \end{pmatrix}^T \begin{pmatrix} 0 & 0 & \frac{(1+c_e)}{2} \lambda_L^\Psi f & 0 & \frac{(1-c_e)}{2} \lambda_L^\Psi f & 0 & 0 & \frac{s_e}{\sqrt{3!}} \lambda_L^\psi f \\ 0 & 0 & \frac{(1+c_e)}{4} \tilde{\lambda}_L^\Psi f & 0 & -\frac{(1-c_e)}{4} \tilde{\lambda}_L^\Psi f & 0 & \frac{s_e}{2} \tilde{\lambda}_L^\psi f & 0 \\ 0 & 0 & -m_\Psi & 0 & 0 & 0 & 0 & 0 \\ 0 & 0 & 0 & -m_{\tilde{\Psi}} & 0 & 0 & 0 & 0 \\ 0 & 0 & 0 & 0 & -m_\Psi & 0 & 0 & 0 \\ 0 & 0 & 0 & 0 & 0 & -m_{\tilde{\Psi}} & 0 & 0 \\ 0 & 0 & 0 & 0 & 0 & 0 & -m_{\psi_b} & 0 \\ \lambda_R^\psi f & 0 & 0 & 0 & 0 & 0 & 0 & -m_{\psi_t} \end{pmatrix} \begin{pmatrix} t_R \\ t'_R \\ T_R \\ T'_R \\ X_R^{2/3} \\ X_R'^{2/3} \\ X_R^0 \\ \tilde{T}_R \end{pmatrix} \quad (6.44)$$

Isospin $(-1/3)$:

$$\begin{pmatrix} \bar{b}_L \\ \bar{b}'_L \\ \bar{B}_L \\ \bar{B}'_L \\ \bar{\bar{B}}_L \end{pmatrix}^T \begin{pmatrix} 0 & 0 & \lambda_L^\Psi f & 0 & 0 \\ 0 & 0 & \frac{c_\epsilon}{2} \tilde{\lambda}_L^\Psi f & 0 & \frac{s_\epsilon}{\sqrt{2}} \tilde{\lambda}_L^\psi f \\ 0 & 0 & -m_\Psi & 0 & 0 \\ \frac{s_\epsilon}{\sqrt{2}} \tilde{\lambda}_R^\Psi f & 0 & 0 & -m_{\tilde{\Psi}} & 0 \\ \frac{(1+c_\epsilon)}{2\sqrt{5}} \tilde{\lambda}_R^\psi f & 0 & 0 & 0 & -m_{\psi_b} \end{pmatrix} \begin{pmatrix} b_R \\ b'_R \\ B_R \\ B'_R \\ \tilde{B}_R \end{pmatrix} \quad (6.45)$$

The t'_R and b'_R fields are completely decoupled, inserted to maintain a square matrix shape. In this model the top mass is generated via a single composite fermion \tilde{T} .

6.3.6 Mass Matrices: 3-3-5-5 Model

In the 3-3-5-5 case mass matrices are obtained from Eq.(6.34) in the same way.

Isospin 5/3:

$$\begin{pmatrix} \bar{X}_{5/3} \\ \bar{X}'_{5/3} \\ \bar{X}_+ \end{pmatrix}^T \begin{pmatrix} -m_\Psi & 0 & 0 \\ 0 & -m_{\tilde{\Psi}} & 0 \\ 0 & 0 & -m_{\psi_b} \end{pmatrix} \begin{pmatrix} X_{5/3} \\ X'_{5/3} \\ X_+ \end{pmatrix} \quad (6.46)$$

Isospin 2/3:

$$\begin{pmatrix} \bar{t}_L \\ \bar{t}'_L \\ \bar{T}_L \\ \bar{T}'_L \\ \bar{X}_L^{2/3} \\ \bar{X}'_L^{2/3} \\ \bar{X}_L^0 \\ \bar{\tilde{T}}_L \end{pmatrix}^T \begin{pmatrix} 0 & 0 & \frac{(1+c_\epsilon)}{2} \lambda_L^\Psi f & 0 & \frac{(1-c_\epsilon)}{2} \lambda_L^\Psi f & 0 & 0 & \frac{s_\epsilon}{\sqrt{3}} \lambda_L^\psi f \\ 0 & 0 & 0 & \frac{(1+c_\epsilon)}{2} \tilde{\lambda}_L^\Psi f & 0 & -\frac{(1-c_\epsilon)}{2} \tilde{\lambda}_L^\Psi f & -\frac{s_\epsilon}{2\sqrt{5}} \tilde{\lambda}_L^\psi f & 0 \\ -\frac{s_\epsilon}{\sqrt{2}} \lambda_R^\Psi f & 0 & -m_\Psi & 0 & 0 & 0 & 0 & 0 \\ 0 & 0 & 0 & -m_{\tilde{\Psi}} & 0 & 0 & 0 & 0 \\ \frac{s_\epsilon}{\sqrt{2}} \lambda_R^\Psi f & 0 & 0 & 0 & -m_\Psi & 0 & 0 & 0 \\ 0 & 0 & 0 & 0 & 0 & -m_{\tilde{\Psi}} & 0 & 0 \\ 0 & 0 & 0 & 0 & 0 & 0 & -m_{\psi_b} & 0 \\ \frac{c_\epsilon}{\sqrt{3}} \lambda_R^\psi f & 0 & 0 & 0 & 0 & 0 & 0 & -m_{\psi_t} \end{pmatrix} \begin{pmatrix} t_R \\ t'_R \\ T_R \\ T'_R \\ X_R^{2/3} \\ X_R'^{2/3} \\ X_R^0 \\ \tilde{T}_R \end{pmatrix} \quad (6.47)$$

Isospin $(-1/3)$:

$$\begin{pmatrix} \bar{b}_L \\ \bar{b}'_L \\ \bar{B}_L \\ \bar{B}'_L \\ \bar{\bar{B}}_L \end{pmatrix}^T \begin{pmatrix} 0 & 0 & \lambda_L^\Psi f & 0 & 0 \\ 0 & 0 & 0 & c_\epsilon \tilde{\lambda}_L^\Psi f & -\frac{s_\epsilon}{\sqrt{10}} \tilde{\lambda}_L^\psi f \\ 0 & 0 & -m_\Psi & 0 & 0 \\ \frac{s_\epsilon}{\sqrt{2}} \tilde{\lambda}_R^\Psi f & 0 & 0 & -m_{\tilde{\Psi}} & 0 \\ \frac{(1+c_\epsilon)}{2\sqrt{5}} \tilde{\lambda}_R^\psi f & 0 & 0 & 0 & -m_{\psi_b} \end{pmatrix} \begin{pmatrix} b_R \\ b'_R \\ B_R \\ B'_R \\ \tilde{B}_R \end{pmatrix} \quad (6.48)$$

6.3.7 Simplified Mass Matrices

We have shown that one can successfully embed the elementary and composite fields into a $SO(11)/SO(10)$ gauge group and write down the mass matrices for them. As such it has been demonstrated that we can have two separate doublets coupling primarily to t_R and b_R respectively. This means the mixings corresponding to the latter could be smaller, in order to facilitate the smaller bottom quark mass. Moving onwards, we are going to neglect the contributions coming from b_R and the second bi-doublet for this reason. Thus, we will present the mass matrices simplified under this assumption.

Mass Matrices: 2-3 Model

Isospin 5/3:

$$\left(\bar{X}_{5/3}\right)^T \left(-m_\Psi\right) \left(X_{5/3}\right). \quad (6.49)$$

Isospin 2/3:

$$\begin{pmatrix} \bar{t}_L \\ \bar{T}_L \\ \bar{X}_L^{2/3} \\ \bar{\tilde{T}}_L \end{pmatrix}^T \begin{pmatrix} 0 & \frac{1}{2}(1+c_\epsilon)\lambda_L^\Psi f & \frac{1}{2}(1-c_\epsilon)\lambda_L^\Psi f & \frac{1}{\sqrt{3!}}s_\epsilon\lambda_L^\psi f \\ 0 & -m_\Psi & 0 & 0 \\ 0 & 0 & -m_\Psi & 0 \\ \lambda_R^\psi f & 0 & 0 & -m_{\psi_t} \end{pmatrix} \begin{pmatrix} t_R \\ T_R \\ X_R^{2/3} \\ \tilde{T}_R \end{pmatrix}. \quad (6.50)$$

Isospin (-1/3):

$$\begin{pmatrix} \bar{b}_L \\ \bar{B}_L \end{pmatrix}^T \begin{pmatrix} 0 & \lambda_L^\Psi f \\ 0 & -m_\Psi \end{pmatrix} \begin{pmatrix} b'_R \\ B_R \end{pmatrix}. \quad (6.51)$$

This is similar to the MCHM **5+1** model with fully composite t_R .

Mass Matrices: 3-3 Model

Isospin 5/3:

$$\left(\bar{X}_{5/3}\right)^T \left(-m_\Psi\right) \left(X_{5/3}\right). \quad (6.52)$$

Isospin 2/3:

$$\begin{pmatrix} \bar{t}_L \\ \bar{T}_L \\ \bar{X}_L^{2/3} \\ \bar{\tilde{T}}_L \end{pmatrix}^T \begin{pmatrix} 0 & \frac{1}{2}(1+c_\epsilon)\lambda_L^\Psi f & \frac{1}{2}(1-c_\epsilon)\lambda_L^\Psi f & \frac{1}{\sqrt{3!}}s_\epsilon\lambda_L^\psi f \\ -\frac{1}{\sqrt{2}}s_\epsilon\lambda_R^\Psi f & -m_\Psi & 0 & 0 \\ \frac{1}{\sqrt{2}}s_\epsilon\lambda_R^\Psi f & 0 & -m_\Psi & 0 \\ \frac{1}{\sqrt{3}}c_\epsilon\lambda_R^\psi f & 0 & 0 & -m_{\psi_t} \end{pmatrix} \begin{pmatrix} t_R \\ T_R \\ X_R^{2/3} \\ \tilde{T}_R \end{pmatrix}. \quad (6.53)$$

Isospin $(-1/3)$:

$$\begin{pmatrix} \bar{b}_L \\ \bar{B}_L \end{pmatrix}^T \begin{pmatrix} 0 & \lambda_L^\Psi f \\ 0 & -m_\Psi \end{pmatrix} \begin{pmatrix} b'_R \\ B_R \end{pmatrix}. \quad (6.54)$$

In this case, the model corresponds to the MCHM 5+5 model. We can obtain the MCHM $\mathbf{5}+\mathbf{5}$ model by $\lambda_L^\psi \rightarrow \sqrt{3}\lambda_L^\psi$ and $\lambda_R^\psi \rightarrow \sqrt{3}\lambda_R^\psi$.

6.3.8 Mass Matrix Diagonalization

In Section 5.1.3 we gave several examples of mass diagonalization for simplified models. In comparison our isospin 2/3 matrices for the 2-3 and 3-3 models, given in the previous section, cannot be analytically diagonalised without making any approximations. Hence, we employ bi-unitary diagonalization numerically.

We can perform a bi-unitary transformation on a complex asymmetric square matrix M as

$$D = U^\dagger M V, \quad (6.55)$$

where U and V are unitary matrices and D is diagonal. We can then write

$$D D^\dagger = U^\dagger M M^\dagger U, \quad (6.56)$$

$$D^\dagger D = V^\dagger M^\dagger M V, \quad (6.57)$$

where $M M^\dagger$ and $M^\dagger M$ are Hermitian. Then U and V can be obtained by diagonalising the corresponding products of M .

Once we have diagonalised our mass matrices we can read-off the masses of top t as well as the five composite fields: $\tilde{T}, T, B, X_{2/3}$ and $X_{5/3}$. Requirement to generate the correct top mass gives a constraint on the masses m_ψ , m_Ψ and couplings λ^ψ , λ^Ψ . For $\xi \ll 1$ this can be written as

$$m_t^2 = \frac{(\lambda_L^\psi \lambda_R^\psi m_\Psi - \lambda_L^\Psi \lambda_R^\Psi m_\psi)^2 f^4 \xi}{2(m_\Psi^2 + (\lambda_L^\Psi)^2 f^2)(m_\psi^2 + (\lambda_R^\psi)^2 f^2)} + \mathcal{O}(\xi^2), \quad (6.58)$$

which has been obtained in [37]. If we set $\lambda_R^\Psi = \lambda_R^\psi = \lambda_R$ and $\lambda_L^\Psi = \lambda_L^\psi = \lambda_L$ this can be put in the form

$$a = (1 - x^2)(x - x_0)^2, \quad (6.59)$$

where $x = m_\psi/(m_\psi^2 + (\lambda_R)^2 f^2)$, $x_0 = m_\Psi/(m_\psi^2 + (\lambda_R)^2 f^2)$ and

$$a = \frac{2m_t^2(m_\Psi^2 + (\lambda_L)^2 f^2)}{(\lambda_L)^2 f^2(m_\psi^2 + (\lambda_R)^2 f^2)}. \quad (6.60)$$

This is a quartic polynomial for x . As we will see in the results, for the 3-3 model this will give at most two distinct solutions for m_ψ .

As all these masses and mixings also enter the Higgs potential, it is generally not true that most combinations of these parameters can generate a realistic EWSB and correct Higgs mass. As a result we have to compute the Higgs potential in order to obtain a second constraint on our parameter space. We will discuss this in the next section.

6.4 Higgs Potential

The Higgs potential receives two main contributions: from gauge bosons and from fermions. In this section, we will derive the potential for our 2-3-4-5 and 3-3-5-5 models. Since we are interested in the coloured NGB mass, we will not neglect them this time.

6.4.1 Gauge Contribution

Following [102, 164], we can integrate out the vector resonances at tree level and write down the effective Lagrangian \mathcal{L}_{eff} for the elementary gauge bosons A^μ as

$$\mathcal{L}_{\text{eff}}^g = \frac{1}{2} \left(g_{\mu\nu} - \frac{p_\mu p_\nu}{p^2} \right) (\Pi_0(p) \text{Tr}(A^\mu A^\nu) + \Pi_1(p) \Sigma A^\mu A^\nu \Sigma^\top), \quad (6.61)$$

where p is Euclidean momentum and $\Sigma = U \Sigma_0$, with $\Sigma_0 = (0, \dots, 0, 1)^\top$. $\Pi_0(p)$ and $\Pi_1(p)$ are the non-perturbative form factors that encode the strong sector dynamics. The gauge bosons generate the Higgs potential, for which at one-loop we have

$$\begin{aligned} V_{\text{gauge}}(h) &= \frac{9}{2} \int_0^{m_*^2} \frac{dp^2}{(4\pi)^2} p^2 \log \left(\Pi_0(p) + \frac{h^2}{4} \Pi_1(p) \right) \\ &+ 8 \frac{3}{2} \int_0^{m_*^2} \frac{dp^2}{(4\pi)^2} p^2 \log \left(\Pi_0(p) + \frac{\mathcal{T}^2}{2} \Pi_1(p) \right). \end{aligned} \quad (6.62)$$

The form factors are given by

$$\Pi_0 = \frac{p^2}{g^2} + \Pi_a, \quad (6.63) \quad \Pi_1 = 2(\Pi_{\hat{a}} - \Pi_a), \quad (6.65)$$

$$\Pi_a = p^2 \frac{f_\rho^2}{p^2 + m_\rho^2}, \quad (6.64) \quad \Pi_{\hat{a}} = p^2 \frac{f_a^2}{p^2 + m_a^2} + \frac{f^2}{2}, \quad (6.66)$$

where g is the weak coupling, while a and ρ are the vector resonances from the broken and unbroken sectors respectively. The SM contribution, for subtraction of the IR divergence, is obtained by setting $\Pi_0 = p^2/g^2$ and $\Pi_1 = f^2$.

6.4.2 Fermion Contribution

Integrating out the composite states and using the mixings and mass terms given in Eqs.(6.32-6.34), we can write down the effective Lagrangian as

$$\mathcal{L}_{eff} = \bar{t}_L \not{p} \mathcal{M}_{LL}^t t_L + \bar{t}_R \not{p} \mathcal{M}_{RR}^t t_R + (\bar{t}_L \mathcal{M}_{LR}^t t_R + \text{h.c.}). \quad (6.67)$$

The fermion contribution to the Higgs potential is given by

$$V = -\frac{g}{2} \int \frac{d^4 p}{(2\pi)^4} (\log \det \mathcal{M}^t), \quad (6.68)$$

where $g = 4$ counts the degrees of freedom (as we treat t_L etc. as Dirac fermions), p is an euclidean momentum, \mathcal{M}^t is the two-point functions appearing in the effective Lagrangian for top quark and the overall minus sign comes from the fermion statistics. We neglect the bottom part, as we expect it to be suppressed by the elementary-composite mixings, and focus on the 2-3 and 3-3 parts of the model. Keeping terms with up to three powers in the NGBs for the 2-3 case we get

$$\begin{aligned} (\mathcal{M}_{LL}^t)^{ij} &= \delta^{ij} - \delta^{ij} \frac{|\lambda_L^\Psi|^2 f^2}{(p^2 - m_\Psi^2)} \\ &+ \left(\frac{h^2}{2} \delta^{ij} + |\mathcal{T}|^2 \delta^{ij} - \mathcal{T}^i \mathcal{T}^{*j} \right) \left(\frac{|\lambda_L^\Psi|^2 f^2}{(p^2 - m_\Psi^2)} - \frac{|\lambda_L^\psi|^2 f^2}{3(p^2 - m_\psi^2)} \right), \end{aligned} \quad (6.69)$$

$$\begin{aligned} (\mathcal{M}_{RR}^t)^{ij} &= \delta^{ij} - \delta^{ij} \frac{|\lambda_R^\psi|^2 f^2}{(p^2 - m_\psi^2)} \\ &+ (|\mathcal{T}|^2 \delta^{ij} - \mathcal{T}^i \mathcal{T}^{*j}) \left(\frac{|\lambda_R^\psi|^2 f^2}{(p^2 - m_\psi^2)} - \frac{|\lambda_R^{\hat{\psi}}|^2 f^2}{2(p^2 - m_{\hat{\psi}}^2)} \right), \end{aligned} \quad (6.70)$$

$$(\mathcal{M}_{LR}^t)^{ij} = -\delta^{ij} \frac{h}{\sqrt{2}} \frac{m_\psi \lambda_R^{*\psi} \lambda_L^\psi f^2}{\sqrt{3}(p^2 - m_\psi^2)}, \quad (6.71)$$

where we have introduced an additional one-index composite partner $\hat{\psi}$, which results in contribution to colour pNGBs only. In the 3-3 model we obtain

$$(\mathcal{M}_{LL}^t)^{ij} = \delta^{ij} - \delta^{ij} \frac{|\lambda_L^\Psi|^2 f^2}{(p^2 - m_\Psi^2)} + \left(\frac{h^2}{2} \delta^{ij} + |\mathcal{T}|^2 \delta^{ij} - \mathcal{T}^i \mathcal{T}^{*j} \right) \left(\frac{|\lambda_L^\Psi|^2 f^2}{(p^2 - m_\Psi^2)} - \frac{|\lambda_L^\psi|^2 f^2}{3(p^2 - m_\psi^2)} \right), \quad (6.72)$$

$$(\mathcal{M}_{RR}^t)^{ij} = \delta^{ij} - \delta^{ij} \frac{|\lambda_R^\psi|^2 f^2}{3(p^2 - m_\psi^2)} + (h^2 \delta^{ij} + |\mathcal{T}|^2 \delta^{ij} + \mathcal{T}^i \mathcal{T}^{*j}) \left(\frac{|\lambda_R^\psi|^2 f^2}{3(p^2 - m_\psi^2)} - \frac{|\lambda_R^\Psi|^2 f^2}{(p^2 - m_\Psi^2)} \right), \quad (6.73)$$

$$(\mathcal{M}_{LR}^t)^{ij} = -\delta^{ij} \frac{(h - h^3/2 - h|\mathcal{T}|^2)}{\sqrt{2}} \left(\frac{m_\psi \lambda_R^{*\psi} \lambda_L^\psi f^2}{3(p^2 - m_\psi^2)} - \frac{m_\Psi \lambda_R^{*\Psi} \lambda_L^\Psi f^2}{(p^2 - m_\Psi^2)} \right). \quad (6.74)$$

The relative factors of 1/3 and 1/2 between the different composite fermion contributions are due to combinatorics. Moving forward we will redefine $\lambda_R^\psi \rightarrow \sqrt{3}\lambda_R^\psi$ for the 3-3 model, $\lambda_L^{\hat{\psi}} \rightarrow \sqrt{2}\lambda_L^{\hat{\psi}}$ for the 2-3 model and $\lambda_L^\psi \rightarrow \sqrt{3}\lambda_L^\psi$ for both models.

Form Factors

In order to compute the integrand of Eq.(6.67), it is convenient to introduce form factors. For the 2-3 model we have

$$(\mathcal{M}_{LL}^t)^{ij} = \Pi_0^q \delta^{ij} + \Pi_1^q \left(\frac{h^2}{2} \delta^{ij} + |\mathcal{T}|^2 \delta^{ij} - \mathcal{T}^i \mathcal{T}^{*j} \right), \quad (6.75)$$

$$(\mathcal{M}_{RR}^t)^{ij} = \Pi_0^t \delta^{ij} + \Pi_1^t (|\mathcal{T}|^2 \delta^{ij} - \mathcal{T}^i \mathcal{T}^{*j}), \quad (6.76)$$

$$(\mathcal{M}_{LR}^t)^{ij} = \frac{M_0^t}{\sqrt{2}} \delta^{ij} h, \quad (6.77)$$

and in the 3-3 case they read

$$(\mathcal{M}_{LL}^t)^{ij} = \Pi_0^q \delta^{ij} + \Pi_1^q \left(\frac{h^2}{2} \delta^{ij} + |\mathcal{T}|^2 \delta^{ij} - \mathcal{T}^i \mathcal{T}^{*j} \right), \quad (6.78)$$

$$(\mathcal{M}_{RR}^t)^{ij} = \Pi_0^t \delta^{ij} + \Pi_1^t (h^2 \delta^{ij} + |\mathcal{T}|^2 \delta^{ij} + \mathcal{T}^i \mathcal{T}^{*j}), \quad (6.79)$$

$$(\mathcal{M}_{LR}^t)^{ij} = \frac{M_0^t}{\sqrt{2}} \left(h - \frac{h^3}{2} - h|\mathcal{T}|^2 \right) \delta^{ij}, \quad (6.80)$$

where the h^3 dependence in $(\mathcal{M}_{LR}^t)^{ij}$ is retained, as it contributes to the quartic Higgs coupling. The form factors for the 2-3 model are given by

$$\Pi_0^q = 1 + \frac{|\lambda_L^\Psi|^2 f^2}{(p^2 + m_\Psi^2)}, \quad (6.81)$$

$$\Pi_0^t = 1 + \frac{|\lambda_R^\psi|^2 f^2}{(p^2 + m_\psi^2)}, \quad (6.82)$$

$$M_0^t = \frac{m_\psi \lambda_R^{*\psi} \lambda_L^\psi f^2}{(p^2 + m_\psi^2)}, \quad (6.83)$$

$$\Pi_1^q = \frac{|\lambda_L^\psi|^2 f^2}{(p^2 + m_\psi^2)} - \frac{|\lambda_L^\Psi|^2 f^2}{(p^2 + m_\Psi^2)}, \quad (6.84)$$

$$\Pi_1^t = \frac{|\lambda_R^\psi|^2 f^2}{(p^2 + m_\psi^2)} - \frac{|\lambda_R^\Psi|^2 f^2}{(p^2 + m_\Psi^2)}, \quad (6.85)$$

and for the 3-3 model we have

$$\Pi_0^q = 1 + \frac{|\lambda_L^\Psi|^2 f^2}{(p^2 + m_\Psi^2)}, \quad (6.86)$$

$$\Pi_0^t = 1 + \frac{|\lambda_R^\psi|^2 f^2}{(p^2 + m_\psi^2)}, \quad (6.87)$$

$$M_0^t = \frac{m_\psi \lambda_R^{*\psi} \lambda_L^\psi f^2}{(p^2 + m_\psi^2)} - \frac{m_\Psi \lambda_R^{*\Psi} \lambda_L^\Psi f^2}{(p^2 + m_\Psi^2)}, \quad (6.88)$$

$$\Pi_1^q = \frac{|\lambda_L^\psi|^2 f^2}{(p^2 + m_\psi^2)} - \frac{|\lambda_L^\Psi|^2 f^2}{(p^2 + m_\Psi^2)}, \quad (6.89)$$

$$\Pi_1^t = \frac{|\lambda_R^\Psi|^2 f^2}{(p^2 + m_\Psi^2)} - \frac{|\lambda_R^\psi|^2 f^2}{(p^2 + m_\psi^2)}, \quad (6.90)$$

after Wick rotation.

The Integrand

Next, we expand the integrand of Eq.(6.67) we around $h = 0$ and $|\mathcal{T}| = 0$. Keeping only the leading h^2 , $|\mathcal{T}|^2$, h^4 and $|\mathcal{T}|^4$ terms, for the 2-3 model we obtain

$$\begin{aligned} \log \det \mathcal{M}^t &= 3 \frac{((M_0^t)^2 + p^2 \Pi_1^q \Pi_0^t)}{2p^2 \Pi_0^q \Pi_0^t} h^2 - \frac{3}{8} \frac{((M_0^t)^2 + p^2 \Pi_1^q \Pi_0^t)^2}{p^4 (\Pi_0^q)^2 (\Pi_0^t)^2} h^4 \\ &+ 2 \frac{(\Pi_0^q \Pi_1^t + \Pi_1^q \Pi_0^t)}{\Pi_0^q \Pi_0^t} |\mathcal{T}|^2 - \frac{((\Pi_0^q)^2 (\Pi_1^t)^2 + (\Pi_1^q)^2 (\Pi_0^t)^2)}{(\Pi_0^q)^2 (\Pi_0^t)^2} |\mathcal{T}|^4 \\ &- \frac{(((M_0^t)^2 (\Pi_0^q \Pi_1^t + \Pi_1^q \Pi_0^t) + p^2 (\Pi_1^q)^2 (\Pi_0^t)^2))}{p^2 (\Pi_0^q)^2 (\Pi_0^t)^2} h^2 |\mathcal{T}|^2 + \dots, \end{aligned} \quad (6.91)$$

and for the 3-3 model we find

$$\begin{aligned} \log \det \mathcal{M}^t &= 3 \frac{((M_0^t)^2 + p^2 (2\Pi_0^q \Pi_1^t + \Pi_1^q \Pi_0^t))}{2p^2 \Pi_0^q \Pi_0^t} h^2 \\ &- \frac{3}{8} \frac{((M_0^t)^4 + 2(M_0^t)^2 p^2 (2\Pi_0^q \Pi_1^t + \Pi_1^q \Pi_0^t) + 2\Pi_0^q \Pi_0^t)}{p^4 (\Pi_0^q)^2 (\Pi_0^t)^2} h^4 \\ &- \frac{3}{8} \frac{4p^4 ((\Pi_0^q)^2 (\Pi_1^t)^2 + (\Pi_1^q)^2 (\Pi_0^t)^2)}{p^4 (\Pi_0^q)^2 (\Pi_0^t)^2} h^4 \\ &+ 2 \frac{(2\Pi_0^q \Pi_1^t + \Pi_1^q \Pi_0^t)}{\Pi_0^q \Pi_0^t} |\mathcal{T}|^2 - \frac{(3(\Pi_0^q)^2 (\Pi_1^t)^2 + (\Pi_1^q)^2 (\Pi_0^t)^2)}{(\Pi_0^q)^2 (\Pi_0^t)^2} |\mathcal{T}|^4 \\ &- \frac{((M_0^t)^2 (2\Pi_0^q \Pi_1^t + \Pi_1^q \Pi_0^t) + 3\Pi_0^q \Pi_0^t)}{p^2 (\Pi_0^q)^2 (\Pi_0^t)^2} h^2 |\mathcal{T}|^2 \\ &- \frac{p^2 (4(\Pi_1^t)^2 (\Pi_0^q)^2 + (\Pi_1^q)^2 (\Pi_0^t)^2)}{p^2 (\Pi_0^q)^2 (\Pi_0^t)^2} h^2 |\mathcal{T}|^2 + \dots \end{aligned} \quad (6.92)$$

By comparing to [37], we can see that our h^2 and h^4 terms for the 3-3 model agree with **5+5** MCHM.

Higgs Potential

We can now extend the expression for Higgs potential, given in Eq.(5.46), to include the coloured NGBs, with additional coefficients γ , δ and ϵ , as

$$V = -\frac{4}{32\pi^2} \int_0^\infty dp^2 p^2 (\log \det \mathcal{M}^t) = \alpha h^2 + \beta h^4 + \gamma |\mathcal{T}|^2 + \delta |\mathcal{T}|^4 + \epsilon h^2 |\mathcal{T}|^2 + \dots \quad (6.93)$$

Contribution from the gauge can also be expanded in this way. Each term can be integrated in the logarithm of the determinant separately. The coefficient β contains logarithmic UV divergences, some of which are cancelled by imposing $\lambda_L^\Psi = \lambda_L^\psi$, $\lambda_R^\Psi = \lambda_R^\psi$ and $f_a^2 = f_\rho^2 - f^2/2$, which are equivalent to Weinberg sum rules in QCD [37]. This also takes care of the quadratic divergences in the α . The remaining divergences are regularised using a cut-off equal to the gauge boson mass $m_* = 2.5$ TeV. We also evolve the quartic from m_* to m_{top} by adding an SM contribution obtained by setting $p^2 \rightarrow 0$ in the form factors and $p^2 \Pi_1 \rightarrow 0$ in the logarithm of the determinant and integrated between m_{top} and m_* .

Coloured pNGB Mass

We can obtain the mass of the coloured pNGB from Eq.(6.93). It is simply given by

$$m_{NGB}^2 = \left. \frac{\partial^2 V}{f^2 (\partial \mathcal{T} \partial \mathcal{T}^*)} \right|_{h=\frac{v}{f}, \mathcal{T}=0} = \gamma/f^2 + \epsilon v^2/f^4, \quad (6.94)$$

which is taken from [163].

6.5 T Parameter

In addition to reproducing the correct top mass and EWSB, composite Higgs models also have to pass the constraints on the oblique parameters, defined in Section 5.3.2. In particular, we focus on the fermion contribution to the T parameter as it is the most sensitive to the field content of our models. The expressions in Eqs.(5.54-5.57) that involve the remaining contributions to S and T hold for our models as well.

To compute the fermion contribution to the T parameter we first diagonalise (Section 6.3.8) the mass matrices, given in Section 6.3.7. We then take the currents we derived in Eqs.(5.70, 5.71) and rotate them to the physical mass basis using the diagonalising

matrices U and V . As discussed in 5.3.2 we insert the currents into the vertices of the vacuum polarisation diagram and integrate over the loop. For Eq.(5.58) we can then obtain the amplitudes A_{ij} , which go directly into the expression for the T parameter in Eq.(5.51).

6.6 Results

In this section we present results for our 3-3 and 2-3 models computed with the Weinberg sum rules imposed, i.e. $\lambda_L^\Psi = \lambda_L^\psi = \lambda_L$, $\lambda_R^\Psi = \lambda_R^\psi = \lambda_R$ and $f_a^2 = f_\rho^2 - f^2/2$. Our 3-3 model has a priori six complex parameters: four elementary-composite mixing terms and two composite masses. A universal rephasing of all six chiral fermion fields leaves them unchanged, such that the remaining five phases can be chosen to eliminate some of the parameter degrees of freedom. Hence, we allow m_ψ to take negative values, while the remaining masses and mixings are real and positive. The parameter scan is generated with $\xi = 0.05 \pm 10\%$, $m_\Psi \in [1, 3]$ TeV, $m_\psi \in [-3, 3]$ TeV for 3-3 and $m_\psi \in [0, 3]$ TeV for 2-3 models, as well as $\lambda_L \in [0, 2]$ and $\lambda_R \in [0, 2]$. For the gauge contribution, we have $f_\rho \in [550, 1550]$ GeV and $m_a \in [1.5, 3]$ TeV with $m_\rho = 2.5$ TeV, $g = 0.6$ and $f = v/\sqrt{\xi}$, where $v = 246$ GeV. Moreover, we take $m_* = 5$ TeV. Each parameter point of the models is required to reproduce correct top (Section 6.3.8) and Higgs masses $m_t = 150$ GeV $\pm 10\%$ and $m_h = 126$ GeV $\pm 10\%$. We note that for the 3-3 model the m_t constraint can be satisfied for up to two values of m_ψ , as discussed in Section 6.3.8. Hence, we will be denoting the points corresponding to the two solutions by different shades of blue.

We start by comparing the gauge and fermion contributions. Then we investigate what effect the Higgs and top mass constraints have on our parameter space. We also look at how the Higgs mass and T depend on the parameter space. Finally, we compare our models with available experimental bounds on fermion masses, S and T parameters as well as compute the coloured pNGB mass.

6.6.1 Gauge versus Fermion Contribution

In Figure 6.1 we present the gauge and fermion contributions to the coefficients α and β of the Higgs potential. Here we use the Higgs field basis from [37], which is also given in Eq.(5.46). The potential has the form

$$V[H] = -\alpha' f^2 \sin^2 \frac{H}{f} + \beta' f^2 \sin^4 \frac{H}{f}. \quad (6.95)$$

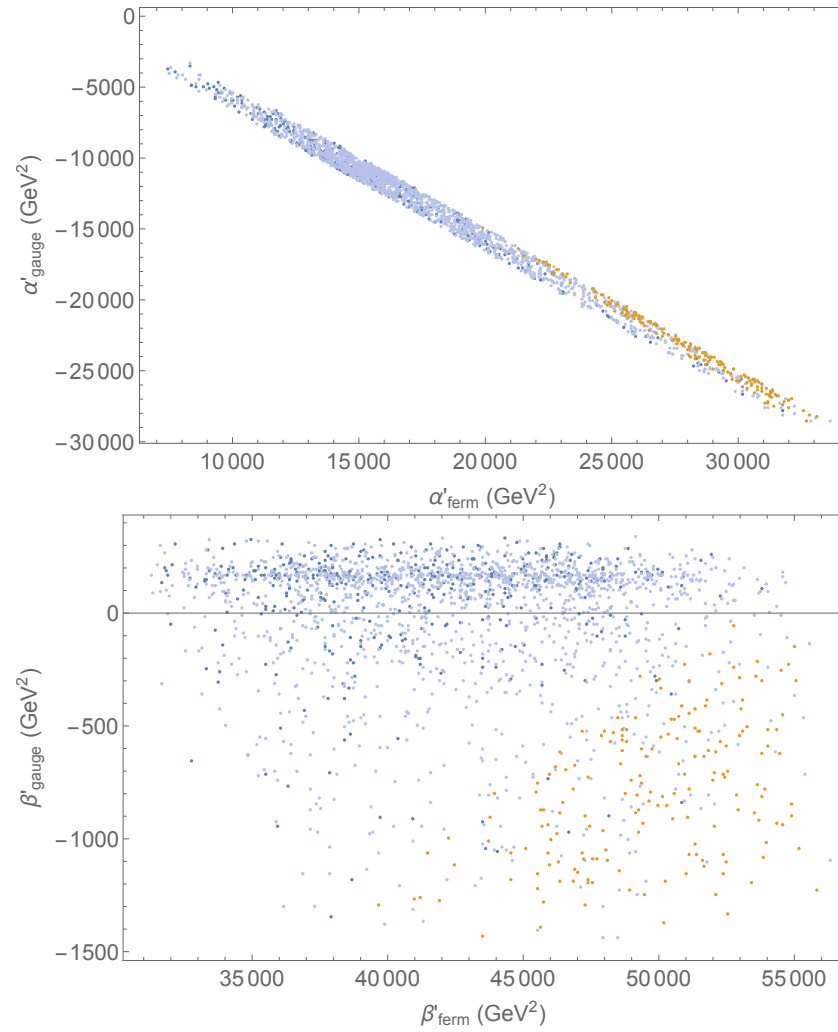


Figure 6.1: Gauge vs. fermion contribution to $\alpha' = -\alpha/f^2$ (above) and $\beta' = -\beta/f^2$ (below) for the 3-3 model (blue and light blue) and the 2-3 model (yellow).

This can be obtained by setting the coloured NGB fields to zero and $h^2 = \sin^2(H/f) = v^2/f^2 = \xi$ with $v = 246$ GeV. Hence, $\alpha' = -\alpha/f^2$ and $\beta' = \beta/f^2$.

We find that the fermion contribution to the Higgs potential dominates due to the large elementary-composite mixings required to reproduce the mass of the top quark as in the MCHM. Furthermore, the gauge sector alone cannot generate the EWSB as α_{gauge} is positive [102, 164]. Figure 6.1 implies that the gauge contribution to α can be just as big as the fermionic one, hence it is important to include it. This strong correlation is necessary to reproduce the value of α required for correct EWSB and Higgs mass. We accept a large range of values for both contributions. As a result a certain degree of fine-tuning is introduced by requiring the two contributions to cancel precisely. For β on the other hand, the gauge contribution is comparably smaller and could be neglected. This also leads to a smaller range for the accepted values of β'_{ferm} . In addition, we notice that 2-3 models tend to give larger values for α than the 3-3 model. As we will see in the following sections, this is due to the smaller range of allowed values for the elementary-composite mixings in the 2-3 model as opposed to the 3-3 one.

6.6.2 Higgs and Top Mass Constraints

Requiring that our models give the correct Higgs and top masses imposes two constraints on our variables. In Figure 6.2, we show how the two composite masses and the two elementary-composite mixings are correlated. We see that for the 2-3 model we have $m_\psi \sim m_\Psi$. On the other hand, for the 3-3 they do not seem to be correlated at all for the heavier m_ψ solution (Section 6.3.8). For lighter m_ψ , we see a smaller correlation with m_Ψ compared to the 2-3 model.

For the mixings we observe an even larger difference between the two models. In the 2-3 case the top mass is generated only via ψ , hence both elementary-composite mixing parameters have to be sufficiently sizeable. In combination with approximately equal composite masses the larger values and more narrow ranges for α_{ferm} and β_{ferm} in the 2-3 model are explained. In the 3-3 model, both Ψ and ψ contribute to the top mass in Eq.(6.58), which depends on both mixings as well as the mass difference between the two composite partners. Hence, for smaller masses we see that both mixings can be sizeable simultaneously. On the other hand, for larger m_ψ solutions, the top mass constraint enforces that only one of the two mixings can be large at a time, while the other one has to be smaller.

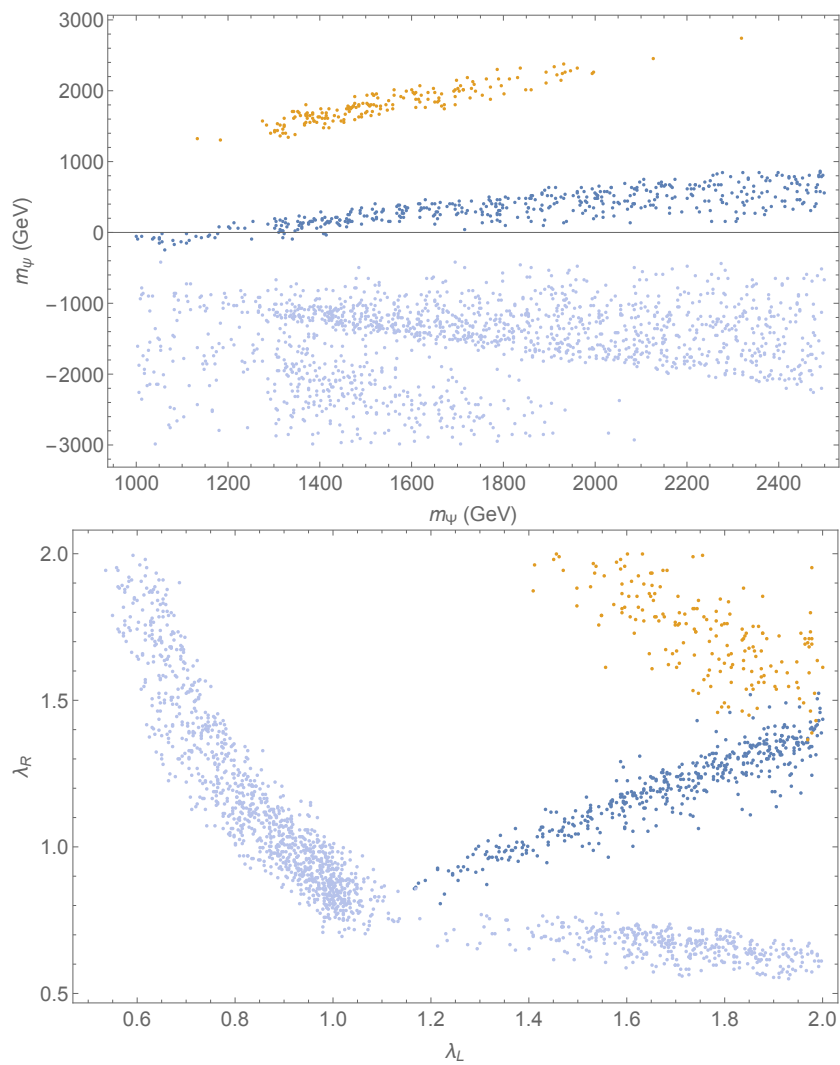


Figure 6.2: m_ψ vs. m_Ψ (above) and λ_R vs. λ_L (below) for the 3-3 model (blue and light blue) and the 2-3 model (yellow).

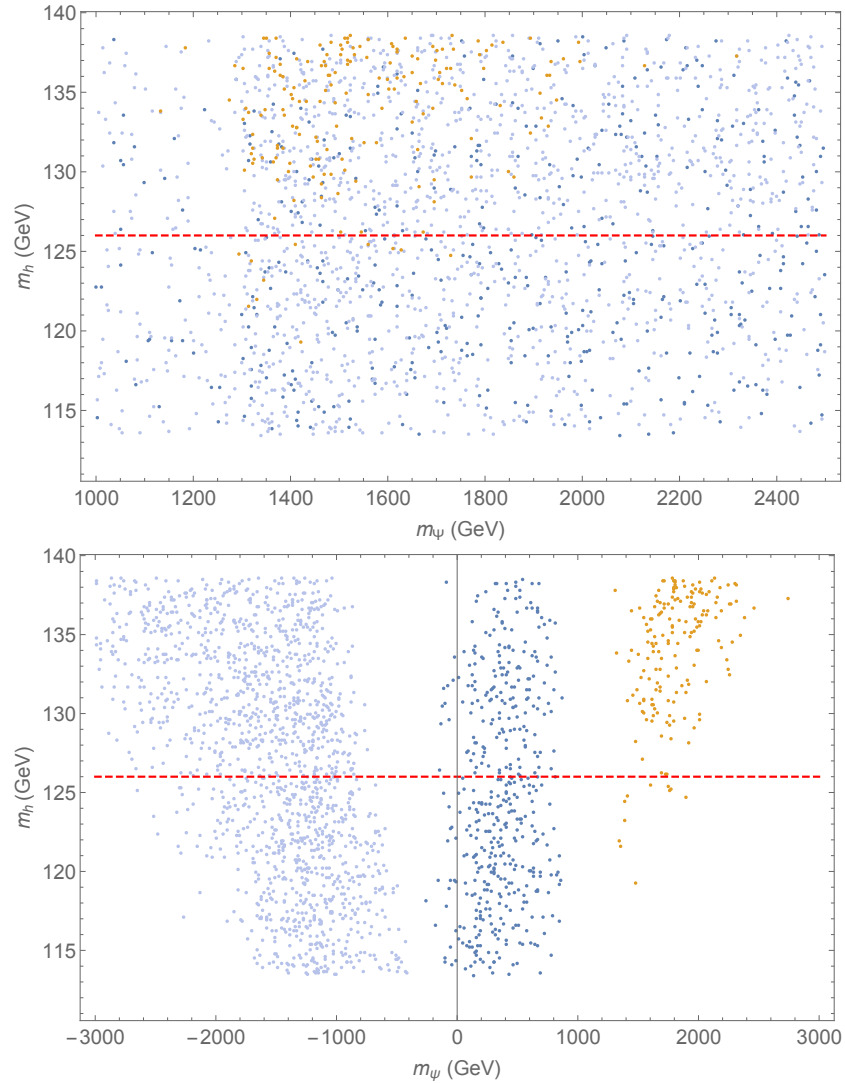


Figure 6.3: Higgs mass vs. m_Ψ , m_ψ (above and below respectively). Red dashed line marks the $m_h = 126$ GeV. The 3-3 model is blue and light blue and the 2-3 model is yellow.

6.6.3 Higgs Mass versus Composite Masses and Mixings

We have seen in the previous sections that Higgs and top mass constraints tend to favour larger mixings for the 2-3 model, while also forcing the ratio of the composite partner masses to remain relatively constant. This has resulted in larger values for α_{ferm} and β_{ferm} as compared to the 3-3 model. As $m_h^2 \propto \beta \propto \alpha$, similar dependences hold for the Higgs mass as well. In particular, Figures 6.3 and 6.4 suggest a slight correlation in m_h for larger values of m_ψ , m_Ψ , λ_L or λ_R . On the other hand, for the 3-3 model we do not observe any strong correlation between the Higgs mass and these parameters. This is due to the fact that either of the two composite partners can give the dominant contribution to the Higgs and the top masses. In the end, only the difference between the two masses matters,

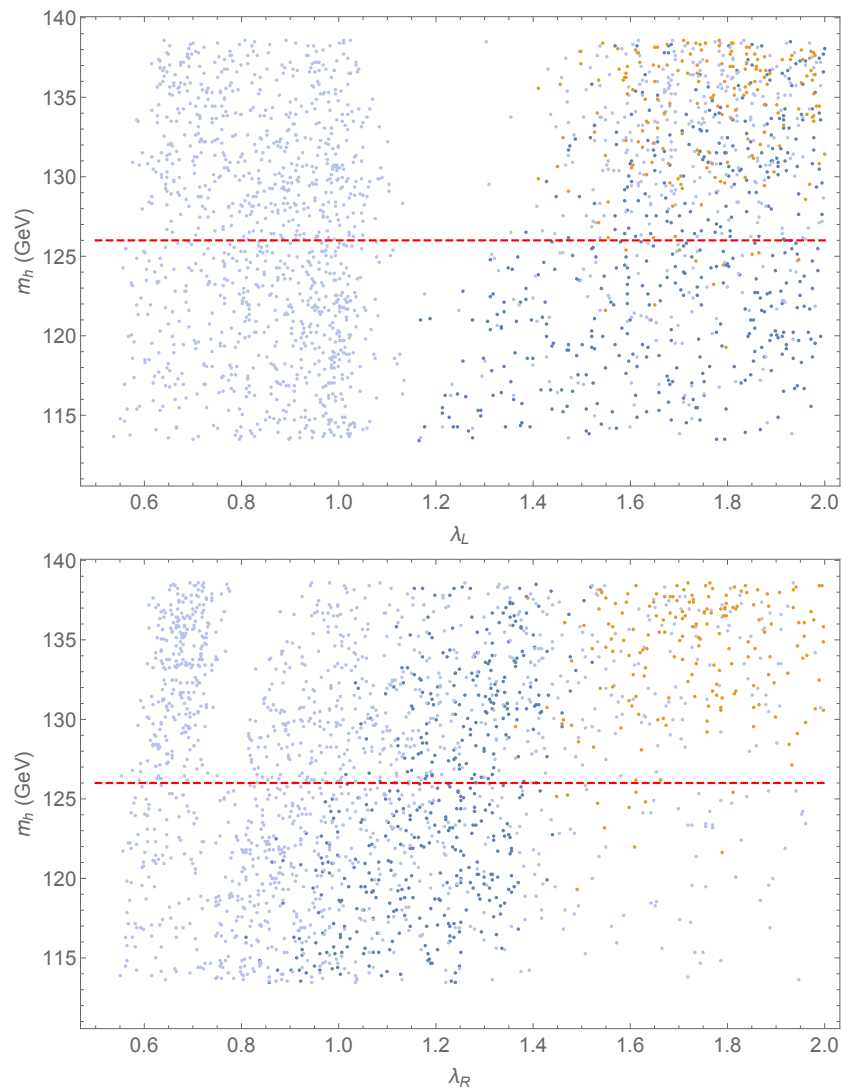


Figure 6.4: Higgs mass vs. λ_L and λ_R (above and below respectively). Red dashed line marks the $m_h = 126$ GeV. The 3-3 model is blue and light blue and the 2-3 model is yellow.

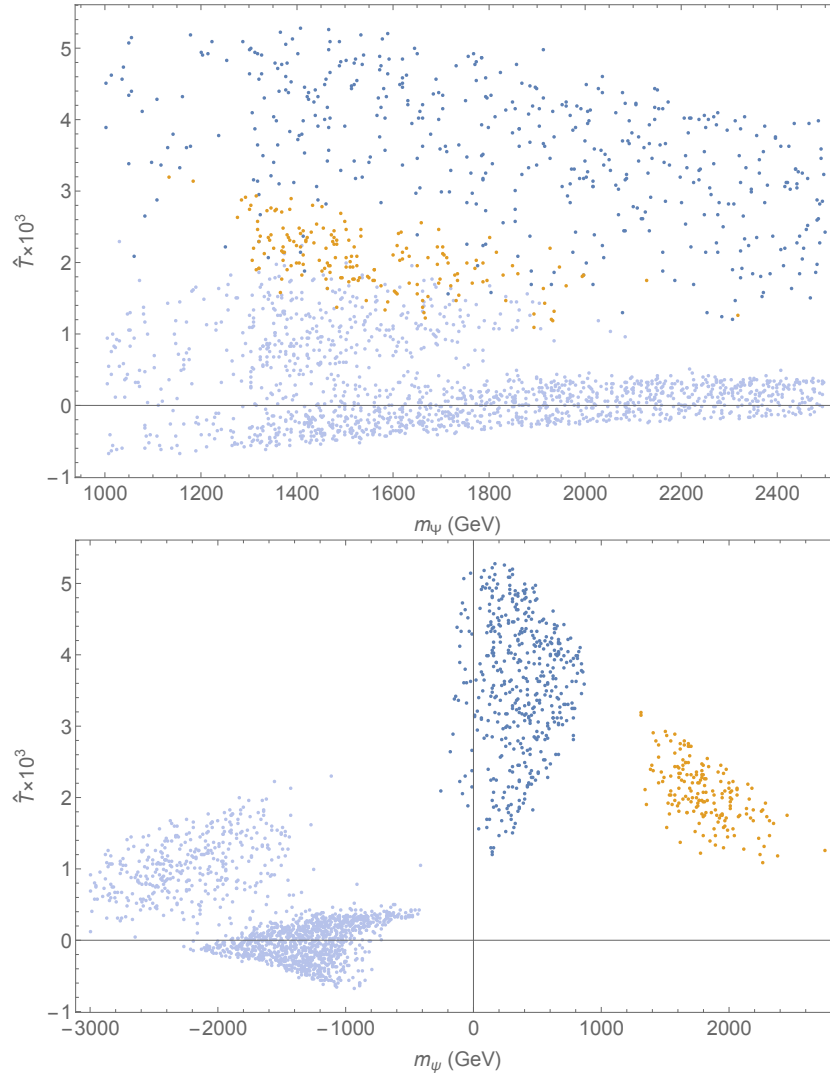


Figure 6.5: Fermion contribution to $\hat{T} \times 10^3$ vs. m_Ψ , m_ψ (above and below respectively) for the 3-3 model (blue and light blue) and the 2-3 model (yellow).

which allows for a wider range of the parameter space to satisfy these constraints.

6.6.4 T Parameter versus Composite Masses and Mixings

The T parameter is an important observable to constrain CH models. In this section we solely focus on the fermion corrections as they give the dominant contributions. Since custodial symmetry prevents such terms from being generated at tree-level, the main contribution stems from fermion loops [37]. We have seen in Section 5.3.2 the phenomenologically preferred values for the T parameter are mostly positive. This is always the case in the 2-3 model, but not necessarily in the 3-3 one, according to Figures 6.5 and 6.6. In particular, the contributions to the T parameter are inversely proportional to the lighter of the two composite resonances [37]. Hence, for the heavier m_ψ solution in the 3-3 model we find contributions close to zero, while for the lighter m_ψ they range between 1 and 5.

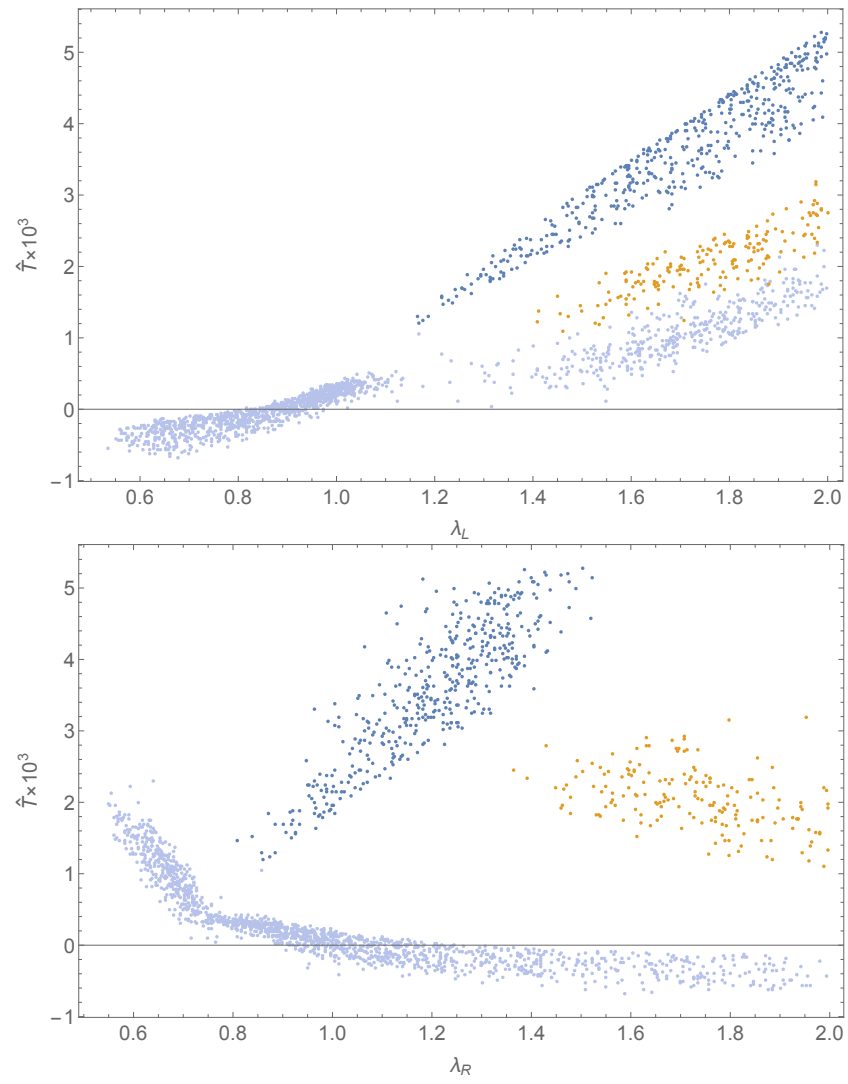


Figure 6.6: Fermion contribution to $\hat{T} \times 10^3$ vs. λ_L and λ_R (above and below respectively) for the 3-3 model (blue and light blue) and the 2-3 model (yellow).

As the masses in the 2-3 model lie in-between the two, so do the contributions to the T parameter range between 2 and 3.

In Figure 6.6 we observe a strong scaling behaviour of T with respect to λ_L . It has been shown in [37], that each elementary composite mixing can be viewed as a spurion insertion. Moreover, for the composite partner in the $(\mathbf{2}, \mathbf{2})$ representation of $SU(2)_L \times SU(2)_R$, one requires four insertions of λ_L to generate contributions to T . These four insertions also ensure that the T is finite. The distributions of λ_R follow from the constraints on m_{top} and m_h outlined earlier.

The lighter singlet ψ tends to give positive contributions to T , while the ones coming from the lighter bi-doublet Ψ are usually negative. In the 3-3 models either one of these contributions could dominate, hence we see both signs of the T parameter. In the 2-3 case both types of contributions are typically positive [37].

6.6.5 Collider, S and T Parameter Constraints

Next we assess the constraints imposed on our models by the electroweak precision observables S and T . To that end, five new fields are introduced via our 2-3 and 3-3 models: $\tilde{T}, T, B, X_{2/3}$ and $X_{5/3}$. Their physical masses are going to be roughly the same as the ones obtained after the diagonalization of the mass matrices. As discussed in Section 5.2.1 the lower bound on these masses coming from collider searches is around 1.3 TeV.

In Figure 6.7 we show the S - T constraints along with our model points. In this section we include both our calculation of fermion contributions to T as well as the remaining IR, vector boson and fermion corrections to S and T given in Eqs.(5.54-5.57). In order to compare with the results in the previous section recall that $\hat{T} = \alpha T$. In addition to the fermion contribution to T , shown previously, this results in an additional shift $\Delta T \times 10^3 = -0.17$, as well as a positive shift in S , which can be seen in the plots. The grey colour indicates the points with the lightest fermion mass being less than 1.3 TeV, while the red shades denote larger masses. We see that for the 3-3 model there are points that both agree with the experimental S - T bounds and pass the collider constraints for the heavier of the two m_{ψ} solutions. For the 2-3 model, the points with heavier masses are also more likely to satisfy the S - T bounds. In Figure 6.8 the analogous plots are shown but in the fermion mass plane. We see that both models can satisfy the constraints for composite masses in the TeV range and $\xi = 0.05$, which is what we prefer for a natural model.

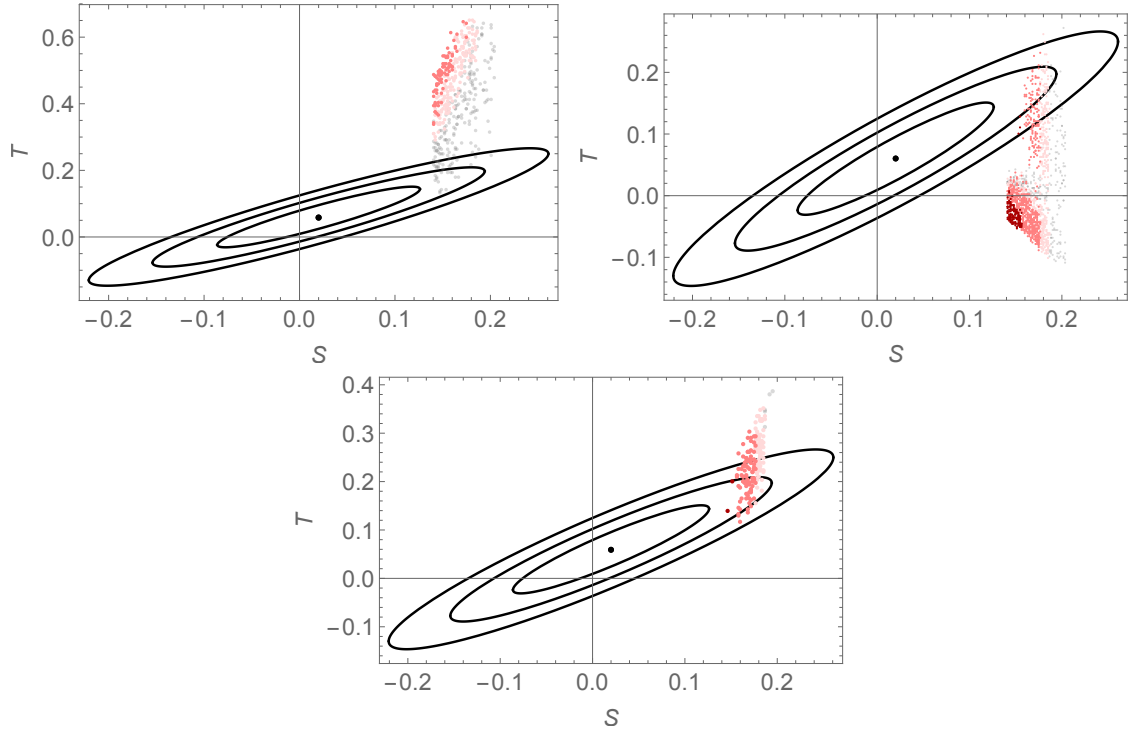


Figure 6.7: T vs. S for the 3-3 model (top left and right) and the 2-3 model (bottom). At each point, it is indicated if the lightest fermion mass is less than 1.3 TeV (grey), 1.5 TeV (pink), 2.0 TeV (dark pink) and less than 2.5 TeV (dark red). Black are the 1, 2 and 3σ S-T constraint from PDG.

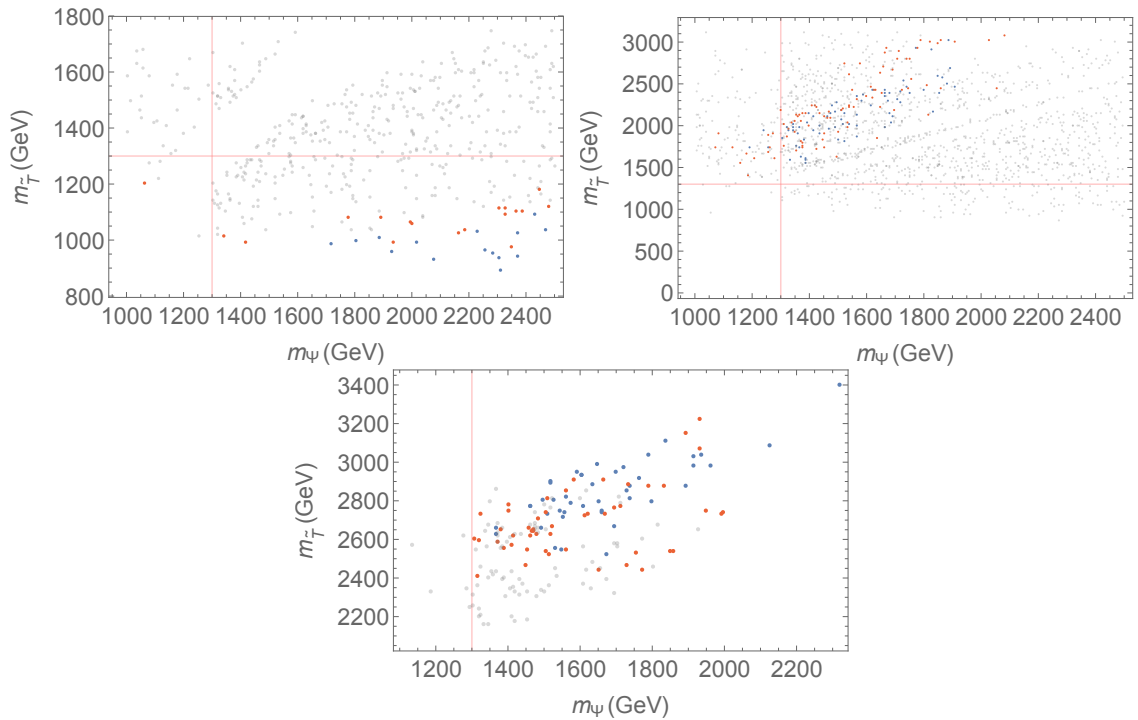


Figure 6.8: $m_{\tilde{\tau}}$ vs. m_{Ψ} for the 3-3 model (top left and right) and the 2-3 model (bottom). Points that fall within the 2σ S-T contour indicated by red, within 3σ - blue, outside 3σ - grey. Pink lines indicate collider mass constraint for our particles: 1.3 TeV.

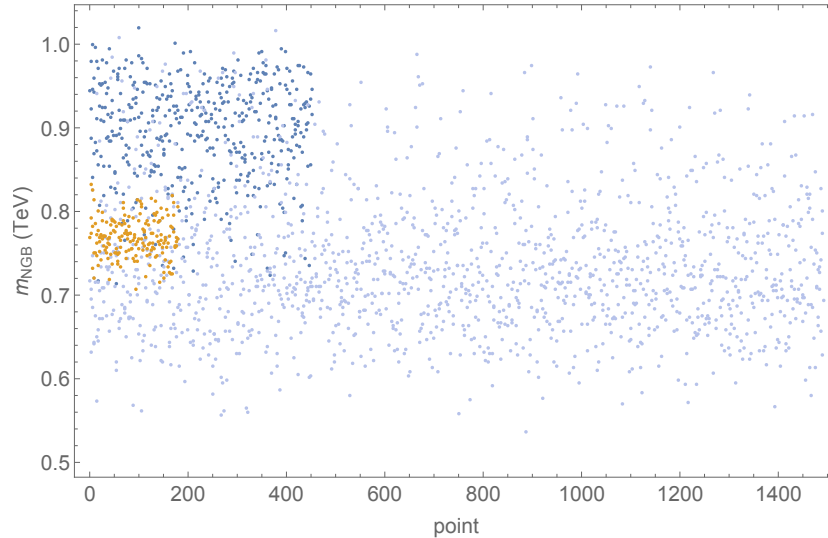


Figure 6.9: Coloured NGB masses for our points. 3-3 model (blue and light blue) and 2-3 model (yellow).

6.6.6 Coloured NGB Mass

Finally, we present results for our coloured NGB mass as given in Eq.(6.94). For the 2-3 model and the 3-3 model with heavier m_{ψ} the gauge and fermion contributions are roughly the same. For the lighter 3-3 model points the fermion contribution is larger. As given in Section 5.2.1 the collider constraints on NGB mass are around 1.3 TeV. Hence, both of the models as formulated here fail to satisfy these constraints for $\xi = 0.05$. It also appears to be difficult to evade this problem by increasing f beyond 1.1 TeV. In addition, it has been argued in [105] that since α contains logarithmic divergences it could be fixed by additional UV contributions. The same could be the case for γ as well, which renders the NGB mass unpredictable by the model. From the status of the current investigation it is not clear whether these models are ruled out. Hence, we conclude that further modifications to our 2-3 and 3-3 models are necessary.

6.7 Summary

In this chapter we have attempted to build two partially composite pNGB Higgs models consistent with unification and passing all collider and EW constraints. These efforts are part of an ongoing project. We have considered two models with $SO(11) \rightarrow SO(10)$ symmetry. In particular, we have identified various parameter points that can reproduce the correct top mass, have heavy enough top partner masses to pass collider constraints, are within bounds on the oblique corrections and produce a correct EWSB. However, this requires relatively small $\xi = 0.05$, particularly for the 3-3 model. Furthermore, having the

scale f large enough to accommodate the aforementioned bounds, does not allow for the coloured pNGB mass to be > 1 TeV, which is in tension with the collider constraints. We expect that introduction of further UV contributions to α and γ could resolve the issue. Hence, this problem will be addressed in future efforts.

Chapter 7

Conclusion

With this thesis, we have made several steps towards constraining and studying new physics solutions to the various open problems of the Standard Model. This includes improving precision observables, constraining BSM collider signatures and constructing SM extensions that resolve multiple issues simultaneously.

In this spirit, we have computed two-loop conversion factors that link high-energy QCD corrections to non-perturbative lattice results. This has led to an increase in precision for the SM prediction of the kaon bag parameter, which parametrises the dominant short-distance contributions to indirect CP violation. Our result exhibits good perturbative behaviour with respect to the one-loop conversion factor. In particular, we find that the NNLO contributions give corrections between 0.4% to 4% with respect to the tree-level, depending on renormalisation scale, gauge fixing and SMOM scheme. In addition, this calculation can be extended to include direct CP violation, BSM operators or QED corrections in future works. Hence, this result is important for constraining new physics contributing to CP violation.

Furthermore, we have studied collider signatures of stable multiply charged particles which are predicted by various extensions of the SM such as SUSY, composite Higgs and Grand Unified theories. For multiply charged coloured particles we find that the mass limits for $\sqrt{s} = 8$ TeV are in the TeV range and nearly charge independent for $|Q| < 4$. For $|Q| > 4$ the bounds are strongly charge dependent. For multiply charged colourless fields the accuracy of existing collider bounds has been improved by the inclusion of photo-production processes. In particular, we have found that the combination of open (pair-production) and closed (resonance production) channels provides complimentary bounds and could be used to determine the particles mass, spin, colour and charge.

We have also studied composite Higgs models, as they promise a natural solution to

the hierarchy problem and explain the heaviness of the top with respect to other quarks. We have found that the p_T spectra of the Higgs+Jet process could be used to distinguish between different top partner signatures. In addition, we obtain the QCD limits for CP-odd contributions to this process.

Moreover, we have constructed two candidate theories that are compatible with realistic Higgs and top masses as well as SM electro-weak symmetry breaking in the IR, while allowing for Grand Unification in the UV and satisfying collider constraints on the top partners. We have found many promising parameter points fulfilling these criteria for $\xi = 0.05$. However, they cannot feature a coloured pNGB heavy enough to satisfy collider constraints. We expect this to be achievable with further modifications to the models. These models are of particular interest as they also have the potential to explain the $R_D^{(*)}$ and $R_K^{(*)}$ flavour anomalies and could be extended to include dark matter candidates.

Bibliography

- [1] S. Jäger, S. Kvedaraitė, G. Perez and I. Savoray, *Bounds and prospects for stable multiply charged particles at the LHC*, *JHEP* **04** (2019) 041 [[1812.03182](#)]. [ii](#), [10](#), [62](#)
- [2] A. Banfi, B. M. Dillon, W. Ketaiam and S. Kvedaraite, *Composite Higgs at high transverse momentum*, *JHEP* **01** (2020) 089 [[1905.12747](#)]. [ii](#), [xiv](#), [xv](#), [10](#), [89](#), [102](#), [103](#), [106](#), [107](#), [108](#), [109](#), [110](#), [111](#), [116](#)
- [3] S. Kvedaraite and S. Jaeger, *SMOM - \overline{MS} Matching for B_K at Two-loop Order*, *PoS LATTICE2018* (2018) 214 [[1901.06861](#)]. [ii](#)
- [4] Y. Aoki et al., *Continuum Limit of B_K from 2+1 Flavor Domain Wall QCD*, *Phys. Rev.* **D84** (2011) 014503 [[1012.4178](#)]. [ix](#), [4](#), [5](#), [11](#), [22](#), [23](#), [24](#), [31](#), [33](#), [34](#), [44](#), [45](#), [46](#), [61](#)
- [5] V. Veeraraghavan, *Search for multiply charged Heavy Stable Charged Particles in data collected with the CMS detector.*, Ph.D. thesis, Florida State U., 2013. 10.2172/1128814. [x](#), [xiii](#), [70](#), [71](#), [72](#), [73](#), [74](#), [174](#)
- [6] Y. Kats, M. McCullough, G. Perez, Y. Soreq and J. Thaler, *Colorful Twisted Top Partners and Partnerium at the LHC*, *JHEP* **06** (2017) 126 [[1704.03393](#)]. [xiii](#), [5](#), [64](#), [74](#), [75](#), [86](#)
- [7] *Key Data for Ionizing-Radiation Dosimetry: Measurement Standards and Applications*, vol. 14. ICRU, Bethesda, MD, 2014. [xiii](#), [71](#), [172](#)
- [8] R. Mackeprang, *Stable Heavy Hadrons in ATLAS*, Ph.D. thesis, Bohr Inst., 2007. [xiii](#), [71](#)
- [9] CMS collaboration, *Searches for long-lived charged particles in pp collisions at $\sqrt{s}=7$ and 8 TeV*, *JHEP* **07** (2013) 122 [[1305.0491](#)]. [xiii](#), [xiv](#), [xvi](#), [66](#), [67](#), [68](#), [69](#), [71](#), [72](#), [73](#), [77](#), [79](#), [82](#), [83](#), [87](#), [179](#)

- [10] CMS COLLABORATION collaboration, *Search for physics beyond the standard model in the high-mass diphoton spectrum at 13 TeV*, Tech. Rep. CMS-PAS-EXO-17-017, CERN, Geneva, 2018. [xiv](#), [xvii](#), [75](#), [78](#), [79](#), [181](#)
- [11] N. D. Barrie, A. Kobakhidze, S. Liang, M. Talia and L. Wu, *Exotic Lepton Searches via Bound State Production at the LHC*, [1710.11396](#). [xiv](#), [7](#), [67](#), [68](#), [74](#), [75](#), [76](#), [82](#), [83](#), [87](#)
- [12] H. Seo, *Rpc hit contribution to cms muon reconstruction at lhc*, *Nuclear Instruments and Methods in Physics Research Section A: Accelerators, Spectrometers, Detectors and Associated Equipment* **718** (2013) 437 . [xvi](#), [172](#)
- [13] E. Molinaro and N. Vignaroli, *Diphoton Resonances at the LHC*, *Mod. Phys. Lett.* **A32** (2017) 1730024 [[1707.00926](#)]. [xvii](#), [83](#), [181](#)
- [14] M. Gell-Mann, *A Schematic Model of Baryons and Mesons*, *Phys. Lett.* **8** (1964) [214](#). [1](#)
- [15] G. Zweig, *An $SU(3)$ model for strong interaction symmetry and its breaking. Version 1*, . [1](#)
- [16] R. K. Ellis, W. J. Stirling and B. R. Webber, *QCD and Collider Physics*, Cambridge Monographs on Particle Physics, Nuclear Physics and Cosmology. Cambridge University Press, 1996, [10.1017/CBO9780511628788](#). [1](#), [12](#)
- [17] S. L. Glashow, *Partial-symmetries of weak interactions*, *Nuclear Physics* **22** (1961) [579](#) . [1](#)
- [18] A. Salam and J. C. Ward, *Electromagnetic and weak interactions*, *Phys. Lett.* **13** (1964) [168](#). [1](#)
- [19] S. Weinberg, *A Model of Leptons*, *Phys. Rev. Lett.* **19** (1967) [1264](#). [1](#)
- [20] F. Englert and R. Brout, *Broken Symmetry and the Mass of Gauge Vector Mesons*, *Phys. Rev. Lett.* **13** (1964) [321](#). [1](#)
- [21] P. W. Higgs, *Broken Symmetries and the Masses of Gauge Bosons*, *Phys. Rev. Lett.* **13** (1964) [508](#). [1](#)
- [22] G. Guralnik, C. Hagen and T. Kibble, *Global Conservation Laws and Massless Particles*, *Phys. Rev. Lett.* **13** (1964) [585](#). [1](#)

- [23] ATLAS collaboration, *Observation of a new particle in the search for the Standard Model Higgs boson with the ATLAS detector at the LHC*, *Phys. Lett. B* **716** (2012) 1 [[1207.7214](#)]. 1, 9
- [24] CMS collaboration, *Observation of a New Boson at a Mass of 125 GeV with the CMS Experiment at the LHC*, *Phys. Lett. B* **716** (2012) 30 [[1207.7235](#)]. 1
- [25] ATLAS, CMS collaboration, *Combined Measurement of the Higgs Boson Mass in pp Collisions at $\sqrt{s} = 7$ and 8 TeV with the ATLAS and CMS Experiments*, *Phys. Rev. Lett.* **114** (2015) 191803 [[1503.07589](#)]. 1
- [26] N. Cabibbo, *Unitary Symmetry and Leptonic Decays*, *Phys. Rev. Lett.* **10** (1963) 531. 2, 3
- [27] M. Kobayashi and T. Maskawa, *CP Violation in the Renormalizable Theory of Weak Interaction*, *Prog. Theor. Phys.* **49** (1973) 652. 2, 3
- [28] Z. Maki, M. Nakagawa and S. Sakata, *Remarks on the unified model of elementary particles*, *Prog. Theor. Phys.* **28** (1962) 870. 2
- [29] B. Pontecorvo, *Inverse beta processes and nonconservation of lepton charge*, *Sov. Phys. JETP* **7** (1958) 172. 2
- [30] G. Branco, L. Lavoura and J. Silva, *CP Violation*, International series of monographs on physics. Clarendon Press, 1999. 3
- [31] A. J. Buras, *Weak Hamiltonian, CP violation and rare decays*, in *Les Houches Summer School in Theoretical Physics, Session 68: Probing the Standard Model of Particle Interactions*, pp. 281–539, 6, 1998, [hep-ph/9806471](#). 3, 4, 21
- [32] A. C. Kraan, *Interactions of heavy stable hadronizing particles*, *Eur. Phys. J.* **C37** (2004) 91 [[hep-ex/0404001](#)]. 6, 66, 71
- [33] Y. Kats and M. J. Strassler, *Probing Colored Particles with Photons, Leptons, and Jets*, *JHEP* **11** (2012) 097 [[1204.1119](#)]. 7, 8, 64, 67, 74, 75, 76
- [34] D. Kahawala and Y. Kats, *Distinguishing spins at the LHC using bound state signals*, *JHEP* **09** (2011) 099 [[1103.3503](#)]. 7, 8
- [35] PARTICLE DATA GROUP collaboration, *Review of Particle Physics*, *Chin. Phys.* **C40** (2016) 100001. 8, 70, 75

- [36] G. 't Hooft, *Naturalness, chiral symmetry, and spontaneous chiral symmetry breaking*, *NATO Sci. Ser. B* **59** (1980) 135. [9](#)
- [37] G. Panico and A. Wulzer, *The Composite Nambu-Goldstone Higgs*, vol. 913. Springer, 2016, [10.1007/978-3-319-22617-0](#), [[1506.01961](#)]. [9](#), [89](#), [91](#), [94](#), [112](#), [114](#), [131](#), [135](#), [140](#), [141](#), [147](#), [149](#)
- [38] PARTICLE DATA GROUP collaboration, *Review of Particle Physics*, *Phys. Rev. D* **98** (2018) 030001. [12](#), [56](#), [111](#), [113](#)
- [39] M. E. Peskin and D. V. Schroeder, *An introduction to quantum field theory*. Westview, Boulder, CO, 1995. [12](#)
- [40] J. C. Collins, *Renormalization: An Introduction to Renormalization, The Renormalization Group, and the Operator Product Expansion*, vol. 26 of *Cambridge Monographs on Mathematical Physics*. Cambridge University Press, Cambridge, 1986, [10.1017/CBO9780511622656](#). [12](#)
- [41] G. Buchalla, A. J. Buras and M. E. Lautenbacher, *Weak decays beyond leading logarithms*, *Rev. Mod. Phys.* **68** (1996) 1125 [[hep-ph/9512380](#)]. [13](#), [21](#)
- [42] A. Freitas, *Numerical multi-loop integrals and applications*, *Prog. Part. Nucl. Phys.* **90** (2016) 201 [[1604.00406](#)]. [15](#), [26](#)
- [43] G. 't Hooft and M. Veltman, *Regularization and Renormalization of Gauge Fields*, *Nucl. Phys. B* **44** (1972) 189. [15](#), [16](#)
- [44] K. Symanzik, *Small distance behavior in field theory and power counting*, *Commun. Math. Phys.* **18** (1970) 227. [16](#)
- [45] J. Callan, Curtis G., *Broken scale invariance in scalar field theory*, *Phys. Rev. D* **2** (1970) 1541. [16](#)
- [46] D. J. Gross and F. Wilczek, *Ultraviolet Behavior of Nonabelian Gauge Theories*, *Phys. Rev. Lett.* **30** (1973) 1343. [17](#)
- [47] H. Politzer, *Reliable Perturbative Results for Strong Interactions?*, *Phys. Rev. Lett.* **30** (1973) 1346. [17](#)
- [48] E. Franco and V. Lubicz, *Quark mass renormalization in the \overline{MS} and \overline{RI} schemes up to the $nnlo$ order*, *Nuclear Physics B* **531** (1998) 641–651. [17](#)

- [49] L. N. Mihaila, J. Salomon and M. Steinhauser, *Renormalization constants and beta functions for the gauge couplings of the Standard Model to three-loop order*, *Phys. Rev. D* **86** (2012) 096008 [[1208.3357](#)]. 17
- [50] G. Martinelli, C. Pittori, C. T. Sachrajda, M. Testa and A. Vladikas, *A General method for nonperturbative renormalization of lattice operators*, *Nucl. Phys. B* **445** (1995) 81 [[hep-lat/9411010](#)]. 19, 22
- [51] RBC AND UKQCD COLLABORATIONS collaboration, *Renormalization of quark bilinear operators in a momentum-subtraction scheme with a nonexceptional subtraction point*, *Phys. Rev. D* **80** (2009) 014501. 19, 20
- [52] J. Brod and M. Gorbahn, *ϵ_K at Next-to-Next-to-Leading Order: The Charm-Top-Quark Contribution*, *Phys. Rev.* **D82** (2010) 094026 [[1007.0684](#)]. 22, 25, 31, 58
- [53] A. Donini, G. Martinelli, C. T. Sachrajda, M. Talevi and A. Vladikas, *Nonperturbative renormalization of the lattice Delta $s = 2$ four fermion operator*, *Phys. Lett. B* **360** (1995) 83 [[hep-lat/9508020](#)]. 22
- [54] A. J. Buras and P. H. Weisz, *QCD Nonleading Corrections to Weak Decays in Dimensional Regularization and 't Hooft-Veltman Schemes*, *Nucl. Phys. B* **333** (1990) 66. 25, 55
- [55] S. Weinzierl, *The Art of computing loop integrals*, *Fields Inst. Commun.* **50** (2007) 345 [[hep-ph/0604068](#)]. 26, 27, 29, 36
- [56] K. Chetyrkin and F. Tkachov, *Integration by Parts: The Algorithm to Calculate beta Functions in 4 Loops*, *Nucl. Phys. B* **192** (1981) 159. 27
- [57] A. Grozin, *Integration by parts: An Introduction*, *Int. J. Mod. Phys. A* **26** (2011) 2807 [[1104.3993](#)]. 27
- [58] C. Anastasiou, E. W. N. Glover and C. Oleari, *The two-loop scalar and tensor pentabox graph with light-like legs*, *Nucl. Phys.* **B575** (2000) 416 [[hep-ph/9912251](#)]. 36
- [59] P. Breitenlohner and D. Maison, *Dimensional Renormalization and the Action Principle*, *Commun. Math. Phys.* **52** (1977) 11. 36

- [60] N. Tracas and N. Vlachos, *Two Loop Calculations in QCD and the $\Delta I = 1/2$ Rule in Nonleptonic Weak Decays*, *Phys. Lett.* **115B** (1982) 419. 36
- [61] A. J. Buras and P. H. Weisz, *QCD Nonleading Corrections to Weak Decays in Dimensional Regularization and 't Hooft-Veltman Schemes*, *Nucl. Phys. B* **333** (1990) 66. 36
- [62] N. I. Usyukina and A. I. Davydychev, *New results for two loop off-shell three point diagrams*, *Phys. Lett.* **B332** (1994) 159 [[hep-ph/9402223](#)]. 45, 53
- [63] A. von Manteuffel and C. Studerus, *Reduze 2 - Distributed Feynman Integral Reduction*, [1201.4330](#). 51
- [64] S. Laporta, *High precision calculation of multiloop Feynman integrals by difference equations*, *Int. J. Mod. Phys. A* **15** (2000) 5087 [[hep-ph/0102033](#)]. 51
- [65] T. Gehrmann and E. Remiddi, *Differential equations for two loop four point functions*, *Nucl. Phys.* **B580** (2000) 485 [[hep-ph/9912329](#)]. 53
- [66] S. Borowka, G. Heinrich, S. Jahn, S. Jones, M. Kerner, J. Schlenk et al., *pySecDec: a toolbox for the numerical evaluation of multi-scale integrals*, *Comput. Phys. Commun.* **222** (2018) 313 [[1703.09692](#)]. 53
- [67] J. Gracey, *Three loop anomalous dimension of nonsinglet quark currents in the RI-prime scheme*, *Nucl. Phys. B* **662** (2003) 247 [[hep-ph/0304113](#)]. 56
- [68] M. Gorbahn and S. Jager, *Precise \overline{MS} -bar light-quark masses from lattice QCD in the RI/SMOM scheme*, *Phys. Rev. D* **82** (2010) 114001 [[1004.3997](#)]. 56
- [69] K. Chetyrkin, J. H. Kuhn and M. Steinhauser, *RunDec: A Mathematica package for running and decoupling of the strong coupling and quark masses*, *Comput. Phys. Commun.* **133** (2000) 43 [[hep-ph/0004189](#)]. 56
- [70] RBC, UKQCD collaboration, *Domain wall QCD with physical quark masses*, *Phys. Rev. D* **93** (2016) 074505 [[1411.7017](#)]. ix, 60
- [71] S. P. Martin, *A Supersymmetry primer*, [hep-ph/9709356](#). 64
- [72] K. Agashe and G. Servant, *Warped unification, proton stability and dark matter*, *Phys. Rev. Lett.* **93** (2004) 231805 [[hep-ph/0403143](#)]. 64
- [73] G. F. Giudice, *Naturally Speaking: The Naturalness Criterion and Physics at the LHC*, [0801.2562](#). 64

- [74] ATLAS collaboration, *Search for heavy long-lived charged R-hadrons with the ATLAS detector in 3.2 fb^{-1} of proton-proton collision data at $\sqrt{s} = 13 \text{ TeV}$* , *Phys. Lett.* **B760** (2016) 647 [[1606.05129](#)]. 66
- [75] ATLAS collaboration, *Searches for heavy long-lived charged particles with the ATLAS detector in proton-proton collisions at $\sqrt{s} = 8 \text{ TeV}$* , *JHEP* **01** (2015) 068 [[1411.6795](#)]. 66
- [76] ATLAS collaboration, *Searches for heavy long-lived sleptons and R-Hadrons with the ATLAS detector in pp collisions at $\sqrt{s} = 7 \text{ TeV}$* , *Phys. Lett.* **B720** (2013) 277 [[1211.1597](#)]. 66
- [77] CMS collaboration, *Search for long-lived charged particles in proton-proton collisions at $\sqrt{s} = 13 \text{ TeV}$* , *Phys. Rev.* **D94** (2016) 112004 [[1609.08382](#)]. 66, 72
- [78] CMS collaboration, *Search for Heavy Stable Charged Particles in pp collisions at $\sqrt{s} = 7 \text{ TeV}$* , *JHEP* **03** (2011) 024 [[1101.1645](#)]. 66
- [79] ATLAS collaboration, *Search for heavy long-lived multi-charged particles in pp collisions at $\sqrt{s} = 8 \text{ TeV}$ using the ATLAS detector*, *Eur. Phys. J.* **C75** (2015) 362 [[1504.04188](#)]. 66, 67, 68
- [80] A. Manohar, P. Nason, G. P. Salam and G. Zanderighi, *How bright is the proton? A precise determination of the photon parton distribution function*, *Phys. Rev. Lett.* **117** (2016) 242002 [[1607.04266](#)]. 67, 68, 75, 77, 82
- [81] NNPDF collaboration, *Parton distributions with QED corrections*, *Nucl. Phys.* **B877** (2013) 290 [[1308.0598](#)]. 67, 82
- [82] ATLAS collaboration, *Measurement of the double-differential high-mass Drell-Yan cross section in pp collisions at $\sqrt{s} = 8 \text{ TeV}$ with the ATLAS detector*, *JHEP* **08** (2016) 009 [[1606.01736](#)]. 67, 82
- [83] A. V. Manohar, P. Nason, G. P. Salam and G. Zanderighi, *The Photon Content of the Proton*, *JHEP* **12** (2017) 046 [[1708.01256](#)]. 67, 68, 82
- [84] J. Alwall, R. Frederix, S. Frixione, V. Hirschi, F. Maltoni, O. Mattelaer et al., *The automated computation of tree-level and next-to-leading order differential cross sections, and their matching to parton shower simulations*, *JHEP* **07** (2014) 079 [[1405.0301](#)]. 68

- [85] T. Sjostrand, S. Ask, J. R. Christiansen, R. Corke, N. Desai, P. Ilten et al., *An Introduction to PYTHIA 8.2*, *Comput. Phys. Commun.* **191** (2015) 159 [[1410.3012](#)]. 68
- [86] T. Sjostrand, S. Mrenna and P. Z. Skands, *PYTHIA 6.4 Physics and Manual*, *JHEP* **05** (2006) 026 [[hep-ph/0603175](#)]. 68
- [87] CMS COLLABORATION collaboration, *Search for multi-charged Heavy Stable Charged Particles*, Tech. Rep. CMS-PAS-EXO-11-090, CERN, Geneva, 2012. 70
- [88] M. Konecki, *The rpc based trigger for the cms experiment at the lhc*, *Journal of Instrumentation* **9** (2014) C07002. 70
- [89] M. Tytgat et al., *The Upgrade of the CMS RPC System during the First LHC Long Shutdown*, *PoS RPC2012* (2012) 063 [[1209.1979](#)]. 70
- [90] V. Gori, *The CMS High Level Trigger*, *Int. J. Mod. Phys. Conf. Ser.* **31** (2014) 1460297 [[1403.1500](#)]. 70
- [91] CMS COLLABORATION collaboration, *Performance of muon identification in pp collisions at $s^{*0.5} = 7$ TeV*, Tech. Rep. CMS-PAS-MUO-10-002, CERN, Geneva, 2010. 71
- [92] J. Pumplin, D. R. Stump, J. Huston, H. L. Lai, P. M. Nadolsky and W. K. Tung, *New generation of parton distributions with uncertainties from global QCD analysis*, *JHEP* **07** (2002) 012 [[hep-ph/0201195](#)]. 72
- [93] K. Blum, A. Efrati, C. Frugiuele and Y. Nir, *Exotic colored scalars at the LHC*, *JHEP* **02** (2017) 104 [[1610.06582](#)]. 75
- [94] S. P. Martin, *Diphoton decays of stoponium at the Large Hadron Collider*, *Phys. Rev.* **D77** (2008) 075002 [[0801.0237](#)]. 76
- [95] J. E. Younkin and S. P. Martin, *QCD corrections to stoponium production at hadron colliders*, *Phys. Rev.* **D81** (2010) 055006 [[0912.4813](#)]. 76
- [96] M. Beneke, J. Piclum, C. Schwinn and C. Wever, *NNLL soft and Coulomb resummation for squark and gluino production at the LHC*, *JHEP* **10** (2016) 054 [[1607.07574](#)]. 76
- [97] Y. Kats and M. D. Schwartz, *Annihilation decays of bound states at the LHC*, *JHEP* **04** (2010) 016 [[0912.0526](#)]. 76

- [98] D. B. Clark, E. Godat and F. I. Olness, *ManeParse : A Mathematica reader for Parton Distribution Functions*, *Comput. Phys. Commun.* **216** (2017) 126 [[1605.08012](#)]. 77
- [99] THE ATLAS COLLABORATION, THE CMS COLLABORATION, THE LHC HIGGS COMBINATION GROUP collaboration, *Procedure for the LHC Higgs boson search combination in Summer 2011*, Tech. Rep. CMS-NOTE-2011-005. ATL-PHYS-PUB-2011-11, CERN, Geneva, Aug, 2011. 77
- [100] ATLAS collaboration, *Search for heavy long-lived multi-charged particles in proton-proton collisions at $\sqrt{s} = 13$ TeV using the ATLAS detector*, [1812.03673](#). 87
- [101] C. Collaboration, *TECHNICAL PROPOSAL FOR A MIP TIMING DETECTOR IN THE CMS EXPERIMENT PHASE 2 UPGRADE*, Tech. Rep. CERN-LHCC-2017-027. LHCC-P-009, CERN, Geneva, Dec, 2017. 87
- [102] K. Agashe, R. Contino and A. Pomarol, *The Minimal composite Higgs model*, *Nucl. Phys. B* **719** (2005) 165 [[hep-ph/0412089](#)]. 89, 136, 143
- [103] G. F. Giudice, C. Grojean, A. Pomarol and R. Rattazzi, *The Strongly-Interacting Light Higgs*, *JHEP* **06** (2007) 045 [[hep-ph/0703164](#)]. 89, 91, 96
- [104] A. De Simone, O. Matsedonskyi, R. Rattazzi and A. Wulzer, *A First Top Partner Hunter's Guide*, *JHEP* **04** (2013) 004 [[1211.5663](#)]. 89, 93, 95, 96, 97
- [105] D. Marzocca, M. Serone and J. Shu, *General Composite Higgs Models*, *JHEP* **08** (2012) 013 [[1205.0770](#)]. 89, 93, 151
- [106] O. Matsedonskyi, G. Panico and A. Wulzer, *Light Top Partners for a Light Composite Higgs*, *JHEP* **01** (2013) 164 [[1204.6333](#)]. 89
- [107] J. Mrazek, A. Pomarol, R. Rattazzi, M. Redi, J. Serra and A. Wulzer, *The Other Natural Two Higgs Doublet Model*, *Nucl. Phys.* **B853** (2011) 1 [[1105.5403](#)]. 89
- [108] G. Panico and A. Wulzer, *The Discrete Composite Higgs Model*, *JHEP* **09** (2011) 135 [[1106.2719](#)]. 91, 118
- [109] K. Agashe, R. Contino, L. Da Rold and A. Pomarol, *A Custodial symmetry for $Zb\bar{b}$* , *Phys. Lett.* **B641** (2006) 62 [[hep-ph/0605341](#)]. 91, 92

- [110] S. R. Coleman, J. Wess and B. Zumino, *Structure of phenomenological Lagrangians. 1.*, *Phys. Rev.* **177** (1969) 2239. 91
- [111] C. G. Callan, Jr., S. R. Coleman, J. Wess and B. Zumino, *Structure of phenomenological Lagrangians. 2.*, *Phys. Rev.* **177** (1969) 2247. 91
- [112] B. A. Kniehl and M. Spira, *Low-energy theorems in Higgs physics*, *Z. Phys.* **C69** (1995) 77 [[hep-ph/9505225](#)]. 103, 105
- [113] A. Azatov and J. Galloway, *Light Custodians and Higgs Physics in Composite Models*, *Phys. Rev.* **D85** (2012) 055013 [[1110.5646](#)]. 103, 105
- [114] I. Low and A. Vichi, *On the production of a composite Higgs boson*, *Phys. Rev.* **D84** (2011) 045019 [[1010.2753](#)]. 103, 105
- [115] A. Banfi, A. Martin and V. Sanz, *Probing top-partners in Higgs+jets*, *JHEP* **08** (2014) 053 [[1308.4771](#)]. 103, 105, 106
- [116] C. Grojean, E. Salvioni, M. Schlaffer and A. Weiler, *Very boosted Higgs in gluon fusion*, *JHEP* **05** (2014) 022 [[1312.3317](#)]. 103, 182, 183
- [117] A. Azatov, C. Grojean, A. Paul and E. Salvioni, *Resolving gluon fusion loops at current and future hadron colliders*, *JHEP* **09** (2016) 123 [[1608.00977](#)]. 103
- [118] V. Sanz and J. Setford, *Composite Higgses with seesaw EWSB*, *JHEP* **12** (2015) 154 [[1508.06133](#)]. 103
- [119] ATLAS collaboration, *Search for pair production of heavy vector-like quarks decaying to high- p_T W bosons and b quarks in the lepton-plus-jets final state in pp collisions at $\sqrt{s}=13$ TeV with the ATLAS detector*, . 104
- [120] CMS collaboration, *Search for heavy vector-like quarks decaying to same-sign dileptons*, . 104
- [121] CMS collaboration, *Search for top quark partners with charge $5/3$ in the single-lepton final state at $\sqrt{s} = 13$ TeV*, . 104
- [122] CMS collaboration, *Search for vector-like T or B quark pairs in leptonic final states in 36 fb^{-1} of proton-proton collisions at $\sqrt{s} = 13$ TeV*, . 104
- [123] CMS collaboration, *Search for a heavy resonance decaying to a top quark and a vector-like top quark in the lepton+jets final state*, . 104

- [124] CMS collaboration, *Search for a vector-like quark decaying to a top quark and a W boson*, . [104](#)
- [125] ATLAS collaboration, *Search for pair production of vector-like top quarks in events with one lepton, jets, and missing transverse momentum in $\sqrt{s} = 13$ TeV pp collisions with the ATLAS detector*, *JHEP* **08** (2017) 052 [[1705.10751](#)]. [104](#)
- [126] ATLAS collaboration, *Search for pair production of heavy vector-like quarks decaying to high- p_T W bosons and b quarks in the lepton-plus-jets final state in pp collisions at $\sqrt{s} = 13$ TeV with the ATLAS detector*, *JHEP* **10** (2017) 141 [[1707.03347](#)]. [104](#)
- [127] CMS collaboration, *Search for single production of a vector-like T quark decaying to a Z boson and a top quark in proton-proton collisions at $\sqrt{s} = 13$ TeV*, *Phys. Lett.* **B781** (2018) 574 [[1708.01062](#)]. [104](#)
- [128] CMS collaboration, *Search for pair production of vector-like quarks in the $bW\bar{b}W$ channel from proton-proton collisions at $\sqrt{s} = 13$ TeV*, *Phys. Lett.* **B779** (2018) 82 [[1710.01539](#)]. [104](#)
- [129] CMS collaboration, *Search for single production of vector-like quarks decaying to a b quark and a Higgs boson*, *JHEP* **06** (2018) 031 [[1802.01486](#)]. [104](#)
- [130] CMS collaboration, *Search for vector-like T and B quark pairs in final states with leptons at $\sqrt{s} = 13$ TeV*, *JHEP* **08** (2018) 177 [[1805.04758](#)]. [104](#)
- [131] ATLAS collaboration, *Search for pair production of heavy vector-like quarks decaying into high- p_T W bosons and top quarks in the lepton-plus-jets final state in pp collisions at $\sqrt{s} = 13$ TeV with the ATLAS detector*, *JHEP* **08** (2018) 048 [[1806.01762](#)]. [104](#)
- [132] ATLAS collaboration, *Search for single production of a vector-like B quark decaying into a bottom quark and a Higgs boson which decays into a pair of photons*, . [104](#)
- [133] Z. Chacko, H.-S. Goh and R. Harnik, *The Twin Higgs: Natural electroweak breaking from mirror symmetry*, *Phys. Rev. Lett.* **96** (2006) 231802 [[hep-ph/0506256](#)]. [104](#)
- [134] Z. Chacko, Y. Nomura, M. Papucci and G. Perez, *Natural little hierarchy from a partially goldstone twin Higgs*, *JHEP* **01** (2006) 126 [[hep-ph/0510273](#)]. [104](#)

- [135] Z. Chacko, H.-S. Goh and R. Harnik, *A Twin Higgs model from left-right symmetry*, *JHEP* **01** (2006) 108 [[hep-ph/0512088](#)]. 104
- [136] N. Craig, A. Katz, M. Strassler and R. Sundrum, *Naturalness in the Dark at the LHC*, *JHEP* **07** (2015) 105 [[1501.05310](#)]. 104
- [137] N. Craig, S. Knapen, P. Longhi and M. Strassler, *The Vector-like Twin Higgs*, *JHEP* **07** (2016) 002 [[1601.07181](#)]. 104
- [138] R. Barbieri, L. J. Hall and K. Harigaya, *Minimal Mirror Twin Higgs*, *JHEP* **11** (2016) 172 [[1609.05589](#)]. 104
- [139] M. Geller and O. Telem, *Holographic Twin Higgs Model*, *Phys. Rev. Lett.* **114** (2015) 191801 [[1411.2974](#)]. 104
- [140] J. Serra and R. Torre, *Neutral naturalness from the brother-Higgs model*, *Phys. Rev.* **D97** (2018) 035017 [[1709.05399](#)]. 104
- [141] C. Csáki, T. Ma and J. Shu, *Trigonometric Parity for Composite Higgs Models*, *Phys. Rev. Lett.* **121** (2018) 231801 [[1709.08636](#)]. 104
- [142] B. M. Dillon, *Neutral-naturalness from a holographic $SO(6)/SO(5)$ composite Higgs model*, [1806.10702](#). 104
- [143] G. Burdman, Z. Chacko, R. Harnik, L. de Lima and C. B. Verhaaren, *Colorless Top Partners, a 125 GeV Higgs, and the Limits on Naturalness*, *Phys. Rev.* **D91** (2015) 055007 [[1411.3310](#)]. 104
- [144] D. Curtin and C. B. Verhaaren, *Discovering Uncolored Naturalness in Exotic Higgs Decays*, *JHEP* **12** (2015) 072 [[1506.06141](#)]. 104
- [145] Z. Chacko, D. Curtin and C. B. Verhaaren, *A Quirky Probe of Neutral Naturalness*, *Phys. Rev.* **D94** (2016) 011504 [[1512.05782](#)]. 104
- [146] A. Ahmed, *Heavy Higgs of the Twin Higgs Models*, *JHEP* **02** (2018) 048 [[1711.03107](#)]. 104
- [147] Z. Chacko, C. Kilic, S. Najjari and C. B. Verhaaren, *Testing the Scalar Sector of the Twin Higgs Model at Colliders*, *Phys. Rev.* **D97** (2018) 055031 [[1711.05300](#)]. 104
- [148] G. Panico, M. Riembau and T. Vantalón, *Probing light top partners with CP violation*, *JHEP* **06** (2018) 056 [[1712.06337](#)]. 104

- [149] ATLAS collaboration, *Search for heavy charged long-lived particles in the ATLAS detector in 36.1 fb^{-1} of proton-proton collision data at $\sqrt{s} = 13 \text{ TeV}$* , *Phys. Rev. D* **99** (2019) 092007 [[1902.01636](#)]. 104
- [150] ATLAS collaboration, *Observation of Higgs boson production in association with a top quark pair at the LHC with the ATLAS detector*, *Phys. Lett.* **B784** (2018) 173 [[1806.00425](#)]. 107
- [151] S. Coleman and E. Weinberg, *Radiative corrections as the origin of spontaneous symmetry breaking*, *Phys. Rev. D* **7** (1973) 1888. 112
- [152] M. E. Peskin and T. Takeuchi, *Estimation of oblique electroweak corrections*, *Phys. Rev. D* **46** (1992) 381. 113
- [153] L. Lavoura and J. a. P. Silva, *Oblique corrections from vectorlike singlet and doublet quarks*, *Phys. Rev. D* **47** (1993) 2046. 113
- [154] J. Haller, A. Hoecker, R. Kogler, K. Mönig, T. Peiffer and J. Stelzer, *Update of the global electroweak fit and constraints on two-Higgs-doublet models*, *Eur. Phys. J. C* **78** (2018) 675 [[1803.01853](#)]. 113
- [155] M. Frigerio, J. Serra and A. Varagnolo, *Composite GUTs: models and expectations at the LHC*, *JHEP* **06** (2011) 029 [[1103.2997](#)]. 118, 120
- [156] L. Da Rold and F. Lamagna, *A vector leptoquark for the B-physics anomalies from a composite GUT*, *JHEP* **12** (2019) 112 [[1906.11666](#)]. 118
- [157] K. Agashe, R. Contino and R. Sundrum, *Top compositeness and precision unification*, *Phys. Rev. Lett.* **95** (2005) 171804 [[hep-ph/0502222](#)]. 118
- [158] R. Barbieri and A. Tesi, *B-decay anomalies in Pati-Salam $SU(4)$* , *Eur. Phys. J. C* **78** (2018) 193 [[1712.06844](#)]. 118
- [159] R. Barbieri, D. Buttazzo, F. Sala, D. M. Straub and A. Tesi, *A 125 GeV composite Higgs boson versus flavour and electroweak precision tests*, *JHEP* **05** (2013) 069 [[1211.5085](#)]. 118
- [160] R. Barbieri, G. Isidori and D. Pappadopulo, *Composite fermions in Electroweak Symmetry Breaking*, *JHEP* **02** (2009) 029 [[0811.2888](#)]. 118
- [161] R. Barbieri, D. Buttazzo, F. Sala and D. M. Straub, *Flavour physics from an approximate $U(2)^3$ symmetry*, *JHEP* **07** (2012) 181 [[1203.4218](#)]. 118

- [162] M. Redi and A. Weiler, *Flavor and CP Invariant Composite Higgs Models*, *JHEP* **11** (2011) 108 [[1106.6357](#)]. 118
- [163] R. Balkin, M. Ruhdorfer, E. Salvioni and A. Weiler, *Charged Composite Scalar Dark Matter*, *JHEP* **11** (2017) 094 [[1707.07685](#)]. 121, 140
- [164] A. Pomarol and F. Riva, *The Composite Higgs and Light Resonance Connection*, *JHEP* **08** (2012) 135 [[1205.6434](#)]. 136, 143
- [165] Y. Vibhuti, S. N. L. Sirisha and B. Sonali, *Study of Stopping Power for proton in different materials- A Geant4 Based Simulation*, *DAE Symp. Nucl. Phys.* **57** (2012) 734. 172
- [166] *Precise mapping of the magnetic field in the cms barrel yoke using cosmic rays*, *Journal of Instrumentation* **5** (2010) T03021. 172
- [167] A. Banfi, A. Bond, A. Martin and V. Sanz, *Digging for Top Squarks from Higgs data: from signal strengths to differential distributions*, *JHEP* **11** (2018) 171 [[1806.05598](#)]. 182
- [168] G. Passarino and M. J. G. Veltman, *One Loop Corrections for $e^+ e^-$ Annihilation Into $\mu^+ \mu^-$ in the Weinberg Model*, *Nucl. Phys.* **B160** (1979) 151. 184
- [169] M. L. Mangano and S. J. Parke, *Multiparton amplitudes in gauge theories*, *Phys. Rept.* **200** (1991) 301 [[hep-th/0509223](#)]. 185, 187
- [170] L. J. Dixon, *Calculating scattering amplitudes efficiently*, in *QCD and beyond. Proceedings, Theoretical Advanced Study Institute in Elementary Particle Physics, TASI-95, Boulder, USA, June 4-30, 1995*, pp. 539–584, 1996, <http://www-public.slac.stanford.edu/sciDoc/docMeta.aspx?slacPubNumber=SLAC-PUB-7106> [[hep-ph/9601359](#)]. 185, 187

Appendix A

Appendix for Chapter 4

A.1 Open-Production Signatures

A.1.1 Cross Sections

The cross sections for above-threshold pair-production of MCHSPs are presented for $\sqrt{s} = 8$ TeV and $\sqrt{s} = 13$ TeV in Figs. [A.1](#) and [A.2](#).

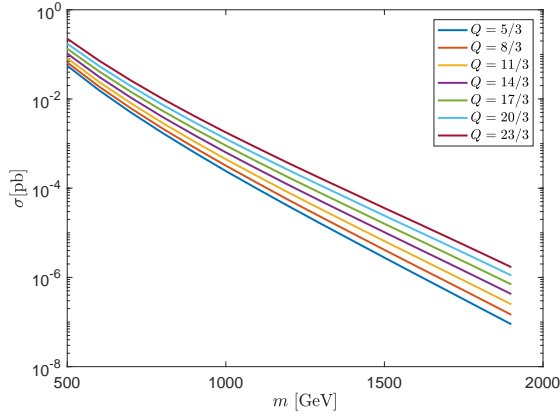
A.1.2 Simplified Efficiency Calculation

TOF Calculation

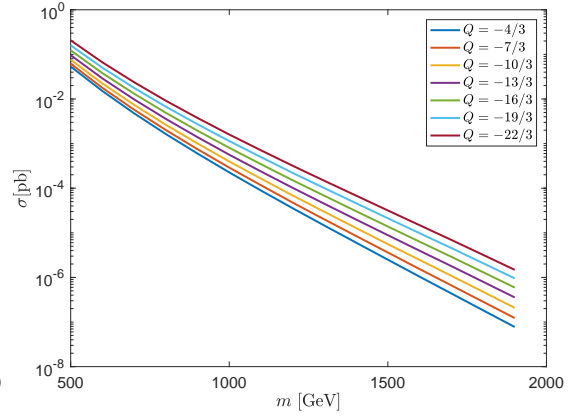
To determine whether a candidate particle is accepted by the muon trigger, we calculate its corresponding TOF by

$$c \cdot t_{\text{TOF}} = \frac{\gamma_0}{\sqrt{\gamma_0^2 - 1}} \cdot x_{\text{HCAL}}^0 + \int_0^{x_{\text{HCAL}}^f - x_{\text{HCAL}}^0} \frac{\gamma_{\text{Brass}}}{\sqrt{\gamma_{\text{Brass}}^2 - 1}} dx + \frac{\gamma_{\text{Brass}}(x_{\text{HCAL}}^f)}{\sqrt{\gamma_{\text{Brass}}(x_{\text{HCAL}}^f)^2 - 1}} \cdot (x_{\text{trigger}} - x_{\text{HCAL}}^f - \Delta x_{\text{IY}}) + \int_0^{\Delta x_{\text{IY}}} \frac{\gamma_{\text{Iron}}}{\sqrt{\gamma_{\text{Iron}}^2 - 1}} dx, \quad (\text{A.1})$$

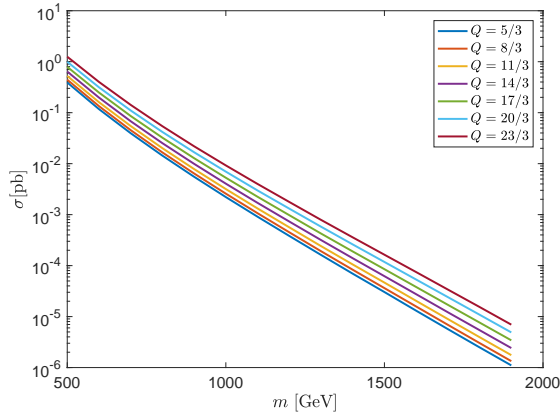
where x_{trigger} is the minimal distance a particle must travel, within the trigger time window, in order to be triggered as a muon. As explained in Section [4.2.2](#), x_{trigger} is η -dependent and it is presented in Figure [A.3\(a\)](#). x_{HCAL}^0 , x_{HCAL}^f are, respectively – the distance a particle would travel to the entrance and to the exit of the Hadronic Calorimeter (HCAL). The minimal distance a triggering particle would travel in the brass absorber of the HCAL, $x_{\text{HCAL}}^f - x_{\text{HCAL}}^0$, and in the iron absorber of the iron yoke, Δx_{IY} , are also η -dependent and are shown in Fig. [A.3\(b\)](#). $\gamma(x)$ is the Lorentz factor $\gamma = 1/\sqrt{1 - \beta^2}$,



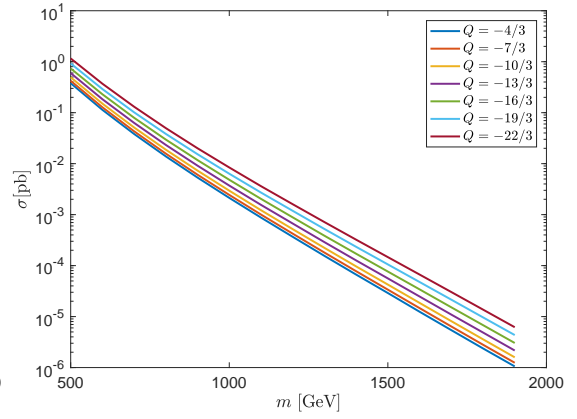
(a) Positively-charged colored scalars.



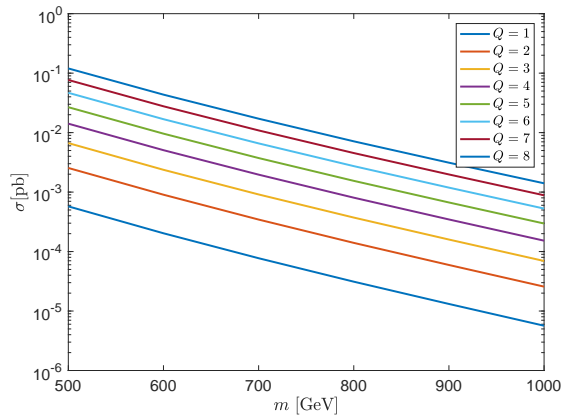
(b) Negatively-charged colored scalars.



(c) Positively-charged colored fermions.

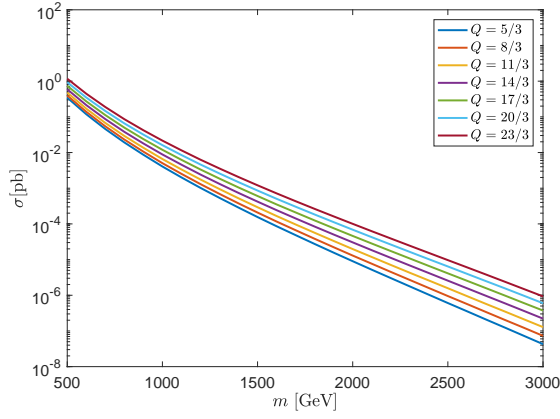


(d) Negatively-charged colored fermions.

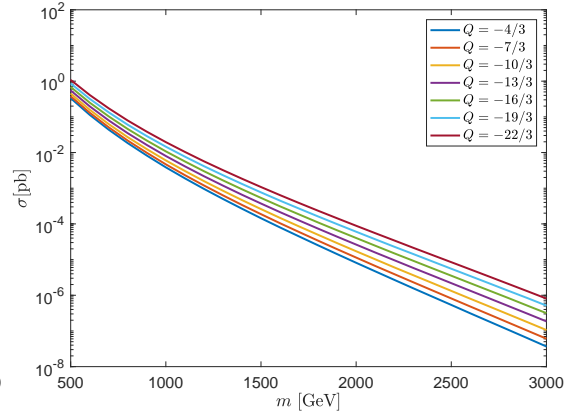


(e) Colorless fermions.

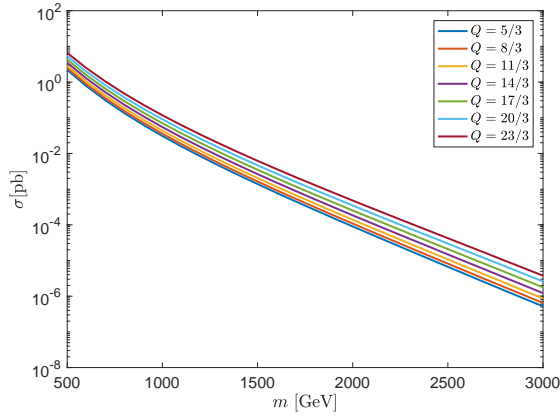
Figure A.1: Open-production cross sections at $\sqrt{s} = 8$ TeV.



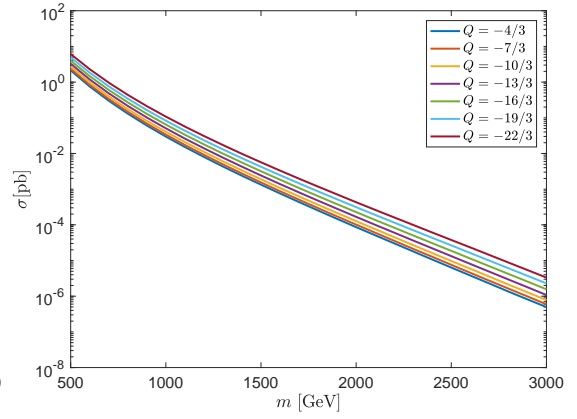
(a) Positively-charged colored scalars.



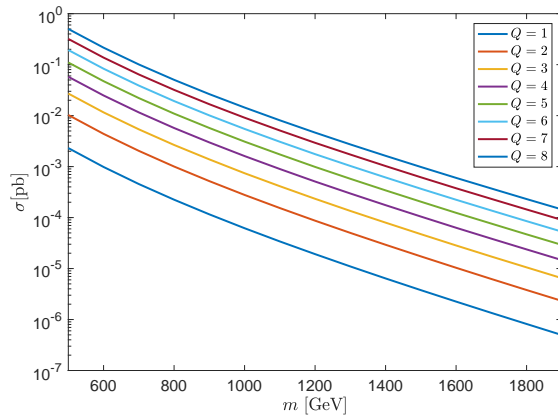
(b) Negatively-charged colored scalars.



(c) Positively-charged colored fermions.



(d) Negatively-charged colored fermions.



(e) Colorless fermions.

Figure A.2: Open-production cross sections at $\sqrt{s} = 13$ TeV.

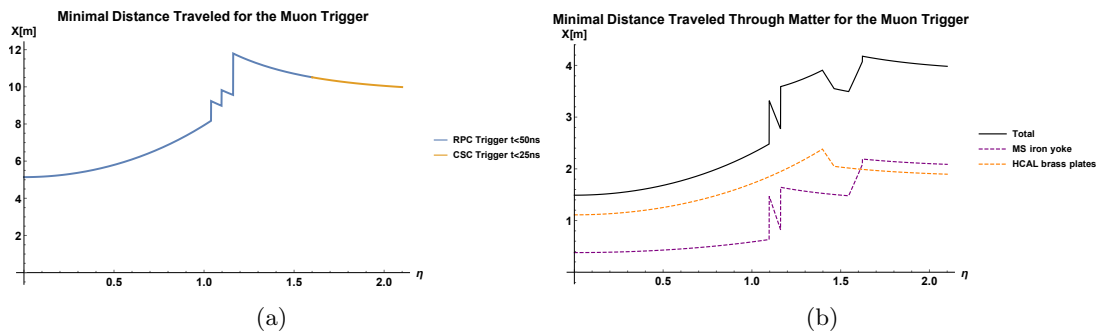


Figure A.3: (a) Minimal distance traveled within the muon trigger time window for high momentum tracks as a function of η . (b) Distance traveled in matter, relevant for ionization energy loss, within the muon trigger time window as a function of η . Both (a) and (b) are based on the layout given in [12].

and it is calculated by numerically solving

$$\frac{d\gamma_{\text{Brass}}}{dx}(x) = \frac{Q^2}{m} \frac{dE}{dx}_{\text{Brass}}(\gamma), \quad \gamma_{\text{Brass}}(0) = \gamma_0 \quad (\text{A.2})$$

$$\frac{d\gamma_{\text{Iron}}}{dx}(x) = \frac{Q^2}{m} \frac{dE}{dx}_{\text{Iron}}(\gamma), \quad \gamma_{\text{Iron}}(0) = \gamma_{\text{Brass}}(x_{\text{HCAL}}^f - x_{\text{HCAL}}^0), \quad (\text{A.3})$$

where γ_0 is γ at production, Q is the charge of the particle and m is the mass of the particle. dE/dx is the energy loss function in the appropriate material for $Q = 1$, and is taken from [165] (brass) and [7] (iron).

Straight Tracks Approximation

We treat candidates as moving in straight lines, since the bending due to the magnetic field is negligible for particles passing the $p_T/Q \geq 40$ selection. A particle tracing a curved track of radius R would travel a distance l in the $r - \theta$ plane before propagating Δr in the radial direction, where

$$l = R \arcsin \frac{\Delta r}{R}, \quad (\text{A.4})$$

$$R = \frac{p_T}{Q \cdot B \cdot 0.303}. \quad (\text{A.5})$$

The magnetic field in the CMS detector is about 2 T in the MS and 3.8 T in the Inner Detector (ID) [166]. Assuming a maximal 4 T magnetic field, the p_T cut allows minimal R of

$$R_{\min} = \frac{40}{4 \cdot 0.303} \approx 33.00. \quad (\text{A.6})$$

Consider the maximal possible Δr distance, which is from the interaction point to the furthest RPC at $\Delta r_{\max} \approx 7$ m,

$$\frac{l}{\Delta r} \Big|_{\max} = \frac{\arcsin \frac{\Delta r}{R} \Big|_{\max}}{\frac{\Delta r}{R} \Big|_{\max}} \approx 1.0077, \quad (\text{A.7})$$

which is indeed a negligible correction to the distance traveled in a straight track.

Global Muon Offline Selection

In the analysis by CMS, the fraction of particles passing the global-muon selection, relative to the total number of particles produced, is given by

$$\begin{aligned} \epsilon_{\text{particles}_{\text{global-muon}}}^{\text{CMS}} &= \epsilon_{\text{online}}^{\text{CMS}} \cdot \epsilon_{\text{offline}_{\text{global-muon}}}^{\text{CMS}} \\ &= \frac{\text{Events}^{\text{CMS}}(\text{muon-trigger} \cup E_T^{\text{miss}})}{\text{Events}} \cdot \epsilon_{\text{offline}_{\text{global-muon}}}^{\text{CMS}}, \end{aligned} \quad (\text{A.8})$$

where $\epsilon_{\text{online}}^{\text{CMS}}$ is the fraction of events passing the online selection, relative to the total number of events. $\epsilon_{\text{offline}_{\text{global-muon}}}^{\text{CMS}}$ is the fraction of particles passing the global-muon criterion, out of the particles passing the online selection. *Events* is the total number of events and $\text{Events}^{\text{CMS}}(\text{selection})$ is the number of events passing a selection. We claim that the particle-level global-muon efficiency can be written as

$$\begin{aligned} \epsilon_{\text{particles}_{\text{global-muon}}}^{\text{CMS}} &= \frac{\text{Events}^{\text{CMS}}(\text{muon-trigger})}{\text{Events}} \cdot \frac{\epsilon_{\text{online}}^{\text{CMS}} \cdot \epsilon_{\text{offline}_{\text{global-muon}}}^{\text{CMS}}}{\epsilon_{\text{events}_{\text{muon-trigger}}}^{\text{CMS}}} \\ &\equiv \alpha^{\text{CMS}}(m, q) \cdot \epsilon_{\text{events}_{\text{muon-trigger}}}^{\text{CMS}} = f(m, q) \cdot \epsilon_{\text{particles}_{\text{muon-trigger}}}^{\text{CMS}}, \end{aligned} \quad (\text{A.9})$$

where $\epsilon_{\text{events}_{\text{muon-trigger}}}^{\text{CMS}}$ is the fraction of events passing the muon-trigger selection, relative to the total number of events. $\epsilon_{\text{particles}_{\text{muon-trigger}}}^{\text{CMS}}$ is the fraction of particles satisfying the muon-trigger requirements, relative to the total number of particles produced, and we hypothesize $f(m, q) \approx 1$.

In our simplified efficiency calculation, we accept only particles that individually satisfy the muon trigger requirements, and omit the global muon selection. So

$$\begin{aligned} \epsilon_{\text{particles}_{\text{global-muon}}}^{\text{sim}} &= \frac{\text{Particles}^{\text{sim}}(\text{muon-trigger})}{\text{Particles}} \\ &= \frac{\text{Events}^{\text{sim}}(\text{muon-trigger})}{\text{Events}} \cdot \frac{\epsilon_{\text{particles}_{\text{muon-trigger}}}^{\text{sim}}}{\epsilon_{\text{events}_{\text{muon-trigger}}}^{\text{sim}}} \\ &\equiv \alpha^{\text{sim}}(m, q) \cdot \epsilon_{\text{events}_{\text{muon-trigger}}}^{\text{sim}}. \end{aligned} \quad (\text{A.10})$$

To check the validity of our assumption, independently of our muon-trigger simulation, we calculate the ratio between $\alpha^{\text{sim}}(m, q)$ and $\alpha^{\text{CMS}}(m, q)$

$$r = \frac{\alpha^{\text{sim}}(m, q)}{\alpha^{\text{CMS}}(m, q)} = \frac{\frac{\epsilon_{\text{particles}_{\text{muon-trigger}}}^{\text{sim}}}{\epsilon_{\text{events}_{\text{muon-trigger}}}^{\text{sim}}}}{\frac{\epsilon_{\text{online}}^{\text{CMS}} \cdot \epsilon_{\text{offline}_{\text{global-muon}}}^{\text{CMS}}}{\epsilon_{\text{events}_{\text{muon-trigger}}}^{\text{CMS}}}}}. \quad (\text{A.11})$$

where the ϵ^{CMS} efficiencies are taken from [5], and ϵ^{sim} efficiencies are obtained from our calculation. Indeed, as seen in Fig. A.4, $r \approx 1$ for all masses and charges for $\sqrt{s} = 8$ TeV. Therefore, we conclude that accepting only particles passing the muon-trigger requirements to be subject for further selection is a reasonable approximation for $\sqrt{s} = 8$ TeV.

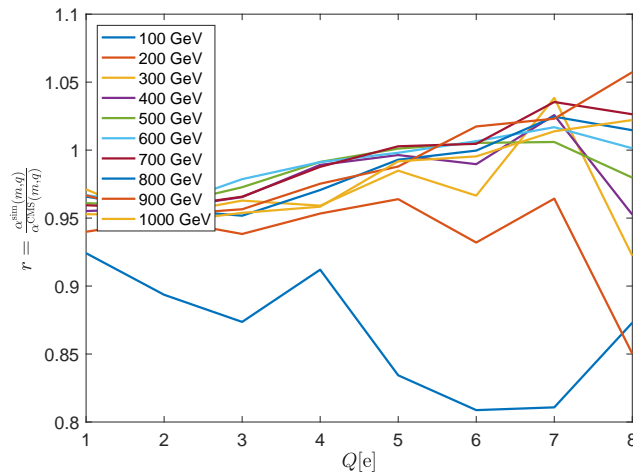


Figure A.4: $r = \alpha^{\text{sim}}(m, q)/\alpha^{\text{CMS}}(m, q)$, the ratio of multiplicative factors required to convert the muon trigger event efficiency into the global-muon offline particle efficiency for our procedure, and for CMS.

Efficiency Values

Here we list the final efficiencies, resulting from our simplified calculation described in Section 4.2.2. The values for a $\sqrt{s} = 8$ TeV search are given for color-triplet scalars, color-triplet fermions and color-singlet fermions in Tables A.1, A.2 and A.3, respectively. The values for a future search at $\sqrt{s} = 13$ TeV are given in Tables A.4, A.5 and A.6, respectively. Masses are in units of GeV.

m/Q	$-\frac{22}{3}$	$-\frac{19}{3}$	$-\frac{16}{3}$	$-\frac{13}{3}$	$-\frac{10}{3}$	$-\frac{7}{3}$	$-\frac{4}{3}$	$\frac{5}{3}$	$\frac{8}{3}$	$\frac{11}{3}$	$\frac{14}{3}$	$\frac{17}{3}$	$\frac{20}{3}$	$\frac{23}{3}$
500	0.043	0.071	0.13	0.22	0.34	0.46	0.55	0.55	0.44	0.32	0.20	0.12	0.072	0.038
600	0.055	0.091	0.16	0.25	0.39	0.50	0.59	0.58	0.50	0.36	0.23	0.14	0.084	0.049
700	0.065	0.11	0.17	0.28	0.41	0.54	0.61	0.60	0.52	0.39	0.26	0.17	0.097	0.059
800	0.071	0.11	0.19	0.30	0.43	0.55	0.63	0.62	0.53	0.41	0.28	0.17	0.10	0.067
900	0.076	0.12	0.20	0.31	0.44	0.56	0.65	0.64	0.54	0.42	0.29	0.18	0.11	0.069
1000	0.074	0.12	0.20	0.32	0.45	0.56	0.63	0.63	0.54	0.42	0.29	0.18	0.11	0.068
1100	0.073	0.12	0.20	0.31	0.45	0.57	0.65	0.64	0.56	0.43	0.30	0.19	0.11	0.065
1200	0.074	0.12	0.20	0.31	0.45	0.57	0.65	0.65	0.55	0.43	0.29	0.18	0.11	0.066
1300	0.070	0.12	0.19	0.31	0.45	0.56	0.66	0.64	0.55	0.42	0.29	0.18	0.11	0.062
1400	0.067	0.11	0.19	0.31	0.45	0.57	0.66	0.65	0.55	0.43	0.28	0.17	0.099	0.058
1500	0.059	0.10	0.18	0.29	0.44	0.56	0.65	0.63	0.54	0.40	0.28	0.16	0.090	0.055
1600	0.054	0.094	0.17	0.28	0.42	0.56	0.65	0.63	0.53	0.40	0.26	0.15	0.087	0.048
1700	0.047	0.087	0.16	0.27	0.41	0.55	0.64	0.63	0.52	0.39	0.25	0.14	0.079	0.041
1800	0.040	0.079	0.15	0.26	0.40	0.53	0.64	0.61	0.52	0.38	0.24	0.13	0.071	0.040
1900	0.039	0.072	0.13	0.25	0.39	0.52	0.63	0.61	0.50	0.37	0.23	0.12	0.062	0.035

Table A.1: Efficiencies for color-triplet scalars at $\sqrt{s} = 8$ TeV.

m/Q	$-\frac{22}{3}$	$-\frac{19}{3}$	$-\frac{16}{3}$	$-\frac{13}{3}$	$-\frac{10}{3}$	$-\frac{7}{3}$	$-\frac{4}{3}$	$\frac{5}{3}$	$\frac{8}{3}$	$\frac{11}{3}$	$\frac{14}{3}$	$\frac{17}{3}$	$\frac{20}{3}$	$\frac{23}{3}$
500	0.049	0.084	0.15	0.24	0.36	0.47	0.55	0.54	0.46	0.34	0.23	0.14	0.077	0.045
600	0.067	0.11	0.17	0.27	0.40	0.51	0.59	0.58	0.49	0.38	0.26	0.16	0.099	0.058
700	0.076	0.12	0.19	0.29	0.42	0.54	0.61	0.60	0.52	0.41	0.28	0.18	0.12	0.075
800	0.084	0.13	0.21	0.32	0.44	0.55	0.62	0.61	0.53	0.43	0.30	0.20	0.12	0.081
900	0.092	0.15	0.22	0.33	0.46	0.55	0.63	0.63	0.55	0.43	0.31	0.21	0.13	0.086
1000	0.094	0.14	0.22	0.33	0.45	0.55	0.62	0.61	0.53	0.44	0.31	0.21	0.14	0.087
1100	0.094	0.14	0.23	0.33	0.46	0.55	0.63	0.62	0.55	0.44	0.32	0.21	0.14	0.085
1200	0.089	0.14	0.23	0.34	0.46	0.56	0.62	0.62	0.55	0.45	0.32	0.21	0.13	0.087
1300	0.088	0.14	0.21	0.33	0.46	0.55	0.63	0.62	0.55	0.44	0.32	0.21	0.14	0.083
1400	0.085	0.13	0.22	0.33	0.46	0.55	0.62	0.60	0.54	0.43	0.31	0.21	0.12	0.081
1500	0.079	0.13	0.21	0.32	0.44	0.55	0.61	0.61	0.54	0.43	0.30	0.20	0.12	0.075
1600	0.074	0.12	0.20	0.31	0.44	0.53	0.61	0.60	0.52	0.41	0.30	0.19	0.11	0.070
1700	0.069	0.11	0.19	0.30	0.43	0.53	0.59	0.59	0.51	0.40	0.28	0.18	0.11	0.062
1800	0.062	0.11	0.18	0.29	0.41	0.51	0.58	0.57	0.50	0.40	0.27	0.16	0.10	0.054
1900	0.055	0.10	0.17	0.27	0.40	0.50	0.56	0.57	0.49	0.38	0.26	0.15	0.089	0.049

Table A.2: Efficiencies for color-triplet fermions at $\sqrt{s} = 8$ TeV.

m/Q	1	2	3	4	5	6	7	8
500	0.61	0.53	0.42	0.28	0.18	0.11	0.061	0.039
600	0.65	0.58	0.47	0.33	0.21	0.13	0.080	0.049
700	0.67	0.60	0.50	0.36	0.23	0.15	0.095	0.061
800	0.69	0.62	0.52	0.39	0.26	0.16	0.11	0.067
900	0.69	0.62	0.53	0.40	0.27	0.17	0.11	0.071
1000	0.68	0.60	0.53	0.41	0.28	0.17	0.11	0.072

Table A.3: Efficiencies for color-singlet fermions at $\sqrt{s} = 8$ TeV.

m/Q	$-\frac{22}{3}$	$-\frac{19}{3}$	$-\frac{16}{3}$	$-\frac{13}{3}$	$-\frac{10}{3}$	$-\frac{7}{3}$	$-\frac{4}{3}$	$\frac{5}{3}$	$\frac{8}{3}$	$\frac{11}{3}$	$\frac{14}{3}$	$\frac{17}{3}$	$\frac{20}{3}$	$\frac{23}{3}$
500	0.041	0.069	0.12	0.19	0.28	0.40	0.48	0.47	0.38	0.27	0.18	0.10	0.061	0.036
600	0.058	0.088	0.14	0.22	0.33	0.43	0.50	0.50	0.42	0.31	0.21	0.13	0.083	0.054
700	0.072	0.11	0.17	0.25	0.36	0.46	0.52	0.52	0.45	0.34	0.24	0.16	0.10	0.067
800	0.084	0.12	0.19	0.28	0.39	0.47	0.54	0.54	0.47	0.37	0.27	0.18	0.11	0.077
900	0.094	0.14	0.21	0.31	0.42	0.50	0.55	0.55	0.49	0.41	0.29	0.19	0.13	0.091
1000	0.10	0.15	0.22	0.31	0.43	0.50	0.56	0.56	0.50	0.40	0.30	0.21	0.14	0.096
1100	0.11	0.15	0.23	0.34	0.45	0.53	0.58	0.57	0.51	0.43	0.31	0.22	0.14	0.10
1200	0.12	0.17	0.25	0.35	0.47	0.55	0.60	0.59	0.53	0.45	0.33	0.23	0.16	0.11
1300	0.12	0.17	0.25	0.37	0.47	0.55	0.61	0.60	0.54	0.45	0.34	0.24	0.16	0.12
1400	0.13	0.18	0.26	0.38	0.49	0.56	0.62	0.61	0.56	0.47	0.36	0.24	0.17	0.12
1500	0.13	0.18	0.27	0.38	0.50	0.58	0.64	0.63	0.57	0.48	0.35	0.25	0.17	0.12
1600	0.13	0.18	0.27	0.39	0.51	0.58	0.65	0.64	0.58	0.48	0.37	0.26	0.18	0.12
1700	0.14	0.19	0.27	0.39	0.51	0.60	0.66	0.64	0.59	0.50	0.37	0.26	0.18	0.12
1800	0.13	0.19	0.27	0.39	0.51	0.60	0.66	0.65	0.58	0.49	0.37	0.26	0.18	0.13
1900	0.13	0.18	0.28	0.39	0.51	0.60	0.66	0.66	0.58	0.49	0.37	0.26	0.17	0.13
2000	0.13	0.18	0.27	0.39	0.52	0.60	0.66	0.65	0.59	0.49	0.37	0.25	0.18	0.12
2100	0.13	0.18	0.26	0.39	0.51	0.60	0.67	0.66	0.58	0.49	0.37	0.25	0.17	0.12
2200	0.12	0.17	0.27	0.39	0.51	0.60	0.66	0.66	0.58	0.49	0.37	0.25	0.16	0.12
2300	0.11	0.17	0.26	0.38	0.51	0.60	0.66	0.65	0.58	0.49	0.35	0.24	0.16	0.11
2400	0.11	0.17	0.25	0.37	0.50	0.59	0.66	0.65	0.58	0.49	0.36	0.24	0.16	0.11
2500	0.11	0.16	0.25	0.37	0.50	0.58	0.66	0.65	0.57	0.48	0.35	0.23	0.15	0.10
2600	0.10	0.15	0.23	0.36	0.49	0.58	0.65	0.64	0.57	0.48	0.35	0.23	0.15	0.099
2700	0.097	0.15	0.23	0.35	0.49	0.57	0.65	0.64	0.55	0.46	0.34	0.21	0.14	0.094
2800	0.094	0.14	0.22	0.34	0.47	0.57	0.65	0.63	0.55	0.45	0.33	0.21	0.14	0.089
2900	0.089	0.14	0.22	0.34	0.46	0.56	0.64	0.63	0.54	0.45	0.32	0.20	0.13	0.085
3000	0.083	0.13	0.21	0.33	0.46	0.55	0.64	0.62	0.54	0.43	0.31	0.20	0.12	0.075

Table A.4: Efficiencies for color-triplet scalars at $\sqrt{s} = 13$ TeV.

m/Q	$-\frac{22}{3}$	$-\frac{19}{3}$	$-\frac{16}{3}$	$-\frac{13}{3}$	$-\frac{10}{3}$	$-\frac{7}{3}$	$-\frac{4}{3}$	$\frac{5}{3}$	$\frac{8}{3}$	$\frac{11}{3}$	$\frac{14}{3}$	$\frac{17}{3}$	$\frac{20}{3}$	$\frac{23}{3}$
500	0.046	0.077	0.13	0.21	0.31	0.40	0.47	0.47	0.40	0.29	0.20	0.12	0.073	0.043
600	0.067	0.10	0.16	0.25	0.35	0.45	0.51	0.50	0.43	0.34	0.23	0.15	0.10	0.063
700	0.083	0.12	0.19	0.28	0.38	0.46	0.52	0.52	0.45	0.36	0.26	0.18	0.12	0.078
800	0.10	0.14	0.21	0.30	0.41	0.49	0.54	0.54	0.48	0.39	0.29	0.20	0.14	0.094
900	0.12	0.16	0.23	0.33	0.42	0.51	0.55	0.55	0.48	0.42	0.31	0.22	0.15	0.11
1000	0.12	0.16	0.24	0.34	0.44	0.50	0.56	0.56	0.50	0.43	0.33	0.23	0.16	0.12
1100	0.14	0.17	0.25	0.36	0.45	0.51	0.58	0.57	0.52	0.45	0.34	0.24	0.18	0.13
1200	0.14	0.19	0.27	0.37	0.48	0.54	0.59	0.58	0.53	0.46	0.35	0.26	0.18	0.13
1300	0.15	0.20	0.28	0.38	0.49	0.55	0.60	0.59	0.55	0.48	0.37	0.27	0.19	0.14
1400	0.15	0.21	0.29	0.39	0.49	0.56	0.61	0.60	0.55	0.48	0.38	0.27	0.20	0.14
1500	0.16	0.21	0.29	0.40	0.50	0.57	0.61	0.61	0.56	0.49	0.39	0.28	0.20	0.15
1600	0.16	0.22	0.30	0.41	0.52	0.58	0.62	0.62	0.57	0.50	0.39	0.29	0.21	0.15
1700	0.16	0.22	0.31	0.41	0.52	0.59	0.63	0.63	0.58	0.51	0.39	0.29	0.21	0.16
1800	0.16	0.22	0.30	0.41	0.52	0.59	0.63	0.63	0.58	0.51	0.40	0.29	0.21	0.16
1900	0.17	0.22	0.31	0.42	0.52	0.59	0.63	0.62	0.57	0.50	0.39	0.29	0.21	0.15
2000	0.16	0.22	0.31	0.42	0.52	0.58	0.64	0.63	0.58	0.52	0.40	0.29	0.21	0.16
2100	0.16	0.22	0.30	0.42	0.51	0.58	0.63	0.63	0.58	0.51	0.40	0.29	0.20	0.15
2200	0.16	0.22	0.31	0.41	0.53	0.59	0.63	0.62	0.58	0.51	0.40	0.28	0.20	0.15
2300	0.15	0.21	0.29	0.41	0.52	0.58	0.63	0.62	0.57	0.50	0.39	0.28	0.20	0.15
2400	0.15	0.20	0.29	0.40	0.52	0.57	0.62	0.61	0.57	0.50	0.38	0.27	0.20	0.14
2500	0.14	0.19	0.28	0.40	0.51	0.58	0.62	0.61	0.56	0.50	0.38	0.27	0.19	0.14
2600	0.14	0.20	0.28	0.39	0.50	0.57	0.62	0.60	0.56	0.49	0.37	0.26	0.19	0.13
2700	0.14	0.19	0.27	0.39	0.50	0.55	0.60	0.59	0.56	0.49	0.37	0.26	0.18	0.13
2800	0.13	0.18	0.26	0.38	0.49	0.55	0.59	0.60	0.54	0.47	0.36	0.25	0.17	0.12
2900	0.12	0.17	0.26	0.37	0.48	0.54	0.58	0.58	0.54	0.47	0.36	0.25	0.17	0.11
3000	0.11	0.17	0.26	0.36	0.48	0.53	0.57	0.57	0.53	0.46	0.35	0.24	0.16	0.11

Table A.5: Efficiencies for color-triplet fermions at $\sqrt{s} = 13$ TeV.

m/Q	1	2	3	4	5	6	7	8
500	0.49	0.44	0.35	0.25	0.16	0.10	0.067	0.041
600	0.54	0.49	0.40	0.29	0.19	0.13	0.086	0.055
700	0.56	0.52	0.44	0.32	0.22	0.15	0.10	0.066
800	0.59	0.53	0.46	0.36	0.26	0.17	0.12	0.082
900	0.61	0.55	0.49	0.38	0.28	0.19	0.13	0.095
1000	0.61	0.55	0.51	0.41	0.29	0.20	0.14	0.10
1100	0.64	0.57	0.53	0.42	0.31	0.21	0.15	0.11
1200	0.65	0.58	0.55	0.44	0.33	0.23	0.16	0.12
1300	0.66	0.60	0.56	0.45	0.33	0.24	0.17	0.13
1400	0.67	0.60	0.57	0.46	0.34	0.24	0.18	0.13
1500	0.68	0.61	0.59	0.48	0.35	0.25	0.18	0.14
1600	0.66	0.60	0.56	0.45	0.35	0.26	0.19	0.15
1700	0.66	0.60	0.57	0.47	0.36	0.26	0.19	0.15
1800	0.66	0.61	0.57	0.47	0.36	0.25	0.19	0.15
1900	0.67	0.61	0.57	0.47	0.36	0.26	0.20	0.15

Table A.6: Efficiencies for color-singlet fermions at $\sqrt{s} = 13$ TeV.

A.1.3 Effective Cross Sections

The effective cross sections for MCHSPs, obtained as a product of the cross sections and the efficiencies corresponding to open-production searches, are presented together with the observed upper limit for $\sqrt{s} = 8$ TeV, and the projected upper limits for $\sqrt{s} = 13$ TeV, in Figs. [A.5](#) and [A.6](#).

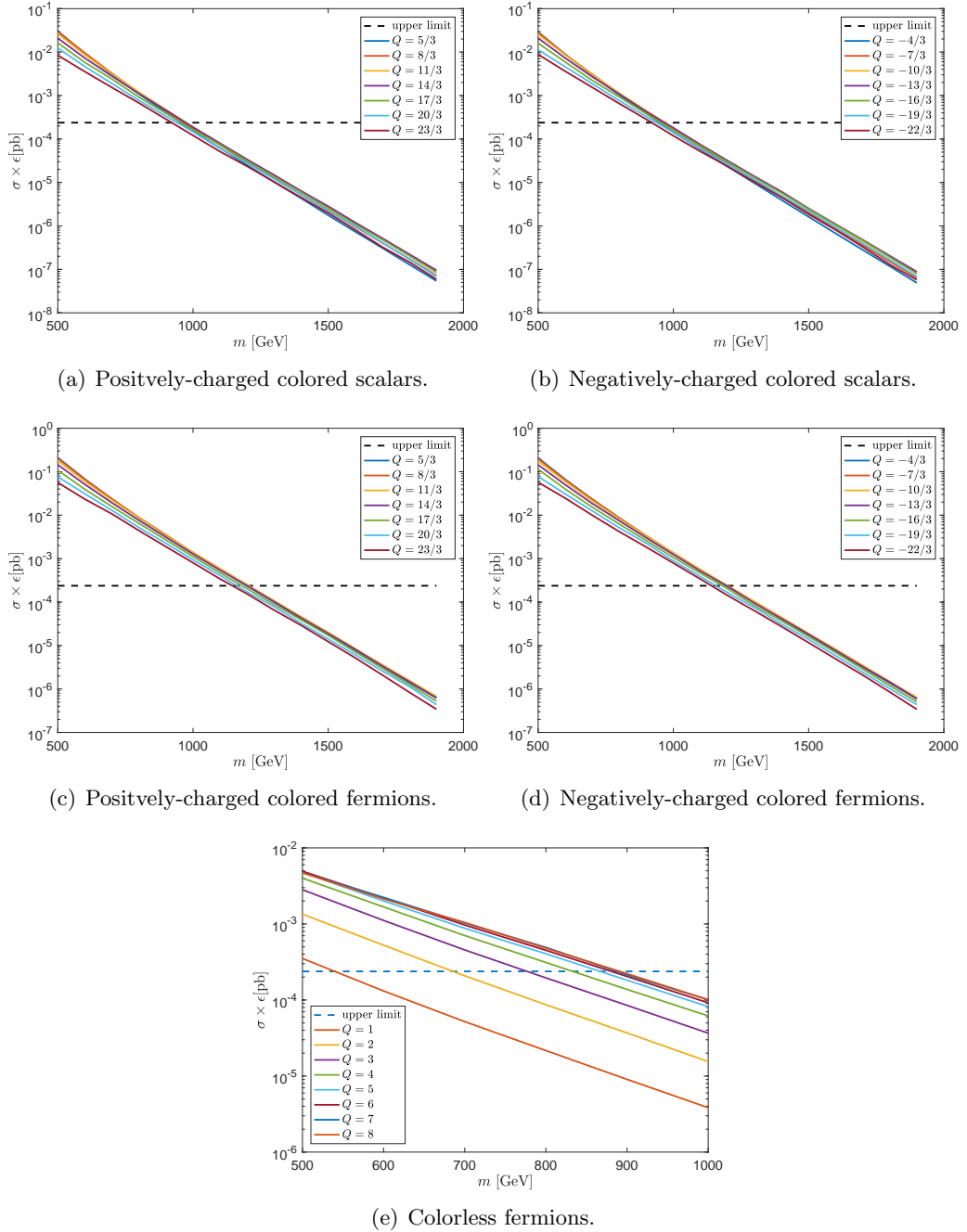


Figure A.5: Open-production channel signatures. Effective cross sections $\sigma \cdot \epsilon$ for CMS search [9] at $\sqrt{s} = 8$ TeV, together with the observed upper bound. *Solid* – theoretical effective cross sections, *dashed* – observed limit.

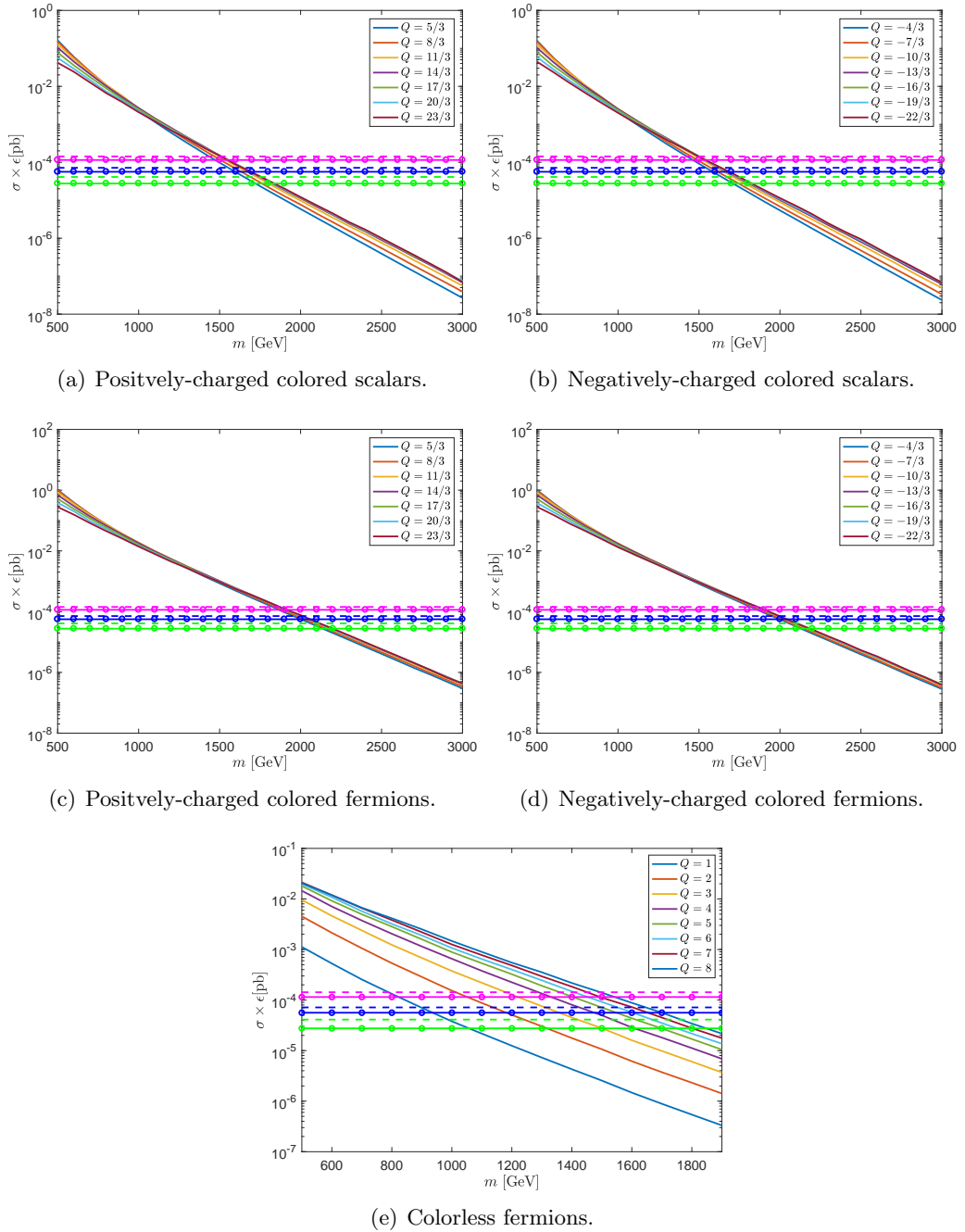


Figure A.6: Open-production channel signatures. Effective cross sections $\sigma \cdot \epsilon$ for future CMS searches at $\sqrt{s} = 13$ TeV, together with expected upper bounds. *Solid* – theoretical effective cross sections. *Round markers* – luminosity scaling. *Dashed* – luminosity scaling and pileup scaling. *Magenta* – $\mathcal{L} = 35.9 \text{ fb}^{-1}$, *blue* – $\mathcal{L} = 100 \text{ fb}^{-1}$, *green* – $\mathcal{L} = 300 \text{ fb}^{-1}$.

A.2 Closed-Production Signatures – Diphoton Cross Sections

The diphoton production cross sections, from a bound state resonance, with observed and future-projected upper limits at $\sqrt{s} = 13$ TeV are presented in Fig. A.7.

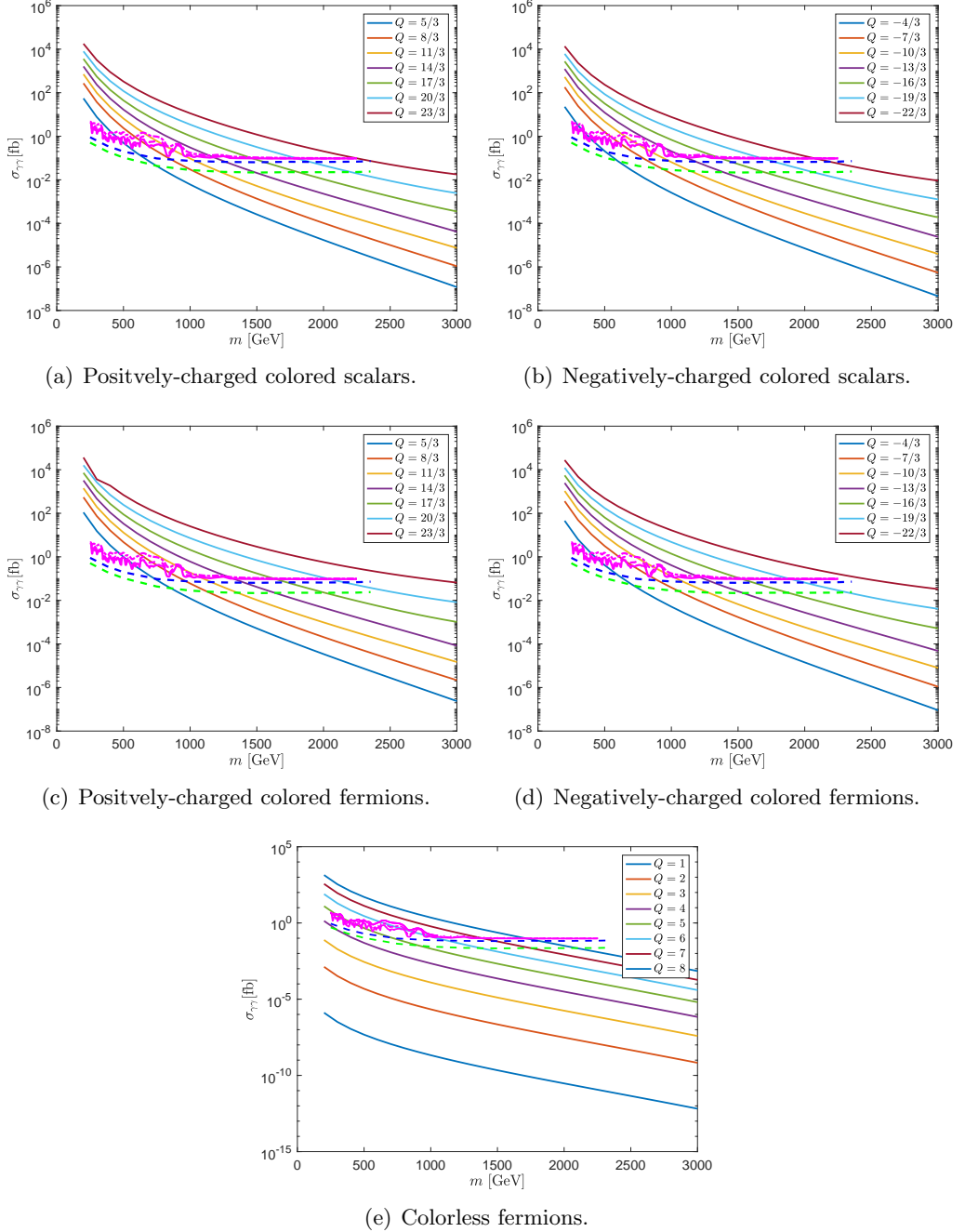


Figure A.7: Diphoton resonant production cross sections, given by a bound state of mass $2m$ at $\sqrt{s} = 13$ TeV. *Magenta* – upper-limits observed at $\mathcal{L} = 35.9 \text{ fb}^{-1}$ [10], (*solid* – narrow, *dashed* – mid-width, *dash-dotted* – wide). *Dashed blue* – upper limits expected at $\mathcal{L} = 100 \text{ fb}^{-1}$ [13]. *Dashed green* – upper-limits expected at $\mathcal{L} = 300 \text{ fb}^{-1}$ [13].

Appendix B

Appendix for Chapter 5

B.1 CP-odd Contribution to Higgs plus One Jet in Relevant Limits

In this appendix we report the expression for the CP-odd contribution to Higgs+Jet production and perform checks in three relevant limits, following the strategy of [167]. This information constitutes an important validation tool for our implementation of the calculation of [116]. This section is structured as follows. We first review the expressions for relevant Higgs production amplitudes. We then discuss the limit in which the mass of the fermion running in the loop is the largest scale. In addition, we consider the limit in which the outgoing gluon is soft. Finally, we study the case in which the outgoing parton is collinear to the beam direction.

B.1.1 Higgs+Jet Production Amplitudes

We first need the expression of the Born matrix element. Due to conservation of angular momentum, the amplitude for the process $gg \rightarrow h$ is non-zero only if the two gluons have opposite helicities. The un-averaged matrix element squared for this process is

$$|M_{gg \rightarrow h}|^2 = \frac{(N_c^2 - 1)\alpha_s^2 \tilde{\kappa}^2 m_H^4}{4\pi^2 v^2} \left| \sum_{i=t, T^1, T^2} \mathcal{M}_{+-}^i \right|^2. \quad (\text{B.1})$$

The index i here refers to the particle running in the loop needed to couple the gluons to the Higgs. The top quark contribution to the above equation is

$$\mathcal{M}_{+-}^i = m_i^2 C_0(m_H^2). \quad (\text{B.2})$$

With this we can report the expression for the matrix element squared for Higgs+Jet production in the various partonic channels contributing to this process: $gg \rightarrow hg$, $q\bar{q} \rightarrow hg$, $qg \rightarrow hq$, qh .

The $gg \rightarrow hg$ amplitude can be expressed in terms of eight primitive helicity amplitudes $\mathcal{M}_{h_1 h_2 h_3}$ corresponding to the possible choices for each gluon helicity $h_i = \pm$. We use the convention that the momenta of gluons p_1 and p_2 are incoming, and that of gluon p_3 is outgoing, so that the Mandelstam variables, in the convention of [116], are defined as

$$s = (p_1 + p_2)^2, \quad t = (p_1 - p_3)^2, \quad u = (p_1 - p_4)^2. \quad (\text{B.3})$$

The helicity amplitudes are then related to the full, un-averaged amplitude squared via

$$|M_{gg \rightarrow Hg}|^2 = \frac{N_c(N_c^2 - 1)\alpha_s^3 \tilde{\kappa}^2}{8\pi v^2} \sum_{h_1, h_2, h_3 = \pm} \left| \sum_{i=t, T^1, T^2} \mathcal{M}_{h_1 h_2 h_3}^i \right|^2. \quad (\text{B.4})$$

After applying parity and crossing symmetry, only four of the helicity amplitudes are independent, which we take to be $\mathcal{M}_{+++}^i, \mathcal{M}_{++-}^i, \mathcal{M}_{-+-}^i, \mathcal{M}_{-++}^i$.

The contributions to the helicity amplitudes due to loops containing a fermion with mass m and coupling to the Higgs $\tilde{\kappa}$, are:

$$\begin{aligned} \mathcal{M}_{+++}^i &= m_i^2 F_1(s, t, u), \\ \mathcal{M}_{++-}^i &= m_i^2 F_1(s, u, t), \\ \mathcal{M}_{-+-}^i &= m_i^2 F_2(s, t, u), \\ \mathcal{M}_{-++}^i &= m_i^2 F_3(s, t, u), \end{aligned} \quad (\text{B.5})$$

where

$$F_1(s, t, u) = \sqrt{\frac{t}{su}} [G(s, t) - G(s, u) + G(t, u)], \quad (\text{B.6})$$

$$F_2(s, t, u) = -\frac{m_H^2}{\sqrt{stu}} [G(s, t) + G(s, u) + G(t, u)], \quad (\text{B.7})$$

$$F_3(s, t, u) = \sqrt{\frac{s}{tu}} [G(s, t) + G(s, u) - G(t, u)], \quad (\text{B.8})$$

and

$$G(x, y) = xyD_0(x, y) + 2xC_1(y) + 2yC_1(x). \quad (\text{B.9})$$

The functions B_1, C_1, D_0 are 1-loop basic scalar integrals. They are functions of (s, t, u) , the mass of the particle in the loop, and the Higgs mass; their definitions can

be found in [168].

The other $pp \rightarrow hj$ subprocesses ($q\bar{q} \rightarrow hg$, $qg \rightarrow hq$, $\bar{q}g \rightarrow h\bar{q}$) are controlled by a third function, the un-averaged amplitude squared

$$\sum |M_{q\bar{q} \rightarrow Hg}|^2(s, t, u) = \frac{2(N_c^2 - 1)\alpha_s^3 \tilde{\kappa}^2 t^2 + u^2}{\pi v^2} \frac{1}{s} \left| \sum_{i=t, T^1, T^2} \mathcal{M}^i(q\bar{q} \rightarrow hg) \right|^2. \quad (\text{B.10})$$

The amplitude for one fermion in the loop is given by

$$\mathcal{M}^i(q\bar{q} \rightarrow hg) = m_i^2 C_1(s). \quad (\text{B.11})$$

We can get the amplitudes for the subprocesses $qg \rightarrow hq$ and $\bar{q}g \rightarrow h\bar{q}$ from the above expression by swapping the Mandelstam variable s and t , and s and u respectively.

B.1.2 Decoupling limit

Here we give analytical expressions for the helicity amplitudes introduced in the previous section in the ‘‘decoupling’’ limit ($m^2 \gg m_H^2, s, |t|, |u|$) where m is the mass of the fermion running in the loops. First, we give the expansion of the scalar integrals appearing in the amplitudes:

$$B_1(q^2) \simeq \frac{q^2 - m_H^2}{6m^2}, \quad C_1(q^2) \simeq -\frac{1}{2m^2} - \frac{q^2 + m_H^2}{24m^4}, \quad D_0(s, t) \simeq \frac{1}{6m^4}. \quad (\text{B.12})$$

This gives

$$\begin{aligned} M_{+++}^i &\simeq -2t\sqrt{\frac{t}{su}}, & M_{++-}^i &\simeq -2u\sqrt{\frac{u}{st}}, \\ M_{-+-}^i &\simeq 2\frac{m_H^4}{\sqrt{stu}}, & M_{-++}^i &\simeq -2s\sqrt{\frac{s}{tu}}. \end{aligned} \quad (\text{B.13})$$

Similarly,

$$\mathcal{M}^i(q\bar{q} \rightarrow hg) \simeq \frac{(N_c^2 - 1)\alpha_s^3 \tilde{\kappa}^2 t^2 + u^2}{2\pi v^2} \frac{1}{s}, \quad (\text{B.14})$$

$$\mathcal{M}^i(qg \rightarrow hq) \simeq -\frac{(N_c^2 - 1)\alpha_s^3 \tilde{\kappa}^2 s^2 + u^2}{2\pi v^2} \frac{1}{t}, \quad (\text{B.15})$$

$$\mathcal{M}^i(g\bar{q} \rightarrow h\bar{q}) \simeq -\frac{(N_c^2 - 1)\alpha_s^3 \tilde{\kappa}^2 t^2 + s^2}{2\pi v^2} \frac{1}{u}. \quad (\text{B.16})$$

B.1.3 Soft limit

The soft limit $p_3 \rightarrow 0$ corresponds to

$$s \rightarrow m_H^2, \quad t, u \rightarrow 0. \quad (\text{B.17})$$

In the soft limit amplitudes are proportional to the tree-level amplitude M_{-+} , therefore we get a non-zero contribution only from \mathcal{M}_{-+-} and \mathcal{M}_{-++} . Keeping the most relevant terms in this limit, Eq.(B.5) gives

$$\mathcal{M}_{-+-}^i \simeq -\frac{m_i^2 m_H^2}{\sqrt{stu}} (stD_0(s, t) + suD_0(s, u) + tuD_0(t, u) + 2sC_1(t) + 2sC_1(u)). \quad (\text{B.18})$$

In the soft limit the relevant integral limits are

$$tC_0(t) \rightarrow 0, \quad uC_0(u) \rightarrow 0, \quad stD_0(s, t) \rightarrow 0, \quad usD_0(u, s) \rightarrow 0, \quad utD_0(u, t) \rightarrow 0, \quad (\text{B.19})$$

which yields

$$\mathcal{M}_{-+-}^i \simeq -4m_i^2 m_H^2 \sqrt{\frac{s}{tu}} C_0(m_H^2) \simeq -(\sqrt{2})^3 \sqrt{\frac{s}{tu}} \mathcal{M}_{+-}^i. \quad (\text{B.20})$$

Similarly, the other helicity amplitude Eq.(B.5) becomes

$$\mathcal{M}_{-++}^i \simeq m_i^2 \sqrt{\frac{s}{tu}} (stD_0(s, t) + suD_0(s, u) - tuD_0(t, u) + 2sC_1(t) + 2sC_1(u)). \quad (\text{B.21})$$

Evaluating again all scalar integrals in this limit we obtain

$$\mathcal{M}_{-++}^i \simeq 4m_i^2 m_H^2 \sqrt{\frac{s}{tu}} C_0(m_H^2) \simeq (\sqrt{2})^3 \sqrt{\frac{s}{tu}} \mathcal{M}_{+-}^i. \quad (\text{B.22})$$

These expressions have to be compared with the universal behaviour of helicity amplitudes [169, 170]¹,

$$\begin{aligned} \mathcal{M}_{-+-}^i &= -(\sqrt{2})^3 \frac{[p_1 p_2]}{[p_1 p_3][p_3 p_2]} \mathcal{M}_{+-}^i, \\ \mathcal{M}_{-++}^i &= (\sqrt{2})^3 \frac{\langle p_1 p_2 \rangle}{\langle p_1 p_3 \rangle \langle p_3 p_2 \rangle} \mathcal{M}_{+-}^i. \end{aligned} \quad (\text{B.23})$$

¹The $\sqrt{2}$ factors comes from the differing normalisation of gauge group generators $\text{tr}[T^a T^b] = \delta^{ab}$ in the spinor helicity formalism, compared to the usual $\text{tr}[T^a T^b] = \frac{1}{2}\delta^{ab}$. This is compensated by a relative $\sqrt{2}$ factor associated to the gauge coupling.

Since we have not used the spinor-helicity formalism, it is not immediate to rephrase our expressions in terms of helicity products. However, for real momenta, spinor products are simply equal to the square root of the relevant momentum invariant, up to a phase. The universal soft factor has an implicit helicity set by the soft gluon, and hence the choice of translating to angle or square bracket spinor products is fixed. We then obtain from Eq.(B.20) and Eq.(B.22) that \mathcal{M}_{-+-}^i and \mathcal{M}_{-++}^i have the correct behaviour (i.e. Eq.(B.23)) in the soft limit, modulo an overall phase that depends on the gluon helicity. This phase is universal for all the particles running in the loop, and therefore can be factored out of each helicity amplitude and will not contribute to the amplitude squared.

B.1.4 Collinear limits

We now consider the limit $t \rightarrow 0$ where p_1 becomes collinear to p_3 . Introducing the splitting fraction $z = \frac{m_H^2}{s}$, the invariants take the values

$$t \rightarrow 0, \quad s = \frac{m_H^2}{z}, \quad u \rightarrow -\frac{1-z}{z}m_H^2. \quad (\text{B.24})$$

In this limit $tC_0(t) \rightarrow 0$, whereas $sC_0(s)$ and $uC_0(u)$ do not vanish. For the box integrals, we have

$$\begin{aligned} suD_0(s, u) &\rightarrow 2 [sC_0(s) + uC_0(u) - m_H^2 C_0(m_H^2)], \\ stD_0(s, t) &\rightarrow 0, \quad tuD_0(t, u) \rightarrow 0. \end{aligned} \quad (\text{B.25})$$

In this limit we get

$$\mathcal{M}_{-+-}^i \simeq -\frac{2m_i^2 m_H^2 (m_H^2 + s + u)}{\sqrt{stu}} C_0(m_H^2) \simeq \frac{4m_i^2 m_H^2 z}{\sqrt{(1-z)\sqrt{-t}}} C_0(m_H^2). \quad (\text{B.26})$$

Similarly, for the other helicity configuration we obtain

$$\mathcal{M}_{-++}^i \simeq \frac{2m_i^2 \sqrt{s} (m_H^2 + s - u)}{\sqrt{tu}} C_0(m_H^2) \simeq -\frac{4m_i^2 m_H^2}{z\sqrt{(1-z)\sqrt{-t}}} C_0(m_H^2). \quad (\text{B.27})$$

Now in the collinear case the limit depends on the helicity of each collinear leg. This means that there are two more possibilities to consider, and therefore we should also look at the limit of the two helicity amplitudes \mathcal{M}_{++-}^i and \mathcal{M}_{+++}^i . For the first we have

$$\mathcal{M}_{++-}^i \simeq \frac{2m_i^2 \sqrt{u} (m_H^2 - s + u)}{\sqrt{st}} C_0(m_H^2) \simeq -\frac{4m_i^2 m_H^2 (1-z)^{3/2}}{z\sqrt{-t}} C_0(m_H^2) \quad (\text{B.28})$$

while the second reads

$$\mathcal{M}_{+++}^i \simeq \frac{2m_i^2 \sqrt{t} (-m_H^2 + s + u)}{\sqrt{su}} C_0(m_H^2) \simeq 0. \quad (\text{B.29})$$

Collecting all results yields

$$\begin{aligned} \mathcal{M}_{-++}^i &\simeq \frac{-(\sqrt{2})^3}{z \sqrt{(1-z)} \sqrt{-t}} \mathcal{M}_{+-}^i, \\ \mathcal{M}_{-+-}^i &\simeq \frac{z(\sqrt{2})^3}{\sqrt{(1-z)} \sqrt{-t}} \mathcal{M}_{+-}^i, \\ \mathcal{M}_{++-}^i &\simeq \frac{-(1-z)^2 (\sqrt{2})^3}{z \sqrt{(1-z)} \sqrt{-t}} \mathcal{M}_{+-}^i, \\ \mathcal{M}_{+++}^i &\simeq 0. \end{aligned} \quad (\text{B.30})$$

To check the correctness of the above limits, we have to translate our conventions for the helicity and the splitting fraction into those available in the literature, in which all momenta are considered to be outgoing. First, we need to flip the helicity of each incoming particle. Additionally, the relation of z to the momenta is different when the collinear gluons are outgoing. One can switch between the two cases by making the replacement $z \rightarrow \frac{1}{z}$. Adopting the usual convention of associating negative momentum signs to angle spinors we expect the behaviour [169, 170]

$$\begin{aligned} \frac{\mathcal{M}_{-++}^i}{\mathcal{M}_{+-}^i} &\simeq \text{Split}_+ \left(-1^-, 3^+; \frac{1}{z} \right) = \frac{-(\sqrt{2})^3}{z \sqrt{1-z} \langle p_1 p_3 \rangle}, \\ \frac{\mathcal{M}_{-+-}^i}{\mathcal{M}_{+-}^i} &\simeq \text{Split}_+ \left(-1^-, 3^-; \frac{1}{z} \right) = \frac{z(\sqrt{2})^3}{\sqrt{1-z} [p_1 p_3]}, \\ \frac{\mathcal{M}_{++-}^i}{\mathcal{M}_{+-}^i} &\simeq \text{Split}_+ \left(-1^+, 3^-; \frac{1}{z} \right) = \frac{-(1-z)^2 (\sqrt{2})^3}{z \sqrt{1-z} \langle p_1 p_3 \rangle}, \\ \frac{\mathcal{M}_{+++}^i}{\mathcal{M}_{+-}^i} &\simeq \text{Split}_+ \left(-1^+, 3^+; \frac{1}{z} \right) = 0. \end{aligned} \quad (\text{B.31})$$

We must now translate Eq.(B.30) to helicity language. The translation from Mandelstam variables to spinor invariants is similar to the soft case, although the helicity consideration is slightly more subtle. As the three legs of the splitting amplitude are collinear, we no longer have information about the contribution from each individual one, since the helicity spinors become proportional. Instead what matters is the overall (outgoing) helicity of the three, which governs whether it is appropriate to translate to angle or square brackets, and with this consideration we indeed find the correct momentum dependence. However, this is not relevant in the end because, up to an overall phase, $[p_1 p_3] \sim \langle p_1 p_3 \rangle \sim \sqrt{-t}$.